



**HAL**  
open science

# Application des méthodes de la géophysique et de télédétection à l'analyse du régolithe et de la géologie du Burkina Faso, Afrique de l'Ouest

Václav Metelka

► **To cite this version:**

Václav Metelka. Application des méthodes de la géophysique et de télédétection à l'analyse du régolithe et de la géologie du Burkina Faso, Afrique de l'Ouest. Géologie appliquée. Université Paul Sabatier - Toulouse III, 2011. Français. NNT: . tel-00670786

**HAL Id: tel-00670786**

**<https://theses.hal.science/tel-00670786>**

Submitted on 17 Feb 2012

**HAL** is a multi-disciplinary open access archive for the deposit and dissemination of scientific research documents, whether they are published or not. The documents may come from teaching and research institutions in France or abroad, or from public or private research centers.

L'archive ouverte pluridisciplinaire **HAL**, est destinée au dépôt et à la diffusion de documents scientifiques de niveau recherche, publiés ou non, émanant des établissements d'enseignement et de recherche français ou étrangers, des laboratoires publics ou privés.



Université  
de Toulouse

# THÈSE

En vue de l'obtention du

## DOCTORAT DE L'UNIVERSITÉ DE TOULOUSE

Délivré par *l'Université Toulouse III - Paul Sabatier*  
Discipline ou spécialité : *Géologie – télédétection*

---

Présentée et soutenue par *Václav METELKA*  
Le *22. Septembre 2011*

**Titre :** *Application des méthodes de géophysique et de télédétection à l'analyse du régolithe et de la géologie du Burkina Faso, Afrique de l'Ouest*

---

### JURY

*Dr. Stanislav OPLUŠTIL - Université Charles à Prague - Président du jury*  
*Prof. John M. MILLER - Université d'Australie-Occidentale - Rapporteur*  
*Dr. Guillaume MARTELET - BRGM - Rapporteur*  
*Dr. Eric de KEMP – Ressources naturelles Canada - Rapporteur*  
*Prof. Jean-Luc BOUCHEZ - GET, UPS - Examineur*  
*Dr. Bohdan KRÍBEK - Service géologique tchèque - Examineur*  
*Prof. Mark W. JESSELL - GET, IRD - Directeur de thèse*  
*Dr. Josef JEŽEK - Université Charles à Prague - Directeur de thèse*

---

**Ecole doctorale :** *Sciences de l'Univers, de l'Environnement et de l'Espace*  
**Unité de recherche :** *GET*

**Directeur(s) de Thèse :** *Mark JESSELL, Josef JEŽEK*  
**Rapporteurs :** *John M. MILLER, Guillaume MARTELET, Eric DE KEMP*

**Charles University in Prague**  
**Faculty of Science**  
**Institute of Geology and Palaeontology**

**University of Toulouse III**  
**Paul Sabatier**  
**Geosciences Environment Toulouse**

Study program: Geology-geological sciences

Specialty: Geology-remote sensing



**Václav Metelka**

# **Geophysical and remote sensing methodologies applied to the analysis of regolith and geology in Burkina Faso, West Africa**

Aplikace geofyziky a dálkového průzkumu Země ve studiu regolitu a geologické stavby

Burkiny Faso, Západní Afrika

Application des méthodes de la géophysique et de télédétection à l'analyse du régolithe et de

la géologie du Burkina Faso, Afrique de l'Ouest

**Ph.D. Thesis**

Thesis supervisors: MARK W. JESSELL, JOSEF JEŽEK

**Prague, Toulouse 2011**

**Prohlášení:**

Prohlašuji, že jsem závěrečnou práci zpracoval samostatně a že jsem uvedl všechny použité informační zdroje a literaturu. Tato práce ani její podstatná část nebyla předložena k získání jiného nebo stejného akademického titulu.

V Praze, 27. 6. 2011

A handwritten signature in blue ink, appearing to read 'Metelka', written in a cursive style.

Mgr. Václav Metelka



---

## Acknowledgements

This work was carried out as a co-tutelle between the Charles University in Prague and Université Toulouse III – Paul Sabatier. I would like to acknowledge the support of both Universities and the French Government. A substantial part of this work would not have been made possible without the aid and support of the WAXI (West African eXploration Initiative) project. During the course of my Ph.D., I have met many people, who have helped me and encouraged me.

I would like to thank Mark Jessell and Lenka Baratoux, who have taken the great risk of accepting me as a student and passed onto me some of their knowledge of modern geology. My thanks belong in the same manner to Josef Ježek, who supported me and provided critical comments to all of the manuscripts. I acknowledge John Miller, Guillaume Martelet, and Eric de Kemp, who kindly accepted to review this thesis. I also want to thank D. Chardon, B. Kříbek, C. McCuaig, K. Martínek, F. Laufek for helpful discussions during the course of the work and Seta Naba for helping in addition to his ideas during the fieldwork in Burkina Faso.

I also need to mention the people at BEAK consultants, who harbored me for several weeks and aided me during my work with neural networks. Thanks goes to Andreas Barth, Andreas Knobloch, Silke Noack, Mathias, Sabine and others. I have been always welcomed at IRD in Burkina Faso, where I have spent a good month during the course of my fieldwork. Equally important was the support from the Czech geological survey.

I have to put forward my family, my parents Václav and Jaromíra, my sisters and their families, my dear aunt Marie, and all of my relatives. They have all supported me immensely.

I am as well indebted to the mining companies SEMAFO, Volta Resources, Avocet Mining, Sanu Resources, and Orezone for providing high-resolution geophysical data, borehole cores, and outcrop maps. I acknowledge in particular M. Crevier, D. Bondé, D. Boisvert, L. Ouedraogo, P. Marquis, A. Zongo, O. Derra, C. Diallo, T. Amoah, and A. Naré for providing us support when conducting fieldwork on the permits of their companies.

I have to acknowledge all of the IRD drivers, who helped us getting around Burkina sometimes to almost unreachable locations without any problems; thank you Salifou, Boukary, and Mathieu.

Cheers to all of my friends both in Czech Republic - Ondra, Petra, Jonáš, Zdenička - I am much obliged for help with translations, Eliška, Igor, Jirka, Jára, Jaruška, DB, Veronika, Katka, and in France - Ana, Tere, Elena, Laurent, Joaquin, Stéphane - thanks for French corrections, Mark, Chris, Herman, David, Camille, Laia and many, many others.

Finally, I have to thank Katka who stood by me, supported me, and cheered me up.

---

## Table of contents

<b>Acknowledgements.....</b>	<b>I</b>
<b>Table of contents .....</b>	<b>II</b>
<b>List of figures.....</b>	<b>V</b>
<b>List of tables .....</b>	<b>IX</b>
<b>List of acronyms.....</b>	<b>XI</b>
<b>Abstract .....</b>	<b>XIII</b>
<b>Abstrakt.....</b>	<b>XIV</b>
<b>Résumé .....</b>	<b>XV</b>
<b>INTRODUCTION AND BACKGROUND.....</b>	<b>16</b>
<b>Introduction et contexte général.....</b>	<b>17</b>
<b>CHAPTER I.....</b>	<b>34</b>
<b>Résumé du chapitre I.....</b>	<b>35</b>
<b>A GEOPHYSICALLY CONSTRAINED LITHO-STRUCTURAL ANALYSIS OF THE EBURNEAN GREENSTONE BELTS AND ASSOCIATED GRANITOID DOMAINS, BURKINA FASO, WEST AFRICA .....</b>	<b>38</b>
1. Introduction .....	39
2. Regional geological setting .....	40
2.1. The Baoulé-Mossi Paleoproterozoic domain .....	40
2.2. Western Burkina Faso .....	42
3. Methodology and data use.....	43
3.1. Airborne magnetometry.....	43
3.2. Airborne gamma ray spectrometry.....	45
3.3. Gravimetric data.....	45
3.4. Remote sensing data.....	46
3.5 Geological outcrop data.....	47
3.6 Digital data integration.....	49
4. Structural framework .....	51
5. Lithological associations and structures: their petrophysics and expression in geophysical data .....	52
5.1. Mafic and ultramafic lithologies .....	53
5.2. Intermediate to acid volcanics.....	54
5.3. Birimian sediments and volcano-sediments.....	55
5.4. Tarkwaian-type sediments .....	55
5.5. Granitoids .....	56
5.6. Doleritic dykes and sills .....	61
5.7. Neoproterozoic sedimentary cover.....	61
5.8. Lateritic weathering of the lithologies.....	61
5.9. Structures.....	62
5.10. Key sub-areas.....	65
6. Discussion .....	69

6.1. Lithologies and structures .....	69
6.2. Strengths and weaknesses of the different datasets .....	71
6.3 Implications for geological evolution of the West African Craton.....	72
7. Conclusions.....	73
<b>CHAPTER II.....</b>	<b>75</b>
<b>Résumé du chapitre II .....</b>	<b>76</b>
<b>JUVENILE PALEOPROTEROZOIC CRUST EVOLUTION DURING THE</b>	
<b>EBURNEAN OROGENY (~2.2–2.0 GA), BURKINA FASO, WEST AFRICA .....</b>	<b>80</b>
1. Introduction.....	81
2. Geological Setting .....	83
2.1. Regional geological framework .....	83
2.2. Distribution of the greenstone belts and granitoid domains .....	88
3. Main lithologies and stratigraphy.....	89
3.1. The Boromo belt .....	89
3.2. The Houndé belt .....	91
3.3. The Banfora belt.....	92
3.4. Tarkwaian-type metasediments.....	92
3.5. Granitoids .....	94
4. Geochemistry of volcanic belts.....	96
5. Structural Evolution .....	100
5.1. Deformation phase D1 .....	100
5.2. Deposition of Tarkwaian-type sediments – Late D1.....	102
5.3. Deformation phase D2.....	103
5.4. Deformation phase D3 and post-Eburnean doleritic dykes .....	105
6. Deep Structure .....	107
6.1. Construction of the models from gravity data.....	107
6.2. Results .....	108
7. Discussion.....	111
7.1. Origin of the greenstone belts .....	111
7.2. Origin of the sedimentary and volcano-sedimentary units .....	112
7.3. Tectonic scenario and mineralization events.....	114
7.4. Geodynamic implications .....	117
8. Conclusions.....	119
<b>CHAPTER III .....</b>	<b>121</b>
<b>Résumé du chapitre III.....</b>	<b>122</b>
<b>VISIBLE AND INFRARED SPECTRAL LIBRARY OF PRECAMBRIAN GRANITE-</b>	
<b>GREENSTONE TERRAINS IN BURKINA FASO, WEST AFRICA .....</b>	<b>126</b>
1. Introduction.....	127
2. Description of sampling area and sampled materials .....	128
3. Observed lithological and soil units .....	129



---

4. Sample measurements and sample preparation .....	132
5. Library description.....	135
6. Spectra description.....	135
6.1 Mafic and intermediate rocks.....	135
6.2 Granitoids.....	136
6.3 Volcano-sediments.....	139
6.4 Tarkwaian-type sediments.....	139
6.5 Taoudeni basin sediments.....	139
6.6 Soils and regolith .....	140
7. Discussion .....	142
8. Conclusions .....	144
<b>CHAPTER IV .....</b>	<b>146</b>
<b>Résumé du chapitre IV .....</b>	<b>147</b>
<b>REGOLITH LANDFORM MAPPING USING AIRBORNE GEOPHYSICS AND REMOTE SENSING DATA IN A NEURAL NETWORK, BURKINA FASO, WEST AFRICA .....</b>	<b>150</b>
1. Introduction .....	151
2. Study area description.....	152
3. Methodology and data use.....	155
3.1 Data preprocessing.....	155
3.2 Training-testing data selection.....	157
3.3 Variable definition .....	160
3.4 Classification .....	163
3.5 Accuracy assessment.....	164
4. Results .....	165
4.1 Neural network classification .....	165
4.2 Comparison between all classification scenarios .....	167
5. Discussion .....	170
5.1 Comparison with the existing maps .....	170
5.2 Perspectives for automated regolith landform mapping .....	171
6. Conclusions .....	172
<b>GENERAL CONCLUSIONS .....</b>	<b>173</b>
<b>Conclusions générales .....</b>	<b>174</b>
<b>General conclusions .....</b>	<b>176</b>
<b>REFERENCES.....</b>	<b>179</b>
<b>LIST OF APPENDICES.....</b>	<b>202</b>

---

---

## List of figures

- Figure 1 *Simplified geological map of the West African Craton (modified after BRGM SIGAfrique); the Paleoproterozoic greenstones are divided into: light grey – intermediate to acid volcano-clastics and volcano-sediments, dark grey – mafic to intermediate lavas and volcanic products.....19*
- Figure 2 *A typical lateritic profile with all regolith facies preserved. (Eggleton, 2001).....21*
- Figure 3 *Distribution of laterites, bauxites, and lateritic soils in Africa, modified from Burke and Gunnell (2008). .....22*
- Figure 4 *A block diagram with typical regolith landforms found in Western Australia and common to West Africa modified after Anand and Paine (2002). .....23*
- Figure 5 *(A) Lateritic regolith surfaces of West Africa; (B) Variations in the spatial extent of lateritic regolith surfaces of West Africa modified after Burke and Gunnell (2008). .....24*
- Figure 6 *Flow Chart of Integrated analysis of remote sensing and traditional field data during geological or regolith landform mapping projects; object in grey belong to traditional field-based mapping, while white object incorporate remote sensing data, modified from Schetselaar et al. (2007). .....27*
- Figure 7 *The electromagnetic spectrum, with regions relevant to remote sensing techniques depicted; VIS-visible, NIR-near infra red, SWIR-short wave infrared, TIR-thermal infrared, C,S,L,P-Band-categories of frequency (wavelength) ranges for radar sensors. ....28*
- Figure I-1 *Schematic maps of the study area. (a) – Simplified geological map of the Leo-Man craton (modified after BRGM SIGAfrique) with the zone of interest outlined; the Paleoproterozoic greenstones are divided into: light grey – intermediate to acid volcano-clastics and volcano-sediments, dark grey – mafic to intermediate lavas and volcanic products. (b) – Simplified geological map derived during this study (Burkina Faso), Ivory Coast area modified after Tagini (1972) and Lüdtke et al. (1998), Ghana area modified after Agyei Duodu et al. (2010); names of the greenstone belts and granitoid domains discussed in the text are displayed; and major shear zones are outlined. ....39*
- Figure I-2 *(a) – Reduced to the pole (RTP) residual magnetic intensity (RMI) grid; (b) – first vertical derivative of the RTP corrected RMI grid overlain by interpreted structures; (c) – Gamma ray ternary grid – corrected absolute concentrations displayed as RGB underlain by the SRTM digital elevation model; (d) – Bouguer anomaly gravimetric grid with an overlay of interpreted structures.....44*
- Figure I-3 *Outcrop map of the study area. Points indicate field-observations from different source databases; polygons outcrop maps and high resolution geophysical data. Outcrop database this study – all points - lithology, detailed structural description and measurement data, selected points – petrography, susceptibility, density, geochemistry; BRGM/BUMIGEB 1 database – all points lithology, selected points – structural measurements and outcrop description, petrography, geochemistry; BRGM/BUMIGEB 2 database – four lithological classes – volcanic, granitoid, sediment, quartz dykes. ....47*
- Figure I-4 *Data analysis scheme; PCA – principal component analysis transformation of the airborne gamma ray data;  $2\frac{3}{4}$  D modeling performed on the gravimetric data (detailed description is given in the companion paper (Baratoux et al., submitted). SRTM – Shuttle Radar Topography Mission, BRGM – Bureau de recherches géologiques et minières, BUMIGEB – Bureau de Mines et Géologie du Burkina Faso, ASTER – Advanced Spaceborne Thermal Emission and Reflection Radiometer. ....49*
- Figure I-5 *Histograms of magnetic susceptibility of selected rock groups. ....52*
- Figure I-6 *Box and whiskers graphs of concentrations of K, eTh and, eU extracted from the airborne data based on locations of selected outcrops and regolith units. bas – basalt, gbr – gabbro, and – andesite, pyr – pyroclastic flow, vs – volcano-sediments, Tkw – Tarkwaian-type sediments, me – magmatic episode, dur – Fe-rich duricrust, spe – soft pediment. ....53*

- Figure I-7 Litho-structural map with the position of four key areas depicted as insets. .... 64
- Figure I-8 Key localities showing details from map shown in figure I- 6. Upper map: RTPMRI (Reduced to the pole residual magnetic intensity) color overlay over first vertical derivative (grey-scale); Intermediate: ternary grid of the airborne gamma ray data or PCA grid; Lower map: geological interpretation. (a) – The western margin of the Boromo belt and the eastern margin of the Houndé belt; (b) – The eastern margin of the Boromo belt and the Koudougou-Tumu granitoid domain ; (c) – The Banfora belt; (d) – The contact zone between the western margin of the Houndé belt and the Sidéradougou GD. HI – high intensity, MI – medium intensity, LI – low intensity, BAS – basalt, GBR – gabbro, AND – andesite, VS – volcano-sediment, TKW – Tarkwaian-type sediments, DOL – doleritic dyke, SPE – soft pediment., DUR – Fe-rich duricrust, intr. – intrusion, w. lith. bnd. – with lithological boundary, subcirc. – subcircular, mag. – magnetic. .... 67
- Figure II-1 Simplified geological map of the Leo-Man Craton (modified after the BRGM SIGAfrique map, Milési et al., 2004), with the study area indicated. Paleoproterozoic greenstones are divided into: light grey – intermediate to acid volcanics and volcanosediments, dark grey – mafic to intermediate lavas and volcanic products. .... 82
- Figure II-2 Revised geological map of the western Burkina Faso (chapter I). The names of the greenstone belts, granitoid domains (GD) and major Birimian (volcano-) sedimentary units referred to in the text are indicated. Radiometric ages are taken from the following sources: (1) Agyei Duodu et al., 2010; (2) Bossière et al., 1996; (3) Castaing et al., 2003; (4) Davis in Schwartz and Melcher, 2003; (5) Lompo, 1991; (6) Lüdtke et al., 1998; some of these ages also published in Hirdes et al., 1996; (7) Siegfried et al., 2009; (8) Thomas et al., 2009. Dating methods U-Pb (U), Pb-Pb (P), K-Ar (K), and Ar-Ar (A) were applied on zircon (z), monazite (m), t – titanite (t), and amphibole (a). The following sources were used for compilation of the geological map: (A) this work; (B) Lüdtke et al., 1998; (C) Tagini, 1972; (D) Agyei Duodu et al., 2010. BA – Banfora, BO – Boromo, BOBO – Bobo-Dioulasso, BT – Batié, DA – Dano, DE – Dédougou, DIE – Diébougou, GA – Gaoua, HO – Houndé, MA – Mana, KA – Kampti, KO – Koudougou, LE – Léo, LO – Loropéni, PE – Perkoa, PK – Ponkélé, PO – Poura, SA – Safané, SID – Sidéradougou, TU – Tumu. GFBSZ – Greenville-Ferkessedougou-Bobo-Dioulasso shear zone (SZ), OFSZ – Ouango-Fitini SZ, BPSZ – Boromo-Poura shear corridor, WBSZ – West Batié SZ. .... 87
- Figure II-3 a) Simplified stratigraphic sequences for the Banfora, Houndé and Boromo belts with the names of the corresponding belts in Ivory Coast and Ghana. Katiola-Marab. – Katiola-Marabadiassa belt. TH – tholeiitic mafic units, THM – tholeiitic megacrystic basalts, TRAN – transitional mafic and intermediate volcanic sequences, CA – calc-alkaline volcanic sequences. b) Radiometric age frequency histograms for Boromo-Lawra-Bole-Nangodi (BLBN) and Houndé-Téhini-Ouango-Fitini (HTOF) greenstone belts (GB) and Koudougou-Tumu (KTGD), Diébougou (DGD) and Sidéradougou (SGD) granitoid domains. The ages shown in the histograms are plotted in figure II- 2. Only U-Pb and Pb-Pb zircon and whole rock ages are taken into account. Note that no radiometric ages exist for the Banfora belt, the Niangoloko granitoid domain and adjacent areas in northern Ivory Coast. .... 90
- Figure II-4 Field photographs of representative structures: a) tholeiitic basalts with plagioclase megacrysts forming pillow lavas, b) megacrystic basalts deformed in the ENE-oriented dextral GFBSZ (Greenville-Ferkessedougou-Bobo Dioulasso shear zone) in the north of the Boromo belt, near Ponkélé (horizontal section), c) penetrative metamorphic foliation S2 in Tarkwaian-type metasediments affected by late steeply dipping spaced cleavage S3, d) steeply dipping NE-trending penetrative magmatic foliation S1 in syntectonic tonalite pluton, e) localized ENE-WSW dextral shear zone S2 in granodiorite, filled by late pegmatite (horizontal section), f) NNE-oriented synkinematic S-C mylonite with dextral sense of movement in two mica granite localized in the GFBSZ close to Banfora (horizontal section), g) penetrative metamorphic foliation S1 in metabasalts folded by F1 folds, h) subvertical NNE-trending shear zone S2 overprinting S1 metamorphic foliation in metabasalts, intruded by syntectonic granite dyke near the contact of the Boromo belt and Diébougou GD; all lithologies are affected by late shallow dipping thrust faults (TF3). .... 93
- Figure II-5 a) AFM diagram of the analyzed volcanic rocks (Irvine and Baragar, 1971), b) TAS diagram of Middlemost (1994); Hb - Houndé belt, Bb - Banfora belt, TH – tholeiites, THM – megacrystic basalts, TRAN – transitional basalts and andesites, CA – Calc-alkaline basalts and andesites. The data were plotted using the GCDkit software (Janoušek et al., 2006). .... 96

Figure II-6 Spiderplots of the four groups a) tholeiites, b) megacrystic basalts, c) transitional basalts and andesites and d) calc-alkaline basalts and andesites, normalized to chondrite (McDonough and Sun, 1995). Black symbols are used for the Boromo belt, white symbols are used for the Houndé belt. ....	97
Figure II-7 Map of geographical distribution of the analysed samples within the greenstone belts. The acronyms are the same as in figure II-5. ....	99
Figure II-8 Structural map showing the orientation S0 bedding and stratigraphic layering, S1 penetrative metamorphic foliation, and the S2 shear zones and high strain zones. L1/L2 lineations are also plotted. Rose diagrams show the strike distribution of dextral (DEX) and sinistral (SIN) shear zones. HO – Houndé, KO – Koumbia, DA – Dano, DI – Diébougou, GA – Gaoua, KTGD – Koudougou-Tumu granitoid domain, DGD – Diébougou granitoid domain, SGD – Sidéradougou granitoid domain, NGD – Niangoloko granitoid domain. Three cross-sections shown in figure II- 12 are indicated. ....	101
Figure II-9 Equal area lower hemisphere stereoplots of the orientation of D1-D3 structures. Rose diagrams show the distribution of the foliation strikes and brittle fractures and faults. ....	103
Figure II-10 Simplified structural map indicating major shear zones/high strain zones and axial planes of the regional scale F1 folds. BPSZ – Boromo-Poura shear corridor; GFBSZ – Greenville-Ferkessedougou-Bobo-Dioulasso Shear zone; OFSZ – Ouango-Fitini shear zone; WBSZ – West Batié shear zone. ....	104
Figure II-11 Densities of the lithologies used in the 2¾ D gravity modeling. Bas – basalt, gbr – gabbro, and – andesite, pyr – pyroclastic flow, vs – volcano-sediments and Birimian sediments, Tkw – Tarkwaian-type sediments, grd – granodiorite, gra – granite. ....	107
Figure II-12 Three geological cross-sections with their corresponding gravity models. The geographic location of the profiles as well as the stations of gravity measurements, which were projected onto the geological profiles for the modeling purposes, is indicated in figure II- 8. ....	109
Figure II-13 Summary table of the tectonic evolution. Ban – Banfora belt, K-M – Katiola-Marabadiassa belt, Ho-W – Houndé belt west of the Boni shear zone, Ho-E –Houndé belt east, OF – Ouango Fitini belt, Téh – Téhini belt, Bor-W –Boromo belt west of the Batié basin, Bor-E –Boromo belt east, Law – Lawra belt. For acronyms, see also figure II- 3. Radiometric ages presented in the histograms are referenced in figure II-2. ....	111
Figure II-14 Tectonic scenario for western Burkina Faso during the Eburnean orogenesis. The surface corresponds to the present-day erosional level. ....	116
Figure III-1 Simplified geological map of the Leo-Man craton modified after BRGM SIGAfrique (Milési et al., 2004) with the zone of interest outlined; the Paleoproterozoic greenstones are divided into: light grey – intermediate to acid volcano-clastics and volcano-sediments, dark gre – mafic to intermediate lavas and volcanic products. ....	128
Figure III-2 Lithological (a) and pedological (b) map of the study area. White stars represent spectral measurement locations. The maps are compiled from Castaing et al. (2003) and the IRD Valpedo GIS ( <a href="http://www.miruram.mpl.ird.fr/valpedo/miruram/Burkina/index.html">http://www.miruram.mpl.ird.fr/valpedo/miruram/Burkina/index.html</a> , respectively. TTG – tonalites-trondhjemitites-granodiorites. ....	130
Figure III-3 Field photographs of principal lithologies with weathered and unweathered surfaces (displayed as insets), a - gabbro, b - andesite, c - volcano-sediments, d - Tarkwaian-type sediments, e - Granodiorite, f - Granite, g - Taoudeni basin sandstones, and h - common Fe-rich duricrust plateaus with cut surface (displayed as inset). ....	134
Figure III-4 Relative reflectance of the main lithological types - Volcanic and volcano-sedimentary rocks. Mean reflectance of each lithological group is drawn with solid line, plus and minus one standard deviation is displayed as dashed line. Absorption features are indicated with vertical lines and horizontal brackets. ....	137
Figure III-5 Relative reflectance of the main lithological types - Granitoids and sedimentary rocks. Mean reflectance of each lithological group is drawn with solid line, plus and minus one standard deviation is	

---

<i>displayed as dashed line. Absorption features are indicated as vertical lines and horizontal brackets.</i> .....	138
Figure III-6 <i>Relative reflectance of the main soil types (spectra are offset for clarity and sorted by increasing reflectance), A - soil formed over basalts and gabbros, B - soil formed over andesites and andesitic pyroclastites, C - soil formed over Tarkwaian-type sediments, D - soil formed over granites and TTGs, E - soil formed over sediments - sandstones, F - soil formed over volcano-sediments.</i> .....	140
Figure III-7 <i>Relative reflectance of Fe-rich regolith materials and vegetation (spectra are offset for clarity), A - Fe-rich duricrust cut surface, B - Fe-rich duricrust exposed surface, C - Fe-rich lag, D - dry vegetation, E - green vegetation.</i> .....	141
Figure III-8 <i>Relative reflectance of surface materials derived from andesites (spectra are offset for clarity), A - Relative reflectance of andesitic rock, B, F - its weathered surfaces, C - associated soil found close to outcrops and on agricultural fields - E, the effect of vegetation residues and lag material - D, G on the soil spectra.</i> .....	142
Figure IV-1 <i>Schematic map of the study area. Geological map of the Northeastern part of the Paleoproterozoic Baoule Mossi domain in the West African Craton (modified after BRGM SIGAfrigue) with study area marked by a rectangle. The Paleoproterozoic greenstones are divided into: light grey – intermediate to acid volcano-clastics and volcano-sediments, dark grey – mafic to intermediate lavas and volcanic products.</i> .....	152
Figure IV-2 <i>Regolith landforms found in the area with chronological and petro-geochemical characteristics given, figure modified after Michel (1973), Grandin (1976) and Gunnel (2003).</i> .....	153
Figure IV-3 <i>Existing 1:500 000 scale pedo-geomorphological and morphological maps of the region, a) pedogeomorphological map (Brossard, 2006), b) geomorphological map (IGN, 2005).</i> .....	154
Figure IV-4 <i>An overview map with normalized slope values draped over shaded relief of the SRTM digital elevation model; the distribution of the training/testing polygons used in the classifications is given.</i>	158
Figure IV-5 <i>ASTER VNIR image showing the study area. Geomorphological units are marked along with examples of burn scars. Small white rectangular patches correspond to agricultural fields.</i> .....	159
Figure IV-6 <i>Combined image with ratio <math>eTh/K</math> image (upper half of the image) and ternary radiometric image <math>K, eTh, eU</math> as RGB (lower half of the image) draped over shaded relief of the SRTM digital elevation model; the geomorphological units are marked with arrows, elev - elevated.</i> .....	161
Figure IV-7 <i>Pauli decomposition of ALOS PALSAR data with the geomorphological units marked where possible. Blue areas correspond to single bounce scattering, red around the Town of Gaoua – double bounce scattering (buildings), green channel-volume scattering related to vegetation, high intensity, white color – residual ridges.</i> .....	162
Figure IV-8 <i>Result of the neural network classification based on 11 input layers. red – Fe-rich duricrusts of the High/Middle glacia, blue – Residual relief, yellow – Alluvium, magenta – Low glacia.</i> .....	165
Figure IV-9 <i>Result of the maximum likelihood classification based on 11 input layers; red – Fe rich duricrusts of the High/Middle glacia, blue – Residual relief, yellow – Alluvium, magenta - Low glacia.</i> .....	167
Figure IV-10 <i>Result of the neural network classification based on 24 input layers; red – Fe rich duricrusts of the High/Middle glacia, blue – Residual relief, yellow – Alluvium, magenta – Low glacia.</i> .....	168

---

---

## List of tables

Table I-1 <i>Outcrop information included in the collected and used databases. Outcrops in the first three databases are stored as point features. BRGM/BUMIGEB 1 – Castaing et al. (2003), * at places contains orientations as text description, BRGM/BUMIGEB 2 – Marcelin (1971), Marcelin and Serre (1971).Data from mining companies contain outcrops as outcrop polygons and points, at places supplemented with structural measurements (points).Obs. count – count of observations made, Litho. – lithological data, Struc. – structural measurements, Susc. – magnetic susceptibility, Dens. – density, Geoch. – geochemistry (only for selected locations).</i> .....	48
Table I-2 <i>Correlation matrix between selected source layers used in the interpretation. RTPMRI – reduced to the pole residual magnetic intensity, TC – total count (airborne gamma ray data), DEM – digital elevation model, GRAV – Bouguer anomaly grid.</i> .....	50
Table I-3 <i>Summary table of the lithologies; their mineralogical, petrophysical characteristics, and expression in the airborne geophysical data. DTM – digital terrain model, andes. – andesite, volc.-sedim. – volcano-sediment, Qtz – quartz , Pl – plagioclase, Cpx – clinopyroxene, Hbl – hornblende, Act – actinolite, Chl – chlorite, Ep – epidote, Bt – biotite, Kfs – K-feldspar, Kln – kaolinite, Czo – clinozoisite, Carb – carbonate, Hem – hematite, Gt – goethite. Folds/Faults – red line – interpreted fault/shear zone, yellow line – lithological contact, turquoise line – interpreted fold hinge.</i> .....	61
Table I-4 <i>Strengths and weaknesses of available geophysical and remote sensing data in lithological and structural mapping.</i> .....	71
Table II-1 <i>Representative geochemical analyses of mafic and intermediate volcanic rocks of the greenstone belts.</i> .....	98
Table II-2 <i>Synthesis of deformation events published in literature, put into the framework of the present study. Direction indications in italics (NE-, NW- etc.A1) stand for the strike, other direction indications signify "vergent" or "oriented". Following acronyms and shortcuts were used: GB - greenstone belt, SZ - shear zone or strike slip fault, Tkw - Tarkwaian, depo. - deposition, defo. - deformation, Birim. sedim. - Birimian sediments, volc. - volcanism, plut. - plutonism, met. or metam. fab. - metamorphic fabric, cren. clv. - crenulation cleavage, iso. - isoclinal, intracont. - intracontinental, comp. - compression, ext. - extension, transpres. - transpression, transten. - transtension, sin. - sinistral, dex. - dextral, react. - reactivation, struct. - structures, juxtapos. of L &amp; H grade metam. - juxtaposition of low and high grade metamorphic terranes.</i> .....	106
Table III-1 <i>Descriptions of principal lithologies and their weathered surfaces, based on petrological macroscopic,microscopic and structural observations; (Qtz - quartz , Pl - plagioclase, Cpx - clinopyroxene, Hbl - hornblende, Act - actinolite, Chl - chlorite, Ep - epidote, Bt - biotite, Kfs - K-feldspar, Kln - kaolinite, Czo - clinozoisite, Carb - carbonate, Hem - hematite, Glt - glauconite, Gth - goethite).</i> .....	131
Table IV-1 <i>Utilized datasets with detailed description on original processing, spatial resolution, and spectral coverage. *Landsat – only 30 m bands used, bands 1-5, 7; **all 14 bands used and resampled to 30m, pol. – polarimetric, abs. – absolute.</i> .....	155
Table IV-2 <i>Training and testing pixels for the mapped classes, N. – number.</i> .....	158
Table IV-3 <i>Confusion matrix for neural network classification compared with the validation data using 11 source data layers including only SRTM derivatives and gamma-ray spectrometry data.</i> .....	166
Table IV-4 <i>Confusion matrix for Neural network classification compared with the validation dataset using 24 source data layers - first 10 PCA bands ASTER, slope, slope roughness, hypsometric integral, residual relief, curvature, height above stream, 6 ALOS PALSAR and Radarsat – 2 Pauli decomposition bands, and two ratio grids eTh/K, eU/K.</i> .....	169
Table IV-5 <i>Confusion matrix for maximum likelihood classification compared with the validation dataset using 24 source data layers. Layers are the same as in table IV-4.</i> .....	169

---

Table IV-6 *Summary of classification results according to the used layers. SRTM – derivative layers (slope, slope roughness, curvature, relative relief, hypsometric integral, height above closest stream), Gamma ray – eTh/K, eU/K,\*(K, eTh, eU), Radarsat-2 – 3 Pauli decomposition channels, ALOS PALSAR – 3 Pauli decomposition channels, Landsat – 6 bands, ASTER – \*\*first 10 PCA bands. ANN – artificial neural network classification, O. A. – overall accuracy, ML – maximum likelihood classification..... 170*

---

## List of acronyms

---

Acronym	Meaning
ACP	Analyse des Composantes Principales
AFM	Al, Fe, Mg diagram
ALOS PALSAR	Advanced Land Observing Satellite Phased Array type L-band Synthetic Aperture Radar
ANN	Artificial Neural Network
ASD	Analytical Spectral Devices
ASTER	Advanced Spaceborne Thermal Emission and Reflection Radiometer
ASU	Arizona State University
ATCOR	Atmospheric/Topographic Correction
BRGM	Bureau de Recherches Géologiques et Minières
BUMIGEB	Bureau des Mines et de la Géologie du Burkina
CA	Calc-alkaline basalts and andesites
CESBIO	Centre d'Etudes Spatiales de la Biosphère
CFA	Crystal Field Absorption
CGIAR	Consultative Group on International Agricultural Research
CPCS	Commission de Pédologie et Cartographie des Sols
CTA	Charge Transfer Absorption
DEM	Digital Elevation Model
DGD	Diébougou Granitoid Domain
DLR	Deutsches Zentrum für Luft- und Raumfahrt (German Aerospace Center)
DPCA	Directed Principal Component Analysis
DTM	Digital Terrain Model
ESA	European Space Agency
eTh	equivalent Thorium
eU	equivalent Uranium
FVD	First Vertical Derivative
Ga	Gigaannum, billions of years
GD	Granitoid Domain
GET	Géosciences Environnement Toulouse
GFBSZ	Greenville-Ferkessedougou-Bobo-Dioulasso Shear Zone
GIS	Geographic Information System
GPS	Global Positioning System
HH, HV, VH, VV	particular combination of transmit/receive wave polarization in radar polarimetry (Horizontal, Vertical)
HREE	Heavy Rare Earth Elements
HSV	Hue, Saturation, Value
HT	High Temperature
ICP-AES	Inductively Coupled Plasma Atomic Emission Spectroscopy
ICRAF	International Centre for Research in Agroforestry
IGN	Institut Géographique National
IGRF	International Geomagnetic Reference Field
IRD	Institut de Recherche pour le Développement
ISRIC	International Soil Reference and Information Centre

---



---

Acronym	Meaning
KTGD	Koudougou-Tumu Granitoid Domain
LANDSAT ETM+	Land remote sensing Satellite Enhanced Thematic Mapper Plus
LiDAR	Light Detection and Ranging
LREE	Light Rare Earth Elements
Ma	Megaannum, millions of years
ME1-4	Magmatic Episode
ML	Maximum likelihood
MP/MT	Medium Pressure/Medium Temperature
NASVD	Noise-Adjusted Singular Value Decomposition
NGD	Niangoloko Granitoid Domain
NIR	Near Infrared
OFSZ	Ouango-Fitini shear zone
ORSTOM	Office de la Recherche Scientifique et Technique d'Outre-Mer
PCA	Principal Component Analysis
REE	Rare Earth Elements
RGB	Red, Green, Blue
RMI	Residual magnetic intensity
RTP	Reduction To the Pole
SFF	Spectral Feature Fitting
SGD	Sidéradougou Granitoid Domain
SIG	Système d'information géographique
SOAR	Sciences and Operational Application Research
SPOT	Système Pour l'Observation de la Terre
SRTM	Shuttle Radar Topography Mission
SWIR	Short Wave Infrared
SYSMIN	System for Mineral Products
TAS	Total Alkali Silica diagram
TES	Temperature/Emissivity Separation algorithm
TH	Tholeiites
THM	Megacrystic basalts
TIR	Thermal Infrared
TRAN	Transitional basalts and andesites
TTG	Tonalite-Trondhjemite-Granodiorite
USGS	United States Geological Survey
VIS	Visible
VNIR	Visible Near Infrared
WAXI	West African Exploration Initiative
XRD	X-ray Diffraction

---

---

## Abstract

The oldest parts of continents, so-called cratons, are the focus of worldwide research not only because they represent primary constraints for our understanding of the early evolution of the Earth, but also because of their significant mineral potential. This work contributes to the understanding of the geological and geomorphological evolution of the West African Craton, by an integrated analysis of airborne geophysical and satellite remote sensing data constrained by field structural, lithological, geophysical, and geomorphological observations acquired around Houndé, Boromo and Banfora greenstone belts and associated granitoid domains in western Burkina Faso.

The results of this integration suggest that the granitoid domains of western Burkina Faso are formed by numerous small- to medium-sized plutons, and the magnetic data provided a better definition of the actual pluton shapes. Airborne gamma ray spectrometry data aided in the mapping process in areas with less regolith cover. Three deformation events (D1-D3) can be distinguished in western Burkina Faso. A megacrystic tholeiitic basalt unit allowed us to establish stratigraphic correlations between the two belts and propose a crustal scale anticline (D1). The D1 penetrative structures, resulting from an E-W to WNW-oriented compression are generally overprinted by the D2 transcurrent shear zones, which is well visible in the magnetic data. Previously unreported and already known S2 shear zones represent prospective areas for gold exploration. The regional-scale system geometry was controlled by coaxial shortening of stiffer volcanic units and coeval magma input. The last D3 N-S compression is either late-Eburnean or perhaps even Pan-African.

The mineralogical composition of rocks and derived regolith surfaces may be assessed by visible and infrared spectroscopy. A new spectral library has been acquired consisting of in situ and laboratory 0.35  $\mu\text{m}$  to 2.5  $\mu\text{m}$  spectra of rocks and derived regolith materials. The reflectance spectra of rocks show the influence of typical arid to semi-arid weathering. Fe-OH and Mg-OH absorption features are observable in the mafic and intermediate volcanic rocks as well as in the granodiorites and tonalites. Al-OH absorptions are typical for volcano-sedimentary and sedimentary rocks, and regolith materials. Ferric and ferrous iron absorptions were observed in most of the sampled materials. The spectra of soils partially reflect the mineral composition of the weathered rock surfaces.

Airborne gamma ray spectrometry data, ASTER, Landsat, and polarimetric radar data, along with morphometric parameters derived from the SRTM digital elevation model, were used to characterize four different regolith landform units in the Gaoua area. An artificial neural network classification was applied to the dataset and compared with a maximum likelihood classifier. The best results were obtained with a combination of gamma-ray spectrometry data and derivatives of the digital elevation model. The classification contributed to an increase in the accuracy of the distribution of the classified units and to an actualization of their respective shapes. The approach demonstrates the potential of neural networks for the combined analysis of airborne geophysical and remote sensing data in regolith landform mapping.

---

## Abstrakt

Nejstarší části kontinentů, takzvané kratony, jsou v současnosti centrem zájmu celosvětového výzkumu nejen proto, že jejich znalost je nezbytná pro porozumění raného vývoje Země, ale také vzhledem k jejich značnému významu v oblasti těžby nerostných surovin. Výsledky této práce přispívají k pochopení geologického a geomorfologického vývoje Západoafrického kratonu. K jejich získání bylo použito integrované analýzy leteckých geofyzikálních dat, satelitních dat dálkového průzkumu Země a dat získaných během terénních měření v západní části Burkiny Faso, v oblastech zelenokamenových pásů Houndé, Boromo, Banfora a přidružených granitoidních domén.

Výsledky tohoto komplexního přístupu ukazují, že granitoidní území západní Burkiny Faso tvoří větší množství malých až středně velkých plutonů. Pomocí magnetometrických dat byly zpřesněny zejména tvary těchto intruzivních těles. V oblasti západní Burkiny Faso můžeme definovat tři deformační fáze (D1-D3). Stratigrafická korelace provedená mezi zmíněnými zelenokamenovými pásy na základě výskytu jednotky megakrystických bazaltů nasvědčuje dřívějšímu propojení obou pásů. Penetrativní struktury D1 vzniklé v režimu vz. až zsz. orientované komprese jsou obvykle přetištěny transkurentními střížnými zónami D2, což je dobře viditelné i v magnetických datech. Nově objevené i stávající střížné zóny S2 představují perspektivní oblasti pro průzkum ložisek zlata. Regionální strukturní stavba vznikala během koaxiální komprese kompetentních vulkanických hornin současně s vmísťováním granitoidních těles. Poslední deformační fáze D3 je zřejmě pozdně Eburnská nebo náleží až k Panafrické orogenezi.

Mineralogické složení horninových a regolitových povrchů lze studovat, metodami dálkového průzkumu Země pomocí viditelné a infračervené spektroskopie. Spektra hornin a z nich odvozených regolitových materiálů naměřených v terénu a laboratoři v rozsahu 0,35–2,5  $\mu\text{m}$  tvoří základ nové spektrální knihovny. Horninová spektra ukazují vliv typického semi-aridního zvětrávání. Fe-OH a Mg-OH absorpční pásy byly pozorovány u mafických a intermediárních vulkanických hornin, granodioritů a tonalitů. Al-OH absorpční pásy jsou typické nejen pro vulkano-sedimentární a sedimentární horniny, ale také pro regolitové povrchy. Absorpční pásy související s obsahem železa byly nalezeny téměř ve všech měřených materiálech. Spektra půd částečně odpovídají minerálnímu složení zvětralých hornin.

Data letecké gamaspektrometrie, data ze senzorů ASTER, Landsat a polarimetrická radarová data byla, společně s parametry odvozenými z digitálního modelu reliéfu SRTM, použita pro popis a analýzu čtyř různých regolitových terénních jednotek v oblasti Gaoua. Ke klasifikaci bylo využito metody neuronových sítí, která byla srovnána s metodou maximální věrohodnosti. Nejlepšího výsledku bylo dosaženo kombinací dat letecké gamaspektrometrie a dat odvozených z digitálního modelu reliéfu. Klasifikace přispěla k celkovému zpřesnění prostorového rozdělení jednotlivých celků a aktualizaci jejich tvarů. Tento přístup ukazuje potenciál neuronových sítí v integrované analýze dat letecké geofyziky a dat dálkového průzkumu Země při mapování regolitových terénních celků.

---

## Résumé

Les parties les plus anciennes des continents, les cratons, sont au centre des recherches mondiales non seulement parce qu'ils représentent des contraintes primaires pour notre compréhension de l'évolution primitive de la Terre, mais aussi en raison de leur potentiel minier important. Ce travail contribue à la compréhension de l'évolution géologique et géomorphologique du craton ouest africain, par une analyse intégrée de géophysique aéroportée, des données de télédétection, et des observations acquises autour des ceintures de Houndé, Boromo et Banfora et des domaines des granitoïdes associés dans l'ouest du Burkina Faso.

Les résultats de cette intégration suggèrent que les domaines de granitoïdes sont formés par de nombreux plutons, d'une taille petite et moyenne. Ainsi, les données magnétiques ont fourni une meilleure définition des formes réelles de ces plutons. Trois événements de déformation (D1-D3) peuvent être distingués dans l'ouest du Burkina Faso. L'unité de basalte tholéiitique à mégacristsaux de plagioclase nous a permis d'établir des corrélations stratigraphiques entre les deux ceintures. Les structures D1 pénétratives, résultant d'une compression orientée EO à ONO-ESE sont généralement recoupées par les zones de cisaillement D2. Ces zones de cisaillement D2 représentent des zones de prospective pour l'exploration aurifère. La géométrie régionale du système est gouvernée par un raccourcissement coaxial des unités volcaniques rigides et par un rajout progressif des magmas granitiques. La dernière compression (D3), est tardi-éburnéenne ou peut-être même panafricaine.

La composition minéralogique des roches et de leurs surfaces d'altération peut être étudiée à l'aide de spectroscopie visible et infrarouge. Une nouvelle bibliothèque spectrale a été acquise, composée des mesures in-situ et en laboratoire (0,35–2,5  $\mu\text{m}$ ) des roches et des matériaux régolithiques. Les spectres de réflectance des roches montrent l'influence d'altérations typiques des zones semi-arides. Les absorptions caractéristiques de Fe-OH et Mg-OH sont observables dans les roches mafiques et volcaniques intermédiaires ainsi que dans les granodiorites et tonalites. Les absorptions Al-OH sont typiques pour les roches volcano-sédimentaires et sédimentaires, et les matériaux de régolithe. Les absorptions de fer ferrique et ferreux ont été observées dans la plupart des matériaux échantillonnés. Les spectres des sols reflètent partiellement la composition minérale de la surface des roches altérées.

Les données de spectrométrie gamma aérienne, ASTER, Landsat et de radar polarimétrique, ainsi que les paramètres morphométriques dérivés du modèle numérique de terrain SRTM, ont été utilisés pour caractériser les unités de régolithe dans la zone de Gaoua. Une méthode de classification par réseaux de neurones a été appliquée à l'ensemble des données, et ensuite comparée à un classificateur par maximum de vraisemblance. Les meilleurs résultats ont été obtenus avec une combinaison de spectrométrie gamma et des dérivés du modèle numérique de terrain. L'approche démontre le potentiel des réseaux de neurones pour l'analyse combinée de géophysique aéroportée et de données de télédétection dans la cartographie de régolithe.

---

# INTRODUCTION AND BACKGROUND

---

## **Introduction et contexte général**

Les parties les plus anciennes des continents, les cratons, sont au centre de recherches mondiales non seulement parce qu'ils représentent des contraintes primaires pour notre compréhension de l'évolution primitive de la Terre, mais aussi en raison de leur potentiel minier important. Sans sous-estimer l'importance des études précédentes, le bouclier ouest-africain reste sous-étudié par rapport à ses équivalents géologiques en Australie et au Canada. Ce craton particulier représente un point tournant dans l'histoire de la terre : un changement des mécanismes de formation de la croûte continentale juvénile. La croûte continentale stable située dans la zone tropicale a permis le développement de processus d'altération superficielle prolongés, dans l'ensemble des lithologies, et a ainsi abouti à un épais manteau de régolithe qui couvre la plupart de la surface du craton Leo-Man, la partie sud du craton ouest-africain. La couverture du régolithe est un obstacle à des études géologiques et géochimiques d'exploration, mais présente également un grand intérêt pour la recherche tectono-géomorphologique de l'évolution de l'Afrique occidentale. La cartographie traditionnelle de la géologie et du régolithe basée sur les observations de terrain est un procès long qui fait face à des difficultés d'extension des observations locales à l'échelle régionale ainsi que d'une couverture des données insuffisante.

Les interprétations des données magnétiques, gravimétriques, de spectrométrie gamma et de télédétection satellitaire, contraintes par les observations de terrain, ont prouvé leur efficacité pour déchiffrer la hiérarchie des cadres litho-structuraux régionaux des terrains précambriens, pourtant presque aucune étude de telle nature n'existe pas en Afrique de l'Ouest. De façon similaire, l'intégration des données géophysiques et satellitaires a été appliquée pour la cartographie du régolithe en Australie. Cependant, très peu d'études utilisant l'approche semi-automatique ont été effectuées en Afrique de l'Ouest pour des fins d'évaluation de distribution et de caractérisation du régolithe et l'approche pleinement automatique n'a jamais été utilisé jusqu'à ce jour. Enfin, à ce jour, très peu d'attention a été accordée à une analyse intégrée des différents types de données avec un accent sur la géologie et le régolithe.

La détection des assemblages lithologiques et des corps géologiques, la définition du cadre structural et l'identification des unités et du relief du régolithe seront réalisés à travers une approche d'intégration des données multiples à l'échelle régionale, en exploitant la vue synoptique des données aéroportées et satellitaires. Les observations de terrain, et les mesures de terrain et de laboratoire serviront de contraintes et de données de validation. Le modèle géodynamique, conçu par une approche intégrée, abordera avec une meilleure précision la géométrie 3D du système ainsi que la chronologie relative de certaines structures à grande échelle.

Avec une disponibilité croissante de nouvelles sources de données qui sont actuellement libérées et qui seront publiées dans les prochaines décennies, des approches similaires à celles proposées dans cette thèse pourront être utilisés dans d'autres régions d'Afrique occidentale et au-delà.

## **Introduction and background**

### **Problem statement**

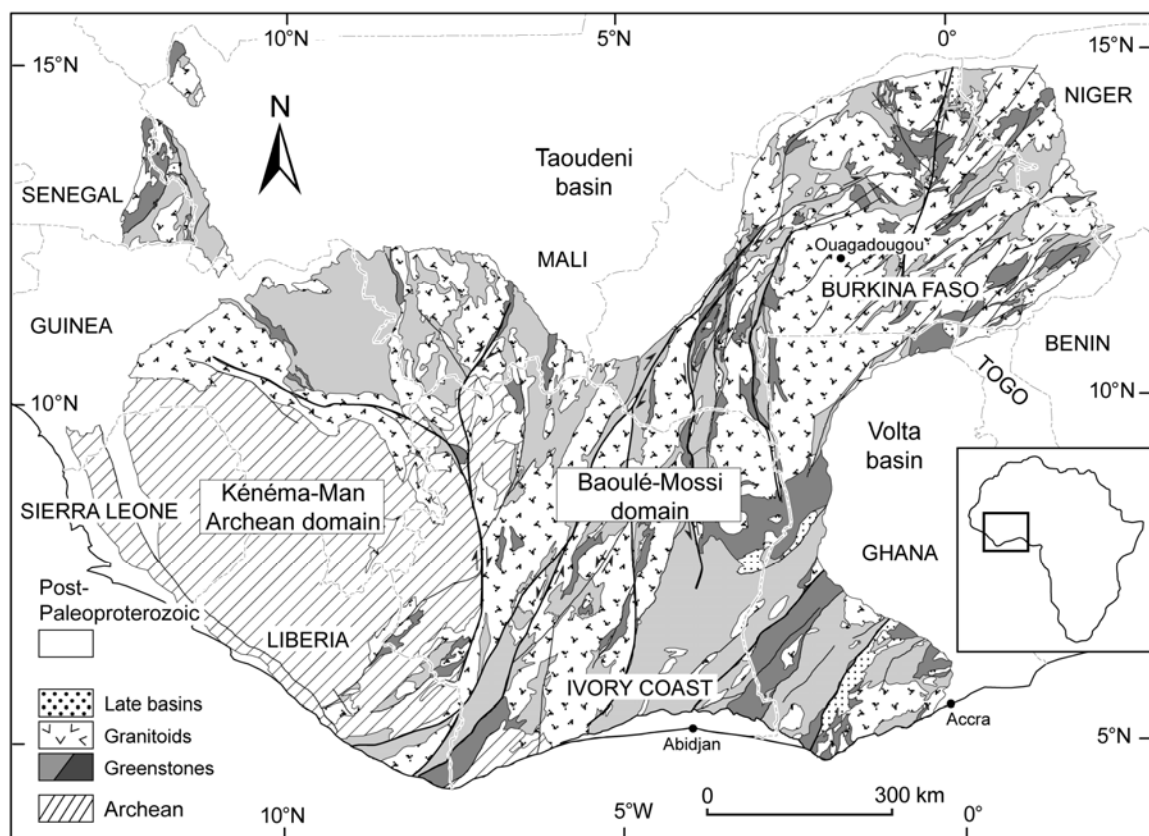
The oldest parts of continents, so-called cratons, are the focus of worldwide research not only because they represent primary constraints for our understanding of the early evolution of the Earth, but also because of their significant mineral potential. Without underestimating the importance of previous studies, the West African shield remains an under-researched craton compared to its geological equivalents in Australia and Canada. This particular craton formed at a turning point in the Earth's history, when the mechanisms of new continental crust formation were changing. The stable continental crust situated in the tropical zone allowed for prolonged weathering of all of the lithologies and resulted in a thick regolith mantle, which covers most of the surface of the Leo-Man Shield, the southern part of the West African Craton. The regolith cover hinders geological studies and geochemical exploration; however, knowing the distribution of different regolith landform units is of great interest for tectono-geomorphic research of the evolution of West Africa. Mapping the geology and regolith over vast areas with traditional field based methods is a lengthy process facing difficulties of extending local observations to regional scale features and insufficient data coverage.

Interpretations of magnetic, gravimetric, gamma ray spectrometry and satellite remote sensing data constrained by field observations proved to be efficient in deciphering the regional litho-structural hierarchies of Precambrian terrains, yet almost no similar studies exist in West Africa. Similarly integrating geophysical and remote sensing data has frequently been applied in regolith landform mapping in Australia; however to date only several studies have been reported from West Africa using a semi-automated approaches in assessing the distribution and characteristics of regolith landform units while no fully automatic approach has been attempted. Finally, to date very little attention has been paid to comprehensive types of studies analyzing different types of data with a focus on both the bedrock geology and the regolith.

Through an integrated approach, the detection of lithological assemblages, geological bodies, definition of the structural framework and identification of regolith landform units will be achieved at regional scales, exploiting the synoptic view of airborne and satellite data. Field mapping, field measurements, and laboratory measurements will serve during the interpretation as constraints and validation data. The geodynamic model acquired through an integrated approach will address with improved accuracy the 3D geometry of the system as well as the relative chronology of some of the large-scale structures. With an increasing availability of new data, which are currently being released, and will be released over the next decades, approaches similar to the proposed research may be used in other regions of West Africa and beyond.

## Overview of the geology of West Africa and Burkina Faso

The greenstone belts of western Burkina Faso represent a typical granite-greenstone terrain of the Paleoproterozoic Baoulé-Mossi domain in the southern part of the West African Craton (figure 1) (Bessoles, 1977; Abouchami et al., 1990; Boher et al., 1992; Taylor et al., 1992; Béziat et al., 2000; Debat et al., 2003). The NNE-SSW to N-S arcuate belts stretch for more than 400 km and are host to multiple gold and base metal deposits (Milési et al., 1992; Béziat et al., 2008). They belong to a polycyclic orogen that formed around the Kénéma-Man Archean nucleus during the Eburnean orogeny (2200–2000 Ma) (Bonhomme, 1962; Liégeois et al., 1991; Milési et al., 1992; Ledru et al., 1994; Egal et al., 2002). Many studies describe the polyphase litho-structural setting and propose in essence two distinct geotectonic models for the evolution of the Paleoproterozoic basement in West Africa. A traditional plate tectonic model of crustal buildup by thrust and fold belts similar to the modern orogens has been proposed by Boher et al. (1992), Feybesse and Milési (1994), Ledru et



**Figure 1** Simplified geological map of the West African Craton (modified after BRGM SIGAfrique); the Paleoproterozoic greenstones are divided into: light grey – intermediate to acid volcanoclastics and volcano-sediments, dark grey – mafic to intermediate lavas and volcanic products.

al., (1994), Hirdes et al., (1996), Debat et al., (2003), Feybesse et al., (2006), Tshibubudze et al.,



(2009), Hein, (2010). Pons et al. (1995) or Vidal et al. (2009) on the other hand favor the dome and basin structures caused by gravitational processes referred to as “vertical tectonics”.

The Baoulé-Mossi domain (figure 1) forms the eastern and northern part of the Leo-Man Craton (Bessoles, 1977). Typical Archean-like greenstone-granitoid assemblages (de Wit and Ashwall, 2006) that principally consist of volcanic, volcano-sedimentary, and sedimentary sequences, which are separated by extensive tonalite-trondhjemite-granodiorite and granitoid provinces, characterize the Paleoproterozoic domain. The volcanic and volcano-sedimentary rocks belong to the Birimian Supergroup, which probably formed in the context of volcanic arcs and oceanic plateaus (Abouchami et al., 1990; Leube et al., 1990; Boher et al., 1992; Taylor et al., 1992; Pouclet et al., 1996; Béziat et al., 2000). Radiometric dating of the volcanic units (Davis et al., 1994; Loh and Hirdes, 1996; Lüdtke et al., 1998; Lüdtke et al., 1999) places the main peak of the Birimian volcanism at around 2190–2160 Ma, while detrital zircons from the sedimentary basins yield ages as young as 2130 Ma (Lüdtke et al., 1999) or 2107 Ma (Doumbia et al. 1998). The Birimian volcanic and volcano-sedimentary units are unconformably overlain at several places across the craton by detrital shallow water sedimentary rocks, which are known as the Tarkwaian sediments (Whitelaw, 1929; Sestini, 1973; Leube et al., 1990; Oberthuer et al., 1998; Feybesse et al., 2006). The whole complex of volcanic, volcano-sedimentary, and sedimentary units was intruded by several generations of granitoids. The granitic plutons were emplaced during several magmatic pulses from 2180 to 1980 Ma (Leube et al., 1990; Pons et al., 1995; Hirdes et al., 1996; Doumbia et al., 1998; Castaing et al., 2003; Gasquet et al., 2003; Naba et al., 2004; Siegfried et al., 2009; Thomas et al., 2009; Agyei Duodu et al., 2010). The general geochemistry of the granitoids evolves from Na-rich calc-alkaline to K-rich alkaline (Boher et al., 1992) while their shape depends on tectonic regime during their emplacement, ranging from undeformed circular plutons to elongate and complex interlocked bodies (Pons et al., 1991; Pons et al., 1992; Pons et al., 1995).

The Eburnean orogeny is generally divided into two major deformation phases. The first phase, which caused major crustal thickening (Boher et al., 1992; Milési et al., 1992; Allibone et al., 2002; Feybesse et al., 2006; Vidal et al., 2009), operated approximately during 2130–2100 Ma. The second phase that lasted up to 1980 Ma was responsible for the formation of regional scale transcurrent shear zones and faults, which transect all lithologies. Gold mineralization in West Africa is generally related to these shear zones (e.g. Milési et al., 1989; Milési et al., 1992; Blenkinsop et al., 1994; Bourges et al., 1998; Allibone et al., 2002; Feybesse et al., 2006). Most of the volcanic and sedimentary rocks underwent lower to upper greenschist facies metamorphism (Béziat et al., 2000; Feybesse et al., 2006; Křibek et al., 2008). Although John et al. (1999) and Galipp et al. (2003) described regional MP/MT conditions (500–600°C, 5–6 kbar) in Ghana, amphibolite facies metamorphism is mostly restricted to the contact aureoles of granitic plutons (Debat et al., 2003). The consolidated Eburnean basement was then locally affected by a N-S oriented compressional event (Nikiéma et al., 1993; Debat et al., 2003; Hein, 2010) and unconformably overlain by the

Neoproterozoic sediments of the large Taoudeni, Lullemeden, and Volta basins. Dyke swarms crosscut the entire Proterozoic domain in several directions and belong to at least six different generations (Jessell et al., 2010).

### Lateritic weathering and geomorphology of West Africa and Burkina Faso

The regolith in West Africa represents an important economic resource (Wright et al., 1985), a constraint on the regions tectono-geomorphic evolution (Michel, 1973; Grandin, 1976; Leprun, 1979; Boeglin, 1990; Tardy, 1997; Beauvais, 1999; Chardon et al., 2006), and a hindrance to geochemical exploration techniques (Craig, 2001; Taylor and Eggleton, 2001). The term regolith stands for all of the weathered and unconsolidated material from basement rock to earth surface including interbedded fresh rocks (Taylor and Eggleton, 2001). A simplified regolith terminology of a typical laterite weathering profile may be found in figure 2. The laterite profile consists of several regolith facies, from the bottom to the top – bedrock, saprock, saprolite, plasmic zone, mottled zone or ferruginous saprolite, lateritic residuum (lateritic duricrust, lateritic gravel). The facies correspond to the intensity of weathering processes and due to mechanical erosion or differences in parent rock materials, not all

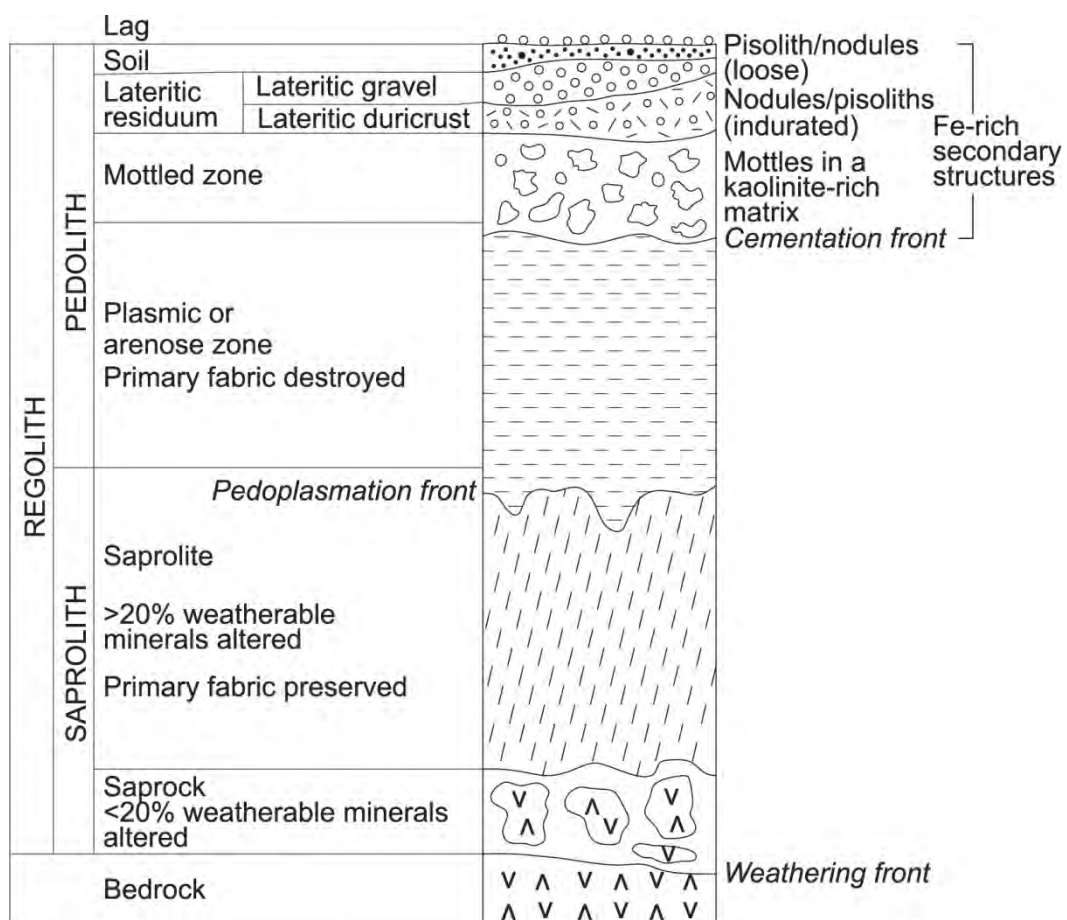
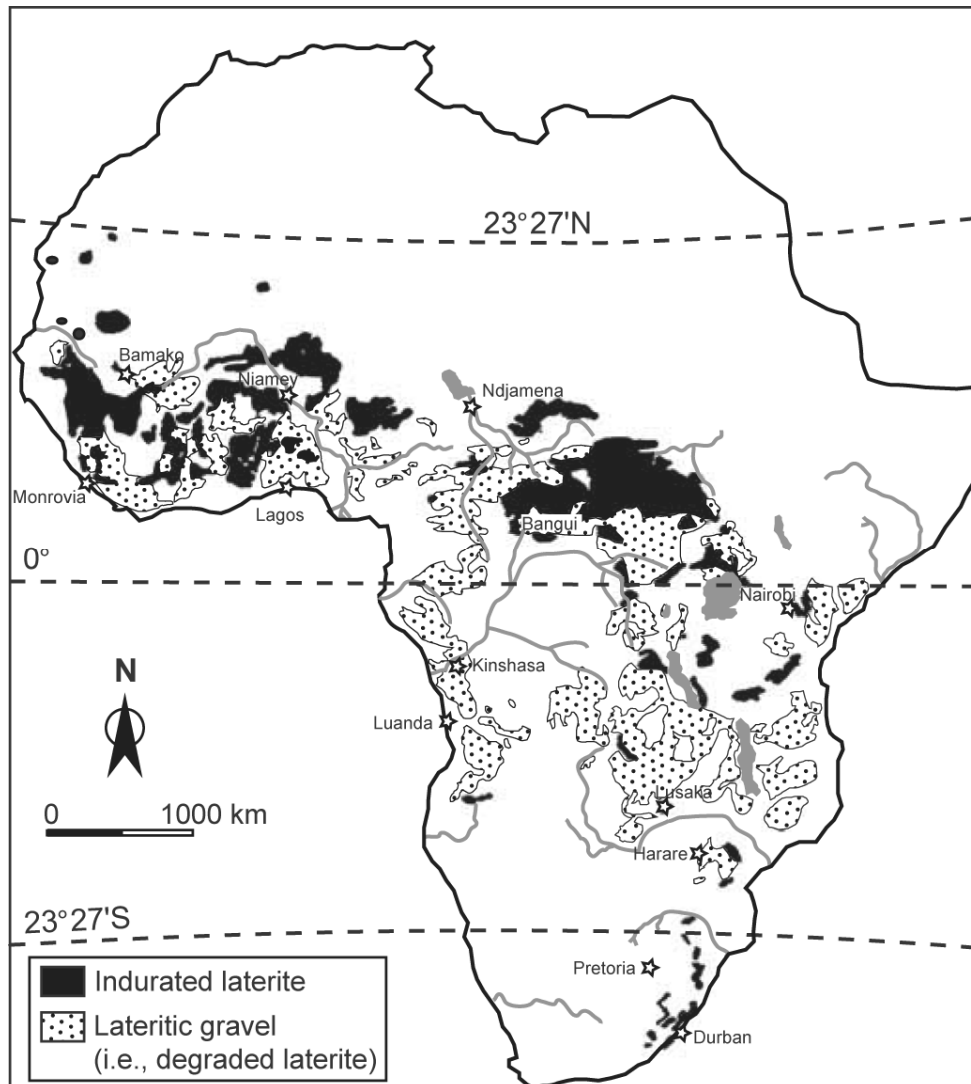


Figure 2 A typical lateritic profile with all regolith facies preserved. (Eggleton, 2001)

of the facies have to be always present. Tardy (1997) estimates that nearly one third of the area of all continents is covered by regolith resulting from lateritic weathering. The distribution of lateritic



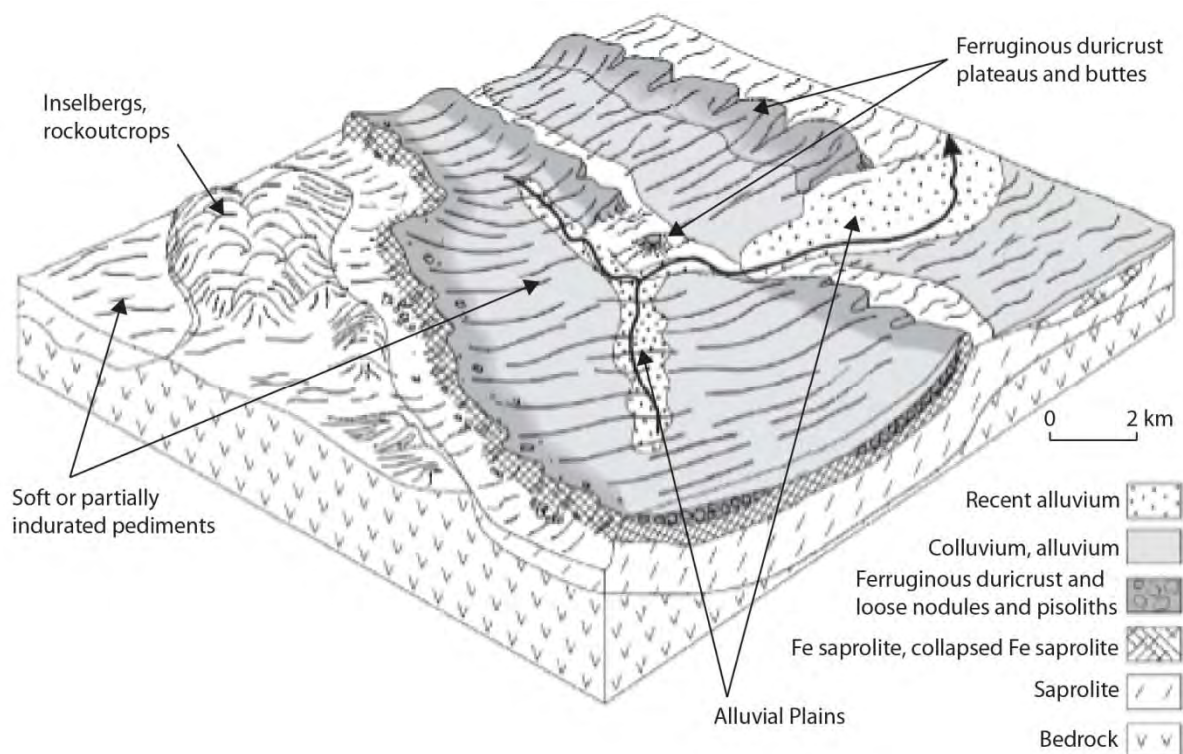
**Figure 3** Distribution of laterites, bauxites, and lateritic soils in Africa, modified from Burke and Gunnell (2008).

materials in Africa is depicted in figure 3.

From a geomorphological point of view, the occurrence of different regolith facies is tied with several types of regolith landforms belonging to the erosional, depositional, or residual regime. The most common and pronounced features include residual Fe-rich duricrust plateaus, erosional inselbergs or rock outcrops, and depositional infill of alluvial plains. Figure 3 shows some of the landform features found in Western Australia and common as well in West Africa.

The planation surfaces of western Burkina Faso, which developed on basement rocks of the West African Craton, are the result of long-term deep weathering, erosion, and gradual uplift of the African continent under varying climatic conditions (King, 1962) mainly after the breakup of Gondwana in the Mesozoic (Wright et al., 1985). In all of West Africa, these surfaces are capped by

ferruginous or aluminous duricrusts, which are ordered in a stepped manner and correspond to a chronological sequence in which they were formed (Michel, 1973; Grandin, 1976; Tardy, 1997). Seven planation surface classes (figure 3A) have been established according to correlations between relative height, geochemistry, and petrology tying the oldest surface with the Gondwanian era and the youngest in age reaching the Quaternary period (Gunnell, 2003; Beauvais et al., 2008; Burke and Gunnell, 2008). The formation mechanism of the duricrusts includes a combination of processes where in situ formation (Leprun, 1979) down slope mechanical displacement and subsequent

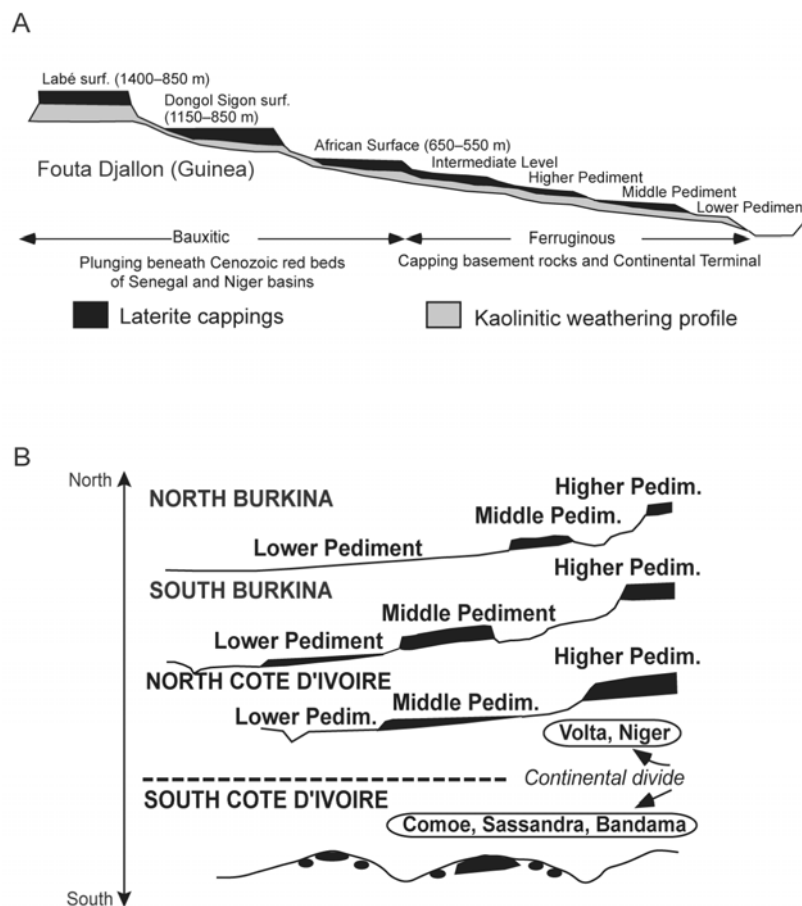


**Figure 4** A block diagram with typical regolith landforms found in Western Australia and common to West Africa modified after Anand and Paine (2002).

recementation acted together (Beauvais, 1999). The lateritization processes are also connected with residual bauxite and manganese deposits, and secondary enrichment of iron ore deposits (Wright et al., 1985; Tardy, 1997; Lavaud et al., 2004).

The lateritic surfaces of southwestern Burkina Faso were thoroughly studied by Boeglin and Mazaltarim (1989) and Boeglin (1990). According to Boeglin (1990), only three of the planation surfaces are present in the south of Burkina Faso. Recently Beauvais et al. (2008) reported dating of the surfaces from northern Burkina Faso. Relics of the highest bauxitic African surface (Eocene, 59–45 Ma) are found at the top of the eroded sequences above 500 m. The Intermediate surface (Oligocene, 34–29 Ma) has not been observed and either has been completely eroded or did not exist in the region. The other ferruginous surfaces belong to the so-called high glaciais (Late Oligocene-Early

Miocene, 24–18 Ma) and middle glacia (Middle to Late Miocene, 12–7 Ma). These surfaces are not easily separable and according to Boeglin (1990), it can be concluded that there has been probably one continuous inclined or undulating surface rather than two distinct levels. The area of southwestern Burkina Faso provides contrasting geological basement of alternating greenstone belt lithologies and granitic bodies. There seems to be at least some linkage between the chemical composition of the iron rich duricrusts and the underlying basement rocks (Boeglin, 1990). Blot et al. (1973) also evaluated



**Figure 5** (A) Lateritic regolith surfaces of West Africa; (B) Variations in the spatial extent of lateritic regolith surfaces of West Africa modified after Burke and Gunnell (2008).

correlations between basement geochemistry and regolith geochemistry; where again at local scale moderate to significant relationship exists. Tardy (1997) however states, that the petrological and mineralogical differences are subtle and become progressively smaller with the evolution and ageing of the lateritic surfaces.

## Approaches to geological mapping in deeply weathered terrains

Geological and structural mapping is a process of creating maps where the distribution of rock materials, which lie near the surface and their interrelationships are portrayed and interpreted. These maps serve as a valuable source of information for decision-making regarding the use of our natural

resources. Geological mapping is an interpretative and subjective process, and because of that, it is crucial to include as much data describing the geological situation as possible to eliminate errors in the interpreted model. In a complex landscape environment or while surveying large areas, data collection is hindered by lack of outcrops caused by vegetation or regolith cover and the inability to cover all of the area using field observations due to time or financial constraints. To overcome some of these problems, magnetic, gravimetric, gamma-ray spectrometry, and satellite remote sensing data constrained by detailed field observations collected at key areas were previously utilized (e.g. Jaques et al., 1997; Schetselaar et al., 2000; Betts et al., 2003; Peschler et al., 2004; Direen et al., 2005; Martelet et al., 2006; Peschler et al., 2006; de Souza Filho et al., 2007; Schetselaar et al., 2007; Schetselaar et al., 2008; Teruiya et al., 2008; Aitken and Betts, 2009a; Stewart and Betts, 2010). The field observations used in the process of geological mapping include lithological observations, petrographic, metamorphic, and geochemical analyses, while incorporating also detailed structural measurements. The effective application of some methods alone (e.g. multispectral satellite data or gamma ray spectrometry data) without an integrated approach may be difficult especially in deeply weathered terrains due to the complex regolith-parent rock relationships (Wilford et al., 1997; Taylor and Eggleton, 2001).

Airborne **magnetic data** allow us to map magnetic anomalies (Boyce and Morris, 2002). Constrained by field structural and geological observations, these data serve as a tool for deriving both lithological information and structural frameworks from which kinematic relationships can be interpreted (Betts et al., 2003; Direen et al., 2005; Betts et al., 2007; Aitken and Betts, 2009a, b). The traditionally performed reduction to pole, which significantly simplifies the interpretations of magnetic data, becomes unstable close to the equator because of the low magnetic inclination (MacLeod et al., 1993; Li, 2008). Moreover, N-S oriented anomalies cannot be portrayed accurately at low latitudes (Beard, 2000; Reeves, 2005). Different methods have been suggested for performing the reduction close to the equator (MacLeod et al., 1993; Li, 2008). Filters, which are routinely used in estimating steep gradients from potential field data (Blakely and Simpson, 1986; Miller and Singh, 1994; Verduzco et al., 2004; Pilkington and Keating, 2009), may be applied to magnetic datasets reduced to the pole. These grids, including the first vertical derivative, horizontal derivatives, and tilt derivative (Milligan and Gunn, 1997; Pilkington and Keating, 2009) aid in the determination of structural and lithological boundaries down to first hundreds of meters. Near the equator or in areas with significant remanent magnetization analytical signal and the total horizontal derivative of the tilt derivative are particularly useful when making interpretations, as these are not affected by the orientation of the Earth's magnetic field (Verduzco et al., 2004; Li, 2006).

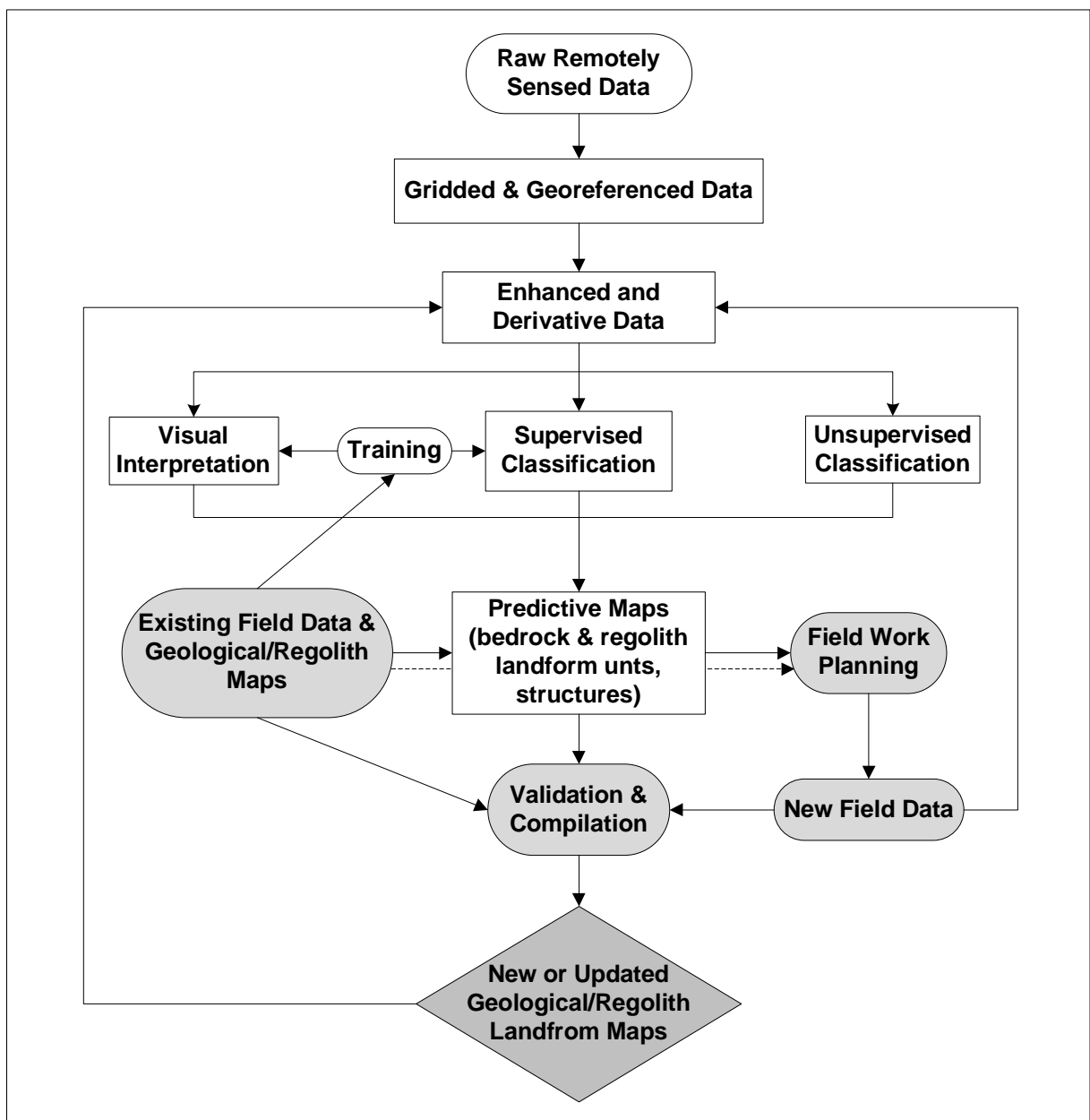
The **gamma ray spectrometry data** acquired over the surface of the Earth reflect the concentrations and distribution of the radioactive elements in both rocks and the derived regolith material. Gamma ray spectrometry is therefore suited for deriving detailed lithological information but serves equally well as a tool for efficient regolith mapping (Jaques et al., 1997; Wilford et al., 1997;

Martelet et al., 2006). Unlike the magnetic data, it reveals the chemical properties of approximately the first 30 cm layer of the Earth's crust (Minty, 1997). Different techniques are proposed in the analysis of airborne gamma ray spectrometry data ranging from the ratios of the gamma ray spectrometry channels (Dickson and Scott, 1997; Wilford et al., 1997), color composites, and color space transformations (Jaques et al., 1997) to integrations with optical and near-infrared datasets (Anderson and Nash, 1997; Schetselaar et al., 2000). Usually the data are analyzed as single band grids e.g. eTh/K, eU/K, and eU/eTh or as ternary grids of K, eTh, and eU as RGB (Red, Green, Blue) or HSV (Hue, Saturation, Value).

The deep regional-scale structures and lithological boundaries are usually well defined in **gravimetric data**. Gravity anomalies are caused by contrasting densities of the crustal rocks. The analyses of gravity data may be subject to similar edge detecting techniques as used for the magnetic data (Blakely and Simpson, 1986). Gravity data often serve as input to 2-D and 3-D geophysical modeling for the interpretation of the geometry of lithological bodies at depth (Attoh, 1982; Peschler et al., 2004; Direen et al., 2005; Stewart et al., 2009).

The recognition of the value of **multispectral and hyperspectral remote sensing data** in lithological and structural mapping dates back to the launch of the first Landsat system (Drury, 1993). However, successful applications are usually constrained to well exposed terrains or terrains where regolith may be linked directly with the underlying geology (e.g. Zumsprekel and Prinz, 2000; Rowan et al., 2004; Rowan et al., 2005). In deeply weathered areas, where the relationships between allochthonous and autochthonous regolith material are not well understood, remote sensing data are instead used for mapping the distribution of the weathered material and so called regolith landform units (Lau et al., 2003).

**Digital elevation models** may be used for the determination of geomorphological parameters of the earth's surface, which are to some extent controlled by the underlying geology. Typically, the digital elevation models stem from remote sensing systems (e.g. SPOT, ASTER, and SRTM). High precision and resolution DEMs acquired by LiDAR (Light Detection and Ranging) are one of the recent research highlights in geological and geomorphological mapping (Grebby et al., 2010; Grebby et al., 2011; Mulder et al., 2011)



**Figure 6** Flow Chart of Integrated analysis of remote sensing and traditional field data during geological or regolith landform mapping projects; object in grey belong to traditional field-based mapping, while white object incorporate remote sensing data, modified from Schetselaar et al. (2007).

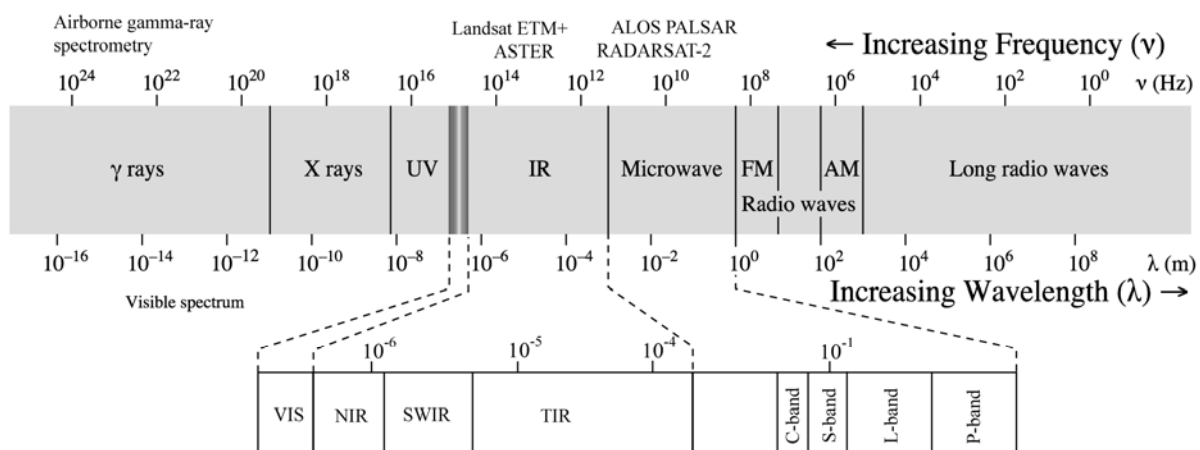
In a GIS environment, layers containing different information may be readily overlain and analyzed as an integrated dataset (Bonham-Carter, 1994; Jaques et al., 1997). These may include digital images, maps, or point layers with field observations. Schetselaar et al. (2007) uses the term “Remote predictive mapping” for an integrated methodology where conventional mapping techniques are coupled with remote sensing data. The word predictive refers to the fact that the produced interpretations are best estimates of the geologic truth. The approach consists from several steps portrayed in figure 4. Similar methodologies, where different sources of data are re-compiled and analyzed in an integrated manner, or parts of the approach proposed by Schetselaar et al. (2007) were described by many others including (Jaques et al., 1997; Schetselaar et al., 2000; Direen et al., 2005;



Betts et al., 2007; Teruiya et al., 2008; Aitken and Betts, 2009a, b). Although the authors integrate different sources of data, the main idea remains similar. The interpretation may be either automatic or visual. Usually before the analysis itself commences different techniques described in the paragraphs above are used to enhance the data. In addition, to evaluate the relationships between the available source layers, the correlations between the source layers may be assessed. For correlated layers PCA (Principal Component Analysis) serves as a tool in determining uncorrelated factors (components) that can be obtained from the original dataset (Drury, 1993). These layers may be more informative than the original dataset and thus be of greater use during the subsequent interpretations. A detailed description of the used data and methodology applied to geological mapping and utilized in the thesis may be found in Appendices 1 and 2.

## Approaches to regolith landform mapping

The term regolith stands for all of the weathered and unconsolidated material from basement rock to earth surface including interbedded fresh rocks (Taylor and Eggleton, 2001). Knowing the distribution of regolith units and understanding the processes, which led to their formation, is important for any kind of successful geological mapping, geochemical or geophysical survey, and mineral exploration. Traditional field-based regolith landform mapping can be a lengthy process, which can be further complicated by difficult access to remote and often large survey areas. At most



**Figure 7** The electromagnetic spectrum, with regions relevant to remote sensing techniques depicted; VIS-visible, NIR-near infra red, SWIR-short wave infrared, TIR-thermal infrared, C,S,L,P-Band-categories of frequency (wavelength) ranges for radar sensors.

scales, West Africa remains poorly covered by regolith landform maps such as those commonly used in Australia (Pain et al., 2007).

Airborne geophysical data and remote sensing data may help to overcome some of the limitations of traditional field-based regolith landform mapping (especially data coverage problems) and were already frequently employed (Wilford et al., 1997; Papp, 2002; Woolrych and Batty, 2007) to assess from afar the diverse physical properties of regolith materials based on the sensed electromagnetic energy (figure 5). One can estimate the chemical composition from airborne gamma-ray spectrometry or spectral remote sensing (Landsat, ASTER), terrain morphology from the digital elevation models (SRTM), and surface roughness or prevailing geometric shapes from radar imagery (ALOS, Radarsat-2).

**Multispectral imagery** from Landsat sensors were frequently employed in regolith mapping (Craig et al., 1999) including directed principal component analysis (DPCA), which is used to separate clay minerals and suppress the effects of vegetation (Fraser and Green, 1987). **Hyperspectral imagery** has been used to assess surficial components of regolith by Dehaan and Taylor (2004) and Lau et al. (2003). Cudahy et al. (2006) studied the relationship between kaolinite disorder and transported versus in situ regolith and found that kaolinite in transported materials tends to be poorly crystalline. In situ infrared spectroscopic measurements form an important component of any multispectral or hyperspectral remote sensing analysis regardless of the scientific discipline involved, providing vital data for calibration, ground truth assessment and serving as modeling input parameters (Milton et al., 2009). Only a relatively small portion of the worldwide measured spectral data are stored in spectral libraries (Christensen et al., 2000; Baldrige et al., 2009; Clark et al., 2007; Becvar et al., 2008; Hueni et al., 2009; ICRAF-ISRIC; 2010) and distributed to the scientific community. Unfortunately, data on regolith materials are almost absent in these libraries, although applications of imaging spectroscopy to granite greenstone terrains or regolith landform mapping have already been reported (Drury and Hunt, 1989; Dehaan and Taylor, 2002; Rowan et al., 2004; Hewson et al., 2005; Deller, 2006).

**SAR (Synthetic Aperture Radar) imagery** constitutes a very useful complement to optical images (Baghdadi et al., 2005). For geologists, radar images provide unique information about structure, morphological, sedimentary features, and moisture content. This information is directly tied to the physical properties of terrain surfaces (Henderson and Lewis, 1998; Drury, 1993). Tapley (2002) showed that VV (vertical transmit – vertical receive) and HV (horizontal transmit – vertical receive) polarizations were better suited for the geological mapping of arid to semi-arid Australia where VV polarization provides increased sharpness and better discrimination between surfaces having similar roughness properties. Polarimetric classification is usually applied via classifying the four polarimetric channels, or classifications based on polarimetric decompositions of the scattering matrix e.g. Cloude-Pottier decomposition (Cloude, 1997), Freeman-Durden decompositions (McNairn et al., 2009). The Pauli decomposition is often used for visual inspection of the data and visual classification; however, automatic classifications based on Pauli decomposition source bands were reported as well (Huang, et al., 2011).

**Gamma ray spectrometry**, which is frequently used in geological studies, was as well recognized as a tool for efficient regolith mapping (Wilford et al., 1997; Wilford, 2002; Woolrych and Batty, 2007). The original data are usually smoothed by NASVD (Noise-Adjusted singular Value decomposition) developed by Hovgaard and Grasty (1997). The concentrations of K, eU, and eTh may be calibrated to absolute values using ground target calibration (Minty, 1997). Wilford et al. (1997) and Martelet et al. (2006) previously described the retention of especially thorium by the Fe-rich weathering products and thus in particular any Fe-rich duricrusts stand out as anomalous features in the gamma ray spectrometry images.

**Digital elevation models** and its derivatives are frequently used for landform mapping in conjunction with other remote sensing data (Henquin and Totté, 1993; Irvin et al., 1997; Giles, 1998; Saadat et al., 2008; Liberti et al., 2009; Siart et al., 2009). Derivatives of the elevation data may be created to characterize and quantify the morphological parameters of the surfaces. These layers may include a variety of morphological descriptors e.g. slope, slope roughness (standard deviation of slope), curvature (Zeverbergen and Thorne, 1987), relative relief (elevation difference), or the hypsometric integral (Pike and Wilson, 1971). The derivatives are usually computed in a moving window of variable size.

Dense vegetation cover or displacement of the regolith units by later erosion may limit the application of most of the described techniques. Indeed, the best results in mapping of the diverse regions in West Africa would require the integration of several data sets. Such integration is thematically related with the approach of Schetselaar et al. (2007) and may be facilitated by simple overlay of different layers in GIS and visual interpretation (Craig et al., 1999; Craig, 2001; Papp, 2002; Woolrych and Batty, 2007) or via automated classification methods, which are not as common (Wilford et al., 2007). The automated classification schemes may follow either unsupervised or supervised classification methods (Campbell, 1996), which have been previously applied in geological mapping or geomorphological mapping. The pixel-based methods include iso-data clustering, hierarchical agglomerative clustering, maximum likelihood, artificial neural networks, or Kohonen's self-organizing maps (Martelet et al., 2006; Grebby et al., 2010; Leverington, 2010). Subpixel based methods, which are suited for multispectral or hyperspectral data (e.g. spectral angle mapper, linear spectral unmixing, mixture tuned matched filtering) were used by Dehaan and Taylor (2004), Rowan et al, (2004), or Leverington, (2011). Recently, object-oriented classifications are also being applied (Dragut and Blaschke, 2006). During automated classifications, it is vital to perform an accuracy assessment of the resulting classified images. Such accuracy assessment is for multiclass classifications best achieved by constructing and examining a confusion (error) matrix as described by Congalton and Green (2009). The classification result should best be rechecked as well in the field. A detailed description of the used data and methodology applied to regolith mapping in this thesis may be found in Appendices 1 and 2.

## **Hypotheses**

1. Greenstone belts and associated granitoid domains form the Paleoproterozoic domain of the West African craton. The physical and geochemical properties of the lithological units differ. Airborne geophysics and remote sensing data are able to map these differences even in areas covered by thick regolith mantle. In addition, geological structures such as faults and folds produce distinct patterns visible in the above-mentioned datasets.
2. The greenstone belts of western Burkina Faso represent either separate or once connected volcano-sedimentary basins. The granitoid domains associated with the greenstone belts are formed by large granitic bodies or numerous smaller scale plutons emplaced by interplay of buoyancy and regional deformation forces. The regional structural grain of the granite-greenstone domains resulted from lateral accretion and nappe stacking or gravity driven processes governed by density differences.
3. The surface properties of rocks and regolith materials covering the study area may be studied with the help of spectral remote sensing. Visible and infrared spectra of rocks and regolith materials help in interpretations of remote sensing data and understanding of surface weathering processes in the area of western Burkina Faso.
4. The lateritic cover, found over most of the studied region, may be automatically or semi-automatically classified into distinct regolith landform units with the help of integrated analysis of geophysical and remote sensing data. The integration of all available and relevant data sources will lead to better classification results.

## **Objectives**

- I. Perform an integrated analysis of field-based observations, geophysical, and remote sensing data. Determine the regional structures and major lithotectonic units utilizing all available data sources and create a new lithostructural map of the studied area. Evaluate the application of the different methods for both lithostructural mapping and regolith landform mapping in the zone of interest.
- II. Propose a new geotectonic scenario with the help of new geochemical data, structural observations, gravity modeling, and interpretations stemming from the integrated analysis of available data. Examine the relationships between the greenstone belts and assess the mechanisms of granitoid pluton emplacement.
- III. Measure the spectral properties of different lithological units, regolith landform units and create a spectral library. Assess the effects of weathering on spectral properties of rocks and determine the spectral properties of soils and regolith materials. Evaluate the possibility of using visible and infrared spectroscopy in mapping surface properties in the studied area.

- IV. Propose a feasible method for automatic regolith landform mapping and evaluate the relative importance of different data sources.

## **Thesis plan**

This thesis presents four chapters. The manuscript begins with a review of the geological evolution of the Paleoproterozoic domain of the West African Craton and lateritic weathering of the region. It presents as well a review of approaches applied to geological mapping in deeply weathered terrains and techniques used for regolith landform analyses.

**Chapter I** studies the lithostructural setting of western Burkina Faso (Metelka, V., Baratoux, L., Naba, S., Jessell, M.W. - *A geophysically constrained litho-structural analysis of the Eburnean greenstone belts and associated granitoid domains, Burkina Faso, West Africa* – published in “Precambrian research”) presents a new regional scale structural and lithological map of western Burkina Faso, based on an integrated analysis of field observations, geophysical, and remote sensing data. Part of this study is formed by an overview of the advantages and drawbacks of geophysical and remote sensing methods in the deeply weathered terrains of West Africa and a comparison of our findings with similar works in other Precambrian terrains. The chapter further discusses in particular the significance of newly discovered structures and lithological relationships, in the light of the geodynamic scenario that is proposed in chapter II.

**Chapter II** presents the tectonic model for western Burkina Faso (Baratoux, L., Metelka, V., Naba, S., Jessell, M.W., Grégoire, M., Ganne, J. - *Juvenile Paleoproterozoic crust evolution during the Eburnean orogeny (~2.2–2.0 Ga), Burkina Faso, West Africa* – published in “Precambrian research”). The model addresses the issues of the source and nature of the volcanic rocks of the greenstone belts, the growth mechanisms of continental crust from dominantly oceanic crust and volcanic arcs, and their transformation into a classical-type greenstone-granitoid terrain pattern. We also discuss the significance of their partitioning into the current greenstone belts, taking into consideration the pre-greenstone belt geodynamic setting of the volcanic island arcs. As the model is based on the integration of multiple datasets (Chapter I), it provides a good constraint on the 3D geometry of the system as well as on the relative chronology of some of the large-scale structures.

**Chapter III** presents a new spectral library for West Africa (Metelka, V., Baratoux, L., Naba, S., Jessell, M.W. - *Visible and infrared spectral library of Precambrian granite-greenstone terrains in Burkina Faso, West Africa* – to be submitted to “Earth surface processes and landforms”). This spectral library contains 110 sampled locations and represents the first publicly available spectral data for West Africa. It contains spectral data of greenschist-metamorphosed lithologies of the greenstone belts, granites, and regolith materials derived from the basement rocks. The results discussed in this chapter are relevant both to geological and regolith interpretation of remote sensing data in West Africa but as well to the understanding of lithological controls on weathering of Precambrian granite-

greenstone terrains in semi-arid environments. The dataset is available through the web page <http://www.geology.cz/extranet-eng/geodata/remote-sensing>.

**Chapter IV** draws partially on the conclusions from chapter I and III aiming at an evaluation of automatic classification methodologies for regolith landform mapping (Metelka, V., Baratoux, L., Jessell, M.W., Barth, A., Ježek, J., Naba, S. - *Regolith landform mapping using airborne geophysics and remote sensing data in a neural network, Burkina Faso, West Africa* – to be submitted to “Remote sensing of environment”). The approach uses a combined analysis of airborne remote sensing data in a moderately to densely vegetated region of southwestern Burkina Faso near the town of Gaoua.

---

## **CHAPTER I**

# **A GEOPHYSICALLY CONSTRAINED LITHO- STRUCTURAL ANALYSIS OF THE EBURNEAN GREENSTONE BELTS AND ASSOCIATED GRANITOID DOMAINS, BURKINA FASO, WEST AFRICA**

---

---

**Résumé du chapitre I****Une analyse litho-structurale des ceintures des roches vertes et des domaines des granitoïdes éburnéens associés contrainte par des données géophysiques, Burkina Faso, Afrique de l'Ouest****1. Introduction**

Les terrains paléoprotérozoïques composés de granitoïdes et de ceintures des roches vertes représentent une cible intéressante pour l'exploration minière, mais également pour la recherche axée sur les mécanismes de formation des boucliers anciens. Malheureusement, il s'agit très souvent de régions affectées par une intense altération de surface (latéritisation) entravant la cartographie géologique de terrain ainsi que les études structurales. Les données géophysiques aéroportées, récemment acquises, intégrées avec les observations de terrain offrent une nouvelle perspective dans la cartographie de ces régions. L'efficacité de ces méthodes a été démontrée dans les terrains précambriens du Canada et de l'Australie (Betts et al., 2003 ; Peschler et al., 2004 ; Direen et al., 2005 ; Peschler et al., 2006 ; Aitken et Betts, 2009a ; Stewart et Betts, 2010). De plus, les données satellitaires et radiométriques sont utilisées pour la cartographie précise du régolithe (Craig, 2001 ; Wilford, 2002).

Cette étude présente une nouvelle carte litho-structurale de l'Ouest du Burkina Faso, contrainte par les données de terrain, les données géophysiques aéroportées et les données satellitaires intégrées dans un environnement SIG. Nous discutons notamment de l'importance des structures découvertes par cette méthodologie en cherchant à les replacer dans le scénario géodynamique proposé dans le chapitre II.

**2. Méthodes**

Nous avons utilisé une méthode d'intégration des observations de terrain (qui elles soient nouvelles ou existantes) avec des données géophysiques aéroportées, des données gravimétriques et des données satellitaires. L'environnement SIG (système d'information géographique) a été utilisé pour cette intégration de données multiples.

Les données de terrain incluent les observations lithologiques, stratigraphiques et les mesures structurales. Les données magnétiques et radiométriques aéroportées que nous avons utilisées ont été acquises lors du projet SYSMIN (Système Minier) qui s'est déroulé entre 1998 et 1999. Les grilles, d'une résolution de 125 et 250 m, ont été calculées à partir des lignes de vol espacées de 500 et 1000



m. Localement, nous avons utilisé des données de haute résolution fournies par des compagnies minières.

Une réduction au pôle des données magnétiques a été effectuée selon la méthode de MacLeod et al. (1993) et Li (2008). De plus, la première dérivée verticale, la dérivée horizontale et la dérivée d'inclinaison (Milligan et Gunn, 1997 ; Pilkington et Keating, 2009) ont été effectuées. Les données radiométriques ont été lissées selon la méthode NASVD (Noise-Adjusted Singular Value decomposition) (Hovgaard et Grasty, 1997) et les concentrations de K, eU, eTh ont été calculées respectivement, sur la base d'émission des éléments fils  $^{214}\text{Bi}$  and  $^{208}\text{Tl}$ . Des grilles composites de eTh/K, eU/K, and eU/eTh ainsi que des images d'Analyse en Composantes Principales (ACP) ont été réalisées. Les données Landsat et ASTER ont été utilisées conjointement avec le modèle numérique de terrain SRTM (Shuttle Radar Topography Mission). Ce dernier, d'une résolution de 90 m, a été intégré aux données radiométriques (Wilford et al., 1997).

Les données gravimétriques sont issues d'une campagne de l'ORSTOM en Afrique de l'Ouest (Albouy et al., 1992). Les points de mesure sont situés le long des routes principales et leur espacement maximum est de 4000 m. Les corrections à l'air libre et de Bouguer ont été appliquées, utilisant  $2,67 \text{ g/cm}^3$  comme densité de réduction. Les données recalculées dans une grille de résolution de 3000 m ont servi à produire une carte d'anomalies de Bouguer.

### 3. Résultats principaux de l'étude

Cette approche, intégrant des données multiples, a mené à la découverte de structures qui n'avaient encore jamais été identifiées dans l'Ouest du Burkina Faso. Les données magnétiques ont servi pour la cartographie des structures et des unités lithologiques jusqu'à des profondeurs relativement importantes, alors que les données radiométriques et satellitaires ont permis de mieux contraindre la nature lithologique de terrains ainsi que les structures de surface. L'aspect structural de la carte est plus cohérent et complet car il a été établi de pair avec la conception du modèle géodynamique de la région étudiée (chapitre II).

Nous avons démontré que les granitoïdes comportent quatre types d'intrusions (ME1-ME4), bien visibles sur les données magnétiques aéroportées. Ces quatre types correspondent aux types de granitoïdes observés sur le terrain : tonalite-trondhjemites-granodiorites riches en Na (ME1) ; granodiorites et granites riches en Na (ME2) ; granites riche en K (ME3) et gabbros (ME4). Les unités lithologiques des ceintures des roches vertes telles que des gabbros, basaltes, andésites et roches volcano-sédimentaires ont été délimitées grâce aux données magnétiques et radiométriques. Les sédiments de type Tarkwaïen sont très faiblement magnétiques et peuvent donc être tracés dans les zones avec un contraste suffisant vis à vis des lithologies adjacentes.

A plusieurs endroits, on peut distinguer la fabrique pénétrative S1 peut être distinguée de la fabrique cisailant S2, tant sur le terrain que dans les données magnétiques aéroportées. Des reliques

de plis P1 d'échelle régionale ont été distinguées dans les ceintures de Houndé et de Boromo. On retrouve ces plis à l'échelle de l'affleurement dans les trois ceintures. De nombreuses zones de cisaillement d'échelle régionale, issues de la phase de déformation D2, ont été mises en évidence : Boromo-Poura, West Batié, Boni, Ouango-Fitini, Bossié, Greenville-Ferkessedougou-Bobo Dioulasso. Ces zones ont un fort potentiel pour l'exploration de l'or.

Nous discutons également les points forts et points faibles de la méthodologie proposée pour la cartographie des zones couvertes par une épaisse couche de latérite et qui présentent très peu d'affleurements des roches saines. Les données magnétiques aéroportées sont très efficaces pour cartographier les roches du socle paléoproterozoïques jusqu'à une profondeur de 300 m. Les données radiométriques et satellitaires ont moins d'utilité pour la cartographie des lithologies, notamment aux endroits où la couverture végétale ou latéritique est forte. Par contre, en combinaison avec le modèle numérique de terrain, elles ont été utilisées avec succès pour la cartographie des sols, carapace latéritique et sédiments alluvionnaires (chapitre IV).

#### **4. Conclusion**

Une nouvelle carte litho-structurale a été réalisée pour l'Ouest du Burkina Faso en utilisant une méthode d'intégration des données géophysiques aéroportées, des données satellitaires et des données géologiques de terrain dans un environnement SIG. Les unités lithologiques des ceintures des roches vertes ont pu, dans la limite du possible, être cartographiées sous les couvertures latéritiques. Quatre générations d'intrusions (ME1-ME4) ont été distinguées dans les domaines des granitoïdes, ce qui a des conséquences importantes pour le modèle géodynamique. De nombreuses zones de cisaillement à l'échelle régionale ont été découvertes. L'application de la méthodologie de l'intégration des données multiples présente un fort potentiel pour la cartographie des régions de l'Afrique de l'Ouest, difficilement accessibles car couvertes par la végétation et les latérites.

# A GEOPHYSICALLY CONSTRAINED LITHO-STRUCTURAL ANALYSIS OF THE EBURNEAN GREENSTONE BELTS AND ASSOCIATED GRANITOID DOMAINS, BURKINA FASO, WEST AFRICA

Václav Metelka <sup>a,b,c</sup>, Lenka Baratoux <sup>a\*</sup>, Séta Naba <sup>d</sup>, Mark W. Jessell <sup>a</sup>

<sup>a</sup> IRD, UR 234, GET, Université Toulouse III, 14 Avenue Edouard Belin, 31400, Toulouse, France

<sup>b</sup> Institute of Geology and Paleontology, Charles University in Prague, Albertov 6, 12843, Prague 2, Czech Republic

<sup>c</sup> Czech Geological Survey, Klárov 3, 11821, Prague 1, Czech Republic

<sup>d</sup> Département de Géologie, Université de Ouagadougou, Burkina Faso

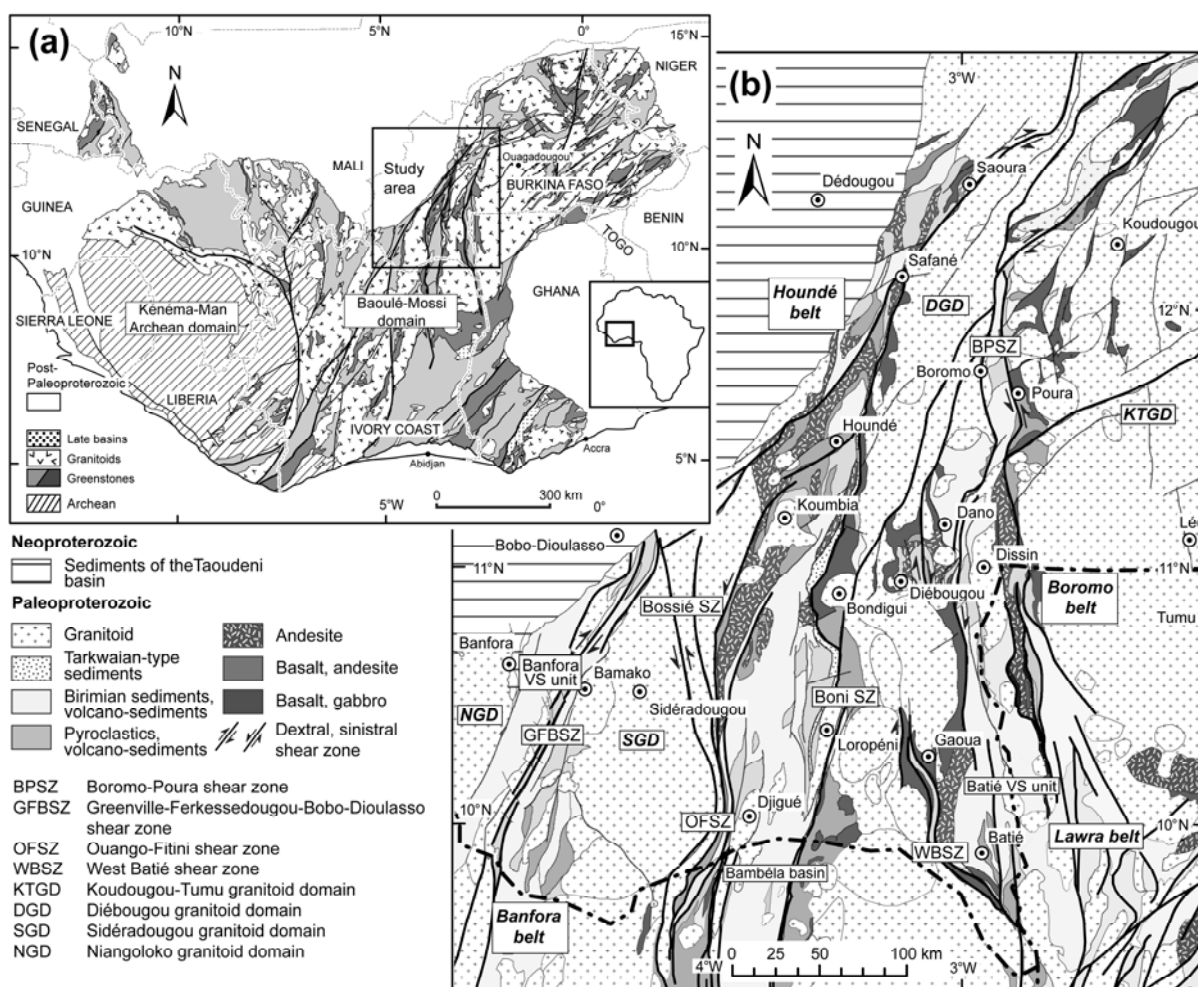
## Abstract

Interpretation of airborne geophysical data integrated with field structural and lithological observation was successfully employed in the creation of the litho-structural framework in a poorly exposed Paleoproterozoic granite-greenstone terrain of the West African Craton. The geophysical data portray with sufficient detail all of the lithological units and structural features present. The results suggest that the granitoid domains are formed by numerous small to medium-sized plutons. The existence of several generations of magmatic episodes has a significant impact on the development of a regional tectonic model. The magnetic data provided a better definition of the actual pluton shapes and several highly magnetic late-orogenic plutons were reliably identified. Relic F1 fold hinges were recognized in the Houndé and Boromo greenstone belts. The D1 penetrative structures are generally affected by the D2 transcurrent shear zones, which often form as well the granite-greenstone belt boundaries. Previously unreported S2 shear zones including the Bossié shear zone, transecting the Sidéradougou granitoid domain and abundant small-scale shear zones affecting all of the lithologies represent prospective areas for gold exploration. Airborne gamma ray spectrometry data aided in the mapping process in areas with less regolith cover including erosional ridges and parts of the Banfora greenstone belt. The magnetic data revealed at least three generations of doleritic dykes crosscutting the western Burkina Faso.

**Keywords:** West Africa; Burkina Faso; Paleoproterozoic; Airborne geophysics; Remote sensing; Structural analysis

## 1. Introduction

The greenstone belts of western Burkina Faso represent a typical granite-greenstone terrain of the Paleoproterozoic Baoulé-Mossi domain in the southern part of the West African Craton (figure I-1) (Bessoles, 1977; Abouchami et al., 1990; Boher et al., 1992; Taylor et al., 1992; Béziat et al., 2000; Debat et al., 2003). The NNE-SSW to N-S elongated belts stretch for more than 400 km and are host to multiple gold and base metal deposits (Milési et al., 1992; Béziat et al., 2008). They belong to a polycyclic orogen that formed around the Kénéma-Man Archean nucleus during the Eburnean orogeny



**Figure I-1** Schematic maps of the study area. (a) – Simplified geological map of the Leo-Man craton (modified after BRGM SIGAfrique) with the zone of interest outlined; the Paleoproterozoic greenstones are divided into: light grey – intermediate to acid volcano-clastics and volcano-sediments, dark grey – mafic to intermediate lavas and volcanic products. (b) – Simplified geological map derived during this study (Burkina Faso), Ivory Coast area modified after Tagini (1972) and Lüdtke et al. (1998), Ghana area modified after Agyei Duodu et al. (2010); names of the greenstone belts and granitoid domains discussed in the text are displayed; and major shear zones are outlined.

(2200–2000 Ma) (Bonhomme, 1962; Liégeois et al., 1991; Milési et al., 1992; Ledru et al., 1994; Egal et al., 2002). Many studies describe the polyphase litho-structural setting and propose in essence two

distinct geotectonic models for the evolution of the Paleoproterozoic basement in West Africa. A traditional plate tectonic model of crustal buildup by thrust and fold belts has been proposed by Boher et al. (1992), Feybesse and Milési (1994), Ledru et al. (1994), Hirdes et al. (1996), Debat et al. (2003), Feybesse et al. (2006), Tshibubudze et al. (2009), Hein (2010). Pons et al. (1995) or Vidal et al. (2009) favor dome and basin structures caused by vertical tectonic gravitational processes.

Field mapping and structural studies in this region are seriously hindered by the presence of thick lateritic cover and scarcity of fresh outcrops. Rock exposure in the study area is about six percent. High-resolution airborne geophysical data have become an indispensable tool for geological mapping (Agyei Duodu et al., 2010) in West Africa. Interpretations of magnetic, gravimetric, gamma-ray spectrometry and satellite remote sensing data constrained by field observations proved to be efficient in deciphering the regional litho-structural hierarchies in the Precambrian terrains (e.g. Jaques et al., 1997; Schetselaar et al., 2000; Betts et al., 2003; Peschler et al., 2004; Direen et al., 2005; Martelet et al., 2006; Peschler et al., 2006; de Souza Filho et al., 2007; Schetselaar et al., 2007; Schetselaar et al., 2008; Teruiya et al., 2008; Aitken and Betts, 2009a; Stewart and Betts, 2010). The effective application of some methods alone without an integrated approach may be difficult in geological mapping especially in deeply weathered terrains due to the complex regolith-parent rock relationships (Wilford et al., 1997; Taylor and Eggleton, 2001). Additionally, the application of gamma-ray spectrometry data or satellite remote sensing data is more appropriate for regolith landform mapping rather than geological mapping (Craig, 2001; Wilford, 2002).

In this study, we present a new regional scale structural and lithological map of western Burkina Faso, based on an integrated analysis of field observations, geophysical, and remote sensing data. We will discuss in particular the significance of newly discovered structures and lithological relationships, in the light of the geodynamic scenario that we propose in chapter II. As a part of this study, we will offer an overview of the advantages and drawbacks of geophysical and remote sensing methods in the deeply weathered terrains of West Africa and compare our findings to similar works in other Precambrian terrains.

## **2. Regional geological setting**

### **2.1. The Baoulé-Mossi Paleoproterozoic domain**

The Baoulé-Mossi domain (figure I-1) forms the eastern and northern part of the Leo-Man Craton (Bessoles, 1977). The Paleoproterozoic domain is characterized by the typical Archean-like greenstone-granitoid assemblages that principally consist of volcanic, volcano-sedimentary, and sedimentary sequences separated by extensive tonalite-trondjemite-granodiorite and granitoid provinces. The volcanic and volcano-sedimentary rocks belong to the Birimian Supergroup, which was probably formed in the context of volcanic arcs and oceanic plateaus (Abouchami et al., 1990;

Leube et al., 1990; Boher et al., 1992; Taylor et al., 1992; Pouclet et al., 1996; Béziat et al., 2000). Radiometric dating of the volcanic units (Davis et al., 1994; Loh and Hirdes, 1996; Lüdtke et al., 1998; Lüdtke et al., 1999) places the main peak of the Birimian volcanism at around 2190–2160 Ma, while detrital zircons from the sedimentary basins yield ages as young as 2130 Ma (Lüdtke et al., 1999) or 2107 Ma (Doumbia et al., 1998). The Birimian volcanic and volcano-sedimentary units are unconformably overlain at several places across the craton by detrital shallow water sedimentary rocks, which are known as the Tarkwaian sediments (Whitelaw, 1929; Sestini, 1973; Leube et al., 1990; Oberthuer et al., 1998; Feybesse et al., 2006). The whole complex of volcanic, volcano-sedimentary and sedimentary units was intruded by several generations of granitoids, which were emplaced during several magmatic pulses from 2180 to 1980 Ma (Leube et al., 1990; Pons et al., 1995; Hirdes et al., 1996; Doumbia et al., 1998; Castaing et al., 2003; Gasquet et al., 2003; Naba et al., 2004; Siegfried et al., 2009; Thomas et al., 2009; Agyei Duodu et al., 2010). The general geochemistry of the granitoids evolves from Na-rich calc-alkaline to K-rich alkaline (Boher et al., 1992) while their shape depends on tectonic regime during their emplacement, ranging from undeformed circular plutons to elongate and complex interlocked bodies (Pons et al., 1991; Pons et al., 1992; Pons et al., 1995).

The polydeformed Baoulé-Mossi domain developed during the Eburnean orogeny (Bonhomme, 1962), which operated between ~2130 and 1980 Ma (Davis et al., 1994; Oberthuer et al., 1998; Feybesse et al., 2006). Most of the volcanic and sedimentary rocks underwent lower to upper greenschist facies metamorphism (Béziat et al., 2000; Feybesse et al., 2006; Křibek et al., 2008). Although John et al. (1999) and Galipp et al. (2003) described regional MP/MT conditions (500–600°C, 5–6 kbar) in Ghana, amphibolite facies metamorphism is mostly restricted to the contact aureoles of granitic plutons (Debat et al., 2003). The Eburnean orogeny is generally divided into two major deformation phases. The first phase, which caused major crustal thickening (Boher et al., 1992; Milési et al., 1992; Allibone et al., 2002; Feybesse et al., 2006; Vidal et al., 2009), operated approximately during 2130–2100 Ma. The second phase that lasted up to 1980 Ma was responsible for the formation of regional scale transcurrent shear zones and faults, which transect all lithologies. Gold mineralization in West Africa is generally related to these shear zones (e.g. Milési et al., 1989; Milési et al., 1992; Blenkinsop et al., 1994; Bourges et al., 1998; Allibone et al., 2002; Feybesse et al., 2006). The consolidated Eburnean basement was then locally affected by a N-S oriented compressional event (Nikiéma et al., 1993; Debat et al., 2003; Hein, 2010) and unconformably overlain by the Neoproterozoic sediments of the Taoudeni, Lullemeden, and Volta basins. Dyke swarms cross the entire Proterozoic domain in several directions and are formed by at least six different generations (Jessell et al., 2010).

## 2.2. Western Burkina Faso

The Paleoproterozoic basement of western Burkina Faso consists of three N-S trending greenstone belts, from east to west known as Boromo, Houndé, and Banfora (Castaing et al., 2003). The greenstone belts are separated by composite granitoid domains, which we call the Koudougou-Tumu, Diébougou, Sidéradougou, and Niangoloko domains for the purpose of this work (figure I-1). The detailed stratigraphic relationships and litho-tectonic evolution are described in detail in chapter II. Shallow water detrital sediments, considered genetically similar to the Tarkwaian meta-sediments in Ghana, occur as a ~400 km long and ~1–2 km wide unit within the Houndé belt (Bossière et al., 1996). In the west, sub-horizontal units of the Neoproterozoic Taoudeni basin overlay the Paleoproterozoic basement (Bronner et al., 1980). Doleritic dykes transect all of the present lithologies.

The greenstone belts of western Burkina Faso and neighboring northern Ivory Coast and Ghana are composed of mafic tholeiitic lithologies, followed by intermediate and acid calc-alkaline effusive suites, typical for volcanic arc environments (Lüdtke et al., 1998; Béziat et al., 2000). U-Pb zircon ages in rhyolites associated to the mafic rocks yield ~2176–2160 Ma (Lüdtke et al., 1998; Le Métour et al., 2003). The volcanic assemblages are often intercalated with volcano-sedimentary units, considered as their lateral stratigraphic equivalents (Hirdes et al., 1996; Lüdtke et al., 1998; Lüdtke et al., 1999; Castaing et al., 2003). The Birimian sediments and volcano-sediments form belt-parallel units, such as the Bambéla volcano-sedimentary unit, which extends to the Ivory Coast where the unit is known as the Bambéla basin (Hirdes et al., 1996; Lüdtke et al., 1998; Lüdtke et al. 1999), or the Batié volcano-sedimentary unit situated within the Boromo belt. These sedimentary units might postdate the main volcanic activity in the region, as suggested by radiometric ages obtained on detrital zircons – 2126 Ma (Lüdtke et al., 1999).

The granitic rocks form a complex assemblage resulting from several magmatic episodes (Castaing et al., 2003), for which several types of classifications have been proposed cratonwide (Leube et al., 1990; Davis et al., 1994; Hirdes et al., 1996; Doumbia et al., 1998; Egal et al., 2002; Castaing et al., 2003; Gasquet et al., 2003; Naba et al., 2004; Lompo, 2009). The petrographic composition of the different suites is variable. Based on field reconnaissance and the character of the intrusive bodies observed in the geophysical data, we will distinguish four groups of granitoid intrusions and associated gabbros, in accord with the previously published work. The oldest tonalites, trondhjemites, and granodiorites (ME1) yield ages of ~2153–2132 Ma (Hirdes et al., 1996; Lüdtke et al., 1998; Chèvremont et al., 2003; Koté et al., 2003) and are generally syntectonic with observable penetrative magmatic layering. Younger granodiorites and amphibole-biotite bearing granites (ME2), dated at ~2113–2097 ± 10 Ma (Hirdes et al., 1996; Chèvremont et al., 2003; Koté et al., 2003; Le Métour et al., 2003), are often affected by mylonitic shear zones, but may be also undeformed. Late potassic biotite-bearing granites (ME3) are mostly undeformed with only localized shear zones and are

best visible in magnetic data due to their high susceptibility. Coarse-grained undeformed gabbros of unknown age (ME4) are at places associated with the granitoid intrusions. More radiometric, petrographic, and geochemical data are needed for a more consistent classification of the plutons into the particular magmatic episodes.

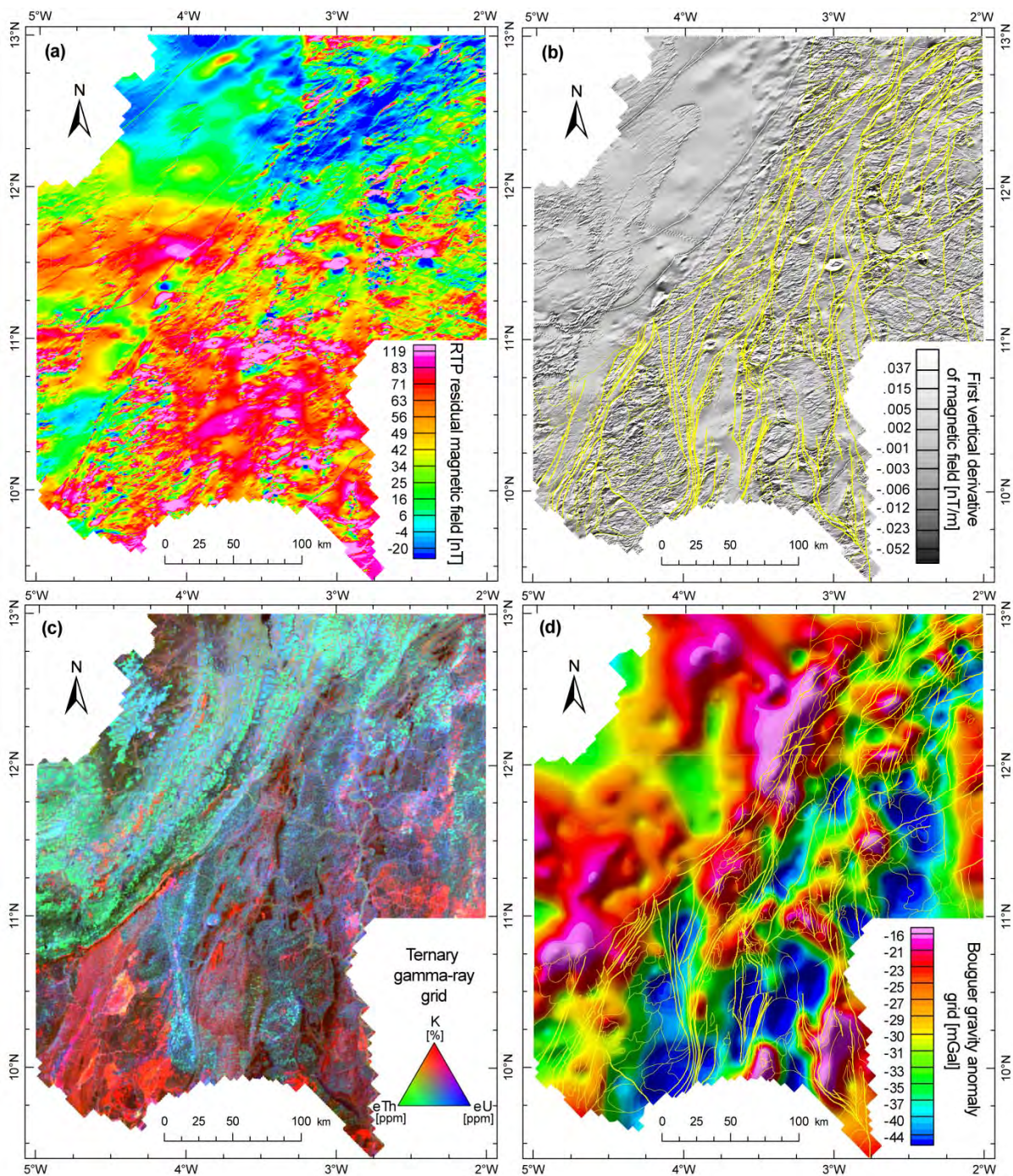
The structural patterns of the granite-greenstone belt contacts vary between bifurcating and linear patterns, as described by Kusky and Vearncombe (1997), which suggest both thrust-fold and strike-slip related deformations. As for the whole Paleoproterozoic domain, the deformation history of western Burkina Faso is polyphase, showing evidence of at least two distinct Eburnean orogenic phases (Ouedraogo and Prost, 1986; Castaing et al., 2003) discussed in detail in chapter II.

### **3. Methodology and data use**

#### **3.1. Airborne magnetometry**

Airborne magnetic surveys allow us to map magnetic anomalies (Boyce and Morris, 2002), constrained by field structural and geological observations, these data serve as a tool for deriving both lithological information and structural frameworks from which kinematic relationships can be interpreted (Betts et al., 2003; Direen et al., 2005; Betts et al., 2007; Aitken and Betts, 2009a, b). The magnetic data available for western Burkina Faso were acquired during the 1998–1999 SYSMIN (System for Mineral Products) airborne geophysics campaign with NW-SE oriented flight lines with 500 m and 1000 m line spacing, 100 m ground separation, and 10000 m NE-SW tie lines. The IGRF (International Geomagnetic Reference Field) referential field corrected data were gridded with 125 and 250 m spatial resolution (depending on the flight line spacing) and merged. The traditionally performed reduction to pole, which significantly simplifies the interpretation of magnetic data, becomes unstable close to the equator because of the low magnetic inclination (MacLeod et al., 1993; Li, 2008). Moreover, N-S oriented anomalies cannot be portrayed accurately at low latitudes (Beard, 2000; Reeves, 2005). A reduction to the pole using the pseudo inclination method developed by Grant and Dods (in MacLeod et al., 1993) and discussed in detail by MacLeod et al. (1993) and Li (2008) was applied to the dataset. Subsequently, a directional cosine filter was used to remove the high amplitude false anomalies generated during the RTP filtering in the direction of the magnetic declination. At places, pre-processed high-resolution data provided by mining companies were used.





**Figure I-2** (a) – Reduced to the pole (RTP) residual magnetic intensity (RMI) grid; (b) – first vertical derivative of the RTP corrected RMI grid overlain by interpreted structures; (c) – Gamma ray ternary grid – corrected absolute concentrations displayed as RGB underlain by the SRTM digital elevation model; (d) – Bouguer anomaly gravimetric grid with an overlay of interpreted structures.

Filters, which are routinely used in estimating steep gradients from potential field data (Blakely and Simpson, 1986; Miller and Singh, 1994; Verduzco et al., 2004; Pilkington and Keating, 2009), were derived from the reduced to the pole magnetic residual field data set (figure I-2a). These grids, including the first vertical derivative (figure I-2b), horizontal derivatives, and tilt derivative (Milligan and Gunn, 1997; Pilkington and Keating, 2009) of the magnetic data aided in the determination

of structural and lithological boundaries down to first hundreds of meters. Near the equator or in areas with significant remanent magnetization analytical signal and the total horizontal derivative of the tilt derivative are particularly useful when making interpretations, as these are not affected by the orientation of the Earth's magnetic field (Verduzco et al., 2004; Li, 2006).

### 3.2. Airborne gamma ray spectrometry

The gamma ray signal sensed over the surface of the Earth reflects the content and distribution of the radioactive elements in both rocks and the derived regolith material including anomalies created by geochemical alterations (mineralization, hydrothermal alterations, weathering). Gamma ray spectrometry is perfectly suited for deriving detailed lithological information but serves equally well as a tool for efficient regolith mapping (Jaques et al., 1997; Wilford et al., 1997; Martelet et al., 2006). Unlike the magnetic data, it reveals the chemical properties of approximately the first 30 cm layer of the Earth's crust (Minty, 1997).

The gamma ray spectrometry data were acquired along with the magnetic data during the 1998–1999 SYSMIN project. The data were supplied as corrected, NASVD (Noise-Adjusted Singular Value decomposition) smoothed (Hovgaard and Grasty, 1997). K, eU, eTh concentrations (U and Th are calculated based on gamma ray emissions from their daughter elements  $^{214}\text{Bi}$  and  $^{208}\text{Tl}$ , respectively and assumed equilibrium in the decay series) and were subsequently gridded at 125 and 250 m spatial resolution (depending on the flight line spacing). At places, high-resolution data provided by mining companies were used. Different techniques are proposed in the analysis of airborne gamma ray spectrometry data ranging from the ratios of the gamma ray spectrometry channels (Dickson and Scott, 1997; Wilford et al., 1997), color composites, and color space transformations (Jaques et al., 1997) to integrations with optical and near-infrared datasets (Anderson and Nash, 1997; Schetselaar et al., 2000). The eTh/K, eU/K, and eU/eTh grids were derived from the original bands along with the K, eTh, and eU RGB (Red, Green, Blue) color composite (figure I-2c) and Principal Component Analysis (PCA) images.

### 3.3. Gravimetric data

The deep regional-scale structures and lithological boundaries are usually well defined by gravity anomalies, which are caused by contrasting densities of the crustal rocks. The analyses of gravity data may be subject to similar edge detecting techniques as used for the magnetic data (Blakely and Simpson, 1986). Gravity data often serve as input to 2-D and 3-D geophysical modeling for the interpretation of the geometry of lithological bodies at depth (Attoh, 1982; Peschler et al., 2004; Direen et al., 2005; Stewart et al., 2009).

The gravity data available for western Burkina Faso stem from the ORSTOM west and central African gravimetric data acquisition campaign and were acquired in 1958 (Albouy et al., 1992). The

---

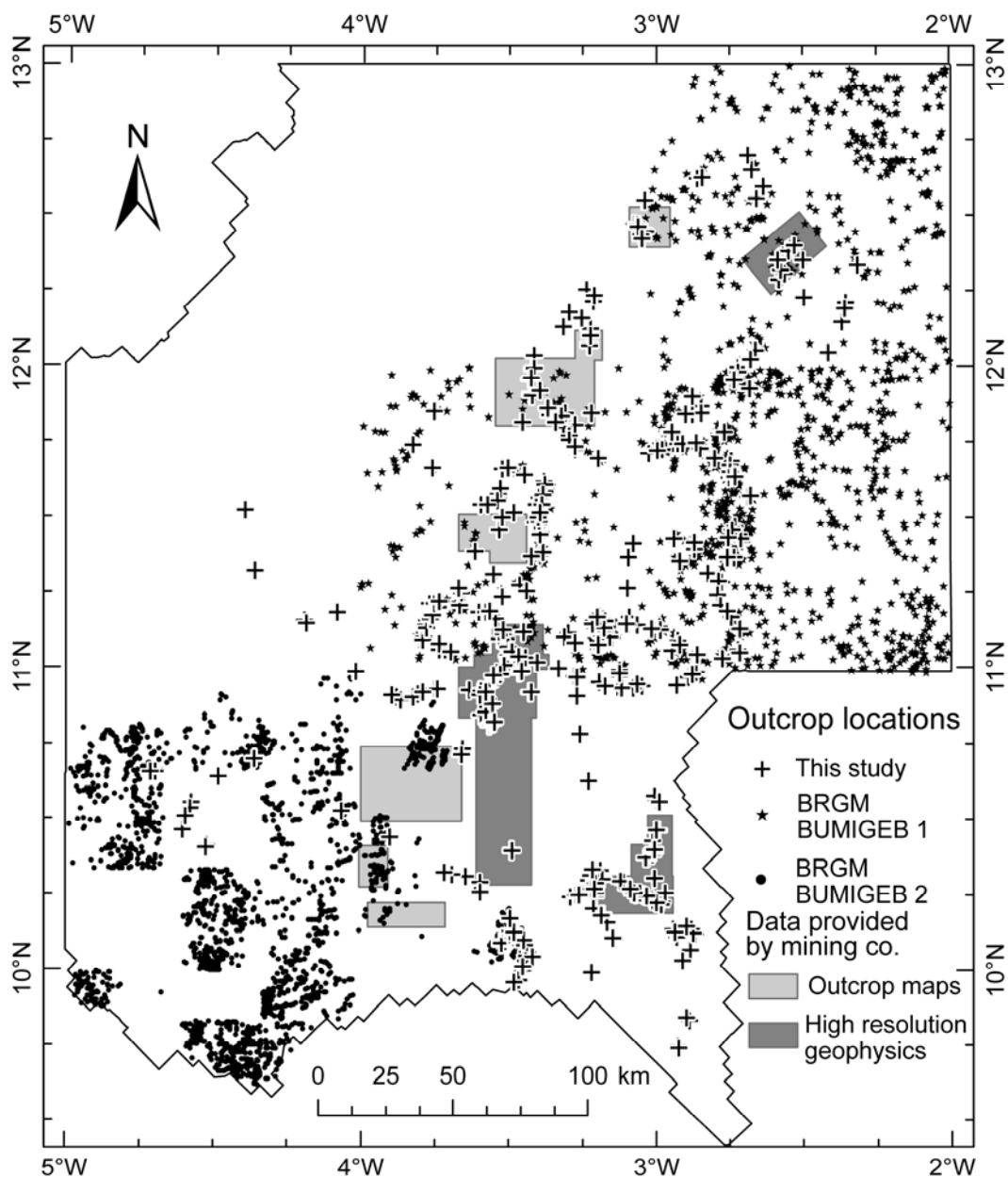
data have a maximum spacing of 4000 m between sampling points and were mainly acquired along major roads. Station locations were determined from topographic maps and elevations by barometric leveling. The reported accuracy of the measurements is about 0.5 mGal and the positioning error is estimated to be less than 5 m in the vertical and about 200 m in the horizontal direction. Free air and Bouguer corrections were applied to the data using  $2.67 \text{ g/cm}^3$  as the reduction density. The data were gridded at 3000 m spatial resolution to produce a Bouguer anomaly map (figure I-2d), which shows deeper structures of regional importance.

### **3.4. Remote sensing data**

The recognition of the value of remote sensing data in lithological and structural mapping dates back to the launch of the first Landsat system (Drury, 1993). However, successful applications are usually constrained to well exposed terrains or terrains where regolith may be linked directly with the underlying geology (e.g. Zumsprekel and Prinz, 2000; Rowan et al., 2004; Rowan et al., 2005). In deeply weathered areas, where the relationships between allochthonous and autochthonous regolith material are not well understood, remote sensing data are instead used for mapping the distribution of the weathered material and so called regolith landform units (Lau et al., 2003). After careful evaluation of Landsat and ASTER data available for the studied area, only weak correlations between the patterns in the data and the field lithological observations could be found. The data were used conjointly with the SRTM (Shuttle Radar Topography Mission) elevation model to assess the distribution and size of outcrops, vegetation, regolith cover, and the extent of the Neoproterozoic Taoudeni basin sediments. Digital elevation models can also be used for the determination of geomorphological parameters of the earth's surface, which are controlled by the underlying geology, weathering, and regolith distribution. The SRTM global digital elevation processed data (Reuter et al., 2007) was acquired from the CGIAR (Consultative Group on International Agricultural Research) institute (Jarvis et al., 2008). This model supplied 90 m spatial resolution elevation data over the studied area. Shaded relief images and derivatives of the elevation data were integrated with the gamma ray spectrometry data (Wilford et al., 1997) to help characterize the surface lithologies and regolith units and assist in differentiating regolith patterns from lithological signatures.

### 3.5 Geological outcrop data

The basis for all of the subsequent analyses was the database of outcrop observations acquired during this study, which served as the first order data source.



**Figure I-3** Outcrop map of the study area. Points indicate field-observations from different source databases; polygons outcrop maps and high resolution geophysical data. Outcrop database this study – all points - lithology, detailed structural description and measurement data, selected points – petrography, susceptibility, density, geochemistry; BRGM/BUMIGEB 1 database – all points lithology, selected points – structural measurements and outcrop description, petrography, geochemistry; BRGM/BUMIGEB 2 database – four lithological classes – volcanic, granitoid, sediment, quartz dykes.

Similarly, outcrop data from the BRGM/BUMIGEB 1/2 (Bureau de recherches géologiques et minières/Bureau des Mines et de la Géologie du Burkina) databases (Marcelin, 1971; Marcelin and Serre, 1971; Castaing et al., 2003) and outcrop maps provided by mining companies were used. The quality as well as the quantity of the field observation data in the databases used varies considerably (table I-1). The spatial distribution of the outcrop data is shown in figure I-3. The primary outcrop database in this study includes lithological data, detailed structural observations, and measured

Outcrop database	Obs. count	Litho.	Struc.	Susc.	Dens.	Geoch.
This study	626	x	x	x	x	x
BRGM BUMIGEB 1	1845	x	x*			x
BRGM BUMIGEB 2	2382	x				
Mining co.	2435	x	x			

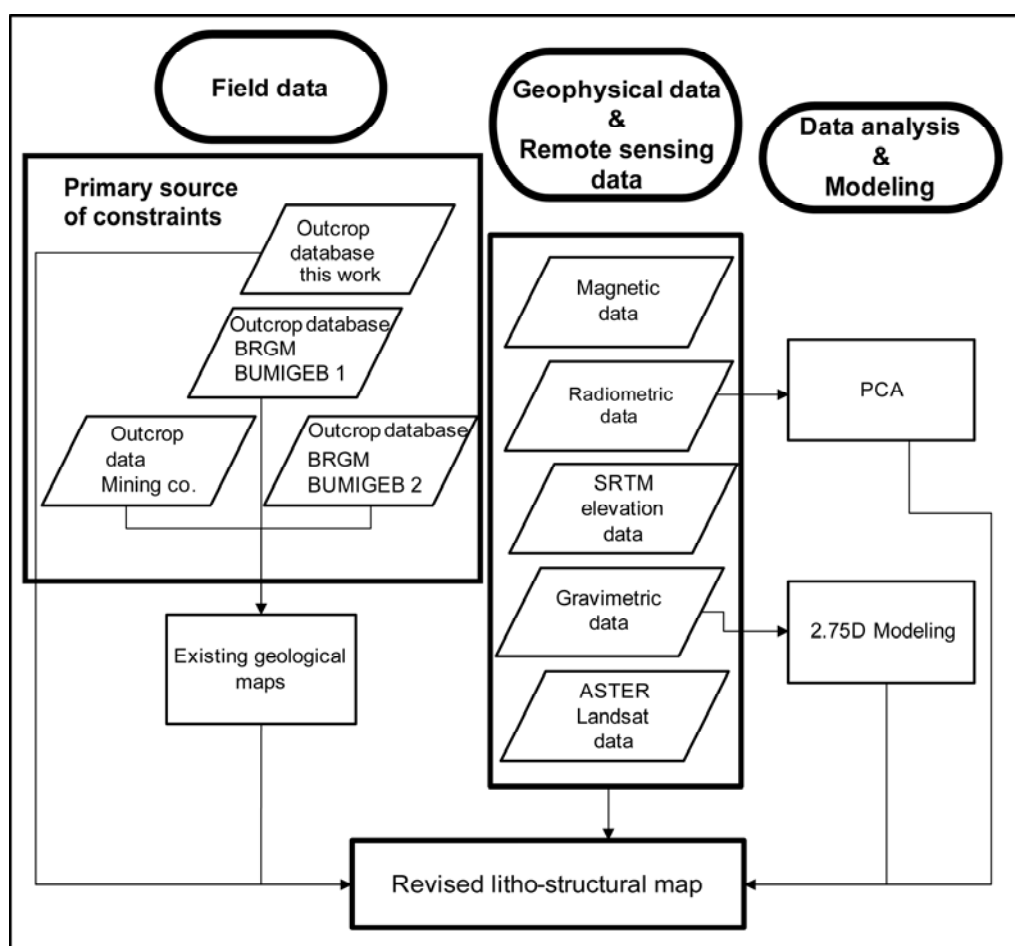
**Table I-1** *Outcrop information included in the collected and used databases. Outcrops in the first three databases are stored as point features. BRGM/BUMIGEB 1 – Castaing et al. (2003), \* at places contains orientations as text description, BRGM/BUMIGEB 2 – Marcelin (1971), Marcelin and Serre (1971). Data from mining companies contain outcrops as outcrop polygons and points, at places supplemented with structural measurements (points). Obs. count – count of observations made, Litho. – lithological data, Struc. – structural measurements, Susc. – magnetic susceptibility, Dens. – density, Geoch. – geochemistry (only for selected locations).*

susceptibility, density and geochemistry at selected locations. The BRGM/BUMIGEB 1 database (Castaing et al., 2003) contains petrographic rock descriptions, geochemical analyses at selected locations. At some outcrops, orientations of dominant structures are given. The BRGM/BUMIGEB 2 database (Marcelin, 1971; Marcelin and Serre, 1971) holds only outcrop stations with four basic lithology categories with no other parameters. The existing maps (e.g. Junner, 1940; Marcelin, 1971; Marcelin and Serre, 1971; Tagini, 1972; Ladmirant and Legrand, 1977; Milési et al., 1989; Lüdtke et al., 1998; Lüdtke et al., 1999; Castaing et al., 2003; Chèvremont et al., 2003; Koté et al., 2003; Le Métour et al., 2003) cover the entire study area at scales of 1:200 000 and 1:1 000 000. We have carefully evaluated these maps; however, the main constraining criteria were derived from the raw outcrop information available.

### 3.6 Digital data integration

In a GIS environment, layers containing different information may be readily overlain and analyzed as an integrated dataset (Bonham-Carter, 1994; Jaques et al., 1997). These may include digital images, maps, or point layers with field observations.

We have used the workflow described in figure I-4 to build a litho-structural framework of the



**Figure I-4** Data analysis scheme; PCA – principal component analysis transformation of the airborne gamma ray data;  $2\frac{3}{4}$  D modeling performed on the gravimetric data (detailed description is given in the companion paper (Baratoux et al., submitted). SRTM – Shuttle Radar Topography Mission, BRGM – Bureau de recherches géologiques et minières, BUMIGEB – Bureau de Mines et Géologie du Burkina Faso, ASTER – Advanced Spaceborne Thermal Emission and Reflection Radiometer.

studied region. In order to extend the observations to areas with regolith cover or areas with difficult access, analysis of the magnetic data was used as the principal source of information. Steep gradients in the magnetic field were obtained from the analysis of the vertical and horizontal derivatives, the tilt derivative, and the analytical signal. The edges were attributed to lithological contacts or faults, according to the field observations and the character of the edges observed in the data (e.g. change in magnetic texture correlates with change in observed lithologies, orientation of structural measurements

correlates with orientation of interpreted edges). The lithological composition for the newly constructed polygons was mainly constrained utilizing the characteristic magnetic signatures that were established between the outcropping lithologies and their magnetic response. In areas with sufficient outcrop, where regolith related patterns in the data were found to be negligible, gamma ray spectrometry datasets provided a further constraint. We benefited from the additional information obtained from shaded relief and slope of the elevation data to evaluate the relationship between the gamma ray spectrometry data and regolith. The slope map showed clearly scarps of different levels of iron-rich duricrust plateaus while shaded relief maps revealed residual erosional ridges formed by

RMIRTP	1						
TC	-0.09	1					
K	-0.01	0.15	1				
eTh	-0.09	0.92	-0.15	1			
eU	-0.09	0.77	-0.11	0.65	1		
DEM	0.11	-0.01	-0.21	0.10	-0.13	1	
GRAV	-0.08	0.05	-0.09	0.12	-0.07	0.05	1
	RTPRMI	TC	K	eTh	eU	DEM	GRAV

**Table I-2** Correlation matrix between selected source layers used in the interpretation. *RTPRMI* – reduced to the pole residual magnetic intensity, *TC* – total count (airborne gamma ray data), *DEM* – digital elevation model, *GRAV* – Bouguer anomaly grid.

outcropping geological units and the overall morphology of the area.

To evaluate the relationships between the available source layers, Pearson's correlation coefficient may be computed (James, 1988). For correlated layers PCA serves as a tool in determining uncorrelated factors (components) that can be obtained from the original dataset (Drury, 1993). Pearson's correlation coefficients were calculated for an integrated dataset consisting of the magnetic, gamma ray spectrometry, digital elevation, and gravity data (table I-2). It is evident from the correlation matrix that only values of total count, K, eTh, eU from the gamma ray spectrometry datasets are moderately correlated. A weak correlation may be observed between the elevation and the gamma ray spectrometry data, in particular with potassium content. Based on these observations, PCA transformation was applied only to the gamma ray spectrometry data and the first three components were used in further analyses as an RGB composite complementary to the ternary K, eTh, eU grids and the r gamma ray spectrometry ratio grids.

## 4. Structural framework

Based on field observations we have defined three major deformation events (D1–D3) in western Burkina Faso, which are described in detail in chapter II. Here we present an abridged summary necessary for the description of the litho-structural map.

The first observed D1 deformation phase, probably lasting from 2160–2115 Ma given by the ages of the syntectonic tonalites and granodiorites (ME1) and maximum deposition age of the Tarkwaian-type sediments, is documented in the volcanic rocks by the S1 metamorphic foliation, and the anastomosing shear zones or high strain zones, which strike N to NNE. During the D1, all lithologies were subject to intensive folding best preserved in the volcano-sedimentary sequences where at outcrop scale isoclinal to open folds with NNE-SSW to NE-SW oriented steeply dipping axial planes are observable. Magmatic foliation S1 in granitoids, corresponding generally to NNW to NNE trending steeply dipping compositional layering is characteristic for the ME1 granitoid bodies. The late stages of the D1 period are tied to the deposition of the Tarkwaian-type sediments in the Houndé greenstone belt. The maximum deposition age was estimated at  $\sim 2124 \pm 9$  Ma according to detrital zircon populations (Bossière et al., 1996).

We suggest that the D2 phase occurred during 2113–2097 Ma, based on the dating of the syn/late tectonic granites. The D2 structures in volcanic rocks are characterized by steeply dipping brittle-ductile to brittle shear zones and faults, at places anastomosing. They crosscut at low angle ( $\sim 30^\circ$ ) the S1 penetrative metamorphic foliation and high strain zones, where both structures are present. When the crosscutting relationship is lacking, the differentiation between the D1 and D2 structures is difficult, especially in massive volcanic rocks such as basalts and gabbros, because both deformation events produce localized high strain zones. In the granitoid domains, ENE-trending dextral and NW to NNE sinistral S2 localized shear zones transect the penetrative S1 magmatic layering and HT mylonitic zones. Microstructural observations support the overprinting relationship between the D1 and D2 structures.

The D3 is marked by the development of crenulation cleavage and chevron or kink folds observed in mechanically anisotropic volcano-sedimentary and sedimentary sequences. NW-SE brittle faults and fractures as well as north and south dipping thrust faults, attributed also to the D3, are developed throughout the region. The age of the D3 event is either late Eburnean or Pan-African.

At least three generations of extension related doleritic dykes and sills were emplaced episodically into the consolidated Paleoproterozoic basement and its Neoproterozoic sedimentary cover during a protracted period from 1800 Ma to 250 Ma (Marcelin and Serre, 1971; Ama Salah et al., 1996; Castaing et al., 2003).

The different rheological behaviors of the lithologies govern the deformation structures. In fine-grained rocks such as Birimian volcano-sediments, phyllites, tuffs, and Tarkwaian-type pelites, penetrative metamorphic foliation develops during D1 compression, while more localized shear zones

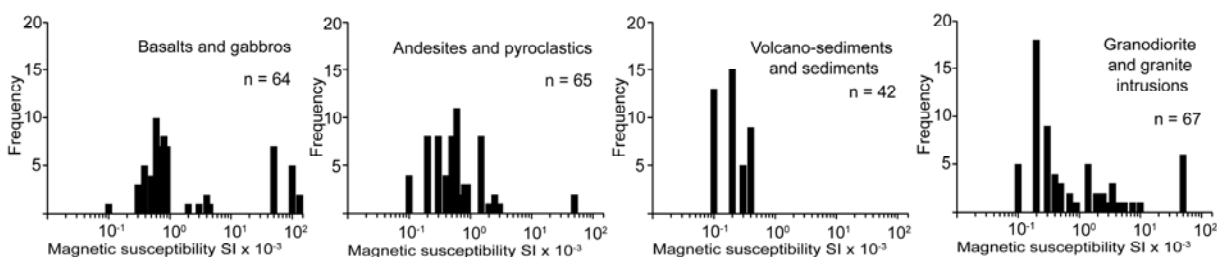


related to D2 event cross-cut the previous structures at low angle. Kink folds and crenulation cleavage form preferentially in zones of high mechanical anisotropy (metamorphic foliation, shear zones). Massive lava flows of basalts and andesites, intrusions of gabbros and granitoids, rhyodacites, and the Tarkwaian-type conglomerates are affected by localized to penetrative shear zones or high strain zones during both D1 and D2 deformation events.

## 5. Lithological associations and structures: their petrophysics and expression in geophysical data

In the following sections, we first introduce the lithological units of the greenstone belts and associated granitoid domains at first, then we describe the major lithological units and structures portrayed in our synthetic map and briefly discuss their response in geophysical and satellite data. Their petrophysical properties (density, magnetic susceptibility, concentration of K, eTh, eU), measured in laboratory, field, or derived from airborne gamma ray data, are summarized in table I-3, along with the characteristic response in airborne magnetic and gamma ray spectrometry grids, mineralogy and typical structures. Histograms of magnetic susceptibility and box-plots of K, eTh, and eU concentrations are shown in figures I-5 and I-6, respectively. In order to illustrate the important features, we have selected four key localities (figure I-7), presented along with the magnetic residual field grid, overlain by the first vertical derivative grid, and the gamma ray (figures I-8a, b, and d) or PCA image (figure I-8c).

The magnetic susceptibility of 238 rock samples collected across the studied area vary by more than four orders of magnitude, from  $0.01 \times 10^{-3}$  SI to  $150 \times 10^{-3}$  SI. Although overlaps exist between the measured susceptibilities, differentiation between the established rock groups is possible. Susceptibility measurements were made for all of the exposed rock types in the field (using a hand held KT-6 susceptibility meter) and in the laboratory (using a Kappabridge, Agico Ltd.). The bulk susceptibility in rocks is mainly a function of the ferro-magnetic minerals content, in particular magnetite; however, biotite has been reported as the main carrier of susceptibility in low magnetic granites of eastern Burkina Faso (Naba et al., 2004; Vegas et al., 2008). The magnetic susceptibility of the volcanic rocks is most probably controlled by the magnetite and titano-magnetite commonly observed in thin sections (Hein et al., 2004; Dioh et al., 2009). The distributions of radioelements in



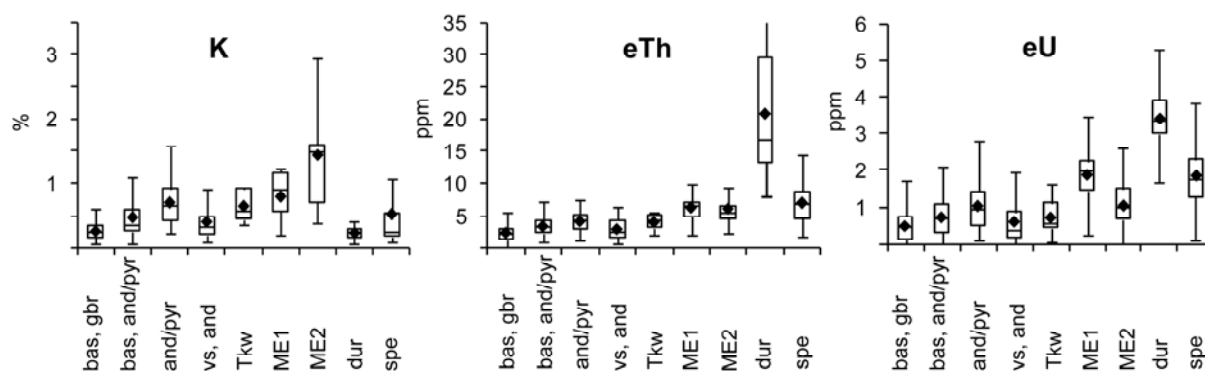
**Figure I-5** Histograms of magnetic susceptibility of selected rock groups.

the different lithologies have been estimated by means of spatial analysis, where 449 outcrop location points served as sampling locations of the processed airborne radioelement grids. Density measurements of 68 fresh rock samples from surface outcrops and drill cores were made at the GET (Géosciences Environnement Toulouse) laboratory.

## 5.1. Mafic and ultramafic lithologies

The basaltic lavas have mostly a tholeiitic composition and form the base of the stratigraphic pile. They are often pillowed suggesting their emplacement in a marine environment. The basalts are microlitic to ophitic and contain typical greenschist facies mineral assemblages (table I-3). Tholeiitic basalts and microgabbros with plagioclase megacrysts were found as sub-units of the basaltic suites. Medium to coarse grained gabbros and gabbro cumulates often accompany the basaltic rocks. In the Boromo greenstone belt, the basal mafic rocks also contain (strongly altered) ultramafic lenses.

Gabbros and basalts show moderate to high susceptibilities with a bimodal distribution ranging from  $0.01\text{--}150 \times 10^{-3}$  SI (figure I-5). The concentration of the radioelements is low and reaches 1% K, 7 ppm of eTh, and 2 ppm of eU (figure I-6). The density of the mafic rocks averages approximately  $3.0 \text{ g/cm}^3$  (with a range of  $2.90\text{--}3.11 \text{ g/cm}^3$ ). In the geophysical grids, these rock types show moderate to strong responses with a pronounced texture. The gamma ray spectrometry response is dominated by low content of all three radioelements and the lithological units appear dark in the ternary grid, if minor or no regolith cover is present, which is generally the case, as outcrops of these rocks often stand out as ridges. In the Bouguer anomaly map, the mafic lithologies correspond to gravity highs with observed maxima surpassing  $-20 \text{ mGal}$ .



**Figure I-6** Box and whiskers graphs of concentrations of K, eTh and, eU extracted from the airborne data based on locations of selected outcrops and regolith units. *bas* – basalt, *gbr* – gabbro, *and* – andesite, *pyr* – pyroclastic flow, *vs* – volcano-sediments, *Tkw* – Tarkwaian-type sediments, *me* – magmatic episode, *dur* – Fe-rich duricrust, *spe* – soft pediment.

The stratigraphically lowermost unit of highly magnetic basalts, gabbros, and basaltic-andesites can be found on the western side of the Boromo belt and the eastern flank of the Houndé belt. The quasi-continuous N-S trending lithological units show both intrusive and tectonic contacts

with the granitoid domains. The maximum thickness reaches 6 km according to our estimations. In both belts, the magnetic textures of these domains display similar NNE-SSW to NE-SW orientations, which are most probably caused by the D3 transcurrent shearing but may be tied to the original lithology. The mafic rocks on the eastern side of the Boromo belt bear some petrological and geochemical resemblance to the above-described lithologies. Even though magnetic and gamma ray spectrometry signatures are comparable, their genetic and structural relationship cannot be established. Gravimetric highs strongly suggest the presence of mafic lithologies underneath the granites near the SE margin of the Houndé belt and the NW segment of the Boromo belt, implying the N-S continuity of the mafic lithologies.

## 5.2. Intermediate to acid volcanics

The massive andesitic lithologies generally consist of intercalated units of andesitic lavas, pyroclastic flows, and tuffs. These lithologies lie stratigraphically above the more mafic assemblages that might be attributed to a more evolved calc-alkaline volcanism associated with volcanic islands (chapter II). The transition from mafic to intermediate volcanism is marked by suites of basaltic andesites. The texture of the andesites and andesitic pyroclastic flows is microlitic characterized by greenschist facies mineral assemblages (table I-3), with variable amounts of porphyric phenocrysts of plagioclase. The subangular to angular lithic fragments in pyroclastic flows range in size from one to twenty cm. The tuffs generally retain microlitic textures; contain rare lapilli and small lithic fragments. Le Métour et al. (2003) differentiate several subfacies including crystal tuffs, hyaloclastites, and cinerites. Dacitic and rhyolitic bodies may be found as minor lenses and bodies throughout the study area. The andesitic suites display generally unimodal distribution of susceptibilities spanning from 0.01 to  $30 \times 10^{-3}$  SI. Rhyolites and dacites have low susceptibilities that do not exceed  $0.15 \times 10^{-3}$  SI. The concentration of K can reach 1.5%, while eTh values remain similar to the mafic rocks (7 ppm), and eU concentrations are slightly higher reaching almost 3 ppm. The measured densities vary from  $2.73 \text{ g/cm}^3$  to  $3.07 \text{ g/cm}^3$ .

In the analyzed grids, the magnetic response of the andesitic lithologies ranges from intermediate to low. The lithological units with abundant pyroclastic flows and intercalations of volcano-sediments show weak responses with a less apparent magnetic grain. The less frequent ridges of mainly andesitic lithologies show a gamma ray spectrometry signature marked by an increased content of potassium, which allows their discrimination from the more mafic rocks. The size of the rhyolitic and dacitic bodies does not allow for their full description in the magnetic or gamma ray spectrometry data. In the Bouguer anomaly map, the felsic rocks are usually incorporated within the high to moderate amplitude anomalies. Moderately magnetic andesites, pyroclastic flows, and volcano-clastics, sometimes intercalated with basalts and volcano-sediments, build up significant parts

of the Boromo and Houndé belts and occur as well in the east of the Banfora belt. The magnetic textures are not so distinct compared to the mafic lithologies, but their orientation remains similar.

### 5.3. Birimian sediments and volcano-sediments

The volcano-sedimentary units comprise mainly wackestones and shales with variable amounts of volcanic material, with intercalations dominated by tuffs, black shales, and frequent ferruginous to manganese cherts. They crop out less frequently due to the more erosion-prone, fine-grained, lepidoblastic texture and intense foliation. The most common mineral assemblage consists generally of quartz, plagioclase, chlorite, muscovite, and carbonate. The magnetic susceptibility of the volcano-sediments remains low and uniform with maximum values of  $0.4 \times 10^{-3}$  SI. The overall maximum concentrations of K, eTh, and eU (~1%, 5 ppm, and 2 ppm, respectively, figure I-6), are lower than expected from their petrological composition. This may be attributed either to high contribution of mafic detrital material or to the fact that the sampling points (one pixel =  $125 \times 125$  m) are adjacent to, or intercalated within, the outcrops of mafic rocks. The densities of the volcano-sedimentary assemblages span from 2.6 to 2.9 g/cm<sup>3</sup>. The volcano-sedimentary rocks are associated with regions of low magnetic intensity with poorly defined magnetic textures. The gamma ray spectrometry data do not allow for unambiguous description of these lithologies due to scarcity of outcrops and deep weathering profiles present over these lithological units. In general, they show relative enhancement of potassium with respect to the concentrations of thorium and uranium. Their low densities correspond to areas of moderately negative gravity anomalies on the Bouguer anomaly map.

The Birimian volcano-sedimentary and sedimentary rocks stratigraphically and sometimes tectonically overlie the felsic and mafic volcanics. In the Boromo and Houndé belts, these units, called the Batié and Bambéla volcano-sedimentary units, respectively, tend to widen towards the south. The Banfora volcano-sedimentary unit constitutes most of the western side of the Banfora belt. At many places, volcano-sediments are stratigraphically or tectonically intercalated with the other volcanic rocks. Magnetic textures are generally smooth without visible structures due to the limited amount of magnetic horizons and overall low susceptibility. Although with some difficulty, abundant folds and shear zones observed at outcrop scale can be traced in the magnetic data. Gravimetric data modeling suggests that a denser basement is present underneath the volcano-sedimentary belt-parallel units (chapter II), which we interpret as andesites.

### 5.4. Tarkwaian-type sediments

The Tarkwaian-type sediments unconformably overlay the volcanic and volcano-sedimentary stack and contain facies ranging from poorly sorted, matrix supported conglomerates, sandstones and gritstones to arkoses and pelites with lepidoblastic textures. At places, original sedimentary structures

such as cross bedding with heavy mineral concentrations, or graded bedding are preserved. Apart from dominant quartz and muscovite, the Tarkwaian-type sediments contain plagioclase, carbonates, and epidote. The magnetic susceptibility of the Tarkwaian-type sediments is similar to the volcano-sedimentary rocks attaining values of  $0.1\text{--}0.12 \times 10^{-3}$  SI. The concentrations of K, eTh, and eU do not surpass 1%, 6 ppm, and 1.9 ppm, respectively. Density measurements concentrate around  $2.74 \text{ g/cm}^3$  ( $2.71\text{--}2.76 \text{ g/cm}^3$ ). The magnetic intensity is usually low and textures are uniform, however adjacent high magnetic intensity lithological units of basalts or gabbros may alter the signature. The relatively high content of K explains why the Tarkwaian-type sediments appear as slightly red (K is mapped to the red channel) in the ternary gamma ray spectrometry grids (table I-3). This continuous but relatively thin sedimentary sequence does not leave an imprint in the Bouguer anomaly map.

The Tarkwaian-type sediments stretch for 400 km in the N-S direction within the Houndé belt. They are tectonically bound by the Boni shear zone and separate the tholeiitic basal mafic unit in the east from the andesitic calc-alkaline volcanic sequences in the west. These shallow water detrital sediments, characterized by low susceptibilities, are hardly recognizable from the Birimian volcano-sediments and sediments in magnetic data. The map thickness varies from 0.5 km to 2 km. This implies that the narrow segments are not well visible on magnetic data, while wider segments bordered by lithologies with higher magnetic susceptibilities (e.g. north and south of Bondigui) are easily traceable. In the south, near Loropéni, the Tarkwaian-type sandstones are folded, which is documented by inverse downward facing sedimentary bedding in the western fold limb. The hypothetical anticline seems to be intruded by a N-S elongate granitoid body, as suggested by magnetic gamma ray and gravimetric data; however, no granite outcrop was found in this area. The northernmost outcrop of the Tarkwaian-type sediments southwest from Saoura (Ouedraogo, L., SEMAFO Inc., pers. communication) indicates that this unit extends much further to the north compared to the existing geological maps (Castaing et al., 2003; Ouedraogo, 2004).

## 5.5. Granitoids

Tonalites, trondhjemites, and granodiorites (ME1) are often amphibole- and biotite-bearing and may contain minor K-feldspar. These rocks frequently display mineral layering and vary from medium to coarse-grained. Intrusions of granodiorites and granites (ME2) contain biotite, K-feldspar, and rare amphibole or muscovite. They are generally medium- to coarse-grained with some porphyritic varieties, affected by a mylonitic foliation. The third group (ME3) is formed by late granitic stocks and plutons, which are K-feldspar rich and sometimes muscovite bearing. These less abundant sub-circular to elliptical relatively small (5–15 km) bodies are mostly undeformed. Coarse-grained gabbro-diorite intrusions (ME4) of unknown age are often associated with the granite and granodiorite intrusions (Castaing et al., 2003). In contrast to the gabbros found in the greenstone belts,

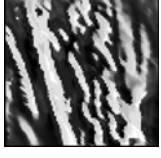
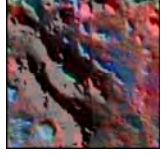
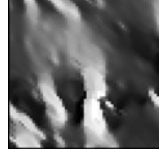

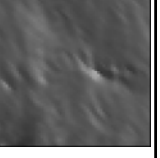
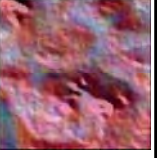
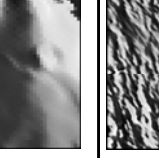



they are unmetamorphosed and contain clinopyroxene and hornblende as dominant minerals, with minor plagioclase.

The tonalitic, granodioritic and granitic domains (ME1 and ME2) exhibit low to moderate susceptibility values. The histogram of susceptibilities shows a multimodal distribution where values range from  $0.1 \times 10^{-3}$  SI to  $37 \times 10^{-3}$  SI. The magnetically zoned late granitic stocks (ME3) are moderately to highly susceptible; however, the limited outcrop conditions impede realistic evaluation of the distribution of susceptibilities. Only one sample from central low magnetic zone was measured in the laboratory yielding  $0.4 \times 10^{-3}$  SI. The susceptibility of the ME4 gabbros varies from  $0.18 \times 10^{-3}$  SI to  $0.39 \times 10^{-3}$  SI. The concentrations of K are lower in the ME1 group (up to 1.2%) than in the ME2 group (up to 3%), and inversely, eU concentrations are higher in the ME1 than in the ME2 (up to 3.5 ppm and 2.5 ppm, respectively). Thorium remains comparable (up to 10 ppm) in both (ME1 and ME2) types. The youngest suite of granites (ME3) and the gabbros (ME4) do not offer enough exposure to be included in the gamma ray spectrometry data analysis. The densities of the ME1 granitoids vary between 2.64 and 2.8 g/cm<sup>3</sup>. The ME2 and ME3 granites and granodiorites are slightly less dense ranging from 2.63 to 2.73 g/cm<sup>3</sup>.

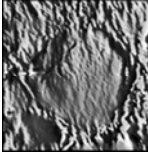
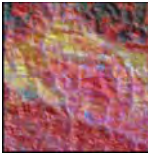
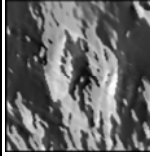
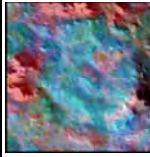
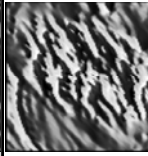
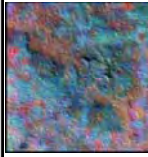
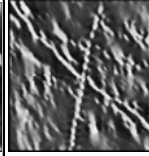




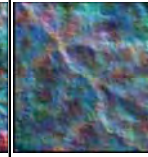
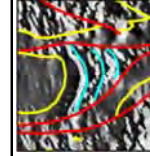

The ME1 granitoids appear in the magnetic grids as low to moderate intensity features with variably oriented magnetic fabric. Their shapes are more complex than simple oval or circular forms likely due to their syn- or post-emplacement deformation. The ME2 granodiorites and granites of the display moderate to high magnetic intensities and usually a sub-elliptical shape. The ME3 granites are distinctively more magnetic and appear as high intensity sub-elliptical, magnetically zoned plutons. The gamma ray spectrometry data portray most of the granitoids similarly due to regolith cover. In areas with less regolith cover, the ME1 group seems to be less enriched in radioelements, appearing darker in the gamma ray spectrometry grids. The ME2 have an overall higher content of radioelements especially K and eTh, which are responsible for their lighter red to violet and yellow colors (table I-3). The Bouguer anomaly map shows the granitoid domains as well-defined highly negative zones.

Most of the granitoid intrusions are concentrated in belt-parallel domains but several individual plutons also intrude the greenstone belts (e.g. Dissin granite in the Boromo belt, Koumbia and Djigué granite in the Houndé belt, or the suite of granites along the Greenville-Ferkessedougou-Bobo Dioulasso SZ in the Banfora belt). Although individual granitoid bodies with contrasting magnetic textures and intensities can be delimited, distinction between the ME1 and ME2 generations is delicate due to scarce gamma ray spectrometry and geochemical data. We are confident about the classification of granitoids in the Diébougou domain. The other three domains (Koudougou-Tumu, Sidéradougou, and Niangoloko) remain challenging, mainly because of less field observations and more complex pluton character. According to our interpretations, the granitoid domains consist of significant amount of individual plutons, which are more or less affected by deformation, depending on the timing of each intrusion with respect to the deformation and on the location of the D1 and D2 shear zones within the granitoid domains. These domains fit the Bouguer gravity lows (figure I-2d)

averaging -40 mGal, and visible subdivisions of the broad gravity lows into several minima (-50 to -45 mGal) further support our conclusion that the granitic domains are formed by several intrusive bodies.

Legend	Lithology & Structures	Mineralogy	Density & Mag. Susceptibility	Airborne Magnetic response	Magnetic image	Airborne Radiometric response	Radiometric + shaded DTM Image
Ultrabasic rock	Dunite; massive Pyroxenite; mass.	ab, ol, serp, ep, chl pl, cpx/hbl	NA	Not distinguishable from basalts and gabbros	 5 km	K, eTh, eU poor	
Basalt, gabbro; Basalt	(micro)gabbro, dolerite; massive, localized SZ Basalt; massive, localized SZ	pl, cpx, hbl/act, chl, ep/czo, qtz pl, hbl/act, chl, ep/czo, qtz	High 2.90 – 3.11 g.cm <sup>-3</sup> 0.1 – 150x10 <sup>-3</sup> SI bimodal	Moderate to high intensity, variable N-S to NE-SW oriented magnetic fabric	 5 km	K, eTh, eU poor	
Basaltic andesite; andesite, pyroclastic flow	Andesite, massive; localized SZ Pyroclastic flow; massive, local. SZ	pl, ep/czo, chl, act, qtz	Medium to high 2.73 – 3.07 g.cm <sup>-3</sup> 0.01 – 30x10 <sup>-3</sup> SI unimodal	Moderate to low intensity andesitic -> basaltic increasingly magnetic Moderate to low intensity, smooth texture, andesitic layers add magnetic fabric	 5 km	Medium to high K, moderate eTh and eU (usually small bodies)	
Pyroclastics, volc.-sedim.	Tuffs, foliated; localized SZ	qtz, ab, ep, chl, ms	NA 0.01-0.12x10 <sup>-3</sup> SI	Not recognizable, small bodies usually	 5 km	Low to moderate K, eU, eTh, affected by regolith	
Rhyolite, dacite	Felsic - dacites, rhyolites; massive	qtz, ab, chl, ms, carb,	Medium to low 2.60 – 2.90 g.cm <sup>-3</sup> 0.01 – 0.4x10 <sup>-3</sup> SI unimodal	Low intensity uniform, andesitic layers add fabric	 5 km	Moderate K, moderate to low eTh, eU	
Birimian sediments, volc.-sedim	Wackestones and argillites; foliated, localized SZ	qtz, ab, ms, carb, ep	Medium to low 2.71 – 2.76 g.cm <sup>-3</sup> 0.1 – 0.12x10 <sup>-3</sup> SI unimodal	Low to moderate intensity, variable NNE-SSW oriented magnetic fabric, complex interlocked bodies	5 km	Moderate to low K, moderate eTh and eU, affected by regolith	
Tarkwaian-type sedim.	Conglomerate; mass., localized SZ Sandstone, gritstone; massive, localized SZ Arkose, pelite; foliated	qtz, ab, ms, carb, ep	Medium to low 2.64 – 2.80g.cm <sup>-3</sup> 0.1 – 34x10 <sup>-3</sup> SI bimodal/ multimodal	Low to moderate intensity, variable NNE-SSW oriented magnetic fabric, complex interlocked bodies	5 km	Moderate to low K, moderate eTh and eU, affected by regolith	
Tonalite, trochilomite, granodiorite (MEI)	Granodiorite, tonalite and diorite; HT banding, mylonitic foliation, locally mylonitic	pl, qtz, bt, hbl	Medium to low 2.64 – 2.80g.cm <sup>-3</sup> 0.1 – 34x10 <sup>-3</sup> SI bimodal/ multimodal	Low to moderate intensity, variable NNE-SSW oriented magnetic fabric, complex interlocked bodies	5 km	Moderate to low K, moderate eTh and eU, affected by regolith	



Legend	Lithology & Structures	Mineralogy	Density & Mag. Susceptibility	Airborne Magnetic response	Magnetic image	Airborne Radiometric response	Radiometric + shaded DTM Im.
Granodiorite, granite (ME2)	Granite and granodiorite; mylonitic foliation, localized SZ, massive	pl, qtz, kfs, bt, (hbl)	Medium to low $2.63 - 2.73 \text{ g.cm}^{-3}$ $0.1 - 37 \times 10^{-3} \text{ SI}$ bimodal/ multimodal	Moderate to high intensity Sub-elliptical bodies		Moderate to high K, eTh and eU, affected by regolith	
Granite (ME3)	Granite, leucogranite; locally mylonitic, massive, mylonitic foliation	pl, kfs, qtz, ms, bt,	Medium to low $2.63 - 2.73 \text{ g.cm}^{-3}$ $> 0.4 \times 10^{-3} \text{ SI}$	High intensity sub-elliptical bodies, magnetic zoning		High K, eTh, eU, affected by regolith	
Gabbro, diorite (ME4)	Gabbro; massive	cpx, hbl, pl, qtz	NA $0.18 - 0.39 \times 10^{-3} \text{ SI}$	Moderate to high intensity		Low	
Dolerite dyke	Dolerite dyke, massive	ol, opx, cpx, hbl, bt, pl	NA $15 - 76.8 \times 10^{-3} \text{ SI}$ unimodal	Highly magnetic, linear features		Not recognizable	
Not on map	Fe-rich duricrust	hem, gt, kln, qtz	NA NA			Low K, high eTh and eU	
Not on map	Soft pediment	hem, gt, kln, sme, qtz	NA NA			Low K, high eTh and eU	
Folds/Faults	folding geometries -of- changes in lithology and structural patterns	NA	NA NA	Folds - curved magnetic patterns Faults - abrupt changes in magnetic patterns, truncation, displacement		Folds - curved patterns Faults - Changes in the content of radioelements when contrasting lithologies are present	

**Table I-3** Summary table of the lithologies; their mineralogical, petrophysical characteristics, and expression in the airborne geophysical data. DTM – digital terrain model, andes. – andesite, volc.-sedim. – volcano-sediment, Qtz – quartz, Pl – plagioclase, Cpx – clinopyroxene, Hbl – hornblende, Act – actinolite, Chl – chlorite, Ep – epidote, Bt – biotite, Kfs – K-feldspar, Kln – kaolinite, Czo – clinozoisite, Carb – carbonate, Hem – hematite, Gt – goethite. Folds/Faults – red line – interpreted fault/shear zone, yellow line – lithological contact, turquoise line – interpreted fold hinge.

## 5.6. Doleritic dykes and sills

The doleritic dykes and sills form discordant crosscutting bodies with rare outcrops. The rock texture is ophitic, reflecting the primary magmatic mineral assemblage of orthopyroxene, clinopyroxene, and plagioclase. Secondary hornblende and biotite may be observed and are probably related to late magmatic autometamorphism caused by fluid-rock interaction. The susceptibility of the dykes and sills was measured at several places and vary between 15 and  $77 \times 10^{-3}$  SI. The dykes are easily traceable in the magnetic data as high intensity linear features (figure I-2b). The dykes are not usually visible in the gamma ray spectrometry grids nor in the gravity data; however, large sills found in the Taoudeni basin, might correspond to highs in the Bouguer anomaly map. At least three generations of doleritic dykes oriented N40°, N100°, and N120°, were identified. All three generations crosscut the Paleoproterozoic basement and two of them (N40°, N100°) intrude sediments of the Taoudeni basin, forming dykes or sills. Hence, the N120° generation pre-dates the deposition of the Taoudeni sediments and the other two generations post-date it. The sills occur exclusively in the sediments of the Taoudeni basin and intrude along the sub-horizontal bedding.

## 5.7. Neoproterozoic sedimentary cover

The present study, along with the accompanying tectonic model, is focused on the lithological assemblages and structures of the Paleoproterozoic basement. Therefore, the Taoudeni basin, which overlies the Paleoproterozoic basement in the west, is considered as one unit in the proposed map. Its limit was established using Landsat and ASTER images, combined with gamma ray data and SRTM digital elevation model. The Bouguer anomaly map suggests that the dense andesitic sequences of the Houndé greenstone belt continue underneath the basin. The continuation of the Banfora belt towards the north is uncertain, as the gravity highs might also be attributed to the numerous intrusions of younger doleritic sills and bodies, which accompany the doleritic dykes that crosscut the basin (Marcelin, 1971; Marcelin and Serre, 1971; Castaing et al., 2003).

## 5.8. Lateritic weathering of the lithologies

The regolith units may be broadly divided into two categories: the iron-rich duricrusts and the soft lateritic soils. The duricrusts form plateaus of various shapes extending over all lithologies. Their mineral composition consists mainly of goethite, haematite, kaolinite, and quartz. Soils forming the

Fe-rich pediments are best developed over granitoid domains and volcano-sediments. Their mineral assemblage is essentially similar to that of the duricrusts although enriched in clay minerals and quartz. The duricrusts (table I-3) are strongly depleted in potassium (less than 0.5%) and enriched in both thorium (up to 40 ppm) and uranium (up to 5 ppm). The soft Fe-rich pediments show higher potassium contents (up to 1%) compared to the duricrust plateaus, while concentrations in thorium (up to 14 ppm) and uranium (up to 4 ppm) are slightly lower but still enriched with respect to the parent rocks. In the gamma ray spectrometry grids, the Fe-rich duricrusts display light turquoise colors while the soft pediment soils appear as more potassium rich in shades of red and violet.

Regolith landform units are not represented in the proposed litho-structural map. However, their omnipresence hampers geological mapping in all of West Africa. Gamma ray spectrometry data combined with SRTM digital elevation model were used in order to delimit the lateritic duricrusts and soils. Presence of the lateritic cover greatly influences gamma ray spectrometry data interpretation because the residual Fe-rich material accumulates thorium and uranium, while potassium is generally leached due to weathering. The soils are richer in K compared to the ferruginous duricrusts due to higher kaolinite content. The erosional escarpments of the iron-rich duricrust plateaus may correspond to the actual lithological contacts, especially, where the duricrust is preserved on the top of granite plutons; however, it is eroded above the adjacent greenstones (e.g. the Gaoua batholith or the Bondigui pluton). Although the chemical compositions of the duricrusts and soils depend on the source rock (Blot et al., 1973), the differences in the radioelement concentrations are too subtle to be mapped by airborne gamma ray spectrometry. Moreover, according to the field observations, significant proportion of regolith cover in the study area was displaced and may not correspond to the underlying lithology.

## 5.9. Structures

### *D1 structures*

The calc-alkaline andesitic province of the Houndé greenstone belt presents evidence of the D1 folding event in the form of a magnetic horizon of basaltic andesites, which seems to form a synform with NNE-SSW oriented steeply dipping axial fold plane (figure I-7, north of Houndé). We suggest the presence of a large-scale D1 antiform in the central part of the Houndé greenstone belt (figure I-7, south of Koumbia), which is formed by andesites and pyroclastic flows and is elongated along the Ouango-Fitini shear zone. Its axial plane is NNE-SSW oriented and steeply dipping. The moderate magnetic intensity, Koumbia granite and the late, high magnetic intensity, granitic stock intrude the presumed fold. The tholeiitic mafic lithologies adjacent to the Gaoua batholith in the south (figure I-7, around Gaoua) display a fold-like shape in the magnetic data. Field mapping also revealed that the megacrystic tholeiitic basalts outline the granite in a curved shape. We interpret this structure as an antiform possibly related to the Gaoua batholith emplacement.

***D2 structures***

The structural grain of the three greenstone belts and the four granitoid domains is controlled by the latest regional scale transcurrent D2 shear and high strain zones. The NNE to NE-trending structures are often localized at the contacts between the greenstones and granitoids. In the magnetic data, these shear zones substantially overprint the D1 structures such as folds and metamorphic foliation, better observable at outcrop scale. The D2 deformation intensity seems to be overall higher in the northern third of the study area, based on both magnetic data and field observations.

The N-S oriented Boni shear zone, most probably seated on a deep pre-existing regional scale structure, delimits the Tarkwaian-type sediments in the Houndé greenstone belt from the east and west. Its expression in the magnetic data either coalesces with the western margin of the highly magnetic lithologies of basalts and gabbros or remains difficult to trace within the low magnetic lithological units of volcano-sediments. The overall shear sense is ambiguous being dextral in the northern part of the Houndé greenstone belt while sinistral movement indicators were found in the central part of the belt. We interpret that the Boni shear zone acted as a conduit for granitic bodies, which were emplaced along its length at depth. Although they do not always crop out, with the noticeable exception of the Bondigui pluton and of several smaller intrusions to the north of the Houndé greenstone belt, their presence is well documented by the gravity lows visible all along its length.

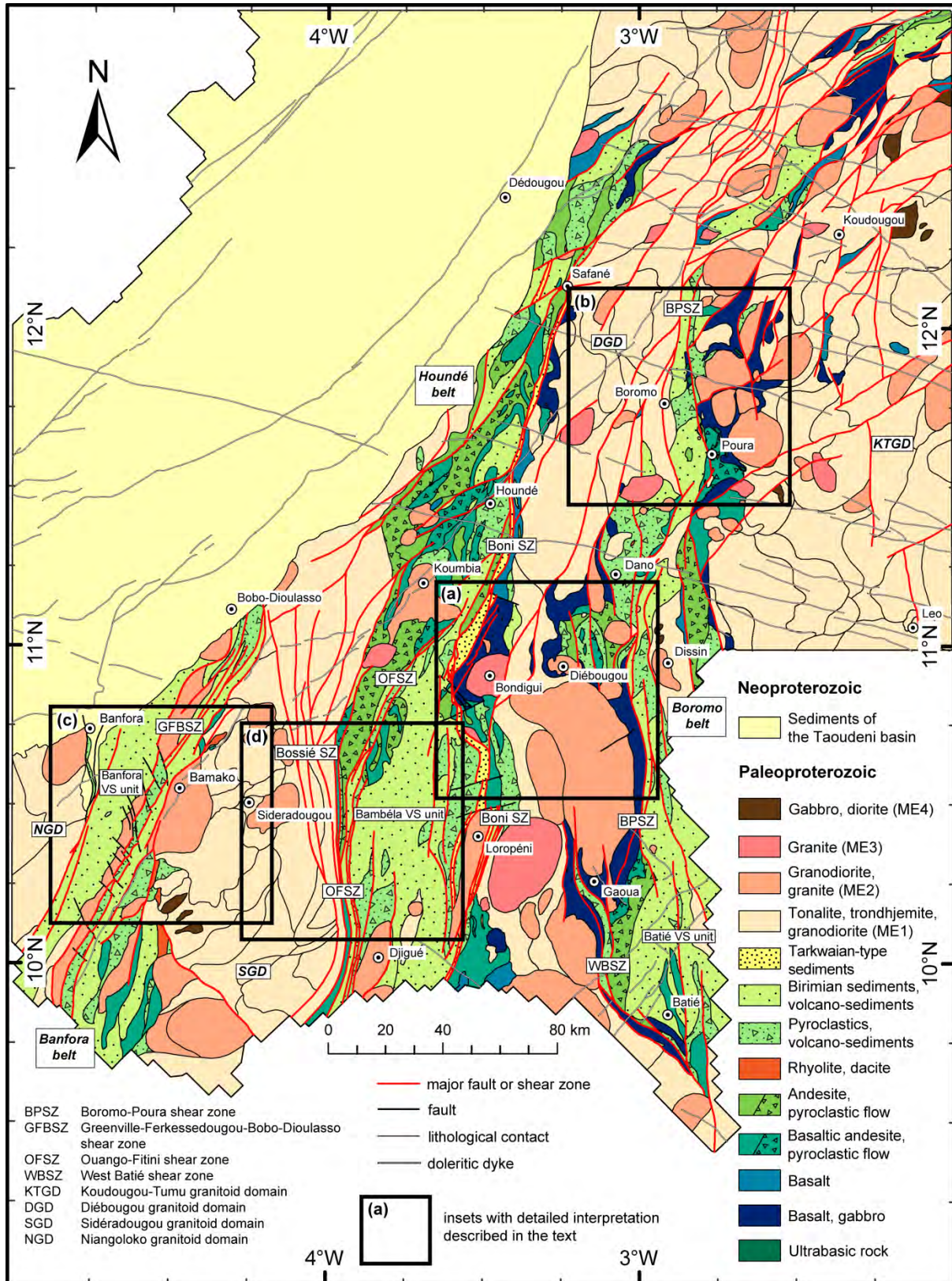


Figure I-7 Litho-structural map with the position of four key areas depicted as insets.

The continuation of the Ouango-Fitini shear zone (OFSZ), previously described by Pouclet et al. (1996), Hirdes et al. (1996), and Lüdtke et al. (1998; 1999) in northern Ivory Coast defines the western margin of the Houndé greenstone belt (figure I-1b). From the border with Ivory Coast in the south, this left-lateral high strain zone results in subparallel stratigraphic units, which continue for approximately 80 km to the north. Further to the north, this zone continues in a NNE direction through the Houndé belt and joins the Boni shear zone. The newly described Bossié shear zone transecting the Sidéradougou granitoid domain acts as a series of splay faults branching from the Ouango-Fitini shear zone. The magnetic data suggest a sinistral sense of shear along the Bossié fault zone and a concomitant activity with the OFSZ during the D2 transpression event.

In the Boromo belt, the deformation is concentrated into a regional-scale anastomosing network of high strain zones, the Boromo-Poura shear zone corridor. The West Batié shear zone forms a part of this network, localized in the south at the contact between the western side of the Boromo belt and Diébougou granitoid domain, extending to the Ivory Coast. The Boromo-Poura shear zone corridor changes its orientation from ~N-S in its southern and central parts to NE-SW direction in its northernmost segments.

In its central part, the Banfora greenstone belt is affected by the belt parallel Greenville-Ferkessedougou-Bobo Dioulasso shear zone (GFBSZ) (figures I-1b and I-7) first recognized by Lemoine (1988). The GFBSZ appears in the magnetic data as a set of demagnetized subparallel NNE-SSW oriented dextral shear zones intruded by elongated granitic bodies and cross-cut by late NW-SE apparently sinistral faults. The zone is visible in regional stitches of magnetic data all the way to Ivory Coast and Liberia documenting its regional scale significance.

### ***D3 structures***

The D3 structures such as E-W trending thrust faults or steeply dipping crenulation cleavage are barely visible in the regional scale geophysical data. Some of the E-W oriented small-scale structures observable in the magnetic data might correspond to the D3 thrust faults. A number of the NW-SE oriented faults and fractures, best recognized in the Banfora belt but abundant all across the area, might be also attributed to the D3 deformation event.

## **5.10. Key sub-areas**

We have selected four key sub-areas to demonstrate the important litho-structural features and show their interpretation in the used datasets. The four map insets indicated in figure I-7 represent: 1) the western margin of the Boromo belt and the eastern margin of the Houndé belt, with the Diébougou GD (granitoid domain) in between (figure I-8a); 2) the contact between the eastern margin of the Boromo belt and the Koudougou-Tumu granitoid domain (figure I-8b); 3) the Banfora belt with the Greenville-Ferkessedougou-Bobo Dioulasso shear zone in the center and the marginal

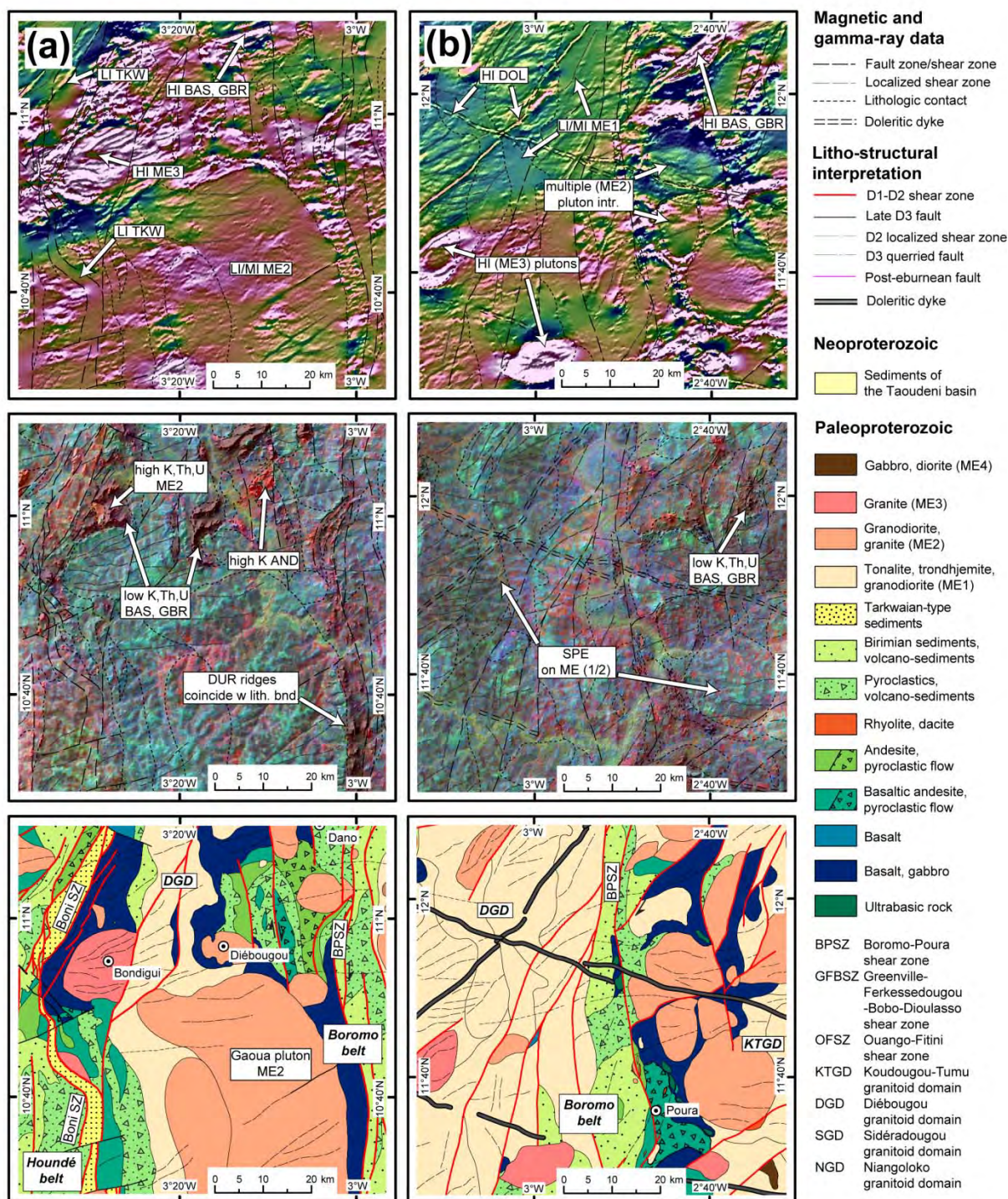
Sidéradoukou and Niangoloko granitoid domains (figure I-8c); and 4) the contact zone between the western Houndé belt and the Sidéradoukou GD (figure I-8d).

The western margin of the Boromo belt also consists of highly magnetic tholeiitic basalts and gabbros (figure I-8a); characterized by high intensity ENE-trending magnetic textures. Rocks with the same petro-chemical, magnetic and gamma ray spectrometry characteristics can be mapped in the eastern flank of the Houndé belt; we suggest that these two units originally formed part of the same oceanic plate/plateau. The magnetic grid illustrates the difference between the strongly sheared, moderately magnetic ME1 granodiorites, the moderately magnetic weakly deformed ME2 Gaoua pluton, and the highly magnetic Bondigui ME3 granite with well-visible concentric magnetic patterns.

The eastern margin of the Boromo belt (figure I-8b) is intruded by the sub-circular, well-defined ME2 granitoids. The surrounding ME1 bodies are characterized by rather elongate irregular shapes, generally affected by N-S to NE- trending shear zones. Three plutons of high magnetic late ME3 granites exhibit ellipsoidal shapes with concentric magnetic zoning, documenting their late tectonic emplacement. Highly magnetic basalts and gabbros with pronounced NE-SW oriented textures visible in gamma ray spectrometry data, are transected by the ME2 granites and clearly differ from other greenstone belt lithologies. Two of the three generations of doleritic dykes (N40° and N100°) are well visible in magnetic data.

The NNE-trending Greenville-Ferkessedougou-Bobo Dioulasso shear zone, intruded by a syn-kinematic ME2 granite, can be clearly traced on both magnetic and gamma ray spectrometry data as well as subsequent NW-SE faults truncating the shear zone (figure I-8c). Volcano-sediments of the Banfora basin show again uniformly low magnetic intensity, which contrast with adjacent lithological units of andesites and basalts. Some of the granites (e.g. the Bamako pluton) can be delimited in gamma ray spectrometry data, including concentric compositional patterns; on the other hand, most of the intrusions can only be outlined using the magnetic grids. Some of the doleritic dykes follow belt-parallel preexisting structures, while others crosscut them.

The southwestern margin of the Houndé belt is tectonically delimited from the Sidéradoukou Granitoid Domain by the Ouango-Fitini shear zone, which is best visible in the PCA (principal component analysis) enhanced gamma ray spectrometry data (figure I-8d). The NNW-SSE oriented Bossié shear zone, affecting the granitoid domain appears yellow and pink in the PCA image. In magnetic data, clear truncation of magnetic textures confirms the fault location. Flat magnetic textures and abundant soils are typical for the volcano-sedimentary and sedimentary rocks, as exemplified by the Bambéla volcano-sedimentary unit.



**Figure I-8** Key localities showing details from map shown in figure I-6. Upper map: RTPMRI (Reduced to the pole residual magnetic intensity) color overlay over first vertical derivative (grey-scale); Intermediate: ternary grid of the airborne gamma ray data or PCA grid; Lower map: geological interpretation. (a)–The western margin of the Boromo belt and the eastern margin of the Houndé belt; (b)–The eastern margin of the Boromo belt and the Koudougou-Tumu granitoid domain; (c)–The Banfora belt; (d)–The contact zone between the western margin of the Houndé belt and the Sidéradougou GD. HI – high intensity, MI – medium intensity, LI – low intensity, BAS – basalt, GBR – gabbro, AND – andesite, VS – volcano-sediment, TKW – Tarkwaian-type sediments, DOL – doleritic dyke, SPE – soft pediment., DUR – Fe-rich duricrust, intr. – intrusion, w. lith. bnd. – with lithological boundary, subcirc. – subcircular, mag. – magnetic.



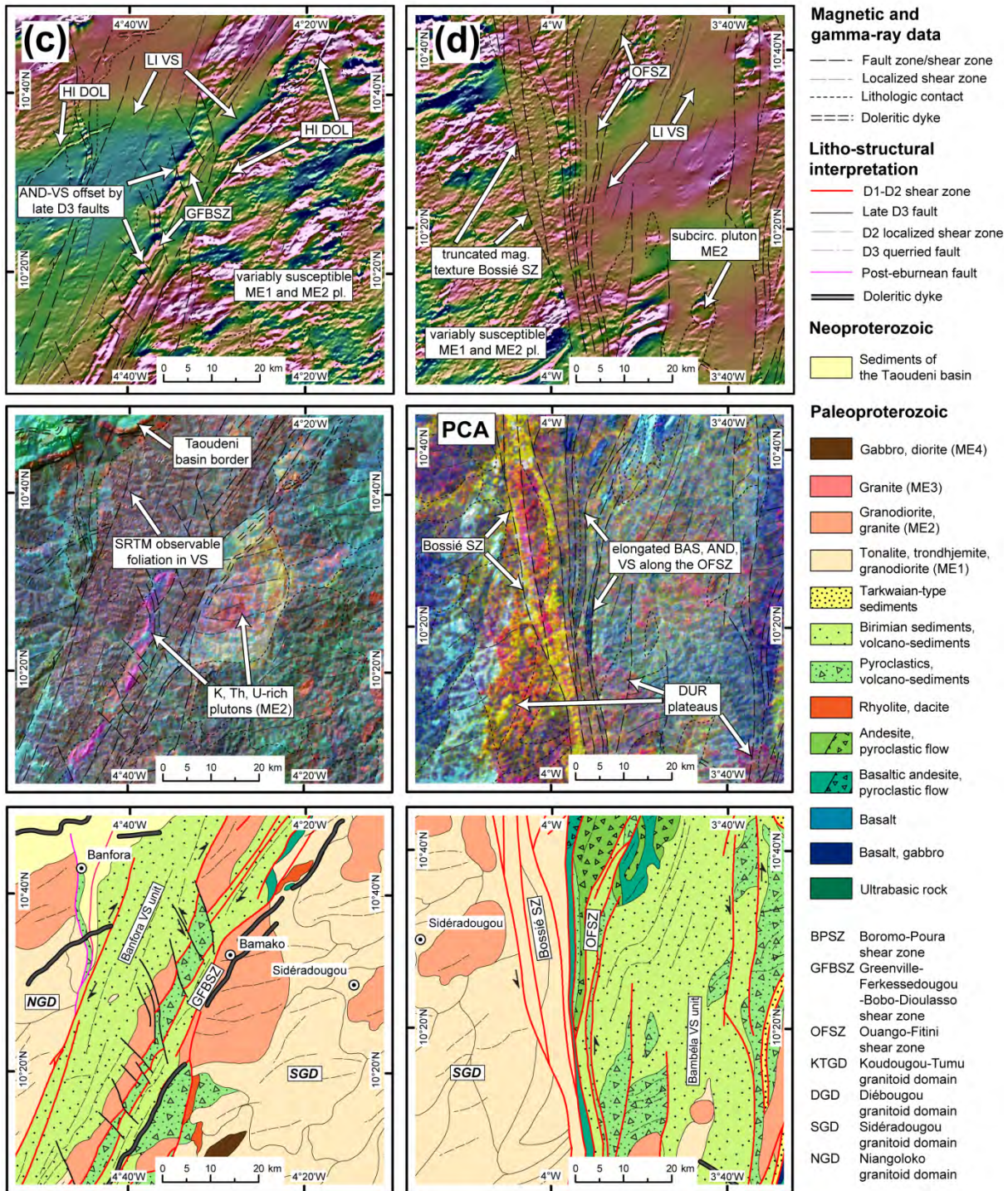


Figure I-8 continued.

---

## 6. Discussion

### 6.1. Lithologies and structures

The new litho-structural map was constructed using field observations integrated with airborne geophysical data, satellite, and SRTM images. We made a significant effort to incorporate existing geological data, including geological maps, outcrop database, and BRGM geochemical analyses database (Marcelin, 1971; Marcelin and Serre, 1971; Lüdtke et al., 1998; Castaing et al., 2003; Chèvremont et al., 2003; Koté et al., 2003; Le Métour et al., 2003); together with unpublished reports and maps from mining companies (figure I-4). This integrated approach and in particular interpretation of airborne geophysical data, led to several important findings, previously unrecognized in the area of western Burkina Faso. The shape and internal structure of the large granitoid domains has been studied in detail and led to the observation that the igneous domains consist of several generations of granitoid intrusions. The structural grain is defined by S1 and S2 metamorphic fabric, shear zones and high strain zones. A well-constrained overprinting relationship was observed between the D1-D2 shear zones both in the field and in airborne magnetic data. The shape and position of these shear-zones was better defined and several new major structures were incorporated in the map. The S2 shearing generally overprints the D1 NW-SE F1 folding structures; however, relic F1 folds were identified in the Houndé greenstone belt. The structural aspect of the geological map is more coherent and complete as it was defined in conjunction with the regional tectonic model presented in chapter II.

From the lithological point of view, basalts, gabbros, and andesites can be easily distinguished in magnetic and gamma ray spectrometry data from volcano-sediments and granitoids. However, some of the highly magnetic plutonic rocks (ME2, ME3, and ME4) resemble gabbros and basalts of the greenstone belts and can be misinterpreted, especially where outcrop information is lacking. Volcano-sediments when intercalated with andesites show similar magnetic response to some of the tonalites and granodiorites (ME1, ME2). Adjacent volcanic rocks frequently suppress the low magnetic intensity signature of the Tarkwaian-type sediments, in particular when the unit becomes narrow.

The airborne magnetic data show that the granitoid domains consist of multiple generations of individual intrusions, which implies an important constraint on the conception of the regional geodynamic model. In our study, we have divided the granitoids based on their petrography, magnetic properties and their geometry into three groups following the schemes discussed by Pons et al. (1995), Doumbia et al. (1998), Castaing et al. (2003), Gasquet et al. (2003), and Naba et al. (2004). One additional group of gabbros of unknown age (ME4) has been designated. This group corresponds to the “late” gabbros and diorites reported by Castaing et al. (2003) in Burkina Faso and Hirdes et al. (1996), Lüdtke et al. (1998) in northern Ivory Coast. Although the shape of plutons itself cannot not give us unequivocally the relative age of the pluton, a better definition of granitoid shapes from magnetic data has contributed significantly to their classification with respect to the deformation. The

character of internal fabric such as magmatic layering or mylonitic foliation in conjunction with geochronological and petrochemical data would reduce the uncertainty in the distinction between the ME1 and ME2 groups. The late K-rich granites (ME3) seem to be systematically highly magnetic, forming small (~5–15 km) ellipsoidal bodies. The gabbros associated with granitoids (ME4) have a magnetic texture similar to the gabbros of the greenstone belts and only field outcrops confirm unambiguously their presence.

In airborne magnetic data, S1 structures are difficult to distinguish from the S2 shear zones due to the similar orientation and high intensity of the D2 event. In the Houndé belt, relic F1 fold hinges are scarcely observed in the magnetic dataset, while isoclinal to open F1 folds with NE trending axial planes occur in all three belts at outcrop scale. The S2 shear zones (Boromo-Poura SZ, West Batié SZ, Boni SZ, Ouango-Fitini SZ, Bossié SZ, and Greenville-Ferkessedougou-Bobo Dioulasso SZ) could be clearly identified at various scales using the magnetic data. Regional scale shear zones often define lithological contacts; hence, they are sharp and linear. Small scale localized NE to ENE-trending S3 shear zones are best visible in individual granitoid plutons; however, they affect all lithologies. The newly discovered shear zones represent perspective areas for gold exploration (Milési et al., 1989; Milési et al., 1992; Blenkinsop et al., 1994; Allibone et al., 2002; Groves et al., 2003; Cox, 2005; Béziat et al., 2008), including shear zones cross-cutting granites (e.g. Bossié SZ), as gold was recently discovered in shear zones affecting granitoid plutons in Ghana (Allibone et al., 2002). Zinc and copper deposits are also found in the study area near Perkoa (Schwartz and Melcher, 2003; massive sulfides) and Gaoua (Sillitoe, R., unpublished reports of Volta Res. Inc., <http://www.voltaresources.com>; porphyry copper), respectively. These mineral deposits are related to dioritic intrusions, which are not easily discernible in the magnetic or gamma-ray spectrometry data. This may be caused by the fact that the gamma ray spectrometry signature of the dioritic intrusions is similar to the surrounding host rocks or masked by regolith cover. Unlike gold, the zinc and copper deposits are not bound to large-scale shear zones that are easily traceable in magnetic data. Given these circumstances, electromagnetic surveying may provide better results than magnetic or gamma ray spectrometry data when prospecting for such deposits.

The NW-SE brittle fault system affecting the eastern margin of the Houndé belt southeast of the town of Houndé (Castaing et al., 2003; Le Métour et al., 2003) was not observed in either magnetic or gamma ray spectrometry data, which suggests no interruption of the volcanic and sedimentary units exists. On the other hand, a system of parallel NW-SE faults with apparent sinistral kinematics clearly displaces volcanic lithologies in the eastern part of the Banfora belt, including the granite intrusion along the GFBSZ.

## 6.2. Strengths and weaknesses of the different datasets

The integration of the available datasets proved to be the most powerful tool in the creation of the new geological map. Each data type and technique is appropriate for different lithologies, structures, areas, depths, or other aspects we are looking for (table I-4). Airborne magnetic data were found to be the most accurately defining lithologies and structures of the Paleoproterozoic basement at all scales, to depths of approximately 100–300 m, similarly to the findings of Jaques et al. (1997) or Betts et al. (2007). Gamma ray spectrometry data, characterizing the first 30 cm of depth (Minty, 1997), in combination with SRTM digital elevation model, provided good results in mapping regolith and outcropping lithologies, in particular basalts, gabbros, and andesites, which form morphological elevations. Landsat and ASTER data are complementary to gamma ray spectrometry datasets in regolith mapping, thanks to their fine spatial resolution. In order to assess deep structures (up to 10 km), we have preformed 2½ D modeling using gravity data in chapter II.

	<b>Magnetic data</b>	<b>Radiometric data</b>	<b>Landsat/ASTER data</b>	<b>SRTM data</b>
<b>Structural mapping</b>	Good (independent of regolith signatures)	Poor (depends on regolith cover)	Poor (with the exception of well exposed terrains)	Limited (for regional structures or foliation patterns depends on exposure)
<b>Lithology</b>	Moderate (lithologies with similar susceptibilities may be misidentified)	Moderate (depends on regolith cover)	Poor (with the exception of well exposed terrains)	Limited (depends on exposure and contrast in lithologies)
<b>Regolith/morphology</b>	Not evaluated	Good (highlights erosional features and iron-rich duricrusts)	Moderate (depends on vegetation cover)	Good (resolution is suited rather for regional scale studies)

**Table I-4** Strengths and weaknesses of available geophysical and remote sensing data in lithological and structural mapping.

One of the major distinguishing parameters in lithostructural mapping is magnetic texture (Jaques et al., 1997; Betts et al., 2003; Aitken and Betts, 2009a; Denith et al., 2009; Stewart et al., 2009). The textural differences helped us to overcome the fact that the magnetic properties of some lithologies are similar (e.g. basalts and andesites, granites, and volcano-sediments). The only drawback of the magnetic data is the application of the reduction to the pole at low latitudes. This limitation was rather successfully overcome with the low-latitude reduction to the pole method (MacLeod et al., 1993; Li, 2008) and inspection of analytical signal grids.

At places with relatively good outcrop conditions, gamma ray spectrometry data were supportive of magnetic data and allowed us to better distinguish between lithologies with similar magnetic properties, such as andesites, which are richer in K than basalts and gabbros. Thick regolith cover in West Africa hampers the use of automatic classification of lithologies based on gamma ray

spectrometry and remote sensing data as applied in Canadian (An et al., 1995; Kettles et al., 2000; Schetselaar et al., 2000) or South American shields (Martelet et al., 2006; Teruiya et al., 2008). These studies rely on the fact that regolith or soil units in the area of interest are in place and derived from the underlying basement rocks. However, in West Africa most of the regolith units experienced some kind of either mechanical or chemical displacement (Grandin, 1976; Tardy, 1997). The regolith was probably formed in situ (Leprun, 1979) and the displacement occurred during subsequent surface processes (Beauvais, 1999). Automatic classification combined with visual evaluation of gamma ray spectrometry data and digital elevation images of the study area was used to differentiate the areas covered by iron-rich duricrusts and lateritic soils from fresh rocks, and will be described in detail in a future paper.

Spatial analysis of the K, eTh, and eU concentrations (figure I-2) highlights the mobility of potassium (Taylor and Eggleton, 2001) and the retention of especially thorium by the Fe-rich weathering products described previously by Wilford et al. (1997) and Martelet et al. (2006). Although geochemical analyses, which are more precise than gamma ray spectrometry, revealed moderate correlation of potassium content between the soil and parent rock at outcrop scale (Blot et al., 1973), this relationship was not fully recognized in the airborne gamma ray data.

The use of Landsat and ASTER data for geological mapping is limited in the study area due to vegetation and regolith cover; nevertheless, we achieved acceptable results in delineation of iron-rich duricrusts and exposed clay-rich regolith units. Similar results were reported in deeply weathered terrains of Australia (Craig, 2001; Wilford, 2002). In well-exposed regions, remote sensing methods were successfully applied to geological mapping of North America (Rowan and Mars, 2003), Australia (Zumsprekel and Prinz, 2000; Rowan et al., 2004), and Africa (Gomez et al., 2005); however, this is not the case of West Africa. In West Africa, Vidal et al. (2009), Tshibubudze et al. (2009), and Hein (2010) have instead applied a widely used method of lineament extraction from SPOT and Landsat images in order to constrain the structural framework. Although this approach may lead to applicable results, their interpretation is often complicated due to abundant vegetation, sand, overall flat morphology, and human activity. Lineaments derived from satellite data may thus be unrelated to geological structures

### **6.3 Implications for geological evolution of the West African Craton**

Establishing lithostructural relationships in the deeply weathered terrains of the West African craton requires links to be found between the meso-scale field observations with regional large-scale architecture. The integration of geophysical data interpretation especially the magnetic data with structural field reconnaissance provides such a connection. A well-constrained overprinting relationship was observed between the D1 penetrative foliation features and the D2 shear zones. At outcrop scale, the D1 penetrative fabrics can be frequently found, while the structural pattern visible in

magnetic data is dominated by the later S2 shear zones. Similarly, the late D3 discrete fabrics were often observed in the field but are barely recognizable in geophysical data. The recognized regional-scale S2 high strain zones reach lengths of hundreds of kilometers suggesting crustal scale movements along these structures. The gamma-spectrometry data combined with digital elevation model aided in defining the granitoid pluton shapes and their geochemical character. This study suggests that for obtaining a more complete vision of the litho-structural framework, an integrated approach is necessary. The revised map contributed significantly to the conception of the geodynamic scenario in chapter II. Our experience from this study suggests that an improved understanding of the geological evolution of West African craton at local but also regional scales depends on an integrated evaluation of all the available datasets, as each one provided distinct constraints to the overall interpretation.

## **7. Conclusions**

In this paper, we present a new synthetic geological map of western Burkina Faso at 1:500 000 scale. The map integrates existing and new field data, airborne geophysical and remote sensing data in order to provide a coherent litho-structural framework for the region. Several important findings were obtained:

1. We have defined four groups of granitoid intrusions and related gabbros based on petrochemistry and magnetic data. The granitoid domains consist of many generations of individual intrusions. This has significant implications for the geotectonic concept.

2. Relic F1 fold hinges were recognized in the magnetic data within the Houndé greenstone belt, while field mapping has confirmed the existence of isoclinal to open folds related to the D1 event across the study area. The D1 structures are generally overprinted by S2 shear zones.

3. Several new S2 shear zones were identified in magnetic data, including the Bossié shear zone transecting the Sidéradougou granitoid domain and abundant small-scale shear zones overprinting granites and other lithologies. These shear zones represent prospective areas for gold exploration.

4. Airborne gamma ray spectrometry data and SRTM digital elevation models allow for lithological discrimination in areas where regolith cover is minimal e.g. erosional ridges formed by volcanic and sedimentary rocks, the regolith stripped part of the Banfora belt, and the Sidéradougou domain.

5. At least three generations of doleritic dykes oriented N40°, N100°, and N120 ° were identified in magnetic data. All three generations crosscut the Paleoproterozoic basement and two of them (N40°, N100°,) intrude sediments of the Taoudeni basin.

## **Acknowledgements**

The project was funded by French government PhD fellowship to V.M., IRD (Institute de recherche pour le développement) post-doctoral research grant to L.B. and aided logistically by the project “West African Exploration Initiative-Phase I” (<http://waxi2.org>). Discussions with P. Debat, D. Chardon, D. Thiéblemont, D. Béziat, C. McCuaig, E. Kaboré, F.M. Ouedraogo, S. Zonou, and J. David at various stages of the project significantly contributed to our understanding of West African geology. We are indebted to the mining companies SEMAFO, Volta Resources, Wega Mining, Sanu Resources, and Orezone for providing us high-resolution geophysical data, borehole cores, and outcrop maps. We acknowledge in particular M. Crevier, D. Bondé, D. Boisvert, L. Ouedraogo, P. Marquis, A. Zongo, O. Derra, C. Diallo, T. Amoah, and A. Naré for providing us support when conducting fieldwork on the permits of their companies. Finally, we would like to thank J.L. Bouchez and J. Ježek for insightful reviews of the early drafts. We acknowledge the careful reviews by E. de Kemp and an anonymous reviewer, which significantly improved the manuscript.

---

## **CHAPTER II**

### **JUVENILE PALEOPROTEROZOIC CRUST EVOLUTION DURING THE EBURNEAN OROGENY (~2.2–2.0 GA), BURKINA FASO, WEST AFRICA**

---



---

## Résumé du chapitre II

# Formation de la croûte Paléoproterozoïque juvénile lors de l'orogénèse éburnéenne (~2.2–2.0 Ga), Burkina Faso, Afrique de l'Ouest

## 1. Introduction

Les mécanismes de croissance de la croûte juvénile dans l'Archéen et Paléoproterozoïque demeurent un sujet de vives discussions depuis des dizaines d'années (Windley, 1992 ; de Wit et Ashwal, 1997 ; Condie, 1998 ; Condie et Pease, 2008). Les boucliers anciens sont typiquement composés d'assemblages de ceintures de roches vertes et de granitoïdes, affectés par des zones de cisaillement d'échelle crustale. Nombreux chercheurs proposent que la tectonique des plaques opérait déjà au Mésoarchéen (Cawood et al., 2006; Condie, 2008; Shirey et al., 2008; Foley, 2008) alors que d'autres proposent qu'une tectonique dite « verticale », gouvernée par les différences de densité entre les roches vertes et les granitoïdes, opérait jusqu'au Paléoproterozoïque (Pons et al., 1995; Vidal et al., 1996; Vidal et al., 2009; Lompo, 2010).

Afin de répondre à ces questions et de mieux comprendre les mécanismes de la formation du craton ouest africain, nous avons étudié un domaine Paléoproterozoïque de l'Ouest du Burkina Faso. Agé de 2200 à 2000 Ma, le craton ouest africain représente un excellent endroit pour tester si la transition entre la tectonique « ancienne » et la tectonique « moderne » a eu lieu progressivement ou s'il s'agissait d'une rupture abrupte, et à quel moment elle est éventuellement arrivée.

L'étude a été ciblée sur trois ceintures de roches vertes (Boromo, Houndé et Banfora) et sur les granitoïdes adjacents. Le but de cette étude est de proposer un scénario géodynamique de la formation de ce domaine composé de roches vertes et de granitoïdes en combinant les données de terrain (structurales, lithologiques, stratigraphiques, géochimiques, métamorphiques) et les données géophysiques (magnétiques, radiométriques). La méthodologie, ainsi que les nouvelles structures découvertes ici, sont présentées dans le chapitre I. Pour mieux contraindre les structures profondes, nous avons réalisé trois modèles 2½ D en utilisant des données gravimétriques.

## 2. Principales lithologies et structures

Les trois ceintures des roches vertes (Boromo, Houndé et Banfora) contiennent une série volcanique mafique tholéïitique à la base qui est superposée par des séries volcaniques intermédiaires à acides d'une composition calco-alkaline. Des bassins de sédiments à grains fins tardi-Birimiens apparaissent dans les trois ceintures. Une unité de sédiments de type « Tarkwaïen » se trouve à

l'intérieur de la ceinture de Houndé et parallèle à celle-ci, délimitée par des zones de cisaillement de part et d'autre.

Quatre groupes majeurs, correspondant à quatre épisodes magmatiques, ont été distingués dans les granitoïdes : 1) les intrusions calco-alcalines de tonalites-trondhjémites-granodiorites, à faible teneur en potassium et à formes irrégulières. Ces roches montrent souvent un litage ou une foliation magmatique bien développée ; 2) les intrusions de granites calco-alcalins potassiques. Ils sont caractérisés par une forme circulaire ou elliptique et transectent les lithologies plus anciennes ; et 3) les granites tardifs potassiques, ou de rares syénites, de forme sigmoïdale à elliptique bien visibles dans les données magnétiques ; enfin 4) de petites intrusions de gabbros d'âge inconnu.

Trois phases de déformation ont été distinguées dans la zone d'étude. La première phase D1 est caractérisée par une fabrique métamorphique pénétrative et des plis serrés à ouverts dans les ceintures des roches vertes. Dans les granitoïdes, une foliation magmatique pénétrative subverticale a été fréquemment observée. Une linéation fortement plongeante est parfois associée avec la foliation S1. L'orientation N-S ou NNE-SSE de ces structures S1 est cohérente dans les ceintures des roches vertes et dans les granitoïdes. Les sédiments de type « Tarkwaien » et une partie des sédiments Birimiens se sont déposés à la fin de D1, ce qui est supporté par l'obliquité angulaire de l'unité des sédiments « Tarkwaiens » par rapport aux niveaux plissés des roches volcaniques de la ceinture de Houndé.

Les structures de la deuxième phase de déformation D2 sont caractérisées par des zones de cisaillements suverticaux discrets développés à plus basse température par rapport aux foliations S1. Localement, des plis asymétriques liés à ces cisaillements sont développés. L'orientation de ces zones de cisaillement dans les ceintures des roches vertes ainsi que dans les granitoïdes varie entre NNO-SSE (senestre) à ENE-OSO (dextre). Les linéations associées aux structures S2 plongent faiblement.

La dernière phase de déformation D3 est tardive, peut-être même Panafricaine, et affecte notamment les lithologies de forte anisotropie à travers toute la zone d'étude. Les structures typiques pour cette phase sont : le clivage de crénulation fortement penté, orienté E-O en moyenne, et les failles inverses de faible pendage vers le N ou le S.

### **3. Caractère géochimique des roches volcaniques**

Les analyses géochimiques de roche totale ont été acquises sur les volcanites de ceintures de Houndé et Boromo afin de pouvoir déterminer l'origine de ces roches. Deux familles principales ont été trouvées dans les deux ceintures : les basaltes tholéiitiques et les basaltes et andésites calco-alcalins, avec quelques andésites de type transitionnel. Les basaltes à grands phénocristaux de plagioclases qui sont observés à l'Est de la ceinture de Houndé et à l'Ouest de la ceinture de Boromo, ont une composition tholéiitique, identique dans les deux ceintures. Ces basaltes sont donc utilisés comme un niveau marqueur stratigraphique.

## 4. Résultats principaux de l'étude et discussion du modèle géodynamique

La composition chimique des roches volcaniques, qui commence par une série des basaltes tholéïtiques, et qui est suivie par des séries volumineuses intermédiaires calco-alcalines, est compatible avec un environnement des arcs volcaniques (2200–1700 Ma). Les premières intrusions des tonalites-trondhémities-granodiorites (2190–2170 Ma) ont leur source dans les plaques océaniques subductées (Martin, 1994 ; Martin et al., 2005) ou la croûte inférieure mafique. Les relations structurales, stratigraphiques, géochimiques et notamment le niveau de basaltes à mégacristaux de plagioclase permettent de corréliser le flanc occidental de la ceinture de Houndé et le flanc oriental de la ceinture de Boromo, suggérant que ces deux ceintures forment des synformes reliées par une antiforme maintenant disparue. Le flambage puis le plissement des ceintures a commencé lors de la première phase de déformation D1 (~2160–2120 Ma), accompagnés d'abondantes intrusions syntectoniques de granitoïdes marquées par une foliation magmatique subverticale portant une linéation d'étirement fortement plongeante. D1 correspond à un raccourcissement E-O avec une déformation prédominante de cisaillement pur. Les séries volcaniques et sédimentaires plissées de la ceinture de Houndé sont recoupées par la faille régionale de Boni, qui contrôle le dépôt des sédiments de type « Tarkwaïen » et une partie des sédiments Birimiens (2200–2100 Ma). Les observations de terrain ne fournissent pas suffisamment d'arguments pour décider si la sédimentation a eu lieu lors d'une extension ou s'il s'agit des bassins internes synorogéniques. La deuxième phase de déformation D2 est caractérisée par des zones de cisaillement d'échelle locale à régionale qui affectent de manière hétérogène les structures préexistantes. Le caractère de cette déformation est transpressif, avec une forte composante de cisaillement simple.

Les granitoïdes ont joué un rôle important pendant toutes les étapes de l'orogénèse éburnéenne, en particulier par l'augmentation du volume de croûte créée durant l'orogénèse précoce, et au stade mature l'accommodation d'une partie du raccourcissement latéral. A l'échelle régionale, la géométrie du système a été contrôlée par le raccourcissement coaxial des unités visqueuses des basaltes, gabbros et andésites composant les ceintures des roches vertes qui ont progressivement formé un pli d'une longueur de 400 km N au S. Raccourcissement et plissement à grand échelle a été accompagnés d'un ajout constant de magmas granitiques.

La dernière phase de déformation D3 est tardi-éburnéenne ou peut-être même panafricaine. Elle correspond au raccourcissement N-S responsable de la crénulation subverticale orientée E-O et des failles inverses à faible pendage vers le N et le S.

## 5. Conclusion

Notre étude de trois ceintures de roches vertes et des granitoïdes associés a mis en évidence trois phases principales de déformation compressive qui ont contribué à la formation de la croûte continentale juvénile lors de l'orogénèse éburnéenne. Les arguments pétrologiques, structuraux,

géochimiques et métamorphiques suggèrent l'existence d'un ou plusieurs arcs volcaniques qui sont rentrés en collision. La tectonique des plaques opérait déjà à cette époque, même si les mécanismes de la croissance crustale ont été modifiés par rapport au présent. Le mécanisme de croissance crustale par plissement des unités mafiques rigides à grande échelle nous semble indéniable, ont en soulignant le rôle important des granitoïdes lors de la croissance crustale.

---

# JUVENILE PALEOPROTEROZOIC CRUST EVOLUTION DURING THE EBURNEAN OROGENY (~2.2–2.0 GA), BURKINA FASO, WEST AFRICA

*Lenka Baratoux*<sup>a\*</sup>, *Václav Metelka*<sup>a,b,c</sup>, *Séta Naba*<sup>d</sup>, *Mark W. Jessell*<sup>a</sup>, *Michel Grégoire*<sup>a</sup>, *Jérôme Ganne*<sup>a</sup>

<sup>a</sup> IRD, UR 234, GET, Université Toulouse III, 14 Avenue Edouard Belin, 31400 Toulouse, France

<sup>b</sup> Institute of Geology and Paleontology, Charles University, Albertov 6, Prague 2, 12843, Czech Republic

<sup>c</sup> Czech Geological Survey, Klárov 3, 11821, Prague 1, Czech Republic

<sup>d</sup> Département de Géologie, Université de Ouagadougou, Burkina Faso

## Abstract

We have investigated three greenstone belts (Boromo, Houndé, and Banfora) and associated granitoid terrains, which form part of the Eburnean orogen, situated in western Burkina Faso. The belts expose tholeiitic basalts (basal unit) followed by calc-alkaline intermediate predominantly effusive volcanic and sedimentary suites geochemically reminiscent of present-day volcanic island arc environments. The basal mafic unit probably corresponds to a juvenile arc crust or oceanic plateau. It contains unusual megacrystic tholeiitic basalts, allowing us to correlate the western margin of the Boromo belt with the eastern margin of the Houndé belt. These two N-S trending belt-parallel tholeiitic units are interpreted as limbs of a crustal scale anticline, intruded and partially obliterated by tonalite-trondhjemite-granodiorite (TTG) and granite intrusions.

Three deformation events (D1-D3) can be distinguished in western Burkina Faso. The first deformation phase (D1) operated under an E-W to WNW-oriented compression. Regional greenschist to lower amphibolite facies metamorphism and intense folding characterize early-Eburnean deformation phases, during which time the crust was thickened by lateral shortening of volcanic island arcs and concomitant magma input. The crustal-scale antiform between the Boromo and Houndé belts is attributed to the D1 event. Shallow water detrital Tarkwaian-type sediments were deposited during the late D1 event within the Houndé belt, in a belt-parallel basin extending for 400 km. The subsequent D2 phase overprints the structural grain of the study area, and is best visible in airborne magnetic data. It is characterized by N to NE-trending transcurrent shear zones, which are considered preferred host structures for gold mineralization. We suggest that the newly formed and thickened crust reached the maximum thickness supportable by a weak and hot mantle during the D1 phase, and the pure shear dominated compressional regime switched to simple shear dominated transpression

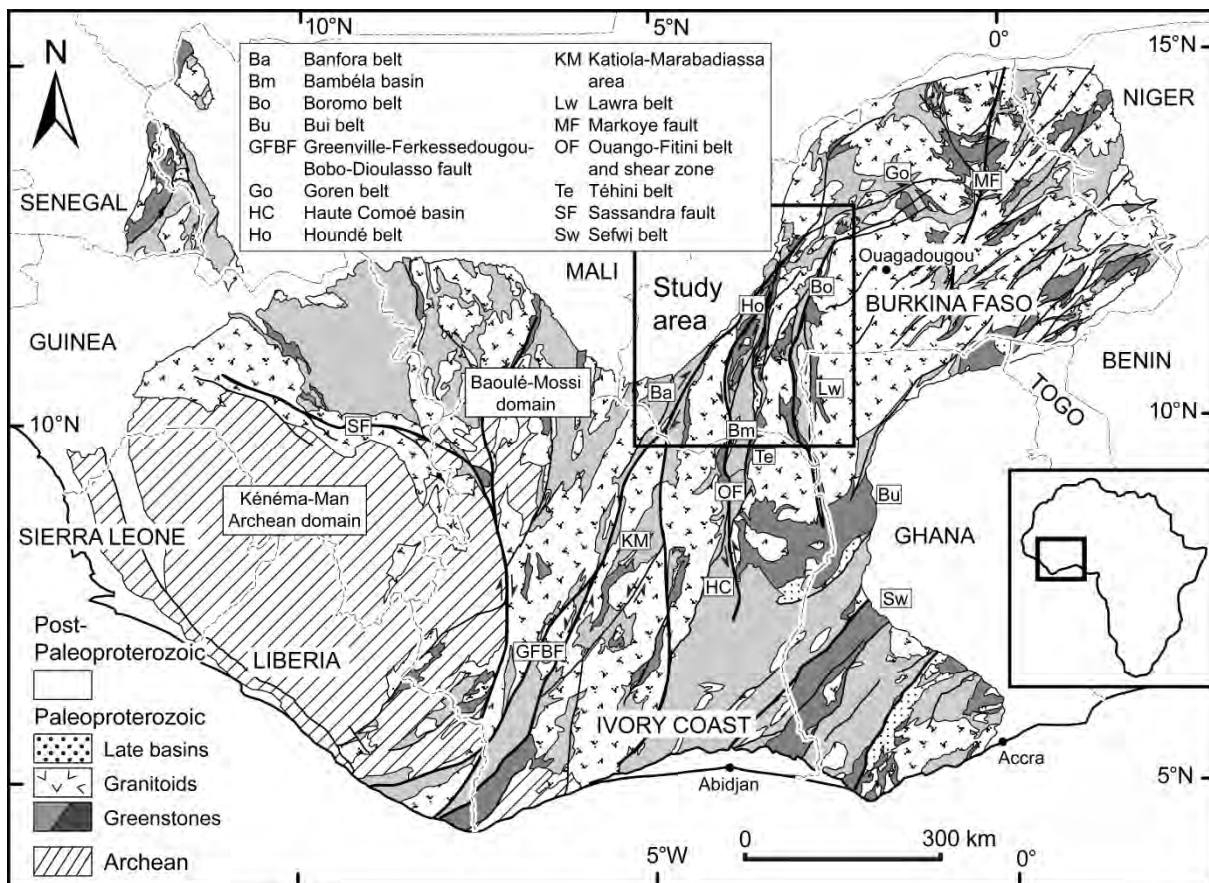
during the subsequent D2 phase. Granitoid diapirism played an important role at all stages of the Eburnean crustal growth processes in particular through volume addition to the newly formed orogen and through accommodating part of the lateral shortening. Pluton emplacement contributed to the greenstone belt structuration at local scales; however, the regional scale system geometry was controlled by coaxial shortening of the viscous volcanic units (basalts, gabbros, and andesites) of the greenstone belts, supported by coeval magma input.

The last D3 deformation, which is either late-Eburnean or perhaps even Pan-African in age, is characterized by shallow N or S dipping minor thrust faults or an E-W trending steeply dipping spaced crenulation cleavage and kink folds, occurring mainly in highly anisotropic lithologies across the study region.

**Keywords:** West Africa; Burkina Faso; Paleoproterozoic; Structural analysis; Magmatic and tectonic accretion; Geodynamic model

## **1. Introduction**

The growth mechanisms of Archean and Paleoproterozoic juvenile continental crust have been a topic of scientific debate for decades (Windley, 1992; de Wit and Ashwal, 1997; Condie, 1998; Condie and Pease, 2008). Many authors propose that plate tectonics existed back to the Mesoarchean (Cawood et al., 2006; Condie, 2008; Shirey et al., 2008; Foley, 2008), nevertheless, the plate movements may have been much faster and slab dips shallower when compared to the present day subduction zones (Choukroune et al., 1997; Goscombe et al., 2009). The existence of Himalayan-type collisional orogens, dominated by nappe stacking along first-order thrust faults, is strongly challenged for Precambrian terrains, mostly due to the absence of a thick and strong continental lithosphere, which would be able to support the overthickened continental crust especially during the periods of massive juvenile crust accretion (Windley, 1995; Chardon et al., 2009; Gapais et al., 2009). Several authors point out that even if lateral accretion of volcanic arcs operated, other processes may have occurred simultaneously in the hot and weak juvenile crust (Choukroune et al., 1995; Chardon et al., 1998; Collins et al., 1998; Rey et al., 2003; Cagnard et al., 2006a; Chardon et al., 2002). These processes include gravitational sinking of dense mafic domains or homogeneous thickening of the crust by combined downward movements of supracrustals and three-dimensional mass redistribution in the viscous lower crust. Archean orogens are characterized by strain patterns which often post-date the principal accretion period (Chardon et al., 2009), with high heat flow related either to plate boundaries or to mantle plume activity, which potentially contributed to crustal growth through the accumulation of voluminous volcanic and plutonic complexes (Sylvester et al., 1997; Arndt et al., 1997; Benn and Moyen, 2008). Lithological assemblages of tonalite-trondhjemites-granodiorites



**Figure II-1** Simplified geological map of the Leo-Man Craton (modified after the BRGM SIGAfrique map, Milési et al., 2004), with the study area indicated. Paleoproterozoic greenstones are divided into: light grey – intermediate to acid volcanoclastics and volcanosediments, dark grey – mafic to intermediate lavas and volcanic products.

(TTG) with intercalated greenstone belts are typical for all of the Precambrian shields including the West African Craton (figure II-1).

In the southern part of the West African Craton, called the Leo-Man shield (Bessoles, 1977; Rocci et al., 1991), Paleoproterozoic rocks are tectonically juxtaposed to the Archean nucleus, separated from it by the Sassandara fault (Bessoles, 1977; Feybesse et al., 1989; Feybesse and Milési, 1994; Kouamelan et al., 1997; Caby et al., 2000; Egal et al., 2002) (figure II-1). In West Africa, two distinct models have been proposed for the tectonic evolution of the granite-greenstone terrains. One model assigns the major crustal thickening phase to nappe stacking along orogen parallel thrust faults (e.g. Milési et al., 1989; Ledru et al., 1991; Allibone et al., 2002; Feybesse et al., 2006). The other model rejects the plate tectonic paradigm and emphasizes the “dome and basin” geometry. This geometry would be the result of vertical movements due to gravitational instabilities (Pons et al., 1995; Vidal et al., 1996; Vidal et al., 2009; Lompo, 2010), operating under an overall lateral shortening regime. Abouchami et al. (1990), Boher et al. (1992), and Taylor et al. (1992) insist on the juvenile character of the greenstone-granitoid terrains in West Africa. The absence of Archean basement under most of the Paleoproterozoic crust has been confirmed by more recent studies (Dia et al., 1997; Doumbia et al., 1998; Hirdes and Davis, 2002; Gasquet et al., 2003;) with some exceptions

along the contact zone with the Archean Kénéma-Man domain (Boher et al., 1992; Kouamelan et al., 1997; Thiéblemont et al., 2004). On the other hand, Begg et al. (2009) conclude that reworked Archean crust and subcontinental lithospheric mantle are present beneath an extensive part of West African craton, based on tomographic data.

The integrated interpretation of airborne geophysical and satellite remote sensing data, field observations, along with a 2½ D gravity modeling is an efficient method for delimiting lithological units and structures in poorly exposed granite-greenstone areas (Hackney, 2004). As a part of this study, we have revised the existing 1:1 000 000 and 1:200 000 geological maps (Marcelin and Serre, 1971; Marcelin, 1971; Castaing et al., 2003; Chèvremont et al., 2003; Koté et al., 2003; Le Métour et al., 2003). The revised litho-structural map at a scale of 1:500 000 along with detailed description of the assumptions and techniques we used is presented in chapter I. Field observations were combined with airborne magnetic and radiometric data with resolutions of 125 m and 250 m obtained during the System for Mineral Products (SYSMIN) project of Bureau de Recherche Géologique et Minière (BRGM) and Bureau de Mines et Géologie du Burkina Faso (BUMIGEB), 1998–2003. Derivatives of the magnetic data (first vertical, horizontal, and tilt derivatives, analytical signal) served to delineate large-scale structures such as shear zones and large-scale folds and the younger doleritic dykes.

In this paper, we present a tectonic model for western Burkina Faso encompassing parts of three N-S trending greenstone belts and four surrounding granitoid domains of Paleoproterozoic age. This model addresses the issues of the source and nature of the volcanic rocks of the greenstone belts, the growth mechanisms of continental crust from dominantly oceanic crust and volcanic arcs, and their transformation into a classical-type greenstone-granitoid terrain pattern. We also discuss the significance of their partitioning into the current greenstone belts, taking into consideration the pre-greenstone belt geodynamic setting of the volcanic island arcs. The tectonic model is based on the integration of multiple datasets. In this context, our method provides a good constraint on the 3D geometry of the system as well as on the relative chronology of some of the large-scale structures.

## **2. Geological Setting**

### **2.1. Regional geological framework**

The Birimian volcano-sedimentary belts with associated granitoids belonging to the Baoulé-Mossi domain of the West African Craton (figure II-1) formed between 2250 and 1980 Ma (Feybesse et al., 2006). The dominant structural grain was formed during the Eburnean orogeny (Bonhomme, 1962). The greenstone belts consist of the so-called Birimian volcanics, and of sedimentary basins, sometimes considered as separate units. The volcanics were first described in the Birim valley in Ghana (Kitson, 1918), and are characterized by tholeiitic and/or calc-alkaline compositions. In several studies, the volcanic formations are considered younger than the sedimentary sequences (e.g. Junner,



1935, 1940; Ledru et al., 1991; Milési et al., 1989, 1991). Leube et al. (1990) suggested that the volcanic sequences and sedimentary basins are contemporaneous lateral facies equivalents, while others place the basalts and andesites at the base, overlain by flysch-type sedimentary sequences (Tagini, 1971, 1972; Bessoles, 1977; Vidal and Alric, 1994; Pouclet et al., 1996). Recent radiometric dates on zircons from rhyolites have shown that the volcanic units were emplaced at ~2190–2160 Ma, whereas some detrital zircons found in Birimian sediments are as young as 2130 Ma, supporting the idea that at least some of the sedimentary basins postdate the principal volcanic activity (Davis et al., 1994; Lüdtke et al., 1999, 1998; Hirdes et al., 1996; Hirdes and Davis, 1998; Oberthuer et al., 1998; Le Métour et al., 2003).

Numerous studies of Precambrian greenstone belts have concluded that the bimodal tholeiitic to calc-alkaline volcanism represents an immature volcanic arc setting, where slight compositional differences exist with respect to the present-day island arcs (Zonou, 1987; Dia, 1988; Moyon et al., 2003, Sylvester and Attoh, 1992; Martin, 1994; Ama Salah et al., 1996; Lüdtke et al., 1998; Béziat et al., 2000; Schwartz and Melcher, 2003; Soumaila et al., 2004; Condie, 2005; Martin et al., 2005). Tholeiitic basalts are considered to pre-date calc-alkaline series in the majority of these works. Other authors invoke oceanic plateaus related to mantle plumes to explain the massive accumulations of basalts within a short period of time (Abouchami et al., 1990; Boher et al., 1992; Pouclet et al., 1996; Arndt et al., 1997; Lompo, 2009). The elongate character of greenstone belts could instead be the result of intra-continental rifting according to Leube et al. (1990), Ratomaharo et al. (1988), Alric (1990), and Pouclet et al. (1996).

The Tarkwaian sediments, first defined in Ghana (Whitelaw, 1929), are regarded as the youngest unit in the greenstone sequence by most authors (Leube et al., 1990; Davis et al., 1994; Bossière et al., 1996; Castaing et al., 2003; Feybesse et al., 2006). They have been deposited after ~2120 Ma, as suggested by ages obtained on detrital zircons. Conglomerates and fine-grained detrital sediments observed within calc-alkaline sequences were attributed to the Birimian volcano-sedimentary series in northeastern Burkina Faso (Roddaz et al., 2007; Tshibubudze et al., 2009), Ivory Coast (Vidal et al., 1996; Doumbia et al., 1998), and Senegal (Bassot, 1987). Despite the conspicuous lithological similarity of the Tarkwaian-like sedimentary sequences all over the craton, their stratigraphic continuity cannot be proved and they might have been deposited at different times in separate basins. In this work, we will retain the term Tarkwaian-type metasediments in accord with the afore-mentioned published works, but we do not establish any spatial or temporal relationship with the Tarkwa stratotype.

Birimian sedimentary basins occur abundantly across the whole Baoulé-Mossi domain. Vidal and Alric (1994) suggest that they unconformably overlay the older basement composed of predominantly tholeiitic volcanics and first generation of granitoids, while Hirdes et al. (1996) and Lüdtke et al. (1998) claim that they are lateral equivalents and contemporary products of the volcanic islands. Pouclet et al. (1996) and Pouclet et al. (2006) suggest that the intracontinental basins formed

quite late in the tectonic history on the consolidated TTG-greenstone basement and were contemporaneous with calc-alkaline magma production.

Voluminous plutonic activity contributed significantly to the growth of continental crust during the Eburnean orogeny. In the West African Craton, plutonic activity spans over the whole period of the orogeny, and is characterized by granitoid intrusions similar to the typical late-Archean suites from the Dharwar, Abitibi, and Yilgarn cratons (Martin, 1994; Champion et al., 2001; Moyen et al., 2003, Martin et al., 2005). Although petrographic variability is large and classification of granitoid suites in the Baoulé-Mossi domain is complex, many authors describe long-lasting calc-alkaline Na-rich plutonism with typical tonalite-trondhjemite-granodiorite (TTG) members, followed by more potassic, often biotite bearing granites, which may evolve to alkaline syenitic magmatism (e.g. Arnould, 1961; Leube et al., 1990; Davis et al., 1994; Hirdes et al., 1996; Doumbia et al., 1998; Lüdtke et al., 1999, 1998; Egal et al., 2002; Gasquet et al., 2003; Naba et al., 2004; Vegas et al., 2008; Lompo, 2009).

A few TTG intrusions occurred contemporaneously with the Birimian mafic to intermediate volcanism at 2195–2172 Ma (U-Pb and Pb-Pb zircon ages, Hirdes et al., 1992; Oberthuer et al., 1998; Siegfried et al., 2009) but the main plutonic activity took place later. Several protracted pulses of syn-tectonic to late-kinematic granitoid intrusions range in age from ~2153 Ma to 2068 Ma (U-Pb and Pb-Pb zircon ages; Liégeois et al., 1991; Hirdes et al., 1996; Doumbia et al., 1998; Oberthuer et al., 1998; Egal et al., 2002; Hirdes and Davis, 2002; Castaing et al., 2003; Gasquet et al., 2003).

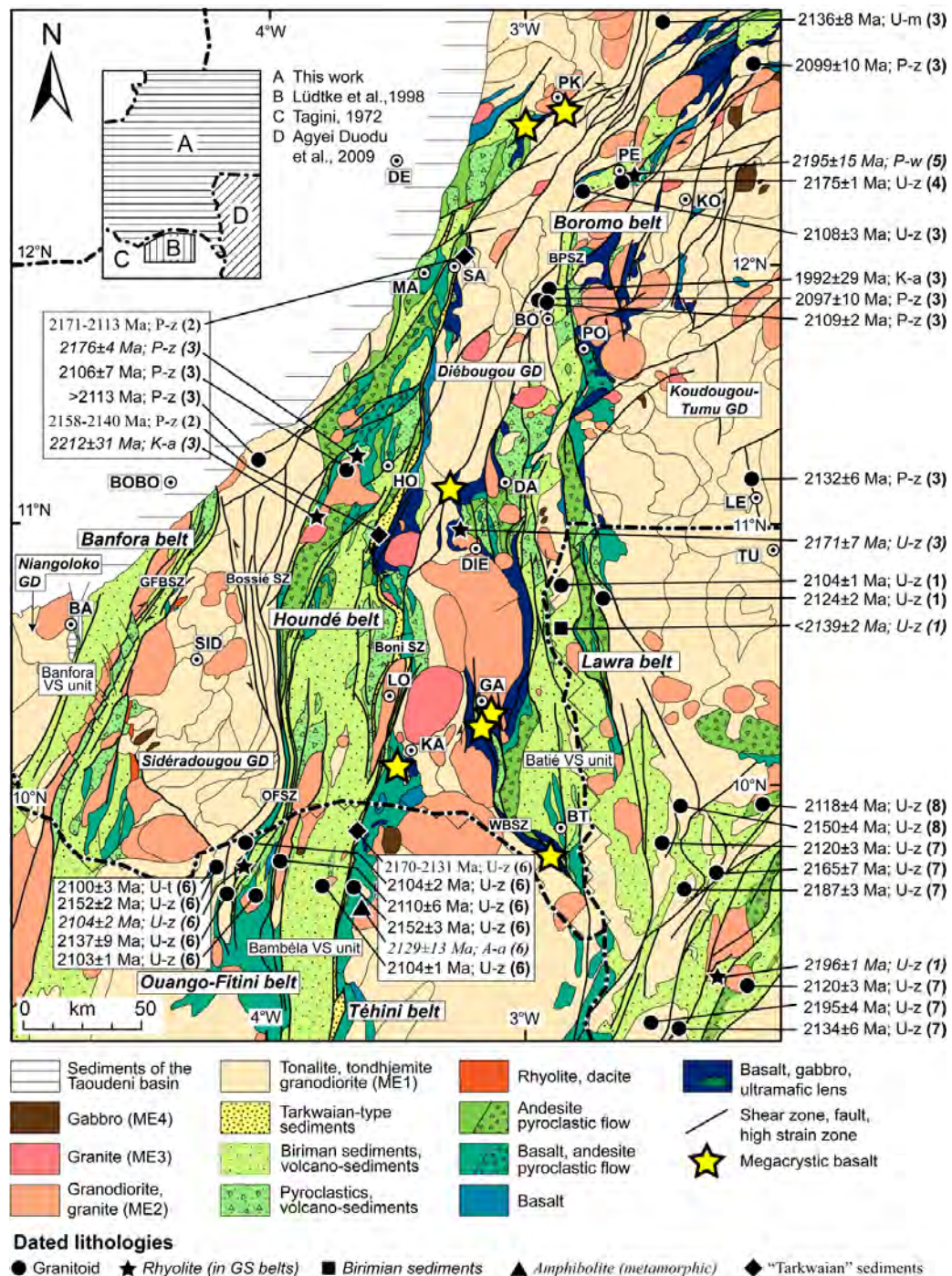
Most of the volcanic suites are metamorphosed at lower (Křibek et al., 2008) to upper greenschist facies (e.g. John et al., 1999; Feybesse et al., 2006). Amphibolite facies conditions are reported only from contact aureoles of granitoid intrusions (Debat et al., 2003; Soumaila and Garba, 2006) or are localized along some of the shear zones (e.g. Chèvremont et al., 2003). Regional amphibolite facies metamorphism has been reported from Ghana (John et al., 1999; Klemd et al., 2002; Galipp et al., 2003). A Sm-Nd isochron on whole rock including metamorphic garnets indicates metamorphism of the mafic volcanic rocks at  $2153 \pm 13$  Ma (Boher et al., 1992).

In the study area, typical metamorphic mineral assemblages consist of variable proportions of chlorite, actinolite/tremolite, albite, epidote, and white mica. The metasediments of the Batié volcano-sedimentary unit are locally unmetamorphosed. Thin sections observations show no lateral field metamorphic gradient across the Houndé and Boromo greenstone belts. The only places where metamorphic conditions reach amphibolite facies ( $665 \pm 35^\circ\text{C}$ , Hbl-Pl thermometer by Holland and Blundy, 1994) are within pluton aureoles such as the Ponkélé shear zone (figure II-2).

The polyphase character of the Eburnean orogeny has been noted by many workers (e.g. Lemoine et al., 1985; Tempier, 1986; Milési et al., 1989; Feybesse et al., 1990; Lemoine et al., 1990; Ledru et al., 1991; Milési et al., 1992; Hirdes et al., 1996; Vidal et al., 1996; Allibone et al., 2002; Feybesse et al., 2006; Pouclet et al., 2006; Vidal et al., 2009; Hein, 2010). In order to explain NW to NNW-trending steeply dipping structures in the north of Burkina Faso, Hein (2010) and Tshibubudze

et al. (2009) introduced a short-lived pre-Eburnean deformation event denominated Tangaean Event. Early Eoeburnean deformation event operating before 2150 Ma was also reported in northern Ghana (de Kock et al., 2011). The first Eburnean phase, which took place between ca. 2200–2130 Ma and 2150–2110 Ma (U-Pb and Pb-Pb zircon ages on rhyolites and granitoids) is called Eburnean I (Allibone et al., 2002), D1 (Milési et al., 1989; Ledru et al., 1991; Feybesse et al., 2006) or Stage I (Vidal et al., 2009). It corresponds to the major phase of either crustal thickening by nappe stacking (Allibone et al., 2002; Feybesse et al., 2006) or “dome and basin” diapiric uprising and greenstone belt sinking (Delor et al., 1995; Vidal et al., 1996; Lompo, 2009; Vidal et al., 2009).

The second phase, Eburnean II, D2-3 or Stage II, took place between ca. 2130–2110 Ma and 2090–1980 Ma (U-Pb and Pb-Pb zircon ages on rhyolites and granitoids; Pouclet et al., 1996; Allibone et al., 2002; Feybesse et al., 2006; Pouclet et al., 2006; Vidal et al., 2009). It is characterized by regional scale N to NE-trending transcurrent faults. These faults, affecting all lithologies, are often localized at contacts between granites and greenstones. Gold mineralization is concentrated along these late-orogenic shear zones (e.g. Milési et al., 1989; Milési et al., 1992; Blenkinsop et al., 1994; Bourges et al., 1998; Allibone et al., 2002; Feybesse et al., 2006; Béziat et al., 2008). Some of the deposits are thought to be remobilized paleoplacers, in particular those situated in Tarkwaian sediments in Ghana (Klemd and Hirdes, 1997).



**Figure II-2** Revised geological map of the western Burkina Faso (chapter I). The names of the greenstone belts, granitoid domains (GD) and major Birimian (volcano-) sedimentary units referred to in the text are indicated. Radiometric ages are taken from the following sources: (1) Agyei Duodu et al., 2010; (2) Bossière et al., 1996; (3) Castaing et al., 2003; (4) Davis in Schwartz and Melcher, 2003; (5) Lompo, 1991; (6) Lüdtke et al., 1998; some of these ages also published in Hirdes et al., 1996; (7) Siegfried et al., 2009; (8) Thomas et al., 2009. Dating methods U-Pb (U), Pb-Pb (P), K-Ar (K), and Ar-Ar (A) were applied on zircon (z), monazite (m), t – titanite (t), and amphibole (a). The following sources were used for compilation of the geological map: (A) this work; (B) Lüdtke et al., 1998; (C) Tagini, 1972; (D) Agyei Duodu et al., 2010. BA – Banfora, BO – Boromo, BOBO – Bobo-Dioulasso, BT – Batié, DA – Dano, DE – Dédougou, DIE – Diébougou, GA – Gaoua, HO – Houndé, MA – Mana, KA – Kampti, KO – Koudougou, LE – Léo, LO – Loropéni, PE – Perkoa, PK – Ponkélé, PO – Poura, SA – Safané, SID – Sidéradougou, TU – Tumu. GFBSZ – Greenville-Ferkessedougou-Bobo-Dioulasso shear zone (SZ), OFSZ – Ouango-Fitini SZ, BPSZ – Boromo-Poura shear corridor, WBSZ – West Batié SZ.

Post-Eburnean structures such as shallow N or S dipping thrust faults or E-W striking steep crenulation cleavage have been reported from northern Burkina Faso (Nikiéma et al., 1993; Debat et al., 2003; Hein, 2010). The Birimian basement is unconformably overlain by Neoproterozoic sediments of the Taoudeni basin (Deynoux, 1983; Bertrand-Sarfati et al., 1990) and intruded by at least six generations of post-Eburnean doleritic dykes cratonwide (Jessell et al., 2010).

## **2.2. Distribution of the greenstone belts and granitoid domains**

The study area consists of three N-S trending greenstone belts (Boromo, Houndé, and Banfora) separated by granitoid domains (figure II-2). The stratigraphic sequences for the Houndé and Boromo belts (figure II-3a) were established using field lithological and structural data, interpretations of regional geophysical data, geochemistry of the volcanic rocks and three gravity models constructed from sections perpendicular to two of the belts. We are less confident about the proposed stratigraphic chart for the Banfora belt as our field observations are scarce. The interpretations are mostly based on the existing outcrop data, the 1:200 000 geological map (Marcelin and Serre, 1971) and on geophysical data.

Geophysical data and field mapping revealed that the granitoid domains are composed of a significant number of 5 to 50 km (maximum dimension) granitoid bodies of variable composition, shape, and age. For the sake of clarity, we will use the following names for the granitoid domains in this work: the Koudougou-Tumu domain for the granitoids east of the Boromo belt in Burkina Faso (and its continuation in northern Ghana, the Lawra belt), the Diébougou domain for the band between the Boromo and Houndé belts, the Sidéradougou domain for the granitoid plutons situated between the Houndé and Banfora belts, and the Niangoloko domain for the granitoids to the west of the Banfora belt (figure II-2).

Unlike other regions of the Leo-Man Craton, where the sedimentary basins can be clearly delineated and separated from the volcanic belts (e.g. the Bambéla-Comoé basins in Ivory Coast and Ghana, the Siguri-Kankan basin in Guinea and Mali, the Kumasi basin in Ghana), the sedimentary basins in western Burkina Faso show complex structural relationship and frequent stratigraphic and/or tectonic intercalations with the adjacent volcanic and volcano-sedimentary units. This hinders unequivocal spatial delimitation of the basin and its distinction from the older Birimian volcanoclastics and sediments associated with the volcanism. The sedimentary units will be therefore described together with the three respective greenstone belts. The stratigraphic and tectonic position of the sediments suggests that they postdate the volcanic belts, which is consistent with the position of the Birimian sedimentary basins in the north of Ivory Coast and north of Ghana (Vidal and Alric, 1994; Vidal et al., 2009; Agyei Duodu et al., 2010).

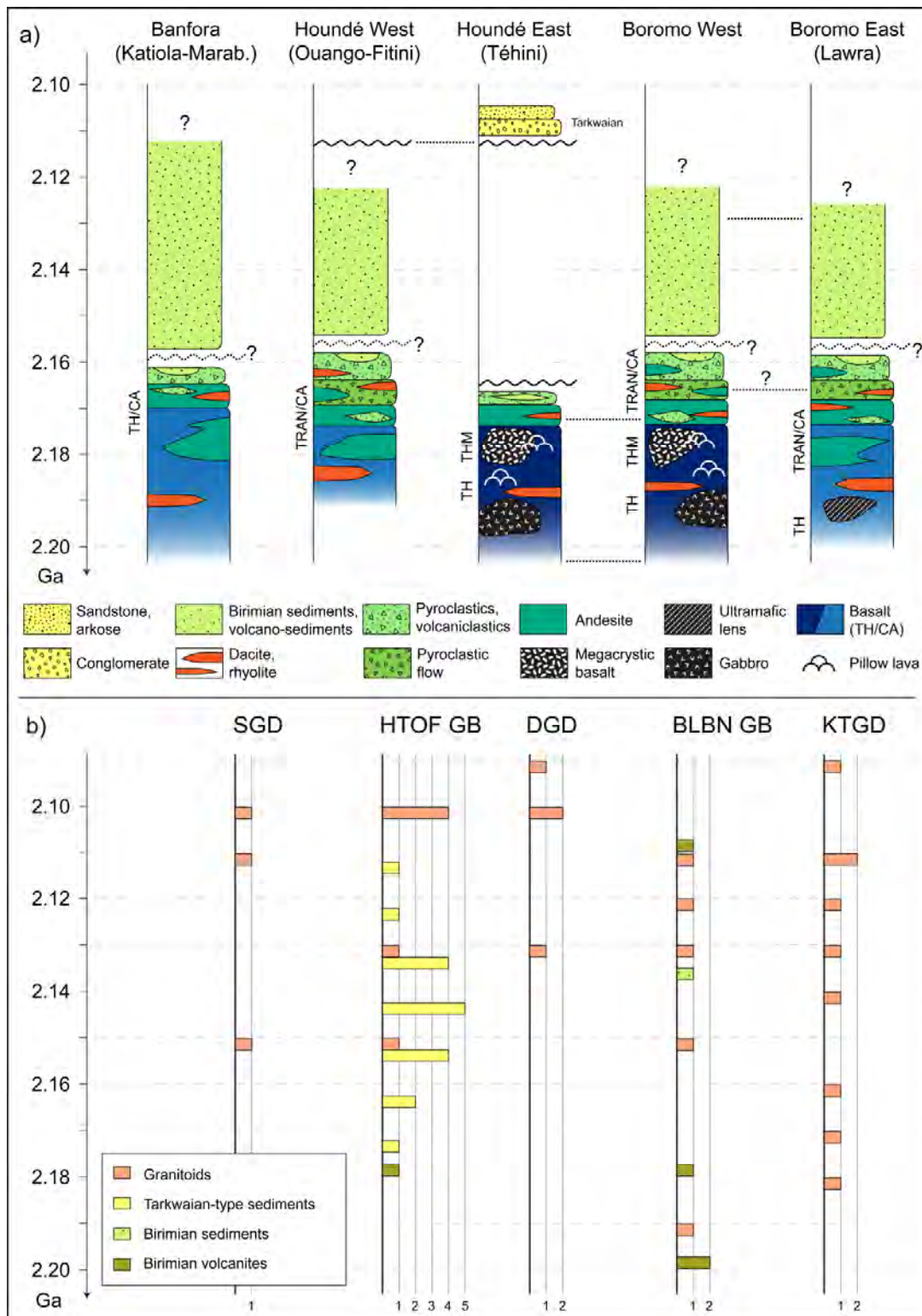
### 3. Main lithologies and stratigraphy

#### 3.1. The Boromo belt

The eastern and western margins of the Boromo belt (figure II-2) consist of a thick sequence of basalts, in places pillowed, intercalated with gabbros, and orthoamphibolites/pyroxenites. The eastern part of the belt consists of intermediate volcanics and several ultramafic bodies. Basic and intermediate volcanism in the east of the belt varies from tholeiitic to calc-alkaline in composition. No radiometric ages exist from basalts or andesites; however, field relationships suggest at some localities that tholeiitic basalts are older than the calc-alkaline series (Béziat et al., 2000). The Boromo belt continues without major interruption down to Ghana, where it is known as the “Lawra” belt (Leube et al., 1990; Agyei Duodu et al., 2010). The western margin of the belt, mostly tholeiitic in composition, crops out from Dano to the south and continues underneath the granites as shown by the gravity data further to the north. Tholeiitic basalts with large (up to 10 cm), locally corroded plagioclase megacrysts and occasional pillow structures (figure II-4a), were found at three localities of the western mafic unit (yellow stars in figure II-2). Some of them contain more than 90% plagioclase and are comparable to the Archean anorthosites described by Ashwal et al. (1983). We interpret these tholeiitic mafic units, which reach 6 km in thickness, to form the base of the complete stratigraphic sequence, based on their geochemistry and structural position within the belts. The litho-structural relationship between the mafic units forming the eastern and western margins of the Boromo belt is hard to verify even with the gravity data; however, a continuity of these units at depth cannot be excluded.

The stratigraphic sequence changes upwards into andesitic lavas of transitional and calc-alkaline composition, which are intercalated with thick sequences of pyroclastic flows and tuffs and rare layers of ferruginous cherts (figure II-2). The stratigraphic thickness of this predominantly calc-alkaline sequence varies between 2 and 5 km. The central part of the Boromo belt referred to here as the Batié volcano-sedimentary unit (figure II-2) is composed of flysch-like metasediments, tuffs, and epiclastic volcano-sediments with occasional intercalations of andesites. The thickness of the Birimian sedimentary units is hard to establish due to their intense folding, but ranges from 5 to 20 km in the map view.

Few radiometric ages are available for the volcanic rocks of the Boromo belt (figure II-3b). One rhyolite found in the westernmost unit, was dated at  $2171 \pm 7$  Ma (U-Pb on zircon; Le Métour et al., 2003), whilst rhyolites and andesites situated near Perkoa (figure II-2) yield ages of  $2195 \pm 15$  Ma (Pb-Pb on whole rock; Lompo, 1991).



**Figure II-3** a) Simplified stratigraphic sequences for the Banfora, Houndé and Boromo belts with the names of the corresponding belts in Ivory Coast and Ghana. Katiola-Marab. – Katiola-Marabadiassa belt. TH – tholeiitic mafic units, THM – tholeiitic megacrystic basalts, TRAN – transitional mafic and intermediate volcanic sequences, CA – calc-alkaline volcanic sequences. b) Radiometric age frequency histograms for Boromo-Lawra-Bole-Nangodi (BLBN) and Houndé-Téhini-Ouango-Fitini (HTOF) greenstone belts (GB) and Koudougou-Tumu (KTGD), Diébougou (DGD) and Sidéradougou (SGD) granitoid domains. The ages shown in the histograms are plotted in figure II- 2. Only U-Pb and Pb-Pb zircon and whole rock ages are taken into account. Note that no radiometric ages exist for the Banfora belt, the Niangoloko granitoid domain and adjacent areas in northern Ivory Coast.

### 3.2. The Houndé belt

The eastern part of the Houndé belt is composed of up to 6 km thick basal unit of tholeiitic basalts and gabbros, revealing very similar petro-chemical properties as the western mafic unit of the Boromo belt. Andesites, volcano-sediments and tuffs of presumably younger age occur in the central and southern part of the predominantly tholeiitic mafic unit. These formations extend down to Ivory Coast, where they are known as the Téhini belt (Hirdes et al., 1996; Pouclet et al., 1996; Lüdtke et al., 1998, 1999). Tholeiitic basalts with equidimensional automorphic, locally deformed plagioclase megacrysts similar to those occurring in the west of the Boromo belt (figures II-4a, b), were found at three localities along the eastern margin of the Houndé belt within the tholeiitic unit (figure II-2). We use them as an important lithostratigraphic marker documenting the structural and litho-stratigraphic continuity between the Houndé and Boromo belts. The basal mafic unit is bound to the west by the Boni shear zone, which defines the contact with a quasi-continuous unit of Tarkwaian-type sediments, described below (figure II-2).

The western part of the Houndé belt, corresponding to the Ouango-Fitini belt in Ivory Coast (Pouclet et al., 1996; Vidal et al., 1996; Lüdtke et al., 1998, 1999; Vidal et al., 2009), is mostly composed of intermediate to acid calc-alkaline volcanic series including voluminous basaltic andesites and pyroclastic flows at the base. It is marked by an upwardly increasing amount of intercalated tuffs and epiclastic volcano-sediments. Abundant layers of cherts (ferruginous, manganiferous) and quartz veins are associated with the volcano-sediments. Due to intense folding of these rocks, it is unclear as to whether the abundant lithological alternations are a result of tectonic repetition or whether they reflect the original stratigraphy. The thickness of the basic to intermediate calc-alkaline volcanic suites may reach up to 5 km in map view.

In the southern part of the Houndé belt, a northern continuation of the Haute Comoé or Bambéla basin (Vidal and Alric, 1994; Hirdes et al., 1996; Lüdtke et al., 1998, 1999), fine-grained sediments predominate. These sediments consist of volcanoclastics, argillites, and wackes and are affected by intense folding. The map thickness of the volcano-sedimentary unit attains 40 km at the widest zone. Strong lithological variability across and along belts is attributed to lateral facies evolution within the volcanic arc as shown in Ghana by Leube et al. (1990).

Rhyodacites from the western Houndé belt were dated at  $2176 \pm 4$  Ma using zircons (Pb-Pb) and  $2212 \pm 31$  Ma using amphiboles (K-Ar) (Le Métour et al., 2003). In the Ivory Coast, two rhyolites and one tuff from Ouango-Fitini belt give similar U-Pb zircon ages,  $2160 \pm 1$  Ma (Lüdtke et al., 1998) and  $2158 \pm 1$  Ma,  $2170 \pm 5$  Ma (Lüdtke et al., 1999), respectively. One rhyolite is much younger, yielding  $2104 \pm 2$  Ma (zircon U-Pb; Hirdes et al., 1996; Lüdtke et al., 1998), which is an age consistent with the nearby granite intrusions and therefore this rhyolite might be their subvolcanic equivalent. Lüdtke et al. (1998) have obtained ages of  $2129 \pm 13$  Ma for an amphibolite from the eastern part of the Téhini belt (Ar-Ar on amphibole), which gives a time constraint for the end of



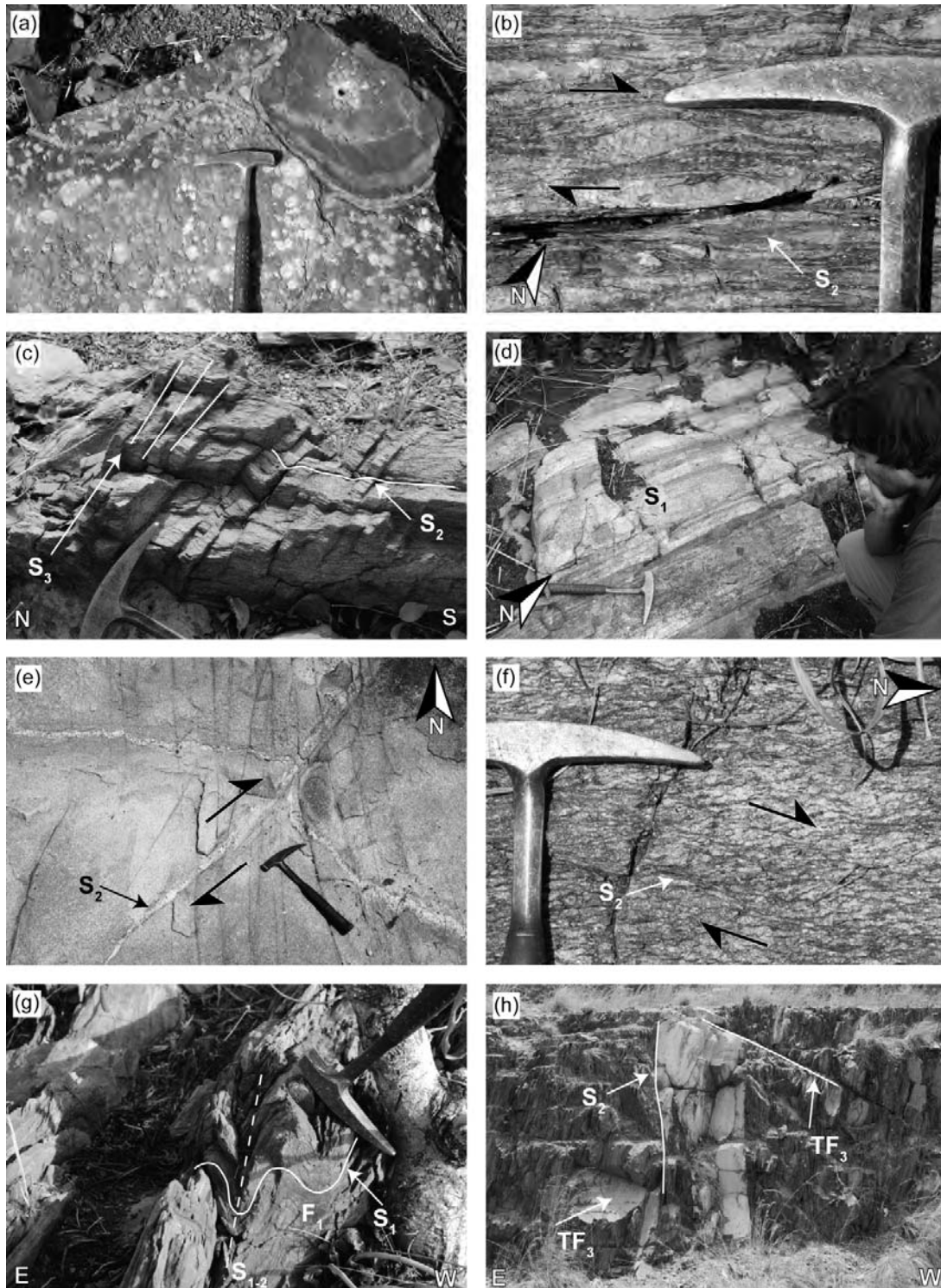
syntectonic contact metamorphism. Detrital zircons (U-Pb) from the Birimian wackes of the Bambéla volcano-sedimentary unit reveal three clusters of ages situated around 2180 Ma, 2150 Ma, and 2126 Ma (Lüdtke et al., 1999).

### 3.3. The Banfora belt

The eastern part of the Banfora belt consists of intercalated units of basalts, andesites, volcano-sediments, and rhyolites, 2 to 4 km thick, while the western part is composed of volcano-sediments only (figure II-2). A first order regional structure, known as the Greenville-Ferkessedougou-Bobo Dioulasso shear zone (GFBSZ) (Lemoine, 1988; Lemoine, 1990) marks the limit between the western and eastern parts, itself intruded by syn-kinematic granites, which are clearly discernible in the radiometric data. This NE-trending dextral shear zone is visible in the craton scale airborne magnetic data, running from Liberia in the south, crossing Ivory Coast and into the Banfora belt in Burkina Faso (figure II-1). As with the Houndé and Boromo belts, we consider the basalts and andesites as forming the base of the stratigraphic sequence, with upward increasing volumes of strongly folded volcano-sediments. The Banfora belt continues into Ivory Coast under the form of the Katiola-Marabadiassa greenstone belt and Bandama volcano-sedimentary basin (Doumbia et al., 1998; Gasquet et al., 2003; Pouclet et al., 2006) also known as the Ferkessedougou domain (Vidal et al., 1996; Vidal et al., 2009). No radiometric dating has been undertaken in this greenstone belt. The only ages available are from granitoids intruding the belt in the Katiola-Marabadiassa area, and range between  $2123 \pm 3$  and  $2097 \pm 3$  Ma (zircon Pb-Pb; Doumbia et al., 1998). Detrital zircons from the sediments of the Bandama basin were dated (Pb-Pb) by these authors at  $\sim 2133$  Ma and  $2107 \pm 7$  Ma. The deposition age was estimated between  $2108 \pm 12$  Ma and  $2097 \pm 3$  Ma based on the zircon Pb-Pb ages of pre- and post-basin granitoid intrusions.

### 3.4. Tarkwaian-type metasediments

A N-S oriented corridor of steeply to moderately dipping shallow-water detrital Tarkwaian type sediments extends parallel to the Houndé belt, adjacent to the unit of tholeiitic basalts situated at the eastern margin of the belt. This unit consists of various types of weakly metamorphosed conglomerates, sandstones, gritstones, arkoses (figure II-4c), and phyllites. The proportion of pebbles of the adjacent greenstone belt lithologies (quartz, rhyolite, schist) decreases from the central part towards the north and south (Bossière et al., 1996).



**Figure II-4** Field photographs of representative structures: a) tholeiitic basalts with plagioclase megacrysts forming pillow lavas, b) megacrystic basalts deformed in the ENE-oriented dextral GFBSZ (Greenville-Ferkessedougou-Bobo Dioulasso shear zone) in the north of the Boromo belt, near Ponkélé (horizontal section), c) penetrative metamorphic foliation  $S_2$  in Tarkwaian-type metasediments affected by late steeply dipping spaced cleavage  $S_3$ , d) steeply dipping NE-trending penetrative magmatic foliation  $S_1$  in syntectonic tonalite pluton, e) localized ENE-WSW dextral shear zone  $S_2$  in granodiorite, filled by late pegmatite (horizontal section), f) NNE-oriented synkinematic S-C mylonite with dextral sense of movement in two mica granite localized in the GFBSZ close to Banfora (horizontal section), g) penetrative metamorphic foliation  $S_1$  in metabasalts folded by  $F_1$  folds, h) subvertical NNE-trending shear zone  $S_2$  overprinting  $S_1$  metamorphic foliation in metabasalts, intruded by syntectonic granite dyke near the contact of the Boromo belt and Diébougou GD; all lithologies are affected by late shallow dipping thrust faults ( $TF_3$ ).

This unit of Tarkwaian-type sediments is shown at some places in the 1:1 000 000 geological map (Castaing et al., 2003); however, our field work and interpretation of geophysical data suggest that this unit is continuous, extending without interruption down to the Ivory Coast, where it was mapped by Lüdtke et al. (1998). At several places, original sedimentary structures such as cross-bedding and graded bedding indicate a younging direction of the sequence towards the west within subvertical or west dipping units of Tarkwaian-type sandstones and gritstones. The whole unit of Tarkwaian-type sediments is approximately 400 km long and 1-2 km wide, with a map thickness of up to 2 km. Being the topmost stratigraphic unit, the preservation potential is limited, which may explain the absence of the Tarkwaian-type sediments in the Boromo and Banfora belts, rather than a change in tectonic style between the belts.

Detrital zircons and zircons from rhyolite pebbles ranging between  $2171 \pm 7$  Ma and  $2113 \pm 23$  Ma have been used to obtain the maximum deposition age of Tarkwaian-type sediments at several places in Burkina Faso (Bonkougou, 1994; Bossière et al., 1996). In Ivory Coast, detrital zircon ages from Tarkwaian-type sediments span between  $2170 \pm 3$  Ma, and  $2130 \pm 6$  Ma (Lüdtke et al., 1999), similar to those found in Burkina Faso. In northern Ivory Coast, sediments resembling the Tarkwaian-type sediments were reported as Sambrigian by Lüdtke et al. (1999). They are included in the Ouango-Fitini belt and contain zircons ranging in age from  $2177 \pm 1$  Ma to  $2115 \pm 2$  Ma.

### **3.5. Granitoids**

Abundant granitoid plutons are found not only in the domains between the three greenstone belts, but sometimes also intrude the greenstone belts as individual granite bodies. In accordance with the previous studies of granitoids in the Baoulé-Mossi domain (e.g. Leube et al., 1990; Hirdes et al., 1992; Davis et al., 1994; Pons et al., 1995; Doumbia et al., 1998; Egal et al., 2002; Gasquet et al., 2003; Castaing et al., 2003; Naba et al., 2004; Lompo, 2009), we distinguish multiple episodes of granitoid intrusions. Each petrographic group will be attributed to a Magmatic Episode (ME) according to the radiometric ages. The four petro-chemical groups are as follows:

1) Calc-alkaline tonalite-trondhjemite-granodiorite intrusions. They often show high temperature steeply dipping magmatic foliation (figure II-4d) and are generally amphibole-biotite bearing, with only small amounts of K-feldspar. These rocks are also called in older literature grey gneisses, orthogneisses, or migmatites due to the pronounced mineral layering and compositional banding. The plutons are usually elongate or irregular in shape.

2) Calc-alkaline potassic granodiorite-granite intrusions. They are undeformed or affected by localized shear-zones (figure II-4e, f) and are biotite and K-feldspar bearing, with rare amphibole or muscovite. They are generally characterized by well-defined sub-circular or elliptical bodies, clearly transecting older lithologies.

3) Potassic granites, sometimes metaluminous, and sporadic syenites. They are undeformed or affected by localized mylonitic zones. K-feldspar is abundant and the granites often contain biotite. Amphibole is scarce or absent. The elliptical to sigmoidal plutons are visible in magnetic data because of their high magnetization (figure II-2).

4) Small calc-alkaline gabbro-diorite bodies of unknown age; often associated with granite, granodiorite, or tonalite intrusions. They are generally coarse grained and consist of amphibole, plagioclase, and clinopyroxene.

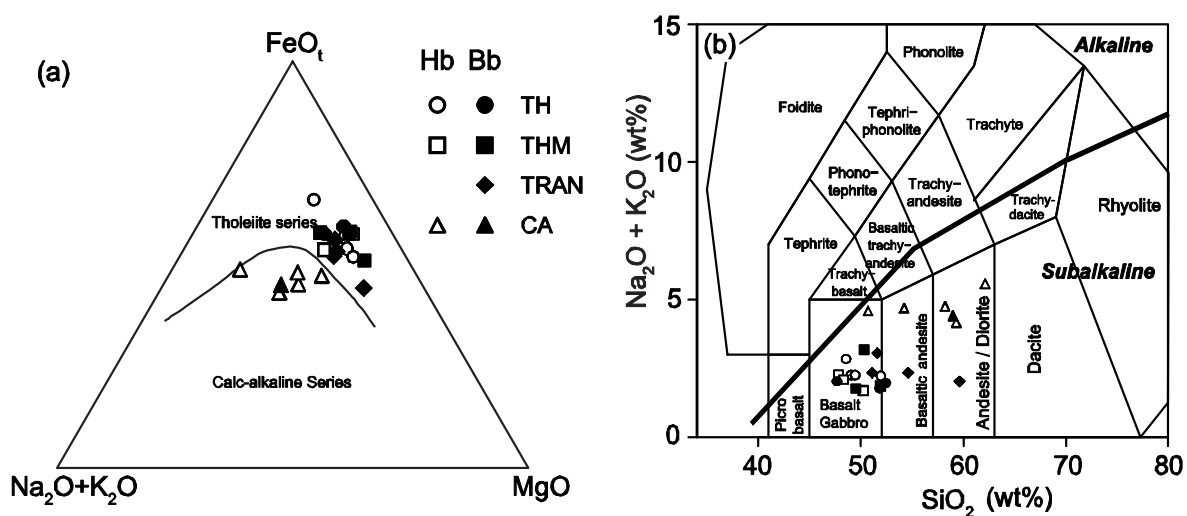
Although more radiometric ages have been reported from granitoids than from greenstone belt rocks, reliable granitoid data are still missing in the south of the study area. The oldest granitoids were reported from Ghana, yielding zircon U-Pb ages of  $2195 \pm 4$  Ma and  $2187 \pm 3$  Ma (Siegfried et al., 2009) (figure II-3b). In the north of Ivory Coast, Lüdtke et al. (1998, 1999) and Hirdes et al. (1996) obtained U-Pb zircon ages of  $2152 \pm 3$  Ma for a granodiorite intrusion in the east of Téhini belt and  $2152 \pm 2$  for another one in the west of the Ouango-Fitini belt (figure II-2) for the oldest granodiorites. Granitoids from the Dabakala region in northern Ivory Coast yield  $2162 \pm 32$  Ma and  $2154 \pm 1$  Ma (Gasquet et al., 2003) and similar ages were obtained on granitoids in northern Ghana (figure II-2, Siegfried et al., 2009; Thomas et al., 2009). In western Burkina Faso, the oldest ages obtained from granitoids correspond to  $2132 \pm 6$  Ma (zircon Pb-Pb; Koté et al., 2003), and  $2136 \pm 8$  Ma (monazite U-Pb; Chèvremont et al., 2003) (figure II-2). Granitoids in northern Ivory Coast were dated at  $2137 \pm 9$  Ma (Hirdes et al., 1996) and  $2123 \pm 3$  Ma (Doumbia et al., 1998). Ages ranging between  $2134 \pm 6$  Ma and  $2118 \pm 4$  Ma were also reported from the Dabakala region (Gasquet et al., 2003) and northern Ghana (Siegfried et al., 2009; Thomas et al., 2009; Agyei Duodu et al., 2010). These granitoids were emplaced according to our scheme during the first Magmatic Episode (ME1).

Most of the ages obtained on zircons from granitoids found between but also within the three studied greenstone belts, range from  $\sim 2113$  Ma to  $2097 \pm 10$  Ma (zircon U-Pb and Pb-Pb; Koté et al., 2003; Chèvremont et al., 2003; Le Métour et al., 2003). Twelve U-Pb zircon ages (Hirdes et al., 1996; Lüdtke et al., 1998, 1999; Gasquet et al., 2003; Agyei Duodu et al., 2010) and three Pb-Pb ages (Doumbia et al., 1998) ranging between  $2113 \pm 2$  Ma and  $2097 \pm 3$  Ma were also obtained on granitoids situated in the north of Ivory Coast and Ghana. Granitoids of these ages are attributed to the second and third Magmatic Episodes (ME2 and ME3). Granites of the ME3 group can be easily distinguished from the ME2 ones in the magnetic data due to their high susceptibility and concentric magnetic patterns.

No radiometric age is available for the gabbro-diorite plutons. We assign them to the ME4 Magmatic Episode but this does not mean that they were the last to be intruded in our tectonic scenario. More radiometric ages and petro-chemical data are needed to attribute with confidence to which magmatic episode each particular pluton belongs. We are the least confident about the distinction between granitoids of the ME1 and ME2 groups, whose petro-chemistry and geophysical properties are similar in many cases.

#### 4. Geochemistry of volcanic belts

Volcanic rocks of the Houndé and Boromo belts were subdivided into three groups based on their lithological character and chemical composition. Moreover, the megacrystic basalts were plotted separately (figures II-5 and II-6) from other basalts, which show mostly homogeneous microlithic texture. Twenty-two samples of volcanic rocks distributed systematically across both Houndé and Boromo belts were analyzed for this study. Major and trace element concentrations were measured by ICP-AES at ALS Chemex (Spain) – 23 samples (table II-1, figures II-5 and II-6). The spatial distribution of these samples, classified according to their composition, is reported in figure II-7. In the



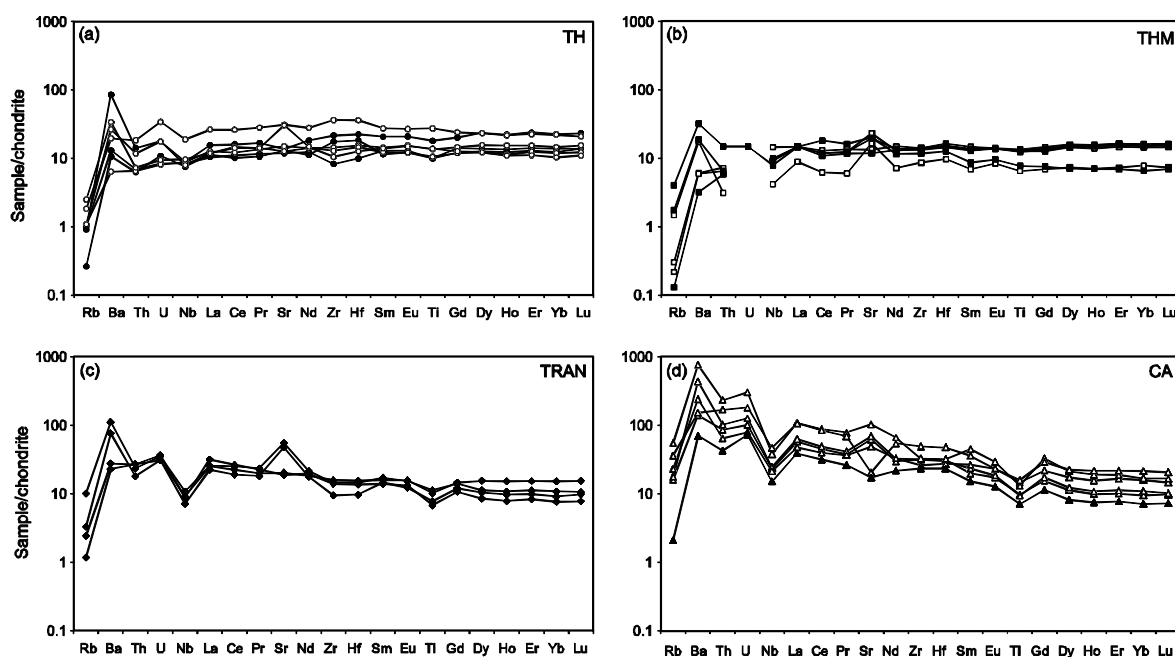
**Figure II-5** a) AFM diagram of the analyzed volcanic rocks (Irvine and Baragar, 1971), b) TAS diagram of Middlemost (1994); Hb - Houndé belt, Bb - Banfora belt, TH - tholeiites, THM - megacrystic basalts, TRAN - transitional basalts and andesites, CA - Calc-alkaline basalts and andesites. The data were plotted using the GCDkit software (Janoušek et al., 2006).

same way, we have plotted the chemical analyses from BRGM/BUMIBEG sample database for comparison (Chèvremont et al., 2003; Koté et al., 2003; Le Métour et al., 2003).

The first group (TH) consists of pillow lavas and massive basalts from both the Boromo and Houndé belts, including one gabbro and two amphibolites. The samples correspond to tholeiitic basalts in the AFM diagram (figure II-5) and to subalkaline basalts ( $47\% < SiO_2 < 53\%$ ;  $1.8\% < Na_2O+K_2O < 2.9\%$ ) in the TAS classification of Middlemost (1994). The (La/Yb) chondrite ratio ranges from 0.7 to 1.2, with the LREE 10 to 30 times enriched with respect to the chondrite (McDonough and Sun, 1995). Some samples yield a slight negative Nb anomaly. Rb, Ba, Sr, Zr, and Hf show weak positive or negative anomalies. Such rather flat patterns of REE (normalized to chondrite) are typical for tholeiites and resemble spectra for similar basalts cratonwide (e.g. Abouchami et al., 1990; Ama Salah

et al., 1996; Pouclet et al., 1996; Lüdtké et al., 1998; Béziat et al., 2000; Pouclet et al., 2006; Lompo, 2009).

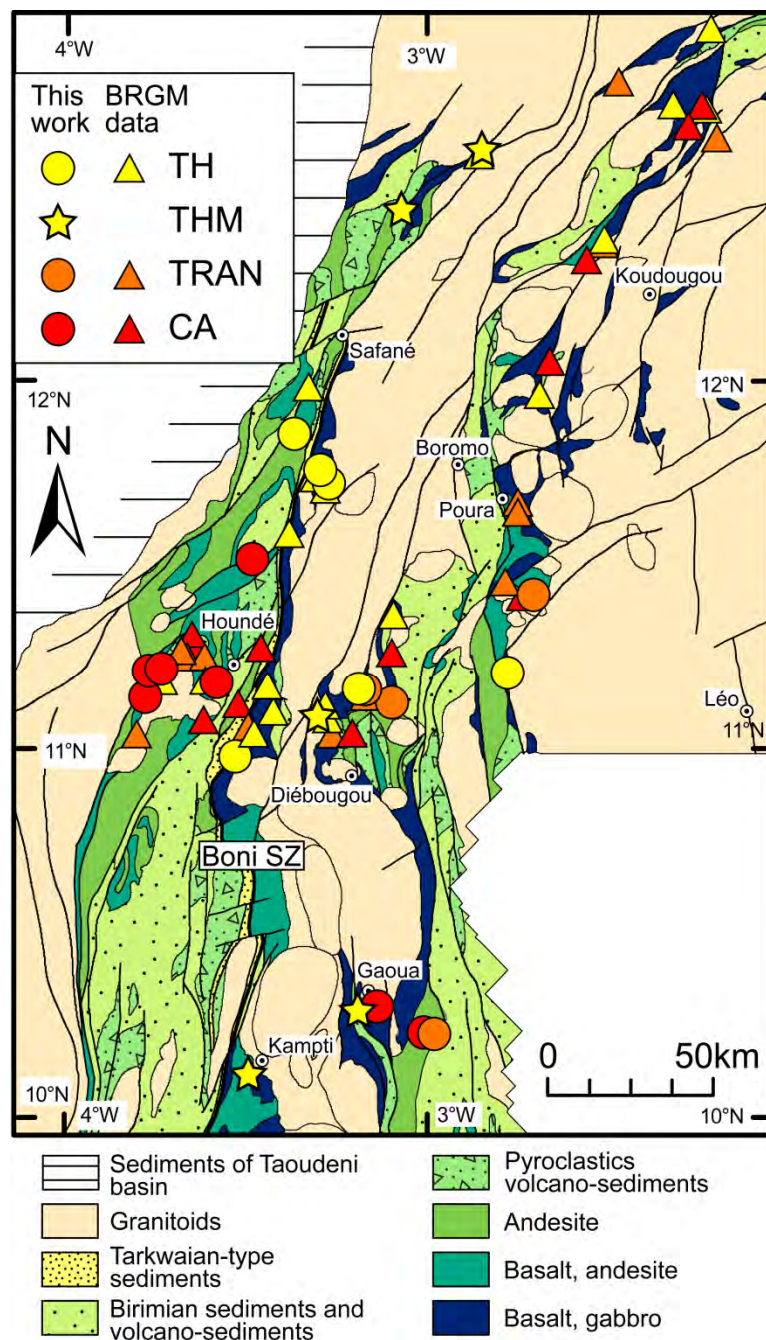
The second group (THM) consists of six porphyritic basalt and microgabbro samples with plagioclase megacrysts from both belts. Matrix was analyzed separately from the megacrysts where possible (all samples except for HO319 shown in figure II-4b). These samples correspond to tholeiites in the AFM diagram. In the TAS diagram, they also correspond to subalkaline basalts ( $47\% < \text{SiO}_2 < 52\%$ ;  $1.7\% < \text{Na}_2\text{O} + \text{K}_2\text{O} < 3.2\%$ ). The REE and trace element spectra of the megacrystic basalts, normalized to chondrite (McDonough and Sun, 1995), are almost identical to those of the TH group (figure II-6) suggesting that they are of the same affinity. Two samples (HO417 and HO389) show slightly lower enrichment in HREE, which can be explained by higher plagioclase content in the analyzed matrix. The more pronounced Sr anomalies are related in the case of some samples to the presence of the large plagioclase megacrysts. Similarly, to the TH group, there is no difference between the samples of the Houndé and Boromo belts.



**Figure II-6** Spiderplots of the four groups a) tholeiites, b) megacrystic basalts, c) transitional basalts and andesites and d) calc-alkaline basalts and andesites, normalized to chondrite (McDonough and Sun, 1995). Black symbols are used for the Boromo belt, white symbols are used for the Houndé belt.

Sample	TH										TRAN										CA									
	HO14	HO23	HO33	HO18	HO52	HO592	HO521	HO389B	HO508	HO536	HO520	HO417	HO531	HO51	HO329	HO405	HO524	HO12	HO71	HO345	HO3	HO9	HO294							
Houndé	Houndé	Houndé	Houndé	Houndé	Boromo	Boromo	Boromo	Houndé	Houndé	Boromo	Boromo	Boromo	Boromo	Boromo	Boromo	Boromo	Boromo	Houndé	Houndé	Houndé	Houndé	Houndé	Boromo							
Lat. (N)	11°45'33"	11°45'32"	11°51'42"	10°58'51"	11°00'04"	11°42'31"	10°18'13"	12°37'36"	12°28'08"	10°07'54"	10°18'13"	11°06'48"	9°44'35"	11°09'16"	11°45'11"	11°07'50"	10°13'45"	11°42'54"	11°11'00"	11°08'33"	11°3'107"	11°13'08"	10°13'57"							
Long. (W)	3°16'33"	3°17'49"	3°22'04"	3°3'149"	3°11'22"	2°46'49"	3°11'01"	2°50'34"	3°03'46"	3°29'42"	3°10'57"	3°18'04"	3°55'23"	3°10'31"	2°42'31"	3°05'56"	2°58'50"	3°46'18"	3°35'05"	3°46'52"	3°29'04"	3°44'17"	3°10'44"							
SiO <sub>2</sub>	519	48.5	49	49.4	518	52.4	47.64	47.8	50.2	49.4	50.3	51.9	49.5	51.6	51.1	59.6	54.6	59.3	58.2	50.7	54.2	62.1	59							
Al <sub>2</sub> O <sub>3</sub>	13.15	13.45	15.1	14.25	13.55	12.2	13.79	22.1	14.2	14.2	15.4	14.45	14.1	14.3	14.9	12	10.45	14.45	14.85	13	13.7	14.8	14.55							
Fe <sub>2</sub> O <sub>3</sub>	13.35	16.85	11.9	11.8	12.75	16.75	13.29	8.27	13	13.95	13.75	11.85	13.55	11.8	11.5	8.68	9.18	8.11	7.36	12.15	10.2	8.33	7.4							
MnO	0.19	0.28	0.16	0.18	0.2	0.24	0.19	0.11	0.2	0.21	0.2	0.18	0.2	0.18	0.17	0.14	0.16	0.1	0.11	0.19	0.16	0.08	0.12							
MgO	6.88	4.94	6.85	7.57	6.01	5.04	7.08	4.13	6.89	7.21	5.74	8.33	6.93	6.66	5.72	4.81	8.04	4.61	3.92	7.5	5.15	2.21	3.68							
CaO	10.4	10.75	11.1	11.55	11.45	8.83	11.41	13.75	10	10.7	9.85	9.6	10.6	9.61	10.3	9.1	8.06	5.46	6.52	8.09	7.88	4.56	5.31							
Na <sub>2</sub> O	2.1	2.63	2.11	1.86	1.68	1.85	1.89	2.05	1.67	1.91	3	1.55	1.72	2.13	2.04	1.88	1.98	3.04	2.86	2.77	1.51	3.47	4.09							
K <sub>2</sub> O	0.12	0.21	0.14	0.39	0.11	0.12	0.14	0.22	0.02	0.03	0.19	0.32	0.05	0.92	0.3	0.15	0.36	1.13	1.9	1.82	3.18	2.11	0.31							
TiO <sub>2</sub>	0.99	2	0.77	1.01	0.74	1.32	0.83	0.48	0.99	0.92	0.96	0.57	0.91	0.82	0.75	0.5	0.57	0.71	0.69	1.08	0.96	1.16	0.52							
P <sub>2</sub> O <sub>5</sub>	0.07	0.19	0.06	0.11	0.01	0.12	0.04	0.06	0.08	0.08	0.08	0.04	0.08	0.2	0.09	0.13	0.15	0.17	0.28	0.38	0.36	0.12	0.12							
LOI	0.89	0.3	3.51	2.17	0.99	0.1	1.75	1.18	3.88	2.97	1.87	2.45	2.48	1.77	1.4	1.87	4.45	2.65	3.74	2.27	2.56	0.77	3.39							
Total	100.04	100.1	100.7	100.29	99.29	98.97	96.89	100.15	101.13	101.58	101.34	101.24	100.12	99.99	98.27	98.86	98	99.71	100.32	99.85	99.88	99.95	98.49							
Rb	2.5	4.2	2.5	5.7	0.6	2.1	2.31	3.4	0.7	0.5	4	9.2	0.3	23.1	5.6	2.7	7.6	36.5	40.8	52.7	125.5	83.2	4.8							
Ba	15.3	47	63.3	81.2	25.4	205	3129	42.1	14.7	14.3	45	77.2	7.7	268	66.4	55.2	184	338	1045	577	1830	367	168.5							
Sr	108	223	92.2	220	94.2	98.6	85.51	119.5	97.3	167	142.5	144.5	87	400	146.5	136	346	449	500	354	743	147.5	125							
U	0.06	0.25	0.13	0.07	0.08	0.13	0.06	0.09	0.21	0.19	0.19	0.43	0.17	0.68	0.78	0.78	0.52	0.23	0.75	0.93	2.24	1.34	0.54							
Th	0.19	0.53	0.34	0.21	0.18	0.41	0.20	0.09	0.21	0.19	0.19	0.43	0.17	0.68	0.78	0.78	0.52	0.23	0.75	0.93	2.24	1.34	0.54							
Ta	0.2	0.1	0.1	0.2	0.1	0.2	0.57	0.2	0.2	0.2	0.2	0.2	0.2	0.2	0.2	0.1	0.1	0.1	0.5	0.3	0.2	0.6	0.9							
Nb	2.1	4.5	1.9	2.3	1.8	2.1	2.01	1	3.5	2.3	2.4	1.9	2.2	2.6	2.2	2.1	1.7	5.6	5.9	5.1	9.1	11.2	3.6							
Hf	1.6	3.7	1.5	1.3	1.9	2.3	1.02	1	1.7	1.5	1.6	1.3	1.5	1.5	1.6	1.4	1	3.2	3.1	2.8	3.3	4.9	2.4							
Zr	55	138	49	40	67	82	3147	33	54	53	54	45	51	55	60	53	36	120	121	100	125	188	89							
Y	217	30.6	16.3	15.4	16.7	32.2	18.74	9.9	21.4	20.5	22	9.4	21.1	15	21.8	11.7	14.8	14.9	15.5	21.5	29.3	32.3	10.9							
Ni	19	47	66	98	95	47	97.68	75	82	90	68	133	99	36	90	89	61	114	59	63	57	41	41							
Cr	170	50	90	300	100	30	327.58	130	230	230	100	230	210	170	120	250	470	240	150	270	220	110	110							
Co	86.6	63.6	65.7	68.1	113.5	52.9	87.83	60.6	64	96	72	71	71	69.6	46	31.6	38.4	63.7	68.5	64.9	53.5	54.6	24.1							
V	296	395	257	249	266	334	156	304	307	315	259	295	295	253	249	197	218	150	138	254	199	110	141							
La	3	6.2	2.8	2.8	2.7	3.7	2.46	2.1	3.1	2.8	2.8	4.3	2.6	6.1	6	7.5	5.3	13.7	14.9	11.3	25.7	25.1	9.2							
Ce	7.4	16	8.9	8.7	6.2	9.8	6.75	3.8	8.3	7.6	7.6	9.9	7.2	15.3	13.7	16.2	11.7	27.6	30	24.3	53.8	51.7	19.4							
Pr	1.25	2.6	1.31	1.31	0.98	1.55	1.08	0.56	1.3	1.6	1.9	1.26	1.14	2.18	1.86	2.1	1.68	3.46	3.85	3.4	7.3	6.44	2.43							
Nd	6.5	12.7	6.4	6.7	5.1	8.3	5.66	3.3	6.8	5.9	6.3	5.3	6	9.8	8.3	9	8.1	13.6	15	15	30.3	24.8	10							
Sm	2.12	4.05	1.82	2.06	1.69	3.04	1.91	1.02	2.17	1.91	2.04	1.28	2	2.52	2.36	2.06	2.14	2.93	3.47	3.9	6.62	5.3	2.25							
Eu	0.87	1.5	0.68	0.84	0.69	1.17	0.73	0.47	0.8	0.78	0.77	0.54	0.78	0.86	0.88	0.74	0.69	0.97	1.04	1.29	1.65	1.31	0.72							
Gd	2.89	4.75	2.38	2.52	2.41	4	2.79	1.38	2.88	2.52	2.7	1.51	2.65	2.8	2.9	2.13	2.39	3.07	3.44	4.35	6.55	5.81	2.26							
Tb	0.55	0.86	0.4	0.42	0.43	0.87	0.48	0.24	0.56	0.51	0.54	0.25	0.52	0.45	0.56	0.35	0.43	0.45	0.49	0.7	0.96	0.91	0.35							
Dy	3.83	5.72	3.03	3	3.1	5.77	3.41	1.8	3.91	3.57	3.81	1.75	3.65	2.77	3.81	2.09	2.78	2.78	3.02	4.27	5.23	5.48	2.01							
Ho	0.84	1.18	0.61	0.6	0.67	1.2	0.74	0.39	0.86	0.76	0.85	0.38	0.81	0.59	0.83	0.43	0.53	0.54	0.59	0.85	1.04	1.18	0.41							
Er	2.46	3.58	2	1.78	2.06	3.78	2.26	1.17	2.62	2.35	2.6	1.11	2.49	1.78	2.46	1.33	1.58	1.61	1.79	2.64	3	3.47	1.24							
Tm	0.4	0.53	0.31	0.27	0.3	0.4	0.33	0.18	0.38	0.35	0.39	0.15	0.37	0.25	0.33	0.15	0.21	0.24	0.26	0.34	0.43	0.54	0.15							
Yb	2.35	3.54	1.92	1.66	2	3.59	2.22	1.26	2.54	2.32	2.58	1.06	2.4	1.74	2.44	1.23	1.47	1.53	1.76	2.57	2.71	3.45	1.15							
Lu	0.38	0.51	0.3	0.27	0.34	0.57	0.34	0.18	0.39	0.36	0.4	0.17	0.38	0.26	0.38	0.19	0.24	0.24	0.25	0.36	0.41	0.51	0.18							
Mg#	0.51	0.37	0.53	0.56	0.48	0.37	0.52	0.50	0.51	0.51	0.45	0.58	0.50	0.53	0.50	0.52	0.63	0.53	0.51	0.55	0.50	0.34	0.50							
(La <sub>2</sub> Yb) <sub>hb</sub>	0.87	1.19	0.99	1.15	0.92	0.70	0.75	1.13	0.68	0.67	0.62	0.74	0.67	2.38	1.67	4.14	2.45	6.08	5.75	2.99	6.44	4.94	5.43							

Table II-1 Representative geochemical analyses of mafic and intermediate volcanic rocks of the greenstone belts.



**Figure II-7** Map of geographical distribution of the analysed samples within the greenstone belts. The acronyms are the same as in figure II-5.

The third group (TRAN) includes four samples ranging from low alkali basalts to andesites ( $51\% < \text{SiO}_2 < 60\%$ ;  $2\% < \text{Na}_2\text{O} + \text{K}_2\text{O} < 3\%$ ) from the Boromo belt. In the AFM diagram, these samples correspond to tholeiites. However, the REE spectra show a slight enrichment of the LREE with respect to HREE,  $(\text{La}/\text{Yb})_{\text{chondrite}} = 1.7\text{--}4.1$ , and the REE are 20 to 30 times higher with respect to the chondrite. We classify them as transitional, because they reveal a prominent negative Nb and Ti anomaly, similar to the calc-alkaline volcanites (CA).



The fourth group (CA) corresponds to calc-alkaline volcanics from both belts and includes six samples of subalkaline basalts and andesites with higher content of alkalis ( $51\% < \text{SiO}_2 < 62\%$ ;  $4.2\% < \text{Na}_2\text{O} + \text{K}_2\text{O} < 5.6\%$ ). They are characterized by high (La/Yb) chondrite ratio (3.0-6.4), REE content 40 to 110 times higher with respect to chondrite, a high content of incompatible elements (Rb, Ba, Th, U) with respect to tholeiitic basalts, and a pronounced negative Nb and Ti anomaly. These calc-alkaline basalts and andesites resemble strongly those analyzed by Béziat et al. (2000) in the Boromo belt and Pouclet et al. (1996) and Lüdtke et al. (1998) in the Ouango-Fitini belt in Ivory Coast (figure II-2).

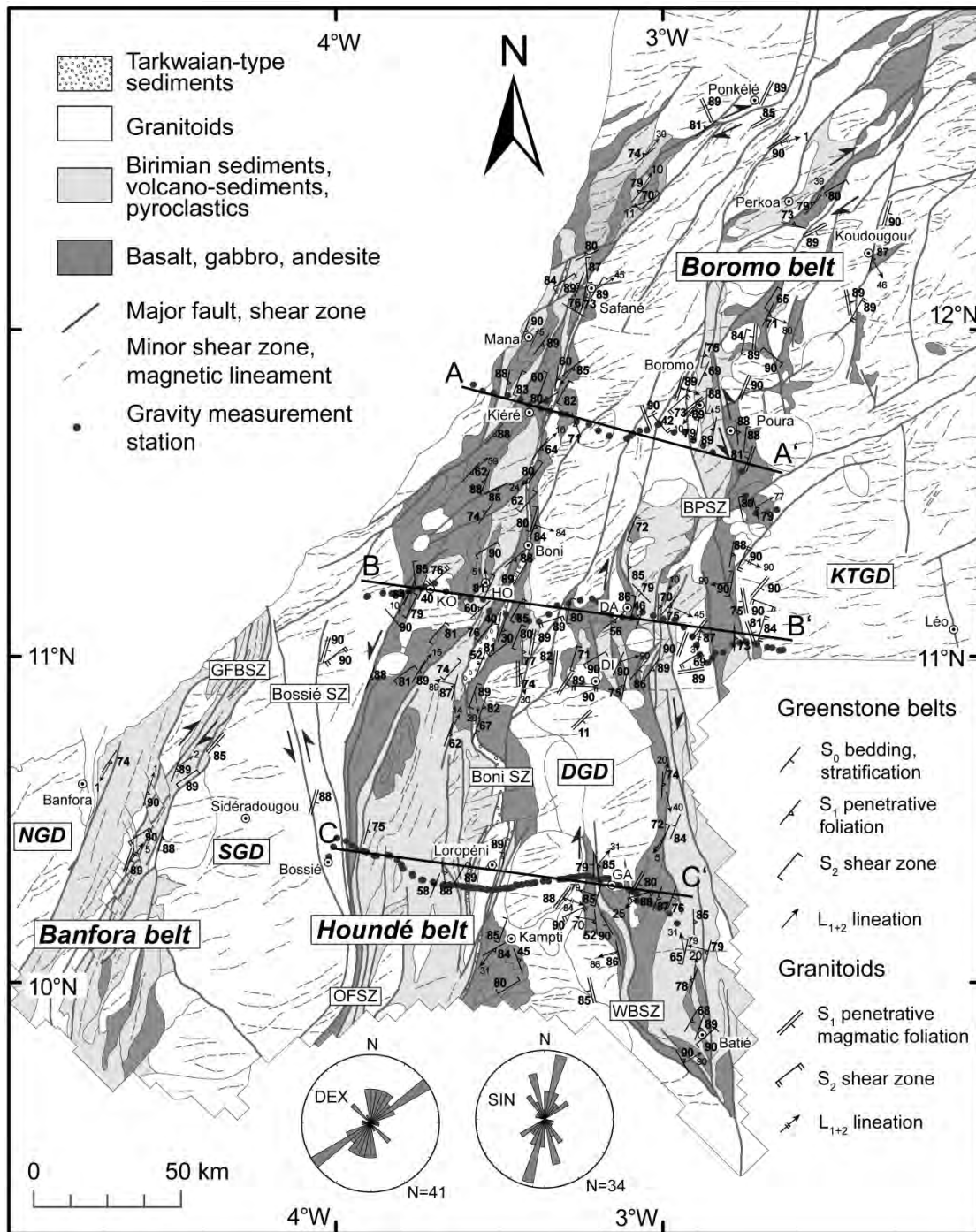
Note that none of the 23 analyzed samples shows an Eu anomaly. Variable Rb, Ba and Sr contents may be due remobilization during the pervasive greenschist to amphibolite facies metamorphism. As a summary, tholeiitic and calc-alkaline volcanics are present in both belts with more transitional members in the Boromo belt (figure II-7). We emphasize the strong resemblance between the eastern margin of the Houndé belt and the western margin of the Boromo belt and in particular between the megacrystic and normal tholeiitic basalts in both belts. The western part of the Houndé belt and the central part of the Boromo belt are formed of calc-alkaline basalts, with transitional basalts present in the Boromo belt.

## **5. Structural Evolution**

We distinguish three deformation events in the Boromo, Houndé, and Banfora greenstone belts and in the surrounding granitoids (figures II-8, II-9, and II-10). The principal deformation imprint of the Eburnean orogenesis is related to the first and second deformation phases D1 and D2. The deposition of the Tarkwaian-type-type sediments is related to the late stages of the D1 deformation phase. Post-Eburnean D3 deformation is recorded only in some lithologies, in particular highly anisotropic greenstones. For the purpose of structural analysis, we have used a combination of field observations and interpretations of airborne geophysical data, which allowed us to correlate small-scale structures with regional structures of the same generation. The deformation phases are summarized and compared to the published works in table II-2.

### **5.1. Deformation phase D1**

The present structural grain results from the protracted deformation phase D1 that strongly affected the Birimian volcanic and volcano-sedimentary units and structured most of the syntectonic intrusions of the first magmatic episode (ME1). Given the clusters of radiometric ages of syntectonic granitoids, the syn-D1 magmatic activity started at around ~2160 Ma. D1 deformation is associated with the major regional metamorphic phase M1.



**Figure II-8** Structural map showing the orientation  $S_0$  bedding and stratigraphic layering,  $S_1$  penetrative metamorphic foliation, and the  $S_2$  shear zones and high strain zones.  $L_1/L_2$  lineations are also plotted. Rose diagrams show the strike distribution of dextral (DEX) and sinistral (SIN) shear zones. HO – Houndé, KO – Koumbia, DA – Dano, DI – Diébougou, GA – Gaoua, KTGD – Koudougou-Tumu granitoid domain, DGD – Diébougou granitoid domain, SGD – Sidéradoukou granitoid domain, NGD – Niangoloko granitoid domain. Three cross-sections shown in figure II- 12 are indicated.

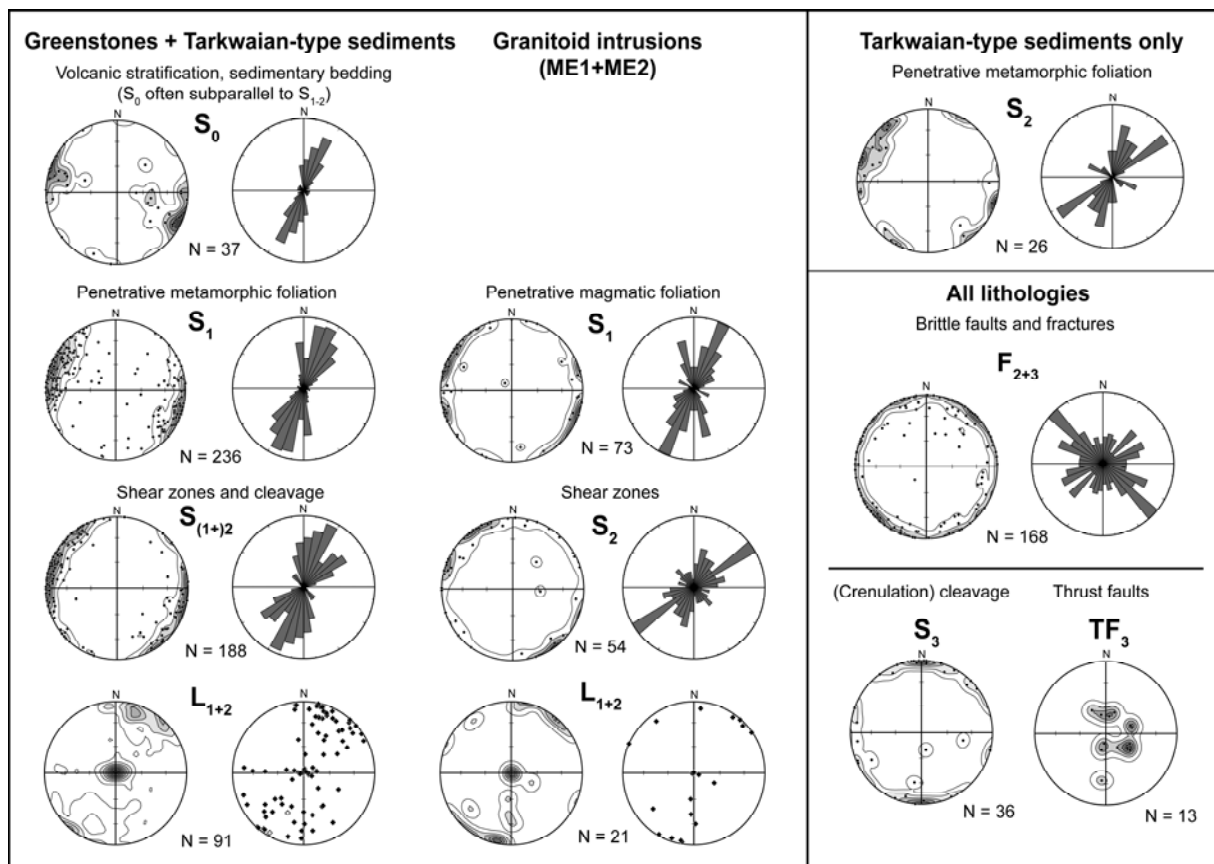
In volcano-sedimentary rocks, pyroclastic flows, volcanic ashes and some andesitic lavas of the greenstone belts, the D1 event is expressed as a penetrative metamorphic foliation (S1), often subparallel to the primary bedding. Localized N and NNE-oriented anastomosing S1 shear zones and high strain zones with no obvious displacement attributed to lack of marker horizons, developed in basalt-andesitic massive lava flows, gabbros, and diorites. Most of these shear zones are sinistral; however, some dextral shear zones were also inferred from sigmoidal pressure shadows around minerals, asymmetric shear structures and scarce sigmoidal shapes of fragments in pyroclastic flows. The NNW to NNE orientation of the S1 metamorphic foliation and shear zones is uniform over the study area (figure II-9). The foliations display more variable dip orientations whereas the shear zones and high strain zones are mostly subvertical. The high strain zones do not typically show a mineral lineation, suggesting a high amount of flattening rather than non-coaxial shearing. The absence of a lineation might also be related to the initial fine grain size of the deformed lithology (Piazolo and Passchier, 2002). When present, stretching lineations cluster around two maxima – subvertical and NE-SW subhorizontal orientations.

Volcano-sediments and other highly anisotropic lithologies are affected at various scales by isoclinal to open F1 folds (figure II-4g). Axial planes, often coincident with a S1 schistosity, are steeply dipping, trending from NNE to NE. Airborne magnetic data consistently reveal tight kilometric-scale fold hinges with the overall N to NNE trending and probably steeply dipping fold axial planes (figure II-10). The basal mafic unit is structurally facing upward or towards the east in the Boromo belt, while in the Houndé belt (Lüdtke et al., 1998), structural facing of the pillow lavas to the west or downward could indicate that they were tectonically overturned.

A well developed steeply dipping S1 compositional banding is typical for granitoid intrusions of the ME1 group (figure II-4d). The strikes of the S1 foliation planes concentrate in a NNE-SSW direction (figure II-9); in particular in the Diébougou and Sidéradougou domains (figure II-8). Magmatic lineation, often defined by elongation of dark co-magmatic enclaves or amphibole grains, is generally steeply dipping.

## **5.2. Deposition of Tarkwaian-type sediments – Late D1**

The Tarkwaian-type sediments stretch for approximately 400 km in remnant basins with a very high length-width ratio; however, the original basin width is unknown. The sediments do not record the high strains associated with D1 but they are overprinted by penetrative S2 shear fabric and faults interpreted to have been active during D2. The entire N-S unit of Tarkwaian-type sediments is bound on both east and west sides by reverse/strike slip sinistral D2 faults (Boni shear zone). The Tarkwaian-type sedimentary unit is along most of its eastern border parallel on the east to the more or less continuous unit of tholeiitic basalts and gabbros. In contrast, on the western side the sediments are juxtaposed with a clear oblique relationship with respect to the folded calc-alkaline volcano-

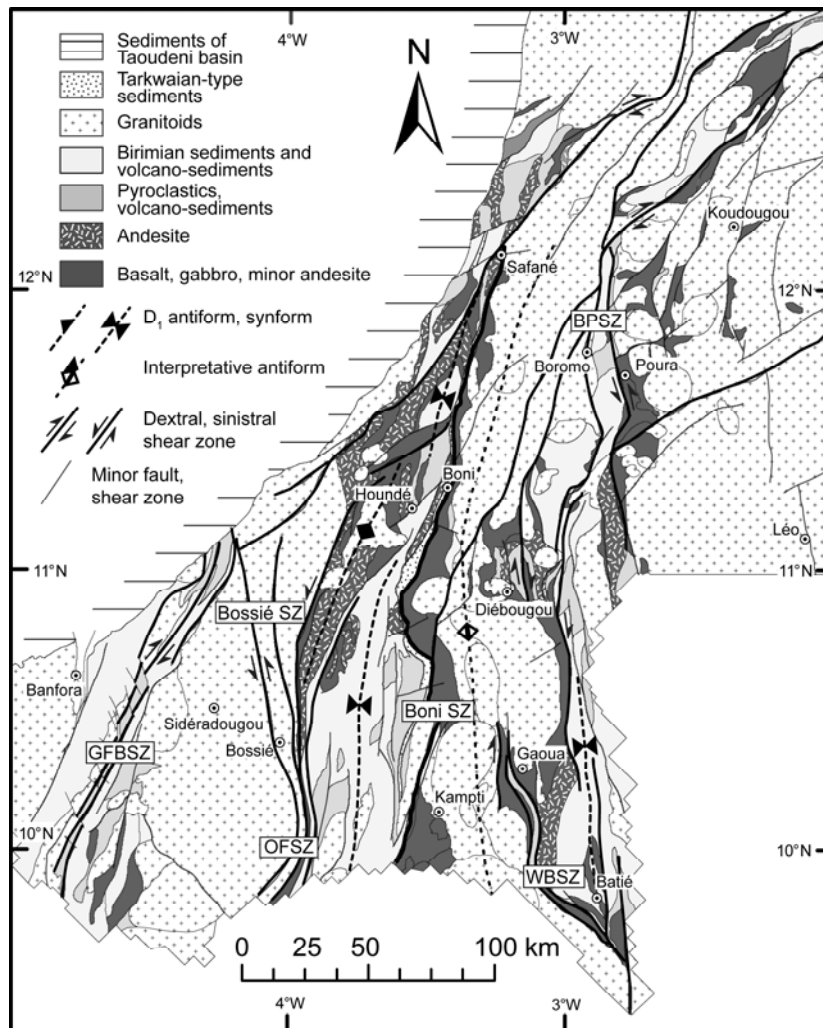


**Figure II-9** Equal area lower hemisphere stereoplots of the orientation of D1-D3 structures. Rose diagrams show the distribution of the foliation strikes and brittle fractures and faults.

sedimentary units (figure II-2). Such relationship may represent a reworked angular unconformity. This basin defines therefore the boundary between D1 and D2, which presumably can be treated as separate orogenic events.

### 5.3. Deformation phase D2

Typical D2 structures consist of anastomosing steeply dipping NNE to ENE oriented shear zones (figure II-4b) and high strain zones with a seldom shallow-dipping lineation. The majority of the transcurrent S2 shear zones operated under lower greenschist facies conditions. This is especially true for those bearing gold mineralization. S2 shear zones are generally brittle to brittle-ductile compared to the mostly ductile S1 penetrative schistosity, suggesting that D2 shear zones operated at lower temperatures with respect to the D1 structures. The orientations of all discrete shear zones and localized high strain zones found in greenstone belts are plotted in figure II-9, even if they do not necessarily belong to the same deformation phase. Two clear maxima of orientations can be distinguished, concentrating in the NNE-SSW and NE-SW directions. Unequivocal distinction between the S1 and S2 shear zones can only be made at the outcrops where crosscutting relationship



**Figure II-10** Simplified structural map indicating major shear zones/high strain zones and axial planes of the regional scale F1 folds. BPSZ – Boromo-Poura shear corridor; GFBSZ – Greenville-Ferkessedougou-Bobo-Dioulasso Shear zone; OFSZ – Ouango-Fitini shear zone; WBSZ – West Batié shear zone.

between the two structures was found. For the same reason, the L1 and L2 lineations are plotted together in the same diagram.

In granitoids, discrete ENE-trending dextral shear zones transecting the NNE penetrative foliation were observed at several places (figure II-4e). Some of the granites, such as the elongate pluton intruding along the Greenville-Ferkessedougou-Bobo Dioulasso shear zone within the Banfora belt (figures II-2 and II-4f) or the Dissin granite intruding into the Boromo belt, show well developed S-C penetrative fabric and are interpreted as being synkinematic with the D2 phase. Locally, we have observed syntectonic granite dykes which intruded parallel to the S2 shear zones (figure II-4h). The time span of the D2 event is well constrained by radiometric ages of many syn/late-tectonic granitoids ranging between 2113 and 2097 Ma.

A penetrative NNE and NE-trending schistosity (figure II-10) found in fine-grained Tarkwaian-type pelites and arkoses (figure II-4c) is attributed to the D2 activity of the Boni shear

zone. Sandstones, gritstones, and conglomerates are generally massive, affected only by sparse localized shear zones of the same orientation. Dextral shear sense indicators were found in the northern segment of the Boni shear zone near Safané (figure II-2) where the eastern contact zone with basalt crops out.

The D2 high strain zones are well defined in regional magnetic data, outlining an anastomosing system of lens-shaped, 5-30 km wide domains (figure II-2). The shear zones either follow pre-existing lithological contacts or transect the units, and are clearly visible in many granitoid bodies where these high strain zones represent demagnetized corridors. Gold mineralization is frequently associated with such regional-scale S3 shear zones (Milési et al., 1989, 1991, 1992; Castaing et al., 2003), a typical example being the Mana mine, situated in the north of the Houndé belt (figure II-2).

#### **5.4. Deformation phase D3 and post-Eburnean doleritic dykes**

The last deformation phase is characterized by the development of crenulation cleavage and chevron or kink folds (figure II-4c) and reverse faults (figure II-4h) observed mostly in highly anisotropic lithologies of the greenstone belts. The E-W striking S3 spaced cleavage, crenulation, and kink fold axes are in general steeply dipping and crosscut the S1 and S2 foliations at a high angle. Related thrust faults are dipping to the north and south (figure II-9).

Abundant NE-SW steeply dipping normal faults and fractures were found throughout the study area (figure II-9). These faults are clearly visible in geophysical data from the Banfora belt (figure II-2) and we attribute them to the D3 deformation event. Nevertheless, some of these faults might have originated during previous deformation phases and they were only re-activated during the D3. The structural pattern of the D3 is consistent with an overall N-S compression. We have no age constraints on this deformation phase, except that it post-dates all major Eburnean structures.

All Eburnean structures are transected by at least three generations of doleritic dykes, two of which also intrude the Neoproterozoic sediments of the Taoudeni basin. The dykes are striking NW-SE, WNW-ESE, and NE-SW and airborne magnetic data suggest that some of them intrude pre-existing structures.

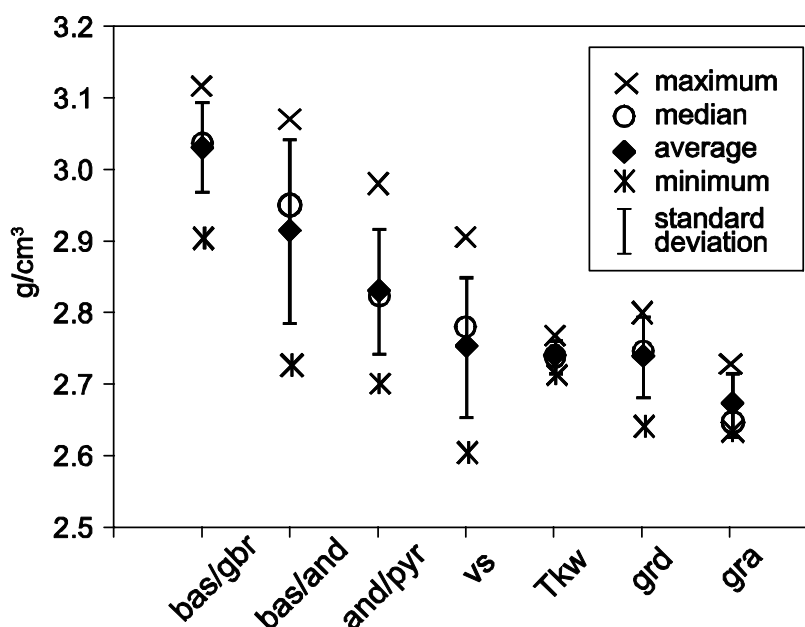
This Study		D <sub>Ext</sub>	D <sub>EarlyEburnean</sub>	D <sub>1</sub>	Late D <sub>1</sub>	D <sub>2</sub>	D <sub>3</sub>	Mafic dykes
		ca. 2200-2160	ca. 2170-2160 Ma	ca. 2160-2120	ca. 2120-2110 Ma	ca. 2110-2109 Ma	Post- 2109 Ma	Post- 2109 Ma
	Boromo, Banf. & Houndé	Arc volc., Birimian sedim. deposition		<i>NE-</i> metam. fab., SZ, iso. folds	Depo detrital sedim. (Tkw)	steep <i>N-S</i> to <i>ENE-</i> SZ, <i>NW-</i> faults	<i>E-W</i> cren. clv, <i>NW-</i> faults, thrusts	<i>NE-SW</i> , <i>NW-SE</i> and <i>WNW-ESE</i>
				WNW-ESE comp.	<i>E-W</i> transten./ext.	NW-SE transpres.	N-S comp.	Extension
Bossière et al., 1996	Houndé GB	Volc., Birimian sedim. deposition	D1: metamorphic fabric, folding		D2: Intracont. ext., depo. of Tkw sedim.	D3: <i>NNE-</i> met. fab., SZ	D4: <i>E-W</i> folds & clv, <i>NE-</i> & <i>NW-</i> faults	
Ouedraogo and Prost, 1986	Boromo GB	Volc., Birimian sedim.	D1: <i>NW-</i> metam. fabric, fold axes	D2: <i>NE-</i> met. fab. and fold axes		D3: <i>NE-</i> SZ, <i>NE</i> to <i>ENE-</i> fold		
Lompo et al., 1991	Boromo GB	Volc., Birimian sedim. deposition		D1: <i>NNE-</i> met. fab., SZ, iso. folds		D2: <i>NE-</i> folds cren. clv., <i>ENE-</i> dex. SZ		
Feybesse et al., 1990	Boromo-Goren GB	Volc., Birimian sedim.	D1: met. fabric, isoclinal folds	D2: <i>N-S</i> & <i>NW-</i> sin. SZ, drag		D3: <i>NE</i> to <i>ENE-</i> dex. SZ, folds		
Hein, 2010	Goren GB	Volc., Birimian sedim. deposition	D1: <i>NW</i> to <i>NNW-</i> folds, thrust faults (Tangean)	D2: <i>NNE</i> to <i>NE-</i> sin. SZ, folds, met. fabric, clv., <i>NW-</i> dex. SZ (Eburnean)		D3: <i>WNW-</i> dex. thrusts, <i>E-W</i> folds (Wabo-	mafic dykes (250 Ma)	
Kfibeke et al., 2008	Kaya-Goren GB	Volc., Birimian sedim. deposition	D1: Crustal accretion, thickening			D2: Exhumation and strike-slip movements		
Nikiéma et al., 1993	Djibo region	Volc., Birimian sedim.	D1: <i>N-S</i> cleavage			D2: <i>NNW-</i> SZ	D3: <i>NE-</i> vergent thrusting	
Debat et al., 2003	Djibo region	Volc., Birimian sedim.		D1: Regional greenschist facies metamorphism, MT/MP contact metam.		D2: <i>N-</i> vergent thrusting		
Bourges et al., 1998	Bouroum-Yalago GB	Volc., Birimian sedim.				D1: <i>N-S</i> to <i>NW-</i> met. fab. and SZ	D2: <i>E-W</i> cren. clv.	
Tshibubudze et al., 2009	Essakane region	Volc., Birimian sedim. deposition	D1: <i>NW-</i> fold-thrust belt			D2: <i>NNE-</i> to <i>NE-</i> met. fabric, SZ, and folds		
Lüdtke et al., 1998; 1999	Téhini & Ouango-Fitini GB	D0: volc., Birimian sedim. deposition	D1: Juxtapos. of L & H grade metam., <i>NNE-</i> steep SZ	D2: <i>NE-</i> folds, <i>NNE</i> sin. SZ, met. fab.		D3: <i>NE-</i> , <i>SE-</i> & <i>E-</i> SZ, cren. clv.	D4: React. of existing struct., <i>NE-</i> dolerite dykes	
Poucllet et al., 1996	Téhini & Ouango-Fitini GB	Stacking of plume derived oceanic basalts		D1: Granitoid emplacement, contact metam.	D3: <i>N-S</i> sin. fault, with CA volc. and Birm.	D4: <i>NW-SE</i> comp., transcurrent		
Vidal et al., 1996	Téhini & Ouango-Fitini GB, Comomé	Ante-Birimian (Dabakalian) deposition	D1: metam. fabric, gently dipping clv. (Dabakalian)	Birimian deposition; D2: <i>NE-</i> folds	Depo detrital sedim. (Tkw)	D3: <i>N-S</i> sin. and <i>WNW-</i> SZ, transpression	D4: <i>WNW-</i> cren. clv., <i>S</i> vergent thrusting	
Poucllet et al., 2006	Katiola - Marabadiassa GB	Ocean crust and volc. arcs		D1: Crust accretion by docking of granitized blocks	D2: Formation of intracontinental basins	D3: <i>N-S</i> sin. SZ, basin closure, transpression		
de Kock et al., 2011	Bole-Nangodi GB	Birimian deposition	D1: metam. fabric, folds; Eoeburnean event	Continental rifting; D2: metam. fabric,		D3: <i>NE-</i> SZ, transpression		
Castaing et al., 2003	Burkina Faso (regional)	Arc volc., Birimian sedim. deposition		D1: Tonalite / adakite intrusions		D2: Tectonic accretion, folding, regional metam.,	Dolerite dykes	
Vidal et al., 2009	Ivory Coast (regional)	Birimian deposition		D1: Dome and basin geometries, no boundary tectonic forces		D2: Coeval diapiric movements and horizontal		
Feybesse et al., 2006	Ghana (regional)	Volcano-plutonism, deposition of Birim. flysh		D1: Crustal thickening by nappe stacking, shearing to the		D2-3: <i>NE-</i> sin. SZ, <i>WNW</i> shortening brittle shearing, steep		
Agyei Duodu et al., 2010	Ghana (regional)	Volcano-plutonism, deposition of			D1: Ext., depo of Tkw. sediments, alkalic plutonism	D2: Folding, regional metam., crustal shortening		
Milési et al., 1989	Leo-Man craton (regional)	Birimian flysh sedim. depo., followed by	D1: Nappe tect., <i>ENE-</i> suture between Archean			D2: <i>NE-</i> folds, <i>N</i> to <i>NE-</i> SZ (Birimian cycle),		
Lompo, 2009, 2010	Leo-Man craton (regional)	E1: Plume related tholeiitic volcanism	E1: Subsidence, granitoid emplacement	E1: Evolution of subsidence, CA volc. & plut., Amp-bearing granitoid emplacement, vertical tectonics		E1: Transcurrent tectonics, Bt-granites		

**Table II-2** Synthesis of deformation events published in literature, put into the framework of the present study. Direction indications in italics (*NE-*, *NW-* etc.) stand for the strike, other direction indications signify "vergent" or "oriented". Following acronyms and shortcuts were used: GB - greenstone belt, SZ - shear zone or strike slip fault, Tkw - Tarkwaian, depo. - deposition, defo. - deformation, Birim. sedim. - Birimian sediments, volc. - volcanism, plut. - plutonism, met. or metam. fab. - metamorphic fabric, cren. clv. - crenulation cleavage, iso. - isoclinal, intracont. - intracontinental, comp. - compression, ext. - extension, transpres. - transpression, transten. - transtension, sin. - sinistral, dex. - dextral, react. - reactivation, struct. - structures, juxtapos. of L & H grade metam. - juxtaposition of low and high grade metamorphic terranes.

## 6. Deep Structure

### 6.1. Construction of the models from gravity data

Three geological cross-sections of the Houndé and Boromo belts were created and validated by 2 $\frac{3}{4}$  D gravity models (figure II-12). We have not performed gravity modeling across the Banfora belt, as our outcrop observations are too scarce to provide useful geological constraints. Gravity-constrained crustal models have proved to be an efficient way to determine the architecture of large-scale deep structures in Precambrian terrains (Hackney, 2004; Peschler et al., 2006). In addition to the field structural observations and interpretations of airborne magnetic data, the gravity models allow us to test the extent and apparent dip of dense (mafic volcanics) vs. less dense (granitoids) at



**Figure II-11** Densities of the lithologies used in the 2 $\frac{3}{4}$  D gravity modeling. Bas – basalt, gbr – gabbro, and – andesite, pyr – pyroclastic flow, vs – volcano-sediments and Birimian sediments, Tkw – Tarkwaian-type sediments, grd – granodiorite, gra – granite.

depth. The gravity data used in the modeling procedure were acquired by ORSTOM in 1958 (Albouy, 1992) along major roads at a maximum spacing of 4000 m between consecutive points (figure II-8).

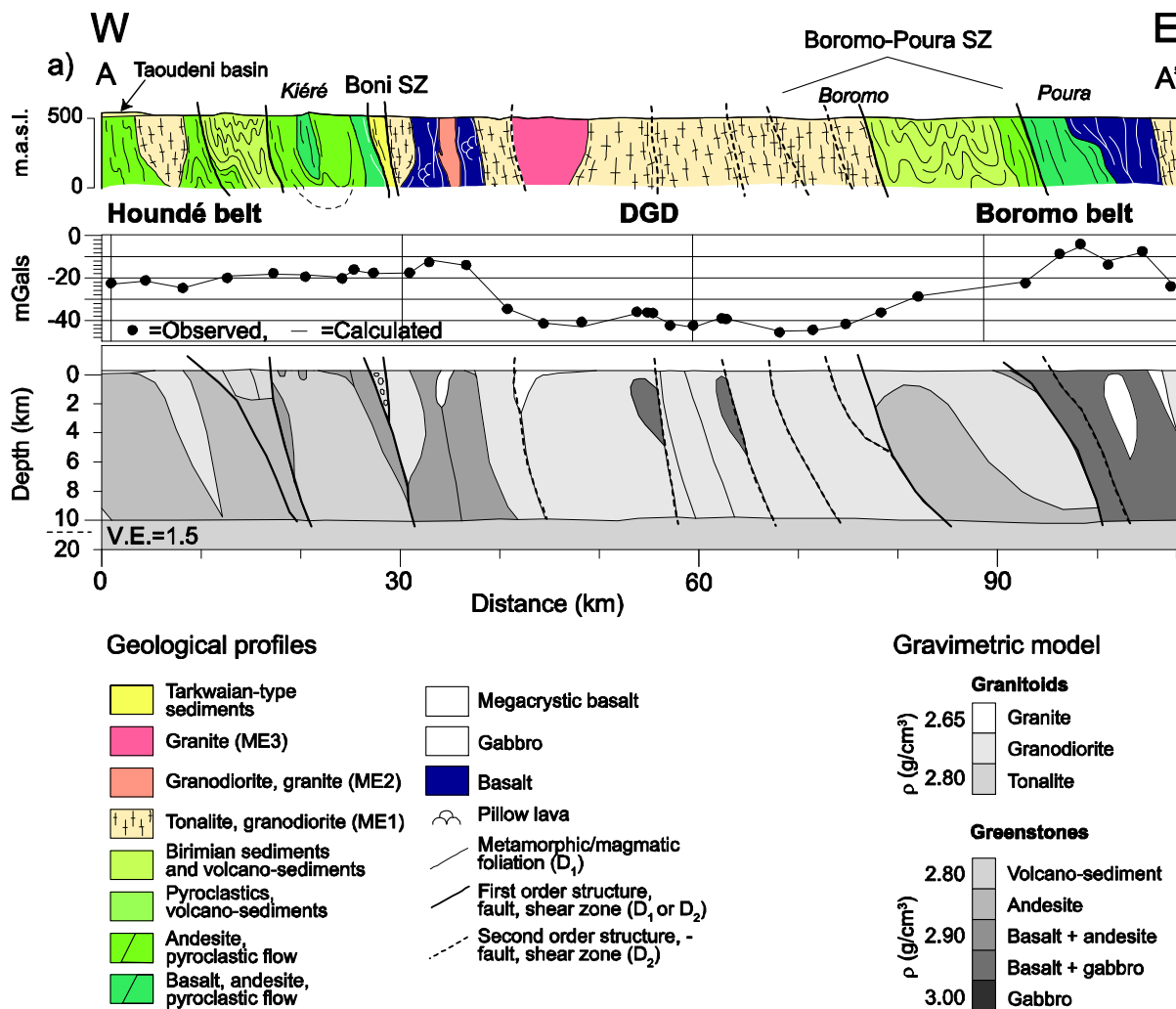
Bouguer corrected data were used (2.67 g/cm<sup>3</sup> as reduction density) as input into the GM-SYS modeling software (Popowski et al., 2009). Altitudes of the points along the modeled profiles were extracted from the gravimetric stations. The gravimetric data were projected onto the modeled straight-line geological profiles. The modeling procedure allows for variable density parameters perpendicular to the profile, for up to 10 km on each side. It also accounts for the variable distances between the positions of the gravimetric stations situated along roads with respect to the straight profile lines (figure II-8). The model (figure II-12) was constrained using the densities measured in



Toulouse on representative rock samples (figure II-11), and similar densities have been reported for granite-greenstone terrains in Senegal (Blot, 1980) and Ghana (Attoh, 1982). We have used the same groups of lithologies as in the revised geological map (chapter I), taking into account the lithological variability and intercalations such as basalts with andesites, or andesites with volcano-sediments, considered as separate units. The three profiles were drawn to a depth of 20 km. The models were constructed so that the solutions appear geologically realistic with an acceptable fit for the modeled gravity. We performed several tests varying the geometry at depth and concluded that the geology below 10 km was poorly constrained by surface geology and gravity data. Therefore, our model includes 10 km of rocks corresponding to the lithologies observed at the surface and an unknown basement of  $2.8 \text{ g/cm}^3$  density below 10 km depth. Where necessary, bodies with low or high densities were placed at depth with respect to possible extension of outcropping geology perpendicularly to the strike of the profile. The forward modeling procedure firstly consists of creating simple polygons of the surface geology, for which different dip angles are tested. After determination of the dip angles, the geometry of the bodies is refined to shapes that are more complex. The points defining the lithological contacts are then adjusted in an iterative manner in order to achieve best fit with the measured gravity. A final adjustment was achieved by applying a constrained inversion, where only selected nodes of certain bodies were free to move.

## **6.2. Results**

Based on the gravity modeling supported by field observations, we have made the following conclusions. Volcanic rocks ( $\rho=2.85 \text{ g/cm}^3$ ) and not granitoids underlay the Taoudeni basin (figure II-12a) in the north, while intermediate to mafic rocks of the Houndé belt ( $\rho=2.85 \text{ g/cm}^3$ ) extend westwards underneath the granitoids in the central section (figure II-12b). Folds can be defined in basalto-andesitic units of the Houndé belt. Volcano-sediments of the central and southern Houndé belt (figures II-12b, c) and northern Boromo belt (figure II-12a) are underlain by a more extensive andesitic layer ( $\rho=2.85 \text{ g/cm}^3$ ). Mafic rocks of the eastern margins of the Houndé (figure II-12b) and Boromo (figure 12a) belts are intruded by younger granitic intrusions ( $\rho=2.67 \text{ g/cm}^3$ ) at depth, emplaced probably along the Boni shear zone in the case of the Houndé belt.



**Figure II-12** Three geological cross-sections with their corresponding gravity models. The geographic location of the profiles as well as the stations of gravity measurements, which were projected onto the geological profiles for the modeling purposes, is indicated in figure II- 8.

Frequent granitic dykes and smaller granitic bodies corroborating this result may be found at the surface near the modeled profiles. Some of these granites are affected by later deformation, which is supported by their tilt to the east inferred from a shift between the gravity low and the outcrop location. The granite intruding the Boromo belt in the east (figure II-12b) is most probably of low density ( $\rho=2.64 \text{ g/cm}^3$ ), therefore rich in alkali feldspar. A high-density unit ( $\rho=2.95 \text{ g/cm}^3$ ) occurring at depth was modeled at the eastern margin of the Houndé belt (figure II-12c) and in the middle of the Diébougou granitoid domain (figure II-12a). These units most probably represent the prolongation of the basalts and gabbros occurring to the north and south. A significant accumulation of dense material ( $\rho=2.95 \text{ g/cm}^3$ ) is needed to explain the gravity highs in the southwest of the Boromo belt in the Gaoua region (figure 12c). The model shows a double thickness of mafic rocks compared to the other profiles, which suggests that the unit of tholeiitic basalts was either originally thicker, or tectonically duplicated.

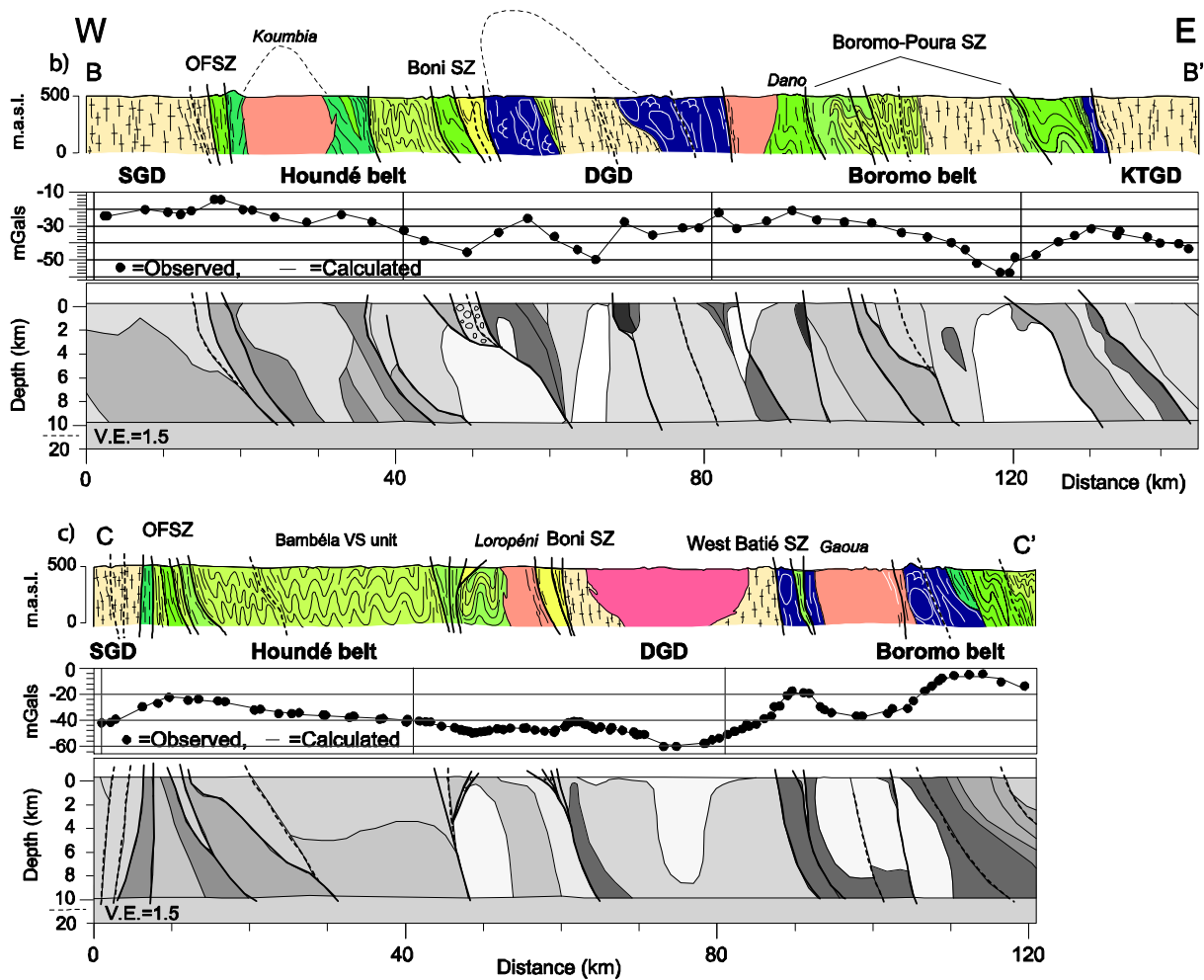
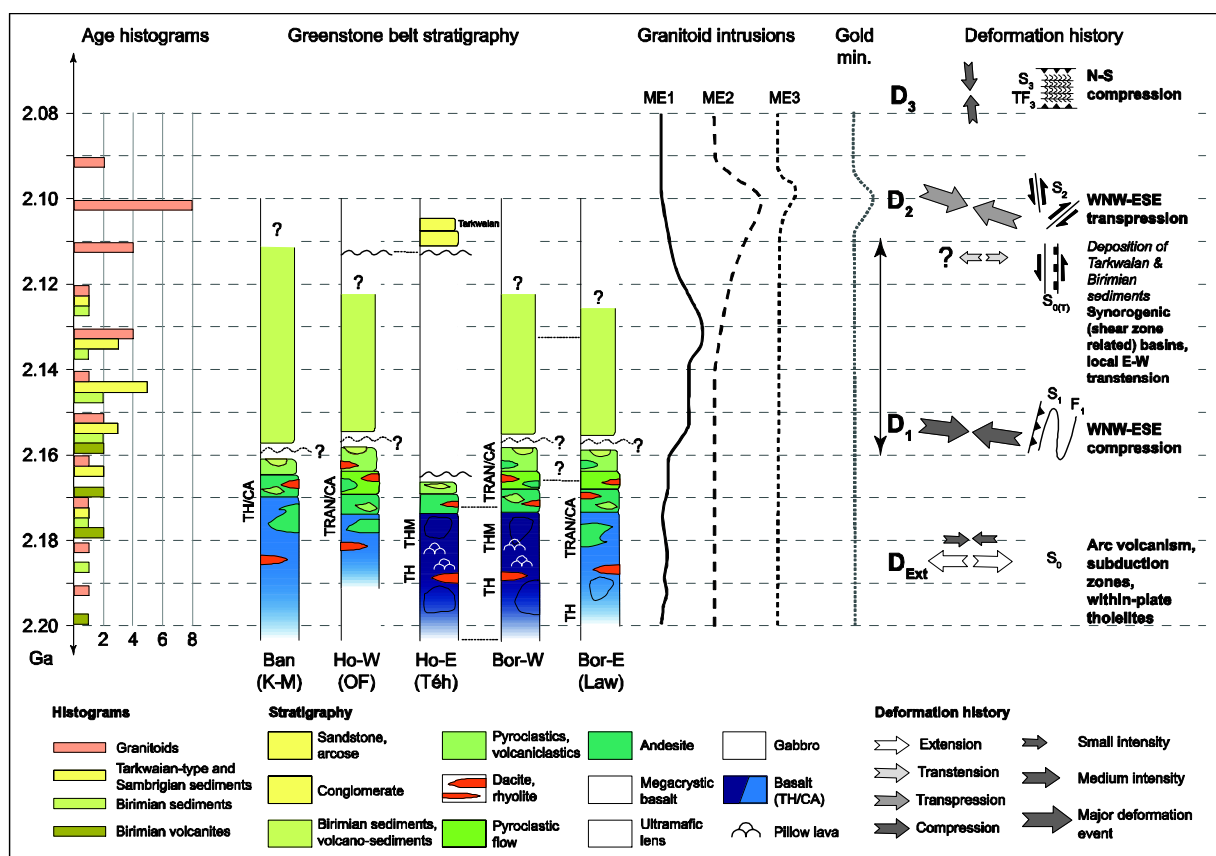


Figure II-12 continued.

All three profiles reveal that the depth of the greenstone belts is at least 10 km, if the lithologies observed at the surface continue without significant changes in densities to depth. In an attempt to model a shallower limit to the greenstone belts of 5–7 km, we had to introduce a significant amount of dense material ( $\rho > 3.2 \text{ g/cm}^3$ ) underneath the basalts. The systematic dip of the units to the east at an average angle of  $70^\circ$ , supported in particular by the easterly shift of gravity highs with respect to the high-density basalt/gabbro outcrops characterizes all three profiles. We cannot model precisely the extent of the Tarkwaian-type sediments because of the low contrast in density between the meta-sediments and the meta-volcano-sediments and granites. The gravity models show that the major shear zones, which transect the greenstone belts or define their boundaries, are generally steeply dipping to the east. Dip angles and directions of the shear zones that transect units with same density contrast, e.g. shear zones localized entirely within granitoids, cannot be determined. The Ouango-Fitini shear zone, separating the Houndé belt from the Sidéradouougou granitoid domain (figure II-12c), seems to be subvertical in the southernmost profile and steeply dipping to the east in the central profile (figure II-12b).

## 7. Discussion

The applied methodology of integrating field and analytical data, interpretation of airborne geophysical data and  $2\frac{3}{4}$  D gravity data constrained modeling allowed us to bring new insights into the model of the formation of juvenile Paleoproterozoic crust. Magnetic and gravity data proved to be very efficient in delimiting lithological units and new structures of large range of depths and scales while radiometric data represent a powerful tool for regolith mapping, with some use for lithology mapping. Combined with the field observations, the geophysical data provide satisfactorily structural information in areas with very limited outcrop conditions. A summary of the interpreted tectonic evolution is given in figure II-13.



**Figure II-13** Summary table of the tectonic evolution. Ban – Banfora belt, K-M – Katiola-Marabadiassa belt, Ho-W – Houndé belt west of the Boni shear zone, Ho-E – Houndé belt east, OF – Ouango Fitini belt, Téh – Téhini belt, Bor-W – Boromo belt west of the Batié basin, Bor-E – Boromo belt east, Law – Lawra belt. For acronyms, see also figure II- 3. Radiometric ages presented in the histograms are referenced in figure II-2.

### 7.1. Origin of the greenstone belts

The volcanic rock compositions are overall in accordance with those obtained by the BRGM/BUMIGEB (figure II-7; Chèvremont et al., 2003; Koté et al., 2003; Le Métour et al., 2003) and published work (e.g. Sylvester and Attoh, 1992; Ama Salah et al., 1996; Pouclet et al., 1996; Vidal et al., 1996; Béziat et al., 2000). They range in composition from tholeiitic basalts and gabbros,

representing oceanic crust or oceanic plateaus (Abouchami et al., 1990), to calc-alkaline bimodal subduction-related arc volcanism. Volcanic series of the Banfora belt were not analyzed; however, tholeiitic basalts and calc-alkaline suites of the Katiola-Marabadiassa belt (southern continuation of the Banfora belt) strongly resemble in composition to the volcanic series of the Houndé and Boromo belt (Pouclet et al., 2006). Associated Na-rich tonalites, trondhjemites, and granodiorites commonly occur in the present-day volcanic island arcs context (Drummond and Defant 1990; Sengör et al., 1993) and are considered by many authors as one of the indirect indices of the existence of Precambrian subduction zones (Martin, 1994; Martin et al., 2005).

Three hypothetical scenarios are plausible in Western Burkina Faso: 1) each of the present-day greenstone belts corresponds approximately to one volcanic arc (Scenario 1 in figure II-14) or 2) there was only one large island arc reaching at least 400 km in width (Scenario 2 in figure II-14), which was shortened and divided into the present belts during the Eburnean orogeny. 3) there was only one arc, which was dismembered during an early deformation phase, prior to the magmatic accretion and large-scale folding (scenario proposed by Ama Salah et al. (1996) for the region of Liptako in Niger). However, the lateral continuity of major units, within and across the Houndé and Boromo belts, and absence of early faults crosscutting the greenstone belts at high angle do not support such hypothesis.

If we suppose that the tholeiitic and calc-alkaline volcanic and plutonic assemblages are indeed related to subduction zone(s), the current datasets give us no constraints on their orientation(s). The petrographic, structural, and geochemical data support the existence of at least one major domain boundary between the tholeiitic and calc-alkaline crust within the Houndé belt. A major domain boundary, referred to as Ouango-Fitini shear zone, running parallel to the Houndé (Téhini/Ouango-Fitini) belt, was already recognized by previous studies in Ivory Coast (Hirdes et al., 1996; Pouclet et al., 1996). The Baoulé Mossi domain was divided into the younger western subprovince and the older eastern subprovince along this shear zone (Hirdes et al., 1996) based on rhyolite and granite radiometric ages and contrasting geochemical compositions; however, such a subdivision is only partially valid in the western Burkina Faso, where rhyolites dated within the Houndé belt yield the same ages as those from the Boromo belt. The geochemical domain boundary roughly corresponds to the Boni and not the Ouango-Fitini shear zone (figure II-7).

## **7.2. Origin of the sedimentary and volcano-sedimentary units**

The origin and the age of the Batié, Banfora, and Bambéla volcano-sedimentary units is questionable. Detrital zircons from the only sample of wacke dated in the Bambéla volcano-sedimentary unit (Lüdtke et al., 1999) yield ages of ~2180 Ma, ~2150 Ma and ~2126 Ma suggesting that they were deposited posterior to or continued after the major calc-alkaline volcanic phase, in a tectonically controlled basin limited by the Ouango-Fitini shear zone in the west and Boni shear zone in the east. The Batié volcano-sedimentary unit was dated in Ghana (Agyei Duodu et al., 2010) and

was deposited after  $2139 \pm 2$  Ma, posterior to the Birimian volcanism. Bambéla basin, which might be an extension of Banfora volcano-sedimentary units yields the youngest ages -  $2107 \pm 7$  Ma (Doumbia et al., 1998). At least part of these volcano-sedimentary units must have been therefore deposited syntectonically in the foreland basins developed during regional shortening and folding of the greenstone belts or during a tectonic quiescence/extension, which implies an angular discordance between the sedimentary units and volcanic suites of the greenstone belts. Transtensional back-arc basin environment was suggested by Vidal and Alric (1994) for the Haute-Comoé basin sediments in Ivory Coast; however, no direct evidence for such extension has so far been found in western Burkina Faso.

The 400 km long and 1-2 km wide quasi-continuous band of Tarkwaian-type shallow water sediments are seated on a major first-order structure, the Boni shear zone, which operated during the late D1 and D2 deformation phases. The Tarkwaian-type sediments were deposited after a significant deformation of adjacent Birimian volcanics was achieved, which is documented by the angular unconformity of the units visible in the map. They represent a boundary between the two distinct domains of the Houndé belt (tholeiitic and calc-alkaline) suggesting that the sedimentary basin was related to some deep-seated structure that may have followed a pre-existing crustal inhomogeneity. The youngest zircons found in the Tarkwaian-type sediments yield ages of  $2115 \pm 2$  Ma and  $2113 \pm 23$  Ma, giving the maximum deposition age. The sediments show a shallow water depositional environment with short transport distances, corresponding to alluvial fans and braided river systems (Sestini, 1973; Bossière et al., 1996). In the Yilgarn (Krapez, 1989; Eriksson et al., 1994) and Abitibi cratons (Mueller et al., 1991) these intracontinental basins are attributed to transcurrent fault related pull-apart basins, however the typical length/width ratio for pull-apart basins is about 3 (Gürbüz, 2010), which is not the case of the Tarkwaian-type sediments in western Burkina Faso. As for the Birimian sediments, no direct evidence for any extensional phase was found in the study area.

Ledru et al. (1994) and Feybesse et al. (2006), propose a synorogenic foreland basin, which operated synchronously with the regional shortening. Present-day large-scale synorogenic basins operating under bulk compression were documented in the northern and central Tibet (Liu-Zeng et al., 2008) or Altiplano-Puna plateau (Vandervoort et al., 1995). Internal drainage within mountain plateau morphology disconnected from adjacent low-lying forelands accounts for smoothing of the relief and for sediment deposition in the plateau interior. Given the similar maximum deposition ages of the Tarkwaian-type sediments and part of the Birimian sedimentary units and their tectonic position with respect to the deformed granite-greenstone terrains, it is plausible that these sediments were deposited approximately at the same time span within large intramontaneous basins, where coarser grained Tarkwaian-type sediments were adjacent to an active fault (Boni shear zone) while the Birimian sediments represent distal facies.

### 7.3. Tectonic scenario and mineralization events

An early Eburnean deformation phase characterized by NW-trending steeply-dipping structures was defined and named Tangaeen Event by Tshibubudze et al. (2009) and Hein (2010) in the Essakane and the Gorom areas (figure II-1) and might also correspond to the early deformation stages of Ouedraogo and Prost (1986) and McCuaig (2007) in northern Burkina Faso. Except for some small-scale structures, all foliations and high strain zones in western Burkina Faso have consistent N-S to NE-SW strikes in the three studied greenstone belts (figures II-8, II-9). This means that the early deformation phase was either completely overprinted by later deformation or it has not operated at all in the study area.

The tectono-stratigraphic framework described in sections 3 and 5 starts with an E-W shortening of immature volcanic arc(s) (proto-Boromo, Houndé, and Banfora belts) contiguous to the pre-existing oceanic plates (tholeiitic basalts). Abundant syntectonic TTG and granite intrusions were coevally emplaced during this E-W compressional phase (D1), which lasted from ca 2160 to 2120 Ma. Penetrative NNE to NE-trending metamorphic foliation S1 in the greenstone belt lithologies has remarkably consistent orientation with the high temperature steeply dipping magmatic banding in granitoids of the ME1 group, suggesting the contemporaneous deformation and pluton emplacement. The compositional banding, typical for many Archean and Paleoproterozoic plutons and observed also within several ME1 bodies, was shown to develop already at magmatic stages operating under the compressional/transpressional deformation regime (Pupier et al., 2008), which corroborates the syn-kinematic emplacement mechanism of the ME1 granitoids. Steep lineations in volcanic rocks, and particularly in the foliated ME1 granitoids, support the vertical growth of individual diapirs. Magnetic data show that regional scale shear zones frequently separate the granitoid domains from the greenstone belts. Outcrops of the granitoid-greenstone contacts are scarce in the study area and they only rarely show the unequivocal D1 deformation structures. However, in Ivory Coast, normal sense of movement of the greenstones with respect to the granitoids was documented at several places (Vidal et al., 2009), leading the authors to propose gravity driven sinking of greenstone belts as a major orogen-forming mechanism. Such normal sense indicators are compatible with granitoid pluton uprising with respect to the adjacent lithology, which is not necessarily sinking, in an overall compressional regime.

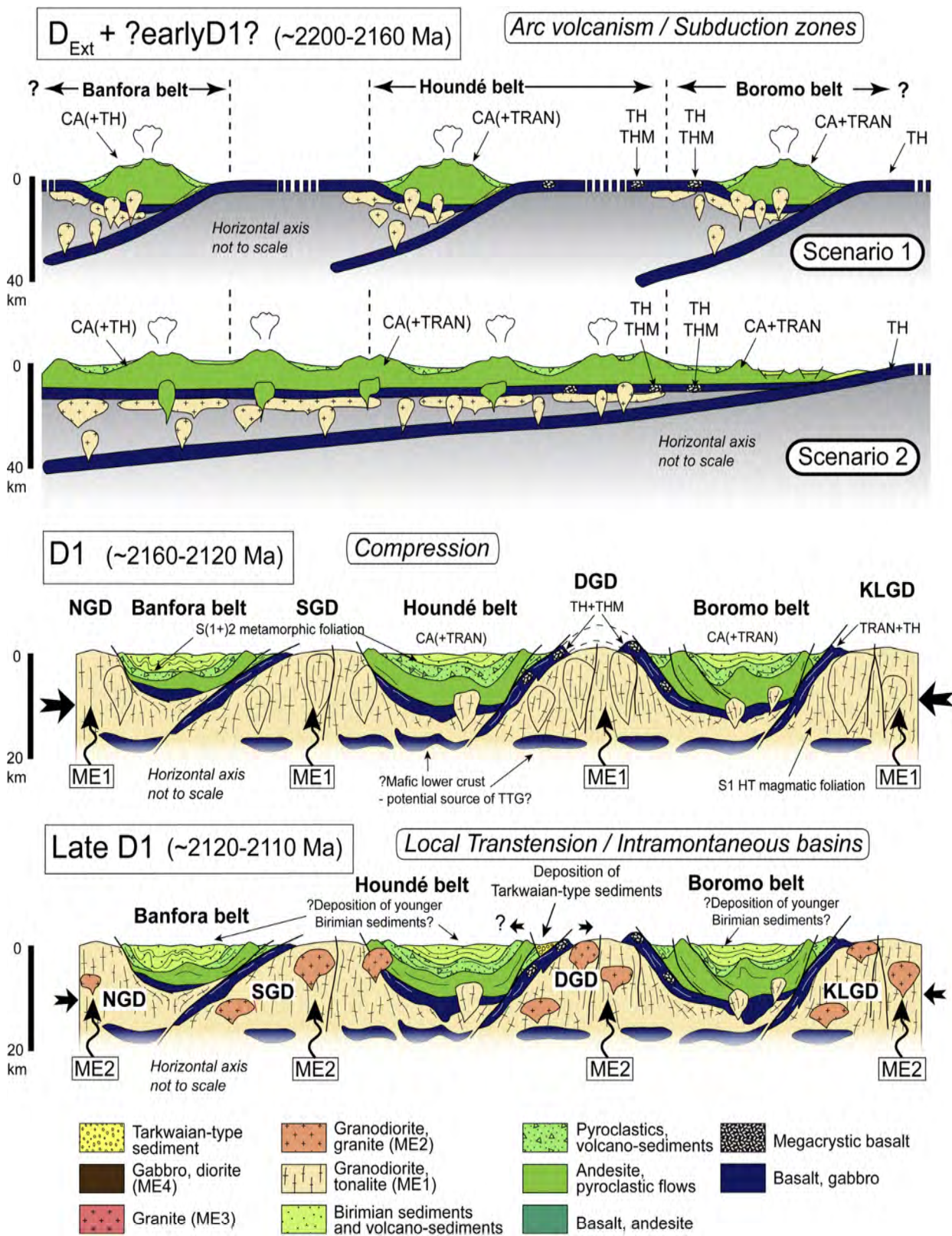
The dominant structural grain represented by three elongate greenstone belts was most probably achieved by the time of the onset of the D2 deformation phase. In contrast to the D1 structures, which are compatible with pure-shear dominated transpression the D2 deformation is characterized by a switch to the strike-slip dominated E-W to WNW-oriented transpressional regime. At a regional scale, the deformation was homogeneously distributed throughout the area while at local scales, the deformation concentrated in narrow shear zones or high strain zones with no measurable offset due to the lack of marker horizons. Moreover, the S2 shear zones are often localized along pre-

existing inhomogeneities such as lithological contacts or faults. Structures may be attributed to the D1 and D2 erroneously at the outcrops lacking a clear crosscutting relationship as S1 and S2 look similar and have a comparable orientation in massive lithologies such as basalts or gabbros in particular. Several new D2 structures of regional importance were discovered by integrated fieldwork and interpretation of geophysical data (chapter I). An anastomosing interconnected network of N-S to NNE-SSW trending S2 shear zones with variable sense of movement affects the entire Boromo and Houndé belts with the Poura-Boromo, Boni, and Ouango-Fitini shear zones being the most important ones. A dextral movement sense was also observed at several places along the Greenville-Ferkessedougou-Bobo Dioulasso shear zone (figures II-8 and II-10). Ongoing westward vergence of compressional deformation would possibly explain the systematic dip of all units to the east shown by the gravity model as well as overturning of the central Diébougou antiform.

The D2 deformation was accompanied by a significant input of mostly biotite and sometimes amphibole bearing K-rich granites and granodiorites, dated between 2113 Ma and 2097 Ma, showing various degrees of tectonic overprint mostly expressed as mylonitic zones or S-C fabrics.

Three major types of mineralization can be distinguished in western Burkina Faso: 1) Zn-Ag Perkoa deposit, classified as a volcanic massive sulfide deposit (Schwartz and Melcher, 2003). In the proposed tectonic scenario, it would be related to the early volcanic island arc setting. 2) Cu-Au Gaoua deposit, interpreted as a porphyry-copper deposit (Sillitoe, R., unpublished reports of Volta Resources Inc.; <http://www.voltaresources.com>). Unpublished radiometric ages and geochemical composition of the host diorite suggest that this mineralization is also related to the early stage volcanic island arc setting. 3) Au deposits, most often related to the transcurrent S2 shear zones and faults (unpublished reports of Orezone Gold Corp., SEMAFO Inc., Volta Resources Inc., Avion Gold Corp., and other companies). Gold is either disseminated or concentrated in quartz veins (Béziat et al., 2008). However, without precise radiometric ages, we cannot place more precisely the mineralization events within the tectonic scenario.





**Figure II-14** Tectonic scenario for western Burkina Faso during the Eburnean orogenesis. The surface corresponds to the present-day erosional level.

The last deformation phase (D3) is probably an equivalent to the D3 Wabo-Tampelse Shear Zone of Hein (2010). In contrast to her observations, our D3 structures are not concentrated into one shear zone but occur all across the studied region. Debat et al. (2003) suggested that south dipping thrust faults found in the northern and central Burkina Faso, first reported by Nikiéma et al. (1993), might be even of Pan-African age. Similar subvertical crenulation cleavage is described as late-Eburnean deformation phase by Allibone et al. (2002) in Ghana.

#### **7.4. Geodynamic implications**

Mechanisms of the juvenile crustal growth emphasizing volcanic arc collision were proposed by Ama Salah et al. (1996) in Niger, by Choukroune et al. (1997) in Superior Province in Canada, by Pouclet et al. (2006) in Ivory Coast, and by Goscombe et al. (2009) in Yilgarn Craton in Australia. Finding direct evidence for nappe stacking as being the dominant crustal thickening mechanism at the early stages (Ledru et al., 1991; Feybesse et al., 2006) is problematic, as no inverse metamorphic gradient is observed in the field. The omnipresent greenschist facies conditions with local increase of temperatures towards the granitoids are rather compatible with isoclinal cylindrical folding and the present surface would thus represent a subhorizontal section through the former upper crust. Folding of volcanic units would occur in conjunction with continuous TTG magma input, which could have a source in the subducting slabs (Martin, 1986, Hastie et al., 2010) but also in the progressively thickened lower mafic crust (Foley, 2008; Chardon et al., 2009). Such a mechanism would lead to the initial homogeneously distributed crustal thickening up to a critical thickness sustainable by the hot and weak lithospheric mantle. At mature stages, the orogen may have deformed by the mechanism proposed by Choukroune et al. (1995), Cagnard et al. (2006b), Chardon et al. (2009), and Gapais et al. (2009), characterized by combined distributed thickening and orogen parallel flow in a transpressional regime.

Most of the granitoids dated in West Africa post-date the juvenile volcanic rocks of greenstone belts (Hirdes et al., 1996; Doumbia et al., 1998; Oberthuer et al., 1998; Castaing et al., 2003), only some of them are contemporaneous with the volcanism (Davis in Schwartz and Melcher, 2003; Siegfried et al., 2009) and the presence of older Archean basement under Birimian units has been negated by several studies (Abouchami et al., 1990, Sylvester et Attoh, 1992; Doumbia et al., 1998). Only thin lower crust existed during the initial stages of island arc formation and it was progressively thickened during the ongoing arc volcanism and D1 deformation phase. The mechanism of crustal scale folding with simultaneous extrusion of lower crustal gneisses (Benn and Peschler, 2005; Peschler et al., 2006) proposed for the greenstone belts in the Abitibi Craton is therefore difficult to argue for in western Burkina Faso, also due to the scarcity of geochronological data. Such a mechanism might have operated to some extent in the study area if sufficient volume of subduction-related TTGs underplated the volcanic arcs since the early orogenic stages (figure II-14).

In the Ivory Coast, Vidal et al. (2009) proposed gravity driven sinking of heavy mafic greenstone belts into lighter uprising granitoids in a “dome and basin” geometry, with cleavage trajectories concentric around the plutons. However, the deformation patterns observed in western Burkina Faso do not show the same characteristics. Granitoid intrusions are concentrated in elongate domains enclosed by the greenstone belts, reaching quite a high length-width ratio (up to 400 km/10-60 km). If the granitoids were responsible for the sinking of the Boromo, Houndé, and Banfora 400 km long greenstone belts, we would imagine a massive amount of magma arriving simultaneously along the three belts, which is inconsistent with the number of 30-50 km plutons of various shape, size, age and chemical composition observed in the field and in the geophysical data. Moreover, contact metamorphism is generally restricted to relatively narrow zones around granitoids, which is also compatible with small size plutons rather than a "magma ocean", which would produce a significant regional metamorphic overprint.

New and existing petrographic and geochemical data show that the western margin of the Boromo belt and eastern margin of the Houndé belt were part of the same oceanic crust. Our mapping has shown that mafic unit extends over 400 km from the north to the south and represented a cold rigid unit of considerable original thickness (up to 7 km, as shown by the gravity data). This unit most probably controlled the architecture of the early Eburnean orogen. The structural setting corroborates that this basal mafic unit form the limbs of the N-S trending crustal scale antiform.

Published radiometric ages document syn-volcanic-arc magmatism, which fed juvenile granitoid material into the system since the early orogenic stages. The tonalite-trondhjemite-granodiorite magmas, generated by melting of the subducting slabs and/or by remelting of lower crust, may have cumulated at the base of the crust or intruded the volcanic islands. When the E-W compression (D1) initiated, the rigid mafic units deformed by early flexural bending. The granitoid plutons were progressively emplaced into the growing antiforms.

The transition from an oceanic crust overlain by volcanic islands (5-7 km thickness) to a mature continental crust (~30 km thickness) was thus achieved through an interplay of long-wavelength low-amplitude buckling of rigid mafic units in conjunction with voluminous magma input and diapirism in a volcanic arc setting. The emplacement of granitoids was structurally controlled and focused into the antiformal domains, which deform the pre-existing greenstone belt geometry. The granitoids played an important role at all stages of crustal growth, in particular through early massive volume addition and later accommodation of part of the lateral shortening. The regular distribution of greenstone belts and elongate granitoid domains, the overall structural framework, as well as the absence of “dome and basin” geometries in western Burkina Faso suggest that gravity instabilities, evoked by many authors in Precambrian terrains (e.g. Leube et al., 1990; Pons et al., 1995; Collins et al., 1998; Chardon et al., 2002; Vidal et al., 2009) were not the dominant driving force during the growth of this part of the Eburnean orogen. However, some structures (e.g., antiform related to the Gaoua batholith emplacement) could be interpreted as gravity-driven processes related to granitoid

diapirism operating at local (pluton) scales. As with other Precambrian orogens, the early fabrics were modified by the regional-scale transcurrent shear zones (S2), which acted as pathways during the gold mineralization events.

## 8. Conclusions

Three greenstone belts and associated granitoid domains of Paleoproterozoic age have been studied in western Burkina Faso. Four deformation events were identified in a polyphase orogenic cycle. Two of the events play a key role for the crustal accretion during the Eburnean orogeny. The principal conclusions drawn from this study are:

1) The geochemical signature of the volcanic rocks is compatible with the evolution from tholeiitic oceanic crust or oceanic plateau to juvenile volcanic island arcs, which formed between ~2200 Ma and 2160 Ma. Zinc (volcanic massive sulphides) and copper (porphyry Cu) deposits are related to this volcanic arc stage.

2) Lateral compression led to the E-W shortening of volcanic arcs during the D1 deformation events, accompanied by syntectonic emplacement of voluminous TTG and granitoid plutons, derived either from the subducting slabs or from the mafic lower crust.

3) The basal tholeiitic unit represents a crustal scale antiform between the Boromo and Houndé belts, which served as a structural conduit for the TTG and granite intrusions during the D1 and D2 deformation phases.

4) Shallow water Tarkwaian-type sediments were deposited at about 2115 Ma during the late stages of the D1 phase. Their deposition was structurally controlled by faults, which were later reactivated as the Boni shear zone.

5) When the orogen reached a critical thickness and the weak and hot mantle was not able to support further thickening, the deformation mechanism switched from pure shear dominated E-W to WNW-oriented compression, to simple shear dominated transpression of the same orientation. The second stage is characterized by an interconnected network of steeply dipping regional-scale transcurrent high strain zones, often bearing gold mineralization. The D2 event was accompanied by numerous granitoid intrusions and took place between ~2115 and 2097 Ma.

6) Pluton emplacement contributed to the structural evolution of the greenstone belt at local scales; however, the regional scale system geometry was controlled by coaxial shortening of the stronger volcanic units (basalts, gabbros, and andesites) of the greenstone belts, supported by coeval magma input.

7) The late-Eburnean or Pan-African N-S compression D3 is responsible for E-W trending crenulation cleavage, kink folds and shallow north or south dipping thrust faults, which were recorded across the study area.

## **Acknowledgments**

The project was funded by IRD (Institute de recherche pour le développement) post-doctoral research grant to L.B. and aided logistically by the project “West African Exploration Initiative” (<http://waxi2.org>). Discussions with D. Thiéblemont, D. Béziat, E. Kaboré, F.M. Ouedraogo, S. Zonou, J. David, G. Tourigny, and W. Claessens at various stages of the project significantly contributed to our understanding of West African geology. We are indebted to the mining companies SEMAFO, Volta Resources, Wega Mining, Sanu Resources, and Orezone for providing us high-resolution geophysical data, borehole cores and outcrop maps. We acknowledge in particular M. Crevier, D. Bondé, D. Boisvert, L. Ouedraogo, P. Marquis, A. Zongo, O. Derra, C. Diallo, T. Amoah, and A. Naré for providing us support when conducting fieldwork on the permits of their companies. Special thanks for the logistical support belong to the IRD center in Ouagadougou, and in particular to the drivers Salifou, Boukary, and Mathieu. We acknowledge J.L. Bouchez, D. Chardon, P. Debat, and C.T. McCuaig for reading early drafts of the manuscript and for the comments that led to significant improvements. Careful reviews by E. de Kemp and an anonymous reviewer helped us to improve the original manuscript.

---

## **CHAPTER III**

# **VISIBLE AND INFRARED SPECTRAL LIBRARY OF PRECAMBRIAN GRANITE-GREENSTONE TERRAINS IN BURKINA FASO, WEST AFRICA**

---

---

**Résumé du chapitre III****Une bibliothèque spectrale visible et infrarouge des terrains précambriens à granitoïdes – ceintures des roches vertes, Burkina Faso, l’Afrique de l’Ouest****1. Introduction**

Les mesures spectroscopiques infrarouges in-situ représentent une importante composante de n’importe quelle analyse de télédétection multispectrale ou hyperspectrale, puisqu’elles fournissent les données nécessaires à la calibration et les paramètres d’entrée pour la modélisation (Milton et al., 2009 ; Hueni et al., 2009). Les projets récents (Christensen et al., 2000 ; Clark et al., 2007 ; Becvar et al., 2008 ; Baldrige et al., 2009 ; Hueni et al., 2009) ont démontré le besoin croissant des bibliothèques spectrales. La majorité des données est spécifique pour le site donné et ne peut pas être transposée à un site géographiquement éloigné. Les bibliothèques spectrales existantes contiennent souvent des données acquises en laboratoire sur les poudres ou fragments des roches fraîches, ce qui limite la comparaison avec les roches retrouvées dans un contexte naturel souvent complexe et altéré (Cloutis, 1992 ; Rivard et al., 1992 ; Younis et al. ; 1997 ; Rowan et al., 2004). Ce problème a été partiellement comblé par les nouvelles bibliothèques ASTER et Auscope National Virtual Core Library qui contiennent également quelques échantillons de roches (Baldrige et al., 2009 ; <http://nvcl.csiro.au>). Aucune bibliothèque spectrale ne s’adresse aux surfaces altérées et très peu de données existent sur les roches métamorphiques (Baldrige et al., 2009).

Notre étude documente les effets de l’altération superficielle sur les roches magmatiques et métamorphiques du socle paléoprotérozoïque dans l’ouest du Burkina Faso. La bibliothèque contient les mesures spectrales de roches fraîches, de surfaces altérées, de matériaux de régolithe (sols, carapace ferrugineuse) et de la végétation dans les spectres visible et infrarouge (0,3-2,5  $\mu\text{m}$ ). La bibliothèque contient les mesures sur 110 échantillons et représente les premières données librement accessibles pour l’Afrique de l’Ouest (<http://www.geology.cz/extranet-eng/geodata/remote-sensing>). Ces données serviront à une interprétation avancée des données satellitaires mais à une meilleure compréhension du contrôle lithologique sur l’altération superficielle des terrains de granitoïdes – ceintures des roches vertes en milieu semi-aride.

**2. Méthodes**

La campagne de terrain s’est déroulée entre février et mars 2008, ce qui correspond en Afrique de l’ouest à la période sèche. Les conditions climatiques durant l’échantillonnage ont été favorables avec un temps clair, localement perturbé par quelques arrivées nuageuses certains jours. La visibilité a

été estimée entre 10 et 15 km pour des températures qui oscillaient entre 30 et 45°C. La distribution des échantillons récoltés avait pour objectif de couvrir toute les unités géologiques ainsi que leurs produits d'altération. Les échantillons de sol ont été prélevés à proximité des roches sources pour éviter de récolter du matériel transporté. Les spectres ont été acquis à l'aide d'un spectromètre ASD FieldSpec Pro FR de 0,35  $\mu\text{m}$  à 2,5  $\mu\text{m}$  comme les facteurs hémisphériques coniques de réflectance (Schaepman-Strub et al., 2006 ; Milton et al., 2009). Un panel de calibration Labsphere spectralon a été utilisé comme cible de référence.

Chaque spectre acquis est constitué d'une moyenne de 25 mesures individuelles. Chaque échantillon a été analysé trois fois sur différents points de la roche, afin de tenir compte des variations naturelles de surface (géométrie rugueuse ou lisse) et de composition de la roche. L'identification des constituants minéraux présents dans la croûte altérée a été facilitée par la diffraction rayon-X. Un diffractomètre INEL CPS-120 à source de cobalt a été utilisé. Les échantillons ont été traités par grattage d'une couche de 0,5 à 1,0 mm de la surface. Cette couche a ensuite été broyée dans un mortier d'agate pour obtenir une poudre pouvant traverser un tamis d'une maille de 200 ( $\sim 0,074$  mm). Une analyse qualitative des phases a été effectuée, basée sur les positions et hauteurs des pics de diffraction.

Les données spectrales ont été corrigées pour de la dérive qui existe entre le détecteur de VNIR et SWIR1 en utilisant la méthode d'addition. Les spectres corrigés ont été traités de façon additionnelle par un filtre de lissage de type Savitzky-Golay (Savitzky and Golay, 1964) avec une dimension de 65 points de données et un polynôme de degré 4. Les spectres bruts et les spectres lissés sont conjointement enregistrés dans la base de données. Les analyses de spectres comprennent d'une part l'inspection de spectres dépourvus de leur enveloppe spectrale (Clark and Roush, 1984) et d'autre par l'application de la méthode de SFF (spectral feature fitting) pour laquelle les spectres sont comparés avec la bibliothèque spectrale d'USGS (Clark et al., 2007) et de ASTER 2.0 (Baldrige et al., 2009).

### **3. Résultats principaux de l'étude**

La réflectance des roches est proportionnelle à l'augmentation de leur teneur en  $\text{SiO}_2$  et inversement proportionnelle à leur teneur en minéraux mafiques. Les bandes d'absorption caractéristiques des gabbros, basaltes et andésites montrent un comportement assez similaire. Les différences comprennent une augmentation de réflectance dans la région infrarouge moyenne. Les molécules de Fe- et Mg-OH qui composent les chlorites et les amphiboles tendent à absorber l'énergie à proximité de 2,32  $\mu\text{m}$  et de 2,25  $\mu\text{m}$ . Les absorptions proches de 1,0  $\mu\text{m}$  sont associées au Fer ferreux dans les chlorites, amphiboles et pyroxènes. Les surfaces altérées de ces lithologies montrent une réflectance plus élevée et une pente de profil spectral plus inclinée. Les bandes d'absorption typiques peuvent être encore identifiées, mais elles sont plus faibles. La présence d'une bande



d'absorption à proximité de 2,2  $\mu\text{m}$  indique la présence d'argiles. Plusieurs bandes d'absorption au-dessous de 1,0  $\mu\text{m}$  sont reliées à l'hématite et la goethite qui sont présentes dans les couches d'altération.

Les échantillons de tonalite et de granodiorite du groupe des TTG présente des caractéristiques spectrales similaires à celles de gabbros. Une plus grande différence peut être observée dans la réflectance générale entre les différentes mesures. Le groupe du granite montre une absorption Al-OH plus prononcée à 2,2  $\mu\text{m}$ , ce qui est probablement causé par l'altération de surface des échantillons. A la différence du groupe des TTG, le groupe de granites ne montre pas de bandes d'absorption du fer ferreux. Les surfaces altérées de chacun des deux groupes sont caractérisées par les bandes d'absorption du groupe des phyllo-silicates kaolinite/smectite vers 2,2  $\mu\text{m}$  et goethite et hématite au-dessous de 1,0  $\mu\text{m}$ .

Les roches volcano-sédimentaires montrent une bande d'absorption Al-OH à 2,2  $\mu\text{m}$  assez distincte, avec une forme symétrique de muscovite/illite, correspondant à la sericitisation ou à l'altération de la roche, jusqu'à une forme fortement asymétrique avec une deuxième absorption proche de 2,17  $\mu\text{m}$ . D'un point de vue spectral, les surfaces altérées sont très similaires aux surfaces fraîches. Les surfaces fraîches des grès de Taoudeni montrent une bande d'absorption de kaolinite centrée à 2,2  $\mu\text{m}$  avec une absorption supplémentaire à 2,17  $\mu\text{m}$ .

Les colorations rougeâtres à jaunes des grès sont liées à la présence d'hématite et de goethite dans la matrice, ce qui est documenté par les bandes d'absorption du fer ferrique à 0,65  $\mu\text{m}$  et au-dessous de 0,6  $\mu\text{m}$ . Les surfaces altérées montrent une baisse de réflectance, de 0,7 à 1,0  $\mu\text{m}$ , ce qui peut être expliqué par la présence d'une plus forte concentration d'hématite/goethite dans ces croûtes. Tous les spectres de sols montrent une bande d'absorption Al-OH à 2,2  $\mu\text{m}$  très claire, qui est reliée à la présence de minéraux argileux. Les sols, qui se sont développés sur les basaltes, gabbros et andésites, montrent les plus faibles réflectance avec des absorptions de kaolinite/smectite faiblement développées.

La forme générale des signatures spectrales de ces sols est très proche de celle des surfaces altérées des roches ayant produit ces sols. Les absorptions associées à la minéralogie originale ont été en revanche totalement effacées dans la région infrarouge moyenne. Les matériaux riches en fer du régolithe, comprennent les chapeaux de fer et les nodules ferrugineux, qui possèdent une signature spectrale caractéristique avec de fortes absorptions associées à la présence d'hématite et de goethite.

## **4. Conclusion**

Une nouvelle bibliothèque spectrale a été créée. Elle contient plus de 700 échantillons de spectres de roche et de régolithe, en plus des données spectrales complémentaires sur la végétation. Le champ spectral de cette bibliothèque (0,35  $\mu\text{m}$ –2,5  $\mu\text{m}$ ) permet de faire des comparaisons avec les données de télédétection acquises par satellites, comme celles des données Landsat, ASTER ou

Hyperion. Les observations de terrain et les données spectrales acquises montrent l'importance des phénomènes liés à l'altération sur les propriétés spectrales de roches soumises à des conditions climatiques semi-arides. La formation d'encroûtements ferrugineux sur les surfaces altérées est à la fois contrôlée par la composition lithologique, la texture et les empreintes structurales des différents types de roches. La variation des signatures spectrales fait qu'il doit être possible, sur la base d'une analyse des données hyperspectrales, de procéder à une discrimination entre les matériaux échantillonnés. La nouvelle bibliothèque spectrale offre une information de base essentielle pour l'analyse des données de télédétection en Afrique de l'ouest.

---

# VISIBLE AND INFRARED SPECTRAL LIBRARY OF PRECAMBRIAN GRANITE-GREENSTONE TERRAINS IN BURKINA FASO, WEST AFRICA

Václav Metelka <sup>a,b,c</sup>, Lenka Baratoux <sup>a\*</sup>, Séta Naba <sup>d</sup>, Mark W. Jessell <sup>a</sup>

<sup>a</sup> IRD, UR 234, GET, Université Toulouse III, 14 Avenue Edouard Belin, 31400, Toulouse, France

<sup>b</sup> Institute of Geology and Paleontology, Charles University in Prague, Albertov 6, 12843, Prague 2, Czech Republic

<sup>c</sup> Czech Geological Survey, Klárov 3, 11821, Prague 1, Czech Republic

<sup>d</sup> Département de Géologie, Université de Ouagadougou, Burkina Faso

## Abstract

A new spectral library has been acquired in West Africa consisting of in situ and laboratory 0.35  $\mu\text{m}$  to 2.5  $\mu\text{m}$  spectra of rocks from a Paleoproterozoic granite-greenstone terrain in western Burkina Faso along with its Neoproterozoic sedimentary cover and derived regolith materials. The reflectance spectra show the influence of typical arid to semi-arid weathering with the formation of desert varnish, iron films, and dust coatings. Fe and Mg-OH absorption features related to chlorite, amphibole, pyroxene, epidote, and biotite are observable in the mafic and intermediate meta-volcanic rocks as well as in the granodiorites and tonalites. Al-OH absorption caused by kaolinite, smectite, and muscovite are typical for meta-volcano-sedimentary schists, Tarkwaian-type detrital meta-sediments, sandstones of the Taoudeni basin, all of the weathered surfaces and regolith materials. Ferric and ferrous iron absorptions related to both primary rock-forming minerals and secondary weathering minerals (goethite, hematite) were observed in most of the sampled materials. The results show that although weathering alters the spectral signature of the fresh rock, indicative absorption features located in the short wave infrared region remain visible. In addition, spectra of soils partially reflect the mineral composition of the weathered rock surfaces. The analysis of the hyperspectral data shows the potential of differentiating between the sampled surfaces. The library presents a primary database for the geological and regolith analysis of remote sensing data in West Africa.

**Keywords:** Spectral measurements, Geology, Regolith, Precambrian, West Africa

## 1. Introduction

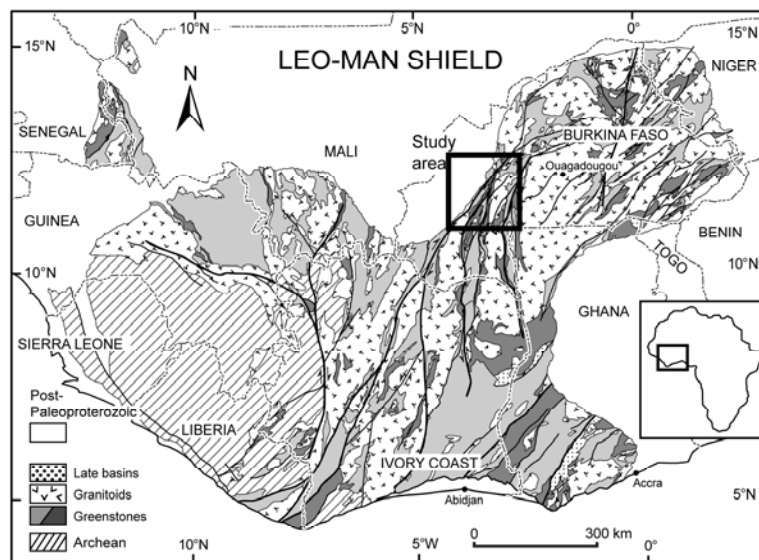
Infrared spectroscopic in situ measurements form an important component of any multispectral or hyperspectral remote sensing analysis regardless of the scientific discipline involved, providing vital data for calibration, ground truth assessment and modeling input parameters (Milton et al., 2009; Hueni et al., 2009). The growing need for spectral data is highlighted by several spectral library projects e.g. ASTER spectral library (Baldrige et al., 2009), ASU Thermal Emission Spectral Library (Christensen et al., 2000), USGS spectral library (Clark et al., 2007), or Specchio (Hueni et al., 2009), DLR spectral archive (Becvar et al., 2008), and the globally distributed soil spectral library ICRAF-ISRIC (2010) that maintain and distribute such data to the scientific community. The acquired data are very often site-specific and cannot be easily transferred from one geographic location to another. Many of these libraries contain laboratory measurements, which have standardized procedures of acquisition and the purity of materials used is well determined; however, such pure materials are difficult to compare with those found in complex natural settings. Moreover, most of the sampled materials are powders or chips of non-altered rocks. Spectral signatures of these materials differ from the weathered exposed surfaces (Cloutis, 1992; Rivard et al., 1992; Younis et al., 1997, Rowan et al., 2004). This limitation has partially been addressed by the new ASTER spectral library 2.0 (Baldrige et al., 2009), which was recently updated and does now contain solid rock samples as well. Another source of information is the Auscope National Virtual Core Library (<http://nvcl.csiro.au>) that provides spectral information on more than 2 km of rock core samples from the Australian continent and will probably grow in the next few years. The spectral coverage of the accessible libraries spans the range between 0.4–15.4  $\mu\text{m}$  as the most widely used sensors such as Landsat and ASTER capture this portion of the electromagnetic spectrum.

Although several remote sensing related studies including spectral in situ measurements have been published for the area of West Africa (Epema and Bom, 1994; Tromp and Steenis, 1996; Tromp and Epema, 1999), none of them focused on the description of spectral properties of the surface materials. Our study presents a spectral library created during the 2008 field campaign of the AMIRA P934 project, the “West African Exploration Initiative”, and documents the effects of rock weathering on the spectral properties of rock surfaces while identifying as well the derived regolith material. The dataset includes spectra of rocks, their weathering crusts, regolith materials (soils, iron rich duricrusts, lags), and vegetation covering the visible through shortwave infrared region 0.3 to 2.5  $\mu\text{m}$ . The unique setting of Paleoproterozoic greenstone belts, where greenschist metamorphism affected most of the lithologies provides the opportunity to obtain novel spectral information. In the current spectral libraries, such as the ASTER spectral library 2.0 (Baldrige et al., 2009), data on greenschist metamorphosed rocks are very sparse and data on regolith materials are absent although applications of imaging spectroscopy to granite greenstone terrains or regolith have already been reported and are not uncommon (Drury and Hunt, 1989; Dehaan and Taylor, 2004, Rowan et al., 2004, Hewson et al.;

2005; Deller, 2006). The presented measurements were acquired in the semi-arid zone of western Burkina Faso. This spectral library of 110 sampled locations represents the first publicly available data for West Africa. The results are relevant both to geological and regolith interpretation of remote sensing data in West Africa as well as for the understanding of lithological controls on weathering of Precambrian granite-greenstone terrains in semi-arid environments. The dataset is available through the web page <http://www.geology.cz/extranet-eng/geodata/remote-sensing>.

## 2. Description of sampling area and sampled materials

All of the gathered samples originate from western Burkina Faso encompassing an area of about 21,000 km<sup>2</sup> (figure III-1). The study area consists of typical West African lateritic landscape (Grandin, 1976; Brown et al., 1994; Bamba et al.; 2002) dominated by a peneplain developed over



**Figure III-1** Simplified geological map of the Leo-Man craton modified after BRGM SIGAfrique (Milési et al., 2004) with the zone of interest outlined; the Paleoproterozoic greenstones are divided into: light grey – intermediate to acid volcano-clastics and volcano-sediments, dark grey – mafic to intermediate lavas and volcanic products.

most of the rock types present. The average height of the studied terrain attains 300 m a.m.s.l. (230-570 m). The climatic conditions are Sahelo-Sudanese with a mean annual rainfall of 900 mm. The land cover type consists primarily of open wood savannah; however, increasing agricultural activity means that more than 50 percent of the total area has been turned to cultivated land (IGN, 2005). Vegetation cover is substantial and changes both from S to N as well as according to the time (dry/rainy season) from nearly total cover (>80% cover) to moderate cover (<40% cover). The field campaign was conducted between February and March of 2008 in the dry period. Weather conditions during the sampling were favorable with clear skies and only few scattered cumulus clouds on some

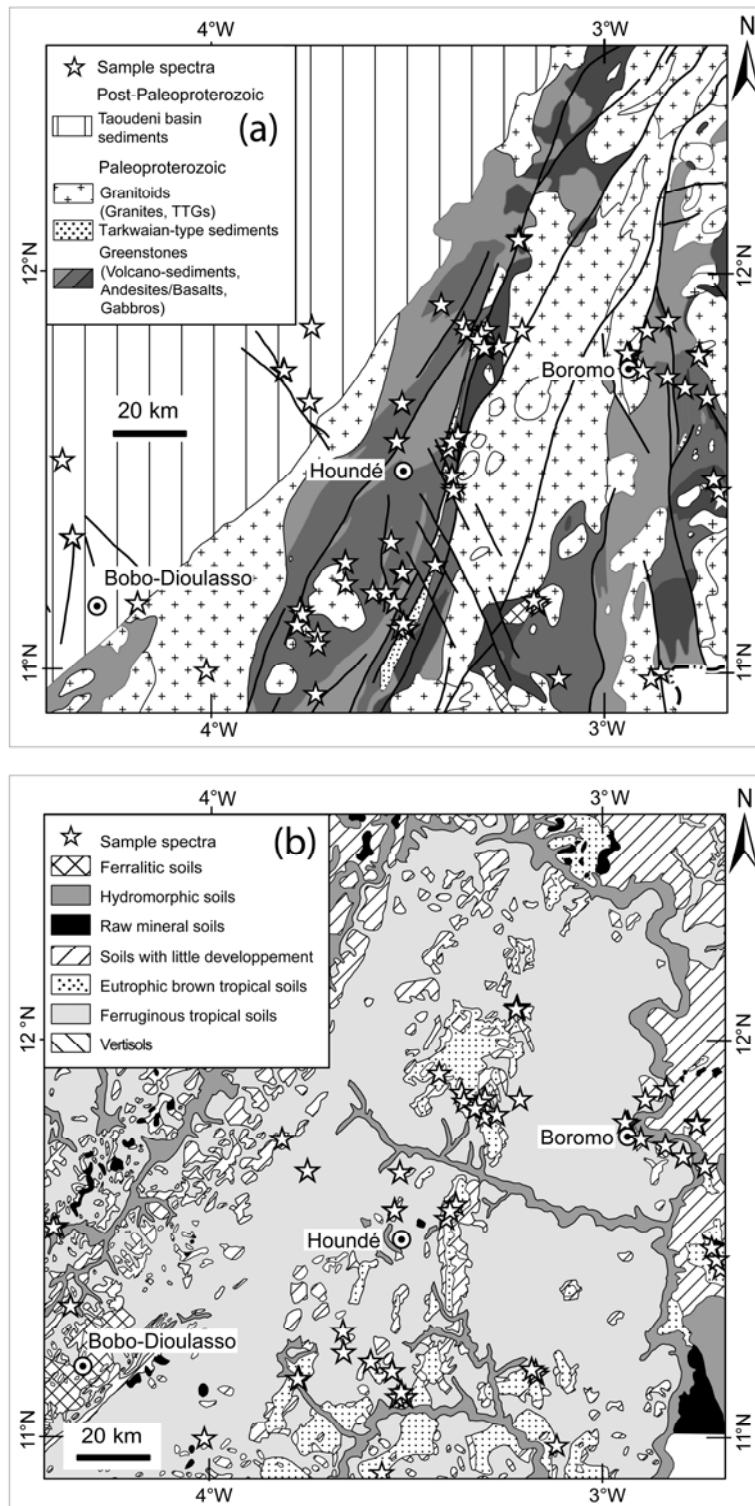
days. Visibility was estimated to be between 10 and 15 km while daytime temperatures oscillated between 30-45°C.

The distribution of samples aimed at covering all of the lithological units and their weathering products. Samples of soils were at all times gathered near the source rock to avoid sampling of transported material except for soils developed over iron-rich duricrusts and soils on agricultural fields. The samples represent mostly poorly developed mineral soils with residual weathered rock material. Samples located on agricultural fields or on planation surfaces developed over granitic terrains may represent soils with deeper weathering profiles as they are sampled further from outcrop and weathering fronts on granite are generally deeper.

The macroscopic description of mineral composition and the type of hydrothermal alteration (if present) is available for all of the samples. Mineral assemblages of selected samples were confirmed by microscopic study and microprobe analyses. Throughout the study region, weathering crusts and desert-like coatings can be observed. Mineral composition of the weathering crusts of selected rock samples was determined by X-ray diffraction. Both dry and green vegetation was sampled, because of the substantial vegetation cover in the area of interest.

### **3. Observed lithological and soil units**

Western Burkina Faso represents a typical granite-greenstone terrain of the Leo-Man Shield (figure III-1) in the West African Craton (Bessoles, 1977) where Paleoproterozoic meta-volcanic and meta-volcano-sedimentary rocks (the prefix meta- will be omitted in the following text) form elongated N-S to NE-SW oriented belts (Houndé belt and Boromo belt) separated by tonalite-trondhjemite-granodiorite (TTG) and late granite intrusions (Castaing et al., 2003; Béziat et al., 2000). All of the lithologies of greenstone belts including Tarkwaian-type sediments (Bossière et al., 1996) were subject to greenschist and locally amphibolite facies metamorphism during the Eburnean orogenesis (~2200-2000 Ma). The sediments of the Neoproterozoic Taoudeni basin unconformably overlay the Paleoproterozoic rocks in the western part of the study area (figure III-2a). The studied rock outcrops include metamorphosed basalts, gabbros, andesites, and andesitic pyroclastic flows, volcano-sedimentary rocks of andesitic to dacitic composition, and detrital sediments of variable grain size, as well as unmetamorphosed TTGs, granites, and sandstones of the Taoudeni basin. Granitoids will be divided into two groups according their petro-chemical composition, to Na-rich low K tonalites and granodiorites and K-rich granites. A summary of the sampled lithological units with petrographic description is given in table II-1. The volcanic and subvolcanic units including gabbros, basalts, andesites, and andesitic pyroclastic flows show similar exposures in the field. They usually form massive non-foliated rock outcrops with only localized high strain zones. Together with some of the volcano-sedimentary rocks, they build up erosional ridges, which are occasionally capped by iron rich duricrusts.



**Figure III-2** Lithological (a) and pedological (b) map of the study area. White stars represent spectral measurement locations. The maps are compiled from Castaing *et al.* (2003) and the IRD Valpedo GIS (<http://www.miruram.mpl.ird.fr/valpedo/miruram/Burkina/index.html>), respectively. TTG – tonalites-trondhjemites-granodiorites.

The weathering surfaces vary from those thickly varnished or coated with iron films and dust films to only slightly weathered ones. Unlike the massive volcanic rocks, the volcano-sedimentary sequences show a higher degree of deformation and are usually strongly foliated. They weather more easily and disintegrate into sheet-like debris. Rock coatings vary depending on the original rock composition. The more resistant layers with higher content of quartz may display both rock varnish and iron coating films while the more easily weathered chlorite and sericite rich layers display only Fe and Mn rich fissuresol coatings that may occasionally be exposed. The Tarkwaian-type sediments can

Lithology	Key minerals	Texture	Structural features	Minerals in weathering crusts (XRD)
Gabbros	Pl, Cpx, Hbl/Act, Chl, Ep/Czo, Qtz	medium grained, random/cumulate	massive, localized high strain zones	Qtz, Amp, Chl, Pl, + Mica, - Czo
Basalts	Pl, Hbl/Act, Chl, Ep/Czo, Qtz	micrograined, ophitic	massive, localized high strain zones	Qtz, Amp, +Kln, -Chl
Andesites (a) andesites, (b) and. pyroclastics (c) andesitic tuffs	Pl, Ep/Czo, Chl, Act, Qtz	(a) microlithic, with porphyritic phenocrysts, (b) microlithic, with porphyritic phenocrysts and/or lithic fragments, (c) fine grained, lepidoblastic	massive, penetrative metamorphic foliation, localized high strain zones	a,b) Qtz, Chl, Amp, +Gth, Pl, Mica, Ep c) Qtz, Kln, +Mica, Gth, - Sme, Hem
Volcano-sediments and sediments - epiclastites, wackestones and argillites	Qtz, Pl, Chl, Ms, Carb, Hem	fine grained, lepidoblastic	penetrative metamorphic foliation	Qtz, +Gth, Kln
Tarkwaian-type sediments (a) matrix supported conglomerate (b) sandstone, gritstone (c) arcoses, pelites	Qtz, Pl, Ms, Carb, Ep	(a) polymictic pebbles of various sizes in unsorted to well sorted matrix, (b) Qtz supported matrix with occasional pebbles, (c) lepidoblastic	(a+b) massive, (b+c) localized shear zones to penetrative metamorphic foliation	a, b) Qtz, +Kln, Mica (Ms), Or, -Pl, Hem, Gth c) Qtz, +Gth, Kln, Mica, - Kfs
Granodiorites, tonalites and diorites	Pl, Qtz, Bt, Hbl	porphyritic, medium to coarse grained, locally lepto- or nemato-granoblastic, with strong preferred orientation of Hbl and Bt	HT banding, mylonitic foliation	Qtz, Pl, -Mica, -Amp, -Or
Granites and granodiorites with biotite, amphibole	Pl, Qtz, Kfs, Bt, Hbl	porphyritic, medium to coarse grained, locally lepto-granoblastic	massive, mylonitic foliation	Qtz, Mica, +Pl, Or, -Kln, Calc
Sediments of the Taoudeni basin - sandstones	Qtz, Kln, Glt	Qtz supported matrix	massive, brittle faulting	Qtz, +Kln, Hem, Or

**Table III-1** Descriptions of principal lithologies and their weathered surfaces, based on petrological macroscopic, microscopic and structural observations; (Qtz - quartz, Pl - plagioclase, Cpx - clinopyroxene, Hbl - hornblende, Act - actinolite, Chl - chlorite, Ep - epidote, Bt - biotite, Kfs - K-feldspar, Kln - kaolinite, Czo - clinozoisite, Carb - carbonate, Hem - hematite, Glt - glauconite, Gth - goethite).

be observed as a 1-2 km narrow band stretching from north to south through the study area. The surface exposure is partially controlled by rock composition as massive sandstones and conglomerates



form erosional ridges whereas finer grained arcose to pelitic layers erode with less difficulty and do not produce prominent geomorphological features except for cases where they are capped by iron rich duricrusts. The weathering surfaces display similar characteristics to the volcano-sedimentary rocks. Although granite and TTG intrusions amass around 37% of the bedrock (Castaing et al., 2003), outcrops are only sparsely distributed throughout the planation surface consisting of isolated boulders or flat lying erosional surfaces. The granitic rocks display onion like sheeted disintegration exposing both rather fresh rock and slightly varnished darker surfaces. Locally, thin iron films are observable owing to the disintegration of mafic minerals. The erosional ridge features observed throughout the study area stem from the differences in depths of the paleo-weathering fronts, which were probably higher for the more felsic volcanic rocks and volcano-sediments as well as for the granites. Clarke (1994) in the Kambalda region, Australia, described similar behavior of geomorphological features. Rock exposure in the study area is around six percent. Overall, most of Burkina Faso including the area of interest displays thick lateritic weathering with iron rich duricrusts formation and development of soil profiles. The soil types (figure III-2b) include (according to the French CPCS (1967) classification system for tropical soils) mainly ferruginous tropical soils, brown eutrophic tropical soils, and soils with little development (eroded) (<http://miruram.mpl.ird.fr/>). The soils developing over basic and intermediate volcanic rocks are usually darker, and are brown in color belonging to the family of brown eutrophic tropical soils. Soils sampled over granites and sediments show lighter grey colors with sandy texture and belong to either the family of ferruginous tropical soils or soils with little development (eroded). The hydromorphic soils are less common and are found around streams, raw mineral soils, ferralitic soils, and vertisols. The soil surfaces are very often covered by iron rich lag nodules, which contribute to the overall spectral reflectance.

#### **4. Sample measurements and sample preparation**

The spectra were acquired with an ASD FieldSpec Pro FR spectrometer from in the range 0.35  $\mu\text{m}$  to 2.5  $\mu\text{m}$  as hemispherical conical reflectance factors (Schaepman-Strub et al., 2006; Milton et al., 2009). A total of 110 sample stations were established in situ. Samples from eight stations were collected and measured at the IRD laboratory in Ouagadougou. The field measurements setup of the instrument included no fore-optics so that the instrument field of view was 25°. A calibrated Labsphere spectralon panel was used as reference which was measured before each sampled station and after every twentieth sample measurements, or when atmospheric conditions changed abruptly. Each spectra acquired constitutes the average of 25 unique measurements. Each sample was captured at least three times at different points to account for the natural inhomogeneity in both surface geometry and surface composition. The viewing geometry was maintained approximately constant with the sensor pointed vertically. The distance between the target and detector varied from around 5 cm to 100 cm (sampled surface diameter ~2.2 cm to 44.3 cm, respectively) depending on the target

size. Geographic location and time was stored with each measurement. In the laboratory, a high intensity contact probe with a halogen bulb light source was used on samples from eight stations. The area sampled had a circular diameter of 1 cm.

Rock measurements consisted of acquiring spectra for both the weathered surface and fresh bare-rock surface. Fresh surface measurements were conducted on rock fragments with little or no visible signs of surface alteration. The same samples were used for thin section analyses, microprobe analyses, and subsequent petrographic descriptions. Weathered surfaces were measured as exposed originally in the field or on the weathered parts of rock hand samples. Examples of the differences between weathered and unweathered surfaces of measured rocks and an example of common Fe-rich duricrusts are depicted in figure III-3.

The soils were measured using two approaches - 1) as non-disturbed surfaces along with lag material, rock debris, and dead vegetation matter; and 2) as clean soil surface only. The latter required the scraping off all detrital organic material, rock debris and lag nodules and exposing a homogeneous soil matrix. As described above, only the exposed top horizon of soils was measured.

As complementary information, spectral characteristics of local vegetation were determined. Vegetation samples included dry vegetation material such as leafs or stems and green healthy vegetation represented by common type of bushes and trees.

Identification of mineral constituents present in the weathering crusts were facilitated by X-ray diffraction (XRD). An INEL CPS-120 diffractometer with a cobalt source was used. The samples were taken by scraping off 0.5-1 mm of the weathered rock surface with an electric drill and ground in an agate bowl to pass the 200-mesh screen (~0.074 mm). A qualitative phase analysis was conducted based on position and intensity of the diffraction peaks. The mineral composition of the crusts is described in table III-1.



**Figure III-3** Field photographs of principal lithologies with weathered and unweathered surfaces (displayed as insets), a - gabbro, b - andesite, c - volcano-sediments, d - Tarkwaian-type sediments, e - Granodiorite, f - Granite, g - Taoudeni basin sandstones, and h - common Fe-rich duricrust plateaus with cut surface (displayed as inset).

## 5. Library description

The spectra are stored as text files with a defined naming convention as follows. Each spectrum name contains the date of acquisition with a sequential measurement number, along with the sample site ID and an abbreviation of the sampled material. The text files are linked to a relational database, which includes rock and outcrop description, petrographic data, photo documentation, and GPS coordinates of the measured locations. For further analyses, the data were corrected for the ASD spectrometer drift between the VNIR and SWIR1 detector using the additive method. The corrected spectra were further processed with the Savitzky-Golay smoothing filter (Savitzky and Golay, 1964) with a filter size of 65 data points and a polynomial degree of 4 (values in the water absorption bands between 1.32-1.47 and 1.75-1.96  $\mu\text{m}$  were replaced with linear interpolation before the application of the filter and bands with high noise levels above 2.4  $\mu\text{m}$  were replaced with last good band values). The processing was aided by the AStools plug-in (Dorigo et al., 2006) and Viper tools plug-in ([www.vipertools.org](http://www.vipertools.org)) for ENVI. Both the smoothed version of spectra and the original files are stored in the database.

## 6. Spectra description

Representative spectra of rock surfaces are shown in figures III-4 and III-5. The mean relative reflectance (hereafter referred to as “reflectance”) of all the measured surfaces along with standard deviations of the spectra are displayed. The analyses of the spectra included inspection of continuum removed spectral curves (Clark and Roush, 1984) and spectral feature fitting using the USGS spectral library (Clark et al., 2007), and the ASTER 2.0 spectral library (Baldrige et al., 2009).

### 6.1 Mafic and intermediate rocks

The reflectance of the rocks increases as the  $\text{SiO}_2$  content of the rock increases and less mafic minerals are present in the rock. The diagnostic absorption features of the gabbros, basalts, and andesites show similar spectral behavior differing slightly by increasing reflectance values in the shortwave infrared region. Fe and Mg-OH molecular vibrations in chlorites, amphiboles, pyroxenes, and epidotes (Hunt and Salisbury, 1970; Hunt et al., 1973a; Hunt, 1977) are centered on 2.32  $\mu\text{m}$  and 2.25  $\mu\text{m}$ . A subdued absorption of Al-OH observable at 2.20  $\mu\text{m}$  in gabbros may be related to the sericitization of plagioclase most probably related to retrograde metamorphism. A broad increase in absorption is visible around 1.0  $\mu\text{m}$  in the basalt and gabbro spectra. This absorption is attributed to ferrous iron and electronic transitions in discrete ions – crystal field effect absorption (CFA) (Hunt and Salisbury, 1970; Hunt et al., 1973a). In this case, it is the iron contained in chlorites, amphiboles, and pyroxenes. The pyroxenes correspond to diopside and augite with very low/weak compositional variations, while amphiboles show whole range of compositions in the fields of edenite, pargasite,

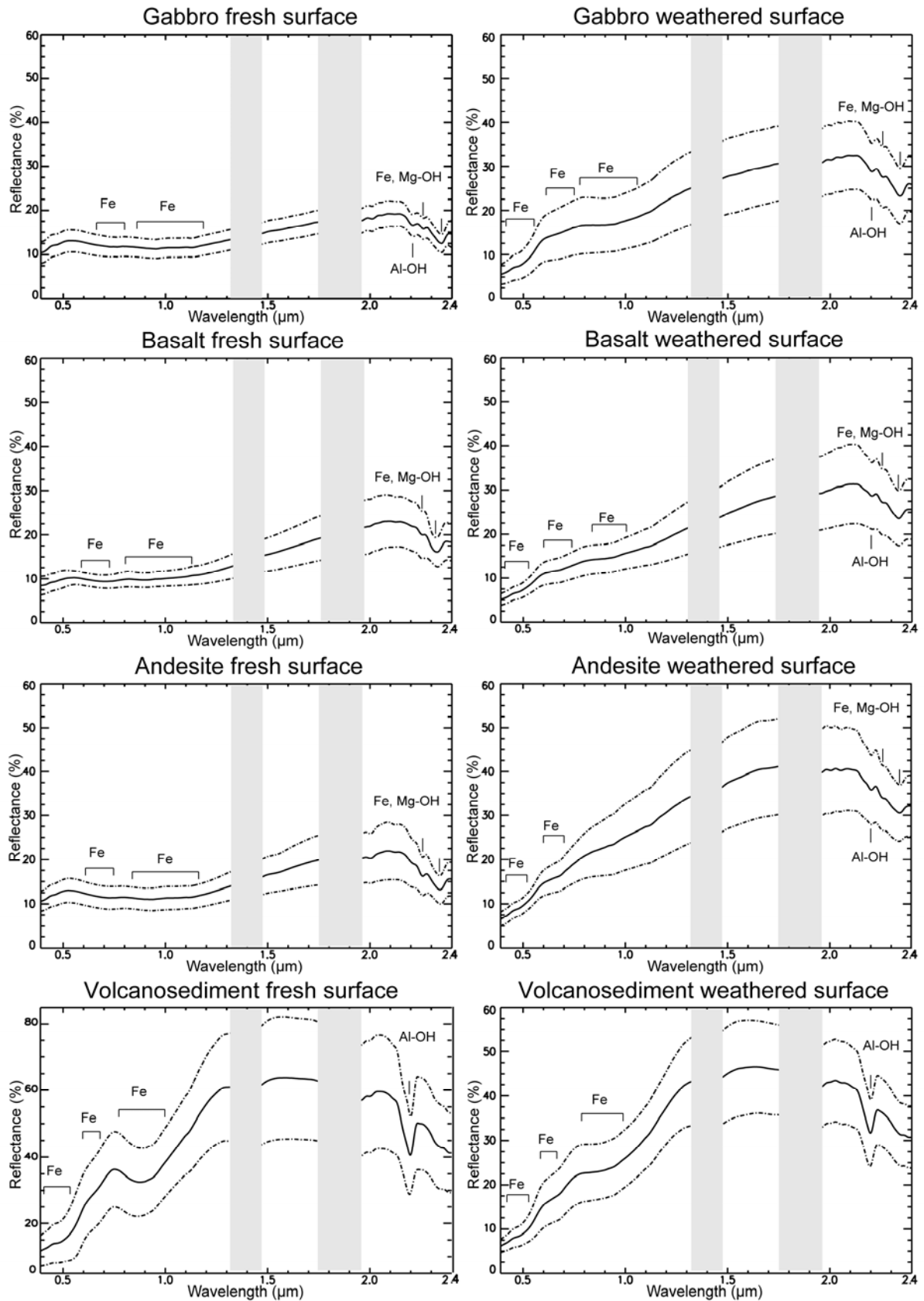
hornblende, and actinolite. The chlorites span between diabantite and different Fe-rich varieties of clinocllore – ripidiolite, pycnochlorite, and brunsvigite.

The weathered surfaces of all three lithologies show an overall increase in reflectance and a steeper profile of the reflectance curve. The diagnostic absorption features of Mg, Fe-OH molecular bonds are still recognizable but are less pronounced. Instead, the presence of an absorption peak near 2.2  $\mu\text{m}$  suggests an influence of Al-OH molecular vibrations in clay minerals (kaolinite/smectite group). This is supported by the field observations of dust coatings and or soiling of the surfaces as well as the presence of varnished surfaces. The appearance of ferric iron absorption, below 0.6  $\mu\text{m}$  (CTA) caused by charge transfer (Hunt et al., 1971; Hunt, 1977), and the shift of the CFA absorptions to shorter wavelengths below 1.0  $\mu\text{m}$  is related to hematite and goethite content in the mineral coatings. The diffraction analyses of the sampled coatings suggest that hematite and goethite form minor phases in the samples (table III-1), notwithstanding the influence of these minerals on the spectra.

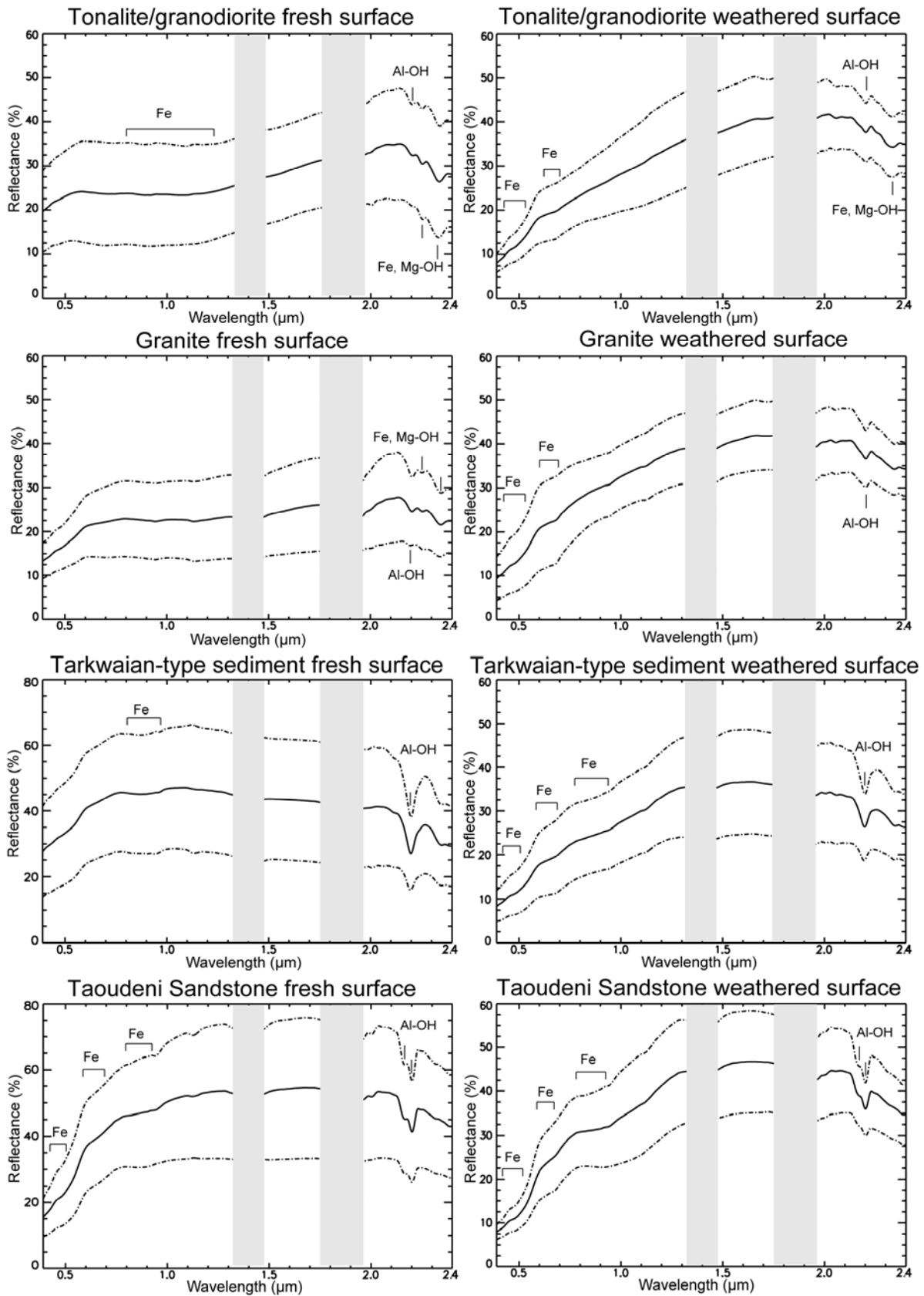
## **6.2 Granitoids**

The sampled tonalites and granodiorites of the TTG group are spectrally similar to the gabbros. A rather large difference may be observed in the overall reflectance between the different measurements. The Fe, Mg-OH absorptions at 2.25 and 2.33  $\mu\text{m}$  are present and indicate amphibole and biotite as mineral constituents. The mean reflectance curve and the positive standard deviation show a third absorption at 2.2  $\mu\text{m}$  related probably to the sericitization of plagioclase. There is a notion of a broad CFA feature related to ferrous iron content in amphiboles and pyroxenes (Hunt and Salisbury, 1970; Hunt et al., 1973a; Hunt, 1977) at around 1.0  $\mu\text{m}$ . The granite group shows more pronounced Al-OH absorption at 2.2  $\mu\text{m}$ , which is most probably caused by surface alteration of the samples. Unlike the TTG suite, it does not exhibit ferrous iron absorptions, but shows a well visible CTA absorption below 0.6  $\mu\text{m}$  connected with surface alteration and the presence of hematite/goethite. The Fe, Mg-OH vibrational absorptions at 2.25 and 2.34  $\mu\text{m}$  confirm the presence of amphibole and biotite.

The weathered surfaces of both groups are characterized by kaolinite/smectite group absorptions around 2.2  $\mu\text{m}$  (Hunt and Salisbury, 1970; Hunt, 1977; Clark et al., 2007). The 2.17  $\mu\text{m}$  shoulder feature typical for kaolinite is less pronounced. The CFA iron absorption shifts to shorter wavelengths in the TTG group and ferric iron absorption related to hematite and goethite in the mineral coatings appears below 0.6  $\mu\text{m}$ .



**Figure III-4** Relative reflectance of the main lithological types - Volcanic and volcano-sedimentary rocks. Mean reflectance of each lithological group is drawn with solid line, plus and minus one standard deviation is displayed as dashed line. Absorption features are indicated with vertical lines and horizontal brackets.



**Figure III-5** Relative reflectance of the main lithological types - Granitoids and sedimentary rocks. Mean reflectance of each lithological group is drawn with solid line, plus and minus one standard deviation is displayed as dashed line. Absorption features are indicated as vertical lines and horizontal brackets.

### 6.3 Volcano-sediments

The Birimian volcano-sedimentary group of rocks includes mostly sericitic and chloritic schists, argillites, and wackestones (Castaing et al., 2003). It should be noted that the outcrops are most of the time strongly altered due to the mineral composition and well-developed schistosity of the rocks. The “fresh” rock surfaces exhibit a distinct 2.2  $\mu\text{m}$  Al-OH absorption ranging from a symmetric muscovite/illite shape, related to the sericitization or weathering of the rock, to a kaolinite doublet shape with the 2.17  $\mu\text{m}$  complementary absorption. Pronounced hematite/goethite related CFA iron absorption centered at 0.9  $\mu\text{m}$  with a subdued 0.65  $\mu\text{m}$  absorption and well visible CTA iron absorption below 0.6  $\mu\text{m}$  may be observed in the visible and near infrared portion of the spectrum. In the spectra of exposed weathered surfaces of these volcano-sediments, the CFA absorption at 0.9  $\mu\text{m}$  related to goethite becomes less pronounced. The 2.2  $\mu\text{m}$  Al-OH absorption feature is less indicative of pure kaolinite and shows the influence of mixing between smectite/kaolinite and muscovite/illite rich surfaces reflecting the wider lithological composition range of the volcano-sedimentary group.

### 6.4 Tarkwaian-type sediments

The fresh rock samples of the Tarkwaian-type sediments show a typical Al-OH muscovite related absorption feature at 2.2  $\mu\text{m}$ . Slight reflectance decrease may be observed at 0.9  $\mu\text{m}$  followed by stronger absorption below 0.5  $\mu\text{m}$  suggesting the presence of hematite and goethite in the matrix. The spectral curve of the weathered surfaces is more inclined revealing the effect of mixed organic/varnish and dust coated surfaces forming especially on the resistant quartz rich layers. The muscovite/illite absorption peak centered at 2.2  $\mu\text{m}$  is still clearly visible although its minor asymmetry implies the presence of kaolinite/smectite minerals in the weathering crusts. Hematite and goethite absorption features below 1.0  $\mu\text{m}$  are subdued.

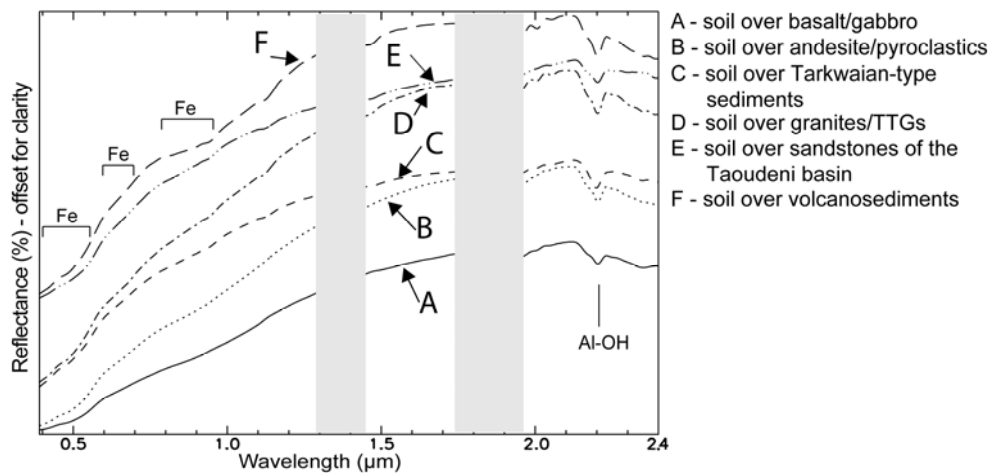
### 6.5 Taoudeni basin sediments

The sampled sandstones belonging to the Neoproterozoic sedimentary cover of the Taoudeni basin range from a pure quartzite to an admixture of quartzose and argillitic compositions (Castaing et al., 2003; Le Métour et al., 2003). The fresh surfaces of the sandstones show a well-expressed kaolinite doublet centered at 2.2  $\mu\text{m}$  with the complementary 1.7  $\mu\text{m}$  left-shoulder absorption. The reddish to yellowish color of the sandstones results from the hematite and goethite content in the matrix of the sandstones (Le Métour et al., 2003) and is documented by CFA and CTA ferric iron absorptions at 0.65 and below 0.6  $\mu\text{m}$ . The weathered surfaces show a decrease in reflectance from 0.7 to 1.0  $\mu\text{m}$  that can be attributed to more hematite/goethite rich weathering crusts. Apart from this difference, the spectra of weathered and fresh sandstones are similar.



## 6.6 Soils and regolith

The spectra of the different top soil horizons, which formed over different lithologies, are shown in figure III-6. The shapes of the spectra are very similar and differ for the most part only in the overall reflectance. All spectra show a clear Al-OH absorption peak at 2.2  $\mu\text{m}$  related to the content of clay minerals. The soils, which formed over basalts, gabbros, and andesites (figure III-6A, B); display the lowest reflectance with subdued kaolinite/smectite absorptions at 2.2  $\mu\text{m}$ , and the complementary

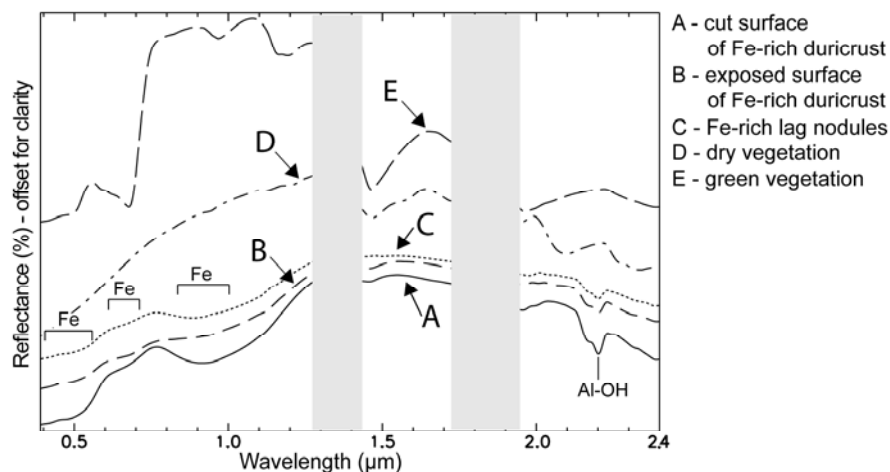


**Figure III-6** Relative reflectance of the main soil types (spectra are offset for clarity and sorted by increasing reflectance), A - soil formed over basalts and gabbros, B - soil formed over andesites and andesitic pyroclastites, C - soil formed over Tarkwaian-type sediments, D - soil formed over granites and TTGs, E - soil formed over sediments - sandstones, F - soil formed over volcano-sediments.

absorption peak of kaolinite at 2.17  $\mu\text{m}$  becomes visible only in continuum-removed spectra. The overall shape of the spectral signatures of the soils is very close to the respective mean spectra of the weathered surfaces of the parent rocks. However, indicative absorptions of original mineralogy, especially in the short-wave infrared region, disappeared completely. The relatively small depth of the absorption indicates that the amount of clay minerals is not high and the shape suggests the presence of a mixture of kaolinite and smectite. The most profound clay absorption may be observed within the spectra of soils over andesites. A minor absorption at around 0.9  $\mu\text{m}$  followed by a decrease in reflectance under 0.5  $\mu\text{m}$  documents the presence of Fe oxides and hydroxides in these soils. The reflectance values for soils developed over volcano-sedimentary rocks differ from the soils developed over the volcanic rocks with overall higher reflectance, but keep similar diagnostic features of clay minerals and iron oxides and hydroxides. Soils sampled near the outcrops of Tarkwaian-type sediments (figure III-6C) reflect the original mineralogy of the parent rock and its weathered surfaces. The 2.2  $\mu\text{m}$  Al-OH symmetric absorption peak is indicative of muscovite. Unlike the weathered parent rock surfaces, CFA absorption is not observable, leaving the absorption centered at around 0.5  $\mu\text{m}$  related to ferric iron to be the dominant feature. Spectra of soils derived over granitic lithologies show a resemblance with the mean reflectance of the weathered surfaces. The Al-OH absorption doublet at

2.2  $\mu\text{m}$  and 2.17  $\mu\text{m}$  is well defined and indicates the prevalence of kaolinite as the main clay mineral constituent. Indices of hematite or goethite are recognizable by the ferric iron absorption below 0.6  $\mu\text{m}$ . Soils sampled over the Neoproterozoic sandstones (figure III-6E) have, unlike all the other soils, lower reflectance than the weathered surfaces of the parent lithology. The Al-OH kaolinite doublet is subdued and the CFA absorption centered near 1.0  $\mu\text{m}$  has disappeared. CTA absorption related to the presence of goethite and hematite in the soil is responsible for the increased absorption below 0.6  $\mu\text{m}$ .

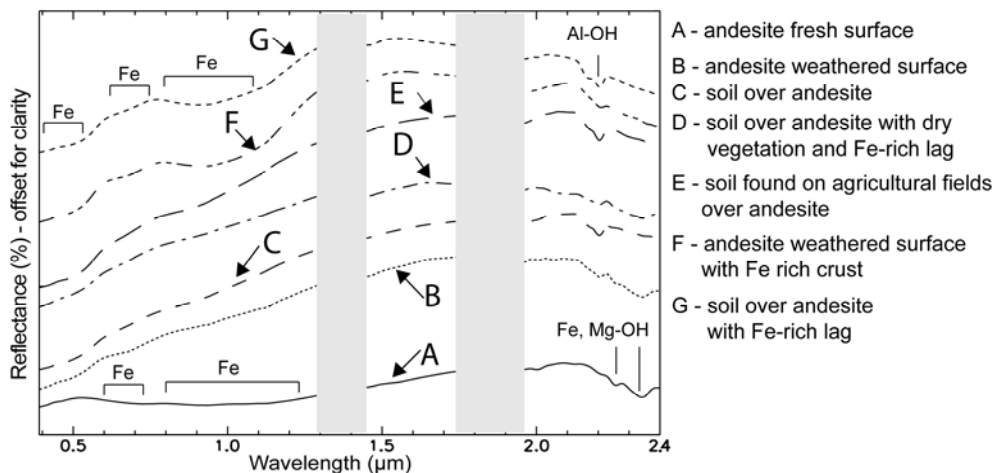
The Fe-rich regolith materials including the duricrusts and lag nodules have a characteristic signature with pronounced absorptions related to iron rich secondary weathering minerals and kaolinite. The cut surfaces of the duricrusts (figure III-7A) offers the best example, where both CFA related absorption centered at 0.9 and 0.65  $\mu\text{m}$  and CTA absorption below 0.6  $\mu\text{m}$  are the most pronounced features in the spectral curve. The Al-OH doublet centered at 2.2  $\mu\text{m}$  with the secondary absorption band at 2.17  $\mu\text{m}$  confirms the presence of kaolinite as the main clay constituent. Weathered surfaces (figure III-7B) display less pronounced hematite/goethite features especially the main 0.9  $\mu\text{m}$  absorption. The spectra of Fe-rich lag nodules (figure III-7C) show again CFA and CTA absorptions, which are more intense similarly to the cut, surface of the duricrust material. The depth of the Al-OH absorption is smaller for both the exposed surfaces and the lag nodules. Complementary mean spectra of measured green and dry vegetation are displayed in figure III-7D, E along with the regolith material.



**Figure III-7** Relative reflectance of Fe-rich regolith materials and vegetation (spectra are offset for clarity), A - Fe-rich duricrust cut surface, B - Fe-rich duricrust exposed surface, C - Fe-rich lag, D - dry vegetation, E - green vegetation.

## 7. Discussion

The steeper profiles of the reflectance curves observed for weathered surfaces may be attributed to the formation of rock coatings and varnish, which are commonly encountered in semi-arid to arid environments (Rivard et al., 1992; Dorn, 2009). The effects of the weathering process on an intermediate andesitic rock are illustrated in figure III-8. The weathering disintegrates the less resistive rock forming a mixture of clays, quartz and secondary iron oxides and hydroxides which have an overall higher reflectance and produce distinct ferric iron absorption features as well Al-OH molecular vibration features related to the formation of clays (Cloutis, 1992; Younis et al. 1997). Some surfaces show higher content of hematite/goethite (figure III-8G, F) and strongly resemble the response of lateritic duricrusts and associated lag nodules. The mineral coatings related to weathering



**Figure III-8** Relative reflectance of surface materials derived from andesites (spectra are offset for clarity), A - Relative reflectance of andesitic rock, B, F - its weathered surfaces, C - associated soil found close to outcrops and on agricultural fields - E, the effect of vegetation residues and lag material - D, G on the soil spectra.

of rocks in arid environments are consistent with the observations discussed by Dorn (2009). Their effect on spectral reflectance of the rocks is evident and should not be disregarded. Although the absorption features in the short wave infrared region of the primary minerals are still recognizable, which was also noted by Rivard et al. (1992) or Younis et al. (1997), the overall shape of the reflectance curve changes and several new absorption features related to secondary iron rich minerals and clays appear. Imaging spectroscopy is able to discern hematite or goethite in very low contents in soils (Madeira et al., 1997; Ben-Dor et al., 2009); however in our samples of weathered rock surfaces we observed that the influence of these minerals on the measured spectra (figures III-4 and III-5) is not so obvious in the XRD phase analysis (table III-1). These discrepancies may either be attributed to the fact that rock varnish is mainly composed of clay minerals (Dorn, 2009), or to the fact that the goethite and hematite minerals are contained mostly in the top most layer as a very thin sheet and hence

became less abundant in the volume of the scraped XRD sample. Alternatively, the absence of hematite/goethite in the XRD spectra could be affected by the crystallinity of these phases. The soils forming around the weathered rocks display similar characteristics as the weathered surfaces. The difference between the weathered rocks and the soils is mainly related to the clay content. This is well documented by deeper or better-developed Al-OH absorption features around 2.2  $\mu\text{m}$ . The spectra of soils acquired over tonalites and granites match well with the top soil horizon spectra, found over granitic rocks in the Gourma plain in eastern Burkina Faso, in the recently published soil spectral library (ICRAF-ISRIC, 2010). The form of the 2.2  $\mu\text{m}$  Al-OH absorption feature reflects the composition of the clay minerals and generally three components can be recognized, namely smectite, illite, and kaolinite (Chabrilat et al., 2002). The discrimination between the soils in the remote sensing data will most probably have to be based on the overall reflectance, which varies for the different lithologies. Broader groups can be established based on the reflectance difference, where soils over basic to intermediate volcanic materials have generally lower reflectance (~8% basic to intermediate volcanics, ~5% volcano-sediments) than the soils derived from granitic materials. The difference becomes more pronounced in the short wave infrared region, where reflectance of soils developing over basalts and gabbros is up to 20% lower than the soils derived from granitic lithologies. Another useful determinant feature could be the absence of hematite/goethite absorption at around 0.9  $\mu\text{m}$  in the spectra of soils from granitic domains; although detection of these features may be compromised by the omnipresence of Fe-rich lag material.

It should be noted that the presence of organic material has a large impact on the measured surfaces (Siegal and Goetz, 1977; Murphy and Wedge 1994; Serbin et al., 2009). Figure III-8D shows that the reflectance curve is modified by the presence of dry organic matter especially in the 2.0–2.3  $\mu\text{m}$  range where the broad absorptions related to lignin and cellulose content may be found (Elvidge, 1990; Serbin et al., 2009). In a similar way, the measured reflectance is affected by green vegetation; nevertheless, some studies show that mapping of lithologies, soils or regolith material is possible, even when substantial vegetation cover is present, either directly or indirectly (Siegal and Goetz, 1977; Rivard et al., 2009; Rodger and Cudahy, 2009).

Because most of the rocks of the greenstone belts contain greenschist mineral metamorphic assemblages their spectra differ considerably from the spectra of their unmetamorphosed protoliths (Baldrige et al., 2009) owing mainly to the transformation of the main rock forming minerals to chlorite, epidote, and actinolite. The effect of retrograde metamorphism and formation of sericite is also very common. In the case of the basic and intermediate rocks, the 1.0  $\mu\text{m}$  broad absorptions related to primary pyroxene, and amphibole contents in the protolith (Hunt and Salisbury, 1970; Hunt et al., 1973b; Hunt et al., 1974; Hunt, 1977; Baldrige et al., 2009) become less evident. The overall increase in the short wave infrared region is typical for rocks containing chlorite or epidote and so are the 2.25  $\mu\text{m}$  and 2.32–2.34  $\mu\text{m}$  absorption features. The large differences in the overall reflectance of the fresh rock in the group of tonalites and granodiorites (figure III-5) may be explained by the

presence of banding and dominance of mafic minerals such as amphibole and biotite in the melanocrate layers. Furthermore, the less evident  $1.0\ \mu\text{m}$  broad absorption for the group of granitic rocks may suggest the presence of less abundant amphibole and biotite in the measured samples. In the Birimian volcano-sediments, the observed CFA and CTA iron absorption suggest an important component of iron minerals in the matrix. The presence of disseminated iron oxides and hydroxides was confirmed by microscopy and was reported by Le Métour et al. (2003). This phenomenon may also be attributed to a secondary alteration of iron rich minerals, as the volcano-sedimentary rocks seem to be deeply weathered. The spectra of Tarkwaian-type sediments are similar to sandstones or conglomerates, which contain sericite in their matrix whereas the sandstones of the Taoudeni basin resemble more to sandstones or conglomerates where the cement constitutes of some amount of argillaceous material (Baldrige et al., 2009). The spectra of Fe-rich duricrusts contain as expected less kaolinite when measured at the exposed surfaces, as the clay material is washed away and only resistant hematite and goethite remains. Under the surface remnants of kaolinite rich spots related to the development of the lateritic profile (Taylor and Eggleton, 2001; Deller, 2006) remain and affect the measured spectra.

## **8. Conclusions**

The collected spectral library contains over 700 spectra of rock and regolith surfaces (soils, Fe-rich duricrusts, and lag) with complementary spectra of vegetation. The spectral range of the library ( $0.35\ \mu\text{m}$  to  $2.5\ \mu\text{m}$ ) allows direct comparisons with remote sensing data acquired by satellites such as Landsat, ASTER, or Hyperion. The field observations and acquired spectral data show the importance of weathering related phenomena on the spectral properties of rock under semi-arid conditions. The lithological composition, texture, and structural features of the different rock types control the formation of rock varnish and iron coatings on the weathered surfaces. The exposures of the lithologies are controlled in a similar manner, where massive volcanic rocks and quartzose sediments crop out more often than foliated volcano-sediments or granitic rocks.

The sampled surfaces show considerable spectral diversity. The Fe, Mg-OH absorption features related to the content of chlorite, amphibole, pyroxene, and epidote in mafic to intermediate volcanic rocks and the TTGs produce distinct spectral features centered at  $2.33\text{--}2.34\ \mu\text{m}$  and  $2.25\ \mu\text{m}$ . These features are still recognizable in the spectra of the weathered surfaces covered by varnish, iron films, and dust coatings.

Al-OH absorptions around  $2.2\ \mu\text{m}$  related to kaolinite, smectite, and muscovite/illite minerals are observable in the spectra of granitic rocks, sediments, sediments and all of the weathered surfaces as well as the surfaces of the sampled soils. Ferrous iron and ferric iron absorptions situated around  $1.0\ \mu\text{m}$ ,  $0.9\text{--}0.8\ \mu\text{m}$ ,  $0.65\ \mu\text{m}$ , and below  $0.6\ \mu\text{m}$  are indicative of iron rich minerals. In the case of fresh rock surfaces of the gabbros, basalts, andesites and the TTGs these absorptions are tied to

chlorite, amphibole, pyroxene, and biotite content. Weathered surfaces of all rocks as well as the fresh surfaces of sediments and volcano-sediments display similar absorptions. These are, related to iron oxides and hydroxides, which are formed as secondary weathering minerals. An abundance of hematite and goethite may be observed in most of the sampled soils and Fe-rich duricrusts as well.

The variation in spectral signatures implies that discrimination between the sampled materials based on hyperspectral data analysis should be possible. The newly acquired spectral library provides primary information for the analysis of remote sensing data in West Africa. These results show that the application of multi- and hyperspectral remote sensing in these terrains and climates will not be hindered by the surficial alteration of the fresh rocks. Nevertheless, an equivalent spectral database for the flora will need to be assembled before its full potential can be realized

### **Acknowledgements**

The project was funded by French government PhD fellowship to V.M., IRD (Institute de recherche pour le développement) post-doctoral research grant to L.B. and aided logistically by the project “West African Exploration Initiative” (<http://waxi2.org>). The support of the mining companies SEMAFO, Wega Mining, Volta Resources, and Orezone is greatly acknowledged. In particular, it was M. Crevier, D. Bondé, D. Boisvert, L. Ouedraogo, P. Marquis, O. Derra, and A. Naré, who aided with fieldwork campaigns on their permits. Thanks belong to the Czech geological survey and F. Laufek for help with the evaluation of the XRD analyses. Finally, an important acknowledgement is owed to the CESBIO laboratory and B. Mugenot for providing access to the ASD field spectrometer.

---

## **CHAPTER IV**

# **REGOLITH LANDFORM MAPPING USING AIRBORNE GEOPHYSICS AND REMOTE SENSING DATA IN A NEURAL NETWORK, BURKINA FASO, WEST AFRICA**

---

---

## Résumé du chapitre IV

# La cartographie des unités de régolithe par la méthode des réseaux des neurones en utilisant des données de géophysique aéroportée et de la télédétection, Burkina Faso, Afrique de l'Ouest

## 1. Introduction

Les roches du craton ouest africain sont couvertes d'une couche épaisse de régolithe résultant de l'altération latéritique prolongée. Le régolithe peut être caractérisé comme tout le matériel entre la surface de la terre et la roche fraîche (Taylor et Eggleton, 2001). En Afrique de l'Ouest le régolithe est une source importante de matières premières (Wright et al., 1985), il est relié avec l'évolution tectono-geomorphique (Michel, 1973 ; Grandin, 1976 ; Leprun, 1979 ; Boeglin, 1990 ; Chardon et al., 2009), mais il rend également difficile la cartographie géologique (Jaques et al., 1997) ainsi que la prospection géochimique (Craig, 2001 ; Taylor et Eggleton, 2001). Les cartes de régolithe couramment utilisées par exemple en Australie (Pain et al., 2007), sont en Afrique de l'Ouest presque inexistantes.

Pour caractériser la composition minéralogique des surfaces de régolithe on peut utiliser des données multispectrales ou hyperspectrales (Craig et al., 1999 ; Dehaan et Taylor ; 2004). La micromorphologie de surface et le mécanisme prédominant de réflexion des ondes de radar peuvent être analysés en utilisant la polarimétrie radar (Henderson et Lewis, 1998 ; Tapley, 2002). L'enrichissement ou l'appauvrissement relatif des surfaces individuelles des éléments radioactifs ont déjà été discutées par Wilford et al. (1997) et Martelet et al. (2006). La spectrométrie gamma aérienne représente donc une autre méthode qui peut être utilisée pour caractériser des unités de régolithe. L'analyse du modèle numérique de terrain aide à la cartographie des formes du relief (Henquin et Totté, 1993 ; Irvin, 1997 ; Saadat et al., 2008). L'analyse intégrée des données peut se faire visuellement dans l'environnement le SIG (Craig et al., 1999 ; Woolrych et Batty, 2007) ou à l'aide de la classification automatique (Wilford et al., 2007). Cette étude se concentre sur l'évaluation des méthodes de classification automatisées de régolithe en utilisant une analyse combinée des données de la géophysique aérienne et de la télédétection dans la région du Gaoua, modérément à densément couverte par la végétation au sud-ouest du Burkina Faso.

## 2. Méthodes

Avant les classifications les données ont été préparées. Toutes les données ont été ré-échantillonnées à la résolution spatiale de 30 m. Les données du capteur Landsat ont servi comme une couche de base à laquelle toutes les autres données ont été enregistrées.



Les bandes visibles et proches infrarouges des capteurs Landsat et ASTER ont été calibrées dans le logiciel ATCOR (Richter, 1996) en utilisant des mesures de terrain (Richter, 1997) et enregistrées comme la réflectance. Les bandes thermiques du capteur ASTER ont été calibrées en émissivité à l'aide de l'algorithme de TES (Gillespie et al., 1998).

Pour les données du radar polarimétrique à partir de capteurs RADARSAT-2 et ALOS PALSAR, un rééchantillonnage « multilooking » a été réalisé pour obtenir des pixels cadrés. Les données de matrice de diffusion ont été transformées en utilisant la décomposition de Pauli (Cloude et Pottier, 1996) en trois bandes, qui ont servi en tant que couches d'entrée pour les classements suivants. La correction géométrique a été réalisée en utilisant l'algorithme de correction du terrain par la simulation de SAR (Schreier, 1993).

Les données de modèle numérique du terrain SRTM ont été ré-interpolées à l'aide de la méthode de Hutchinson (1989) en incréments de 30 m. Le modèle nouvellement obtenu a été utilisé pour dériver des couches comme pente, la rugosité de la pente (déviations standard de la pente), la courbure de la surface (Zeverbergen et Thorne, 1987), l'altitude relative (gamme de hauteurs) et l'intégrale hypsométrique (Pike et Wilson, 1971) en une fenêtre de 3x3 pixels. En outre, un réseau hydrographique a été dérivé avec une couche de distance des fleuves principaux et de la hauteur relative du relief au-dessus des fleuves principales.

Les données de spectrométrie gamma aérienne, calibrées comme valeurs de concentrations absolues et corrigées pour le bruit en utilisant NASVD (Hovgaard et Grasty, 1997), ont été interpolées en utilisant la courbure minimale (Briggs, 1974). De plus les couches eTh/K et eU/K en ont été dérivées.

Comme données d'apprentissage et de validation, 56 449 pixels ont été sélectionnées ce qui représente d'environ 13% de la superficie totale étudiée. La moitié des points a été choisi au hasard pour l'apprentissage et l'autre moitié pour la validation. Les méthodes de classification des réseaux de neurones (RN) (An et al., 1995 ; Zhang et al., 2009 ; Leverington, 2011) et du maximum de vraisemblance (MV) (Campbell, 1996) ont été comparées. L'algorithme ADVANGEO de classification qui est basé sur RN, a été mis en œuvre dans ArcGIS (Barth et al., 2009). Pour chaque catégorie classée un nouveau réseau a été conçu. Les résultats de la classification ont ensuite été combinés de telle sorte que chaque pixel est attribué une classe en fonction de la plus forte probabilité d'inclusion dans la classe. Globalement, quatre scénarios ont été testés avec 24, 20, 14 et 11 couches d'entrée. On a ensuite évalué l'évaluation de l'exactitude de classification en utilisant une matrice d'erreur (Congalton et Green, 2009).

### **3. Résultats principaux de l'étude**

Les meilleurs résultats de classement ont été obtenus pour le scénario de 11 couches d'entrée contenant les données de spectrométrie gamma aérienne et les données issues du modèle numérique de

terrain. Dans ce scénario, une précision globale de classement de 95,71% a été obtenue avec une valeur du coefficient kappa de 0,94. La classe de bas glacis a été classée avec la moindre précision. Cette catégorie comprend un mélange des surfaces différentes avec des propriétés variables, non seulement en termes de morphométrie, mais aussi en termes de contenu des éléments radiogéniques. Sur le terrain, ces surfaces peuvent souvent être recouvertes d'un matériel provenant d'unités morphologiquement supérieures (les Hauts/Moyens glacis, le Relief résiduel). La classe des sédiments alluviaux est la plus précisément classée et définissable grâce à la base des couches dérivées du modèle numérique de terrain. Les Hauts/Moyens glacis et le Relief résiduel ont été classés constamment bien. La divisibilité des Hauts/Moyens glacis est généralement plus élevée à cause de leurs caractéristiques typiques en spectrométrie gamma (des hautes valeurs d'eTh et eTh/K). Dans la classe des surfaces résiduelles, les crêtes d'érosion et les inselbergs y ont été classés correctement. Pour le même scénario analysé à l'aide de la méthode de maximum de vraisemblance on a obtenu une précision globale de 91,55% avec une valeur du coefficient kappa de 0,88. Les résultats de classification en utilisant les réseaux de neurones ont toujours été meilleurs que ceux issus de classement de la méthode du maximum de vraisemblance, dans tous les scénarios correspondants. Dans le cadre de classement des scénarios analysés par les réseaux de neurones les résultats de classification n'ont pas amélioré même en incluant un plus grand nombre de couches d'entrée. Toutefois, il convient de noter que tous les résultats diffèrent d'un maximum de cinq pour cent. Une exception est la classification basée sur le MV avec des couches d'entrée, qui comprennent les données de polarimétrie radar. Ici, la précision globale a diminué à 88,78% avec un coefficient kappa de 0,84.

#### **4. Conclusion**

L'étude a présenté une procédure de classement automatique des unités de régolithe. Quatre unités de terrain régolithique - Hauts/Moyens glacis, le Relief résiduel, Sédiments alluviaux et Bas glacis ont été cartographiés. Le meilleur résultat a été obtenu en utilisant la classification des réseaux de neurones pour un scénario composé de 11 couches d'entrée comprenant la spectrométrie gamma aérienne et les dérivations de modèle numérique de terrain. L'ajout d'autres couches d'entrée n'affecte pas de manière significative les résultats de la classification. La méthode de réseaux de neurones a donné des résultats meilleurs que celle du maximum de vraisemblance. Les résultats représentent une amélioration des cartes existantes, en particulier en termes de précision spatiale pour les surfaces riches en Fe des Hauts/Moyens glacis et le Relief résiduelle. Les résultats de la cartographie peuvent être utilisés pour la prospection géochimique et l'analyse de l'évolution géomorphologique.

---

# REGOLITH LANDFORM MAPPING USING AIRBORNE GEOPHYSICS AND REMOTE SENSING DATA IN A NEURAL NETWORK, BURKINA FASO, WEST AFRICA

Václav Metelka <sup>a,b,c</sup>, Lenka Baratoux <sup>a</sup>, Mark W. Jessell <sup>a</sup>, Andreas Barth <sup>d</sup>, Josef Ježek <sup>b</sup>, Séta Naba <sup>e</sup>

<sup>a</sup> IRD, Université Toulouse III, UR 234, LMTG, 14 avenue E. Belin, 31400, Toulouse, France

<sup>b</sup> IGP, IAMIT, Charles University in Prague, Albertov 6, 12843, Prague 2, Czech Republic

<sup>c</sup> Czech Geological Survey, Klárov 3, 11821, Prague 1, Czech Republic

<sup>d</sup> Beak Consultants GmbH, Am St. Niclas Schacht 13, 09599 Freiberg, Germany

<sup>e</sup> Département de Géologie, Université de Ouagadougou, Burkina Faso

## Abstract

We have studied the regolith landform distribution in the area of Gaoua, western Burkina Faso using an integration of geophysical and remote sensing data. Concentration maps of K, eTh and eU and their ratios were computed from airborne gamma ray spectrometry data. In situ spectral measurements were used to calibrate ASTER and Landsat scenes. Pauli-decomposition data retrieved from polarimetric radar images were included as additional source data. Morphometric variables such as slope, curvature, and aspect were derived from the freely available SRTM digital elevation model to characterize the topographic parameters of the different regolith landform units. An artificial neural network, ADVANGEO, was then applied to classify the regolith landform units according to the variables obtained from satellite and airborne data. Ferruginous duricrusts rich in hematite and goethite belonging to the High and Middle glacis, relic erosional surfaces and rock outcrops, alluvial sediments, and soft pediment materials of the Low glacis were mapped successfully in the region. The results were compared with existing geomorphological maps, pedo-geomorphological maps, and field observations. We found that in particular, the distribution and shape of the iron rich duricrust is more accurate than in the current maps. The best results were obtained for a combination of gamma-ray spectrometry data and derivatives of the SRTM digital elevation model. The approach demonstrates the potential of neural networks for the combined analysis of airborne geophysics and remote sensing data in regolith landform mapping.

**Keywords:** Regolith, Remote sensing, Airborne geophysics, SRTM, Neural networks

## 1. Introduction

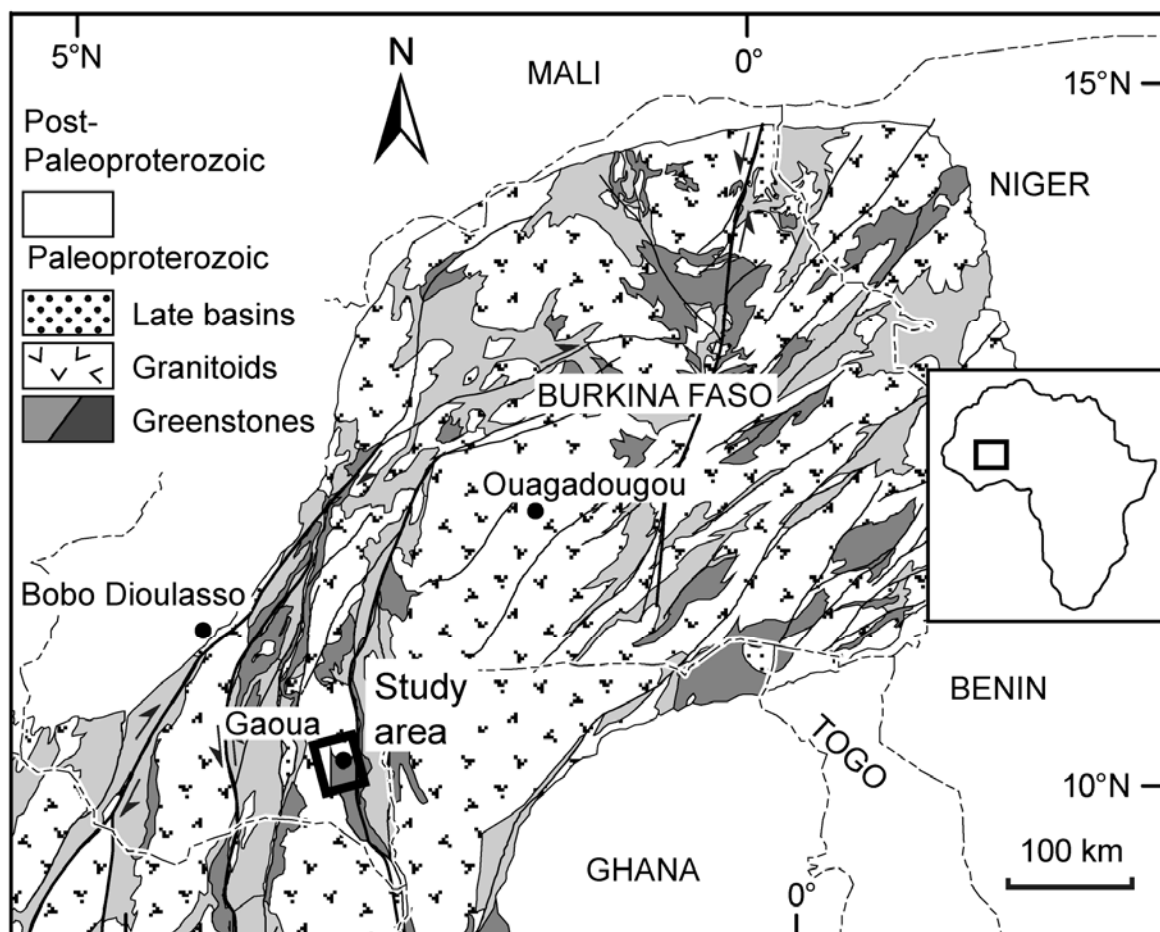
The regolith in West Africa represents an important economic resource (Wright et al., 1985), a constraint on the regions tectono-geomorphic evolution (Chardon et al., 2006), and a hindrance to geochemical exploration techniques (Taylor and Eggleton, 2001). The term regolith stands for all of the weathered and unconsolidated material from basement rock to earth surface including interbedded fresh rocks (Taylor and Eggleton, 2001). Knowing the distribution of regolith units and understanding the processes, which led to their formation, is important for any kind of successful geological mapping, geochemical or geophysical survey, and minerals exploration. Traditional field-based regolith landform mapping can be a lengthy process, which can be further complicated by difficult access to remote and often large survey areas. At most scales, West Africa remains poorly covered by regolith landform maps such as those commonly used in Australia (Pain et al., 2007). Airborne geophysical data and remote sensing data are frequently employed in regolith mapping (Wilford et al., 1997; Papp, 2002; Woolrych and Batty, 2007) to assess the diverse physical properties of regolith materials. Martelet et al. (2006) used an Agglomerative Hierarchical Clustering algorithm to classify airborne gamma spectrometry data in French Guyana and noticed that ferralitic and bauxitic duricrusts display elevated U, Th content relative to K. These areas correspond to lateritic plateaus. One can estimate the chemical composition from airborne gamma-ray spectrometry or multispectral/hyperspectral remote sensing (provided the terrain is not extensively covered by vegetation), terrain morphology from the digital elevation models (SRTM), and surface roughness or prevailing geometric shapes from radar imagery (ALOS PALSAR, Radarsat-2). Landsat imagery was commonly employed in regolith mapping (Craig et al., 1999) including directed principal component analysis (DPCA), which is used to separate clay minerals and suppress the effects of vegetation (Fraser and Green, 1987). Hyperspectral remote sensing has been used to assess surficial components of regolith by Dehaan and Taylor (2004), Lau et al. (2003), while Cudahy et al. (2006) studied the relationship between kaolinite disorder, transported versus in situ regolith, and observed that poorly crystalline kaolinite is found mostly in transported regolith material. SAR (Synthetic Aperture Radar) imagery constitutes a very useful complement to optical images (Baghdadi et al., 2005). For geologists, radar images provide unique information about structure, morphological, sedimentary features, and moisture content. This information is directly tied to the physical properties of terrain surfaces (Henderson and Lewis, 1998; Drury, 1993). Tapley (2002) showed that VV (vertical transmit-vertical receive) and HV (horizontal transmit-horizontal receive) (VH) polarizations were better suited for the geological mapping of arid to semi-arid Australia where VV polarization provides increased sharpness and better discrimination between surfaces having similar roughness properties. Digital elevation models and its derivatives are frequently used for landform mapping in conjunction with other remote sensing data (Henquin and Totté, 1993; Irvin et al., 1997; Giles, 1998; Saadat et al., 2008; Liberti et al., 2009; Siart et al., 2009). Dense vegetation cover or displacement of the regolith

units may limit the application of most of the described techniques. Indeed, the best results in mapping of the diverse regions in West Africa require the integration of several data sets. Such integration may be facilitated by simple overlay of different layers in GIS and visual interpretation (Craig et al., 1999; Craig, 2001; Papp, 2002; Woolrych and Batty, 2007) or via automated classification methods, which are not as common (Wilford et al., 2007).

This study aims at evaluating automatic classification of regolith landform units in West Africa through combined analysis of airborne geophysical and remote sensing data, in a region moderately to densely covered by vegetation.

## 2. Study area description

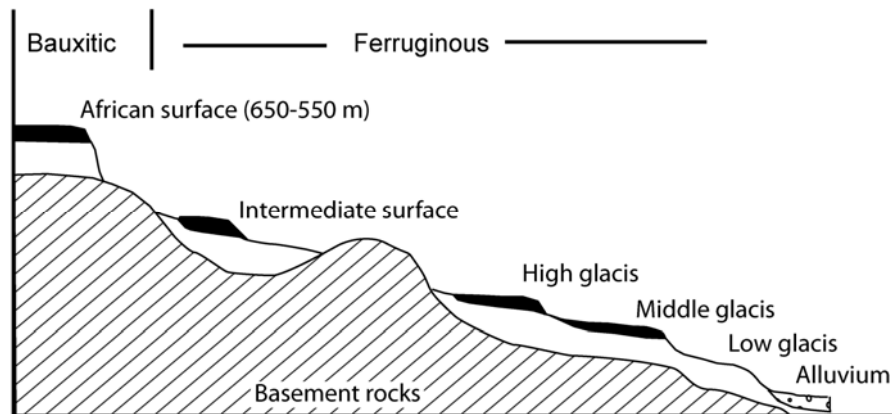
The planation surfaces of western Burkina Faso, which developed on basement rocks of the West African Craton (figure IV-1), are the result of long term deep weathering, erosion and gradual



**Figure IV-1** Schematic map of the study area. Geological map of the Northeastern part of the Paleoproterozoic Baoule Mossi domain in the West African Craton (modified after BRGM SIGAfrrique) with study area marked by a rectangle. The Paleoproterozoic greenstones are divided into: light grey – intermediate to acid volcano-clastics and volcano-sediments, dark grey – mafic to intermediate lavas and volcanic products.

uplift of the African continent under varying climatic conditions (King, 1962) mainly after the breakup

of Gondwana in the Mesozoic (Wright et al., 1985). In all of West Africa, these surfaces are capped by ferruginous or aluminous duricrusts, which are ordered in a stepped manner and correspond to a chronological order in which they were formed (Michel, 1973; Grandin, 1976; Tardy, 1997). Seven classes have been established according to correlation between relative height, geochemistry, and petrology tying the oldest surface with the Gondwanian era and the youngest in age reaching the Quaternary period (figure IV-2). The formation mechanism of the duricrusts includes a combination of

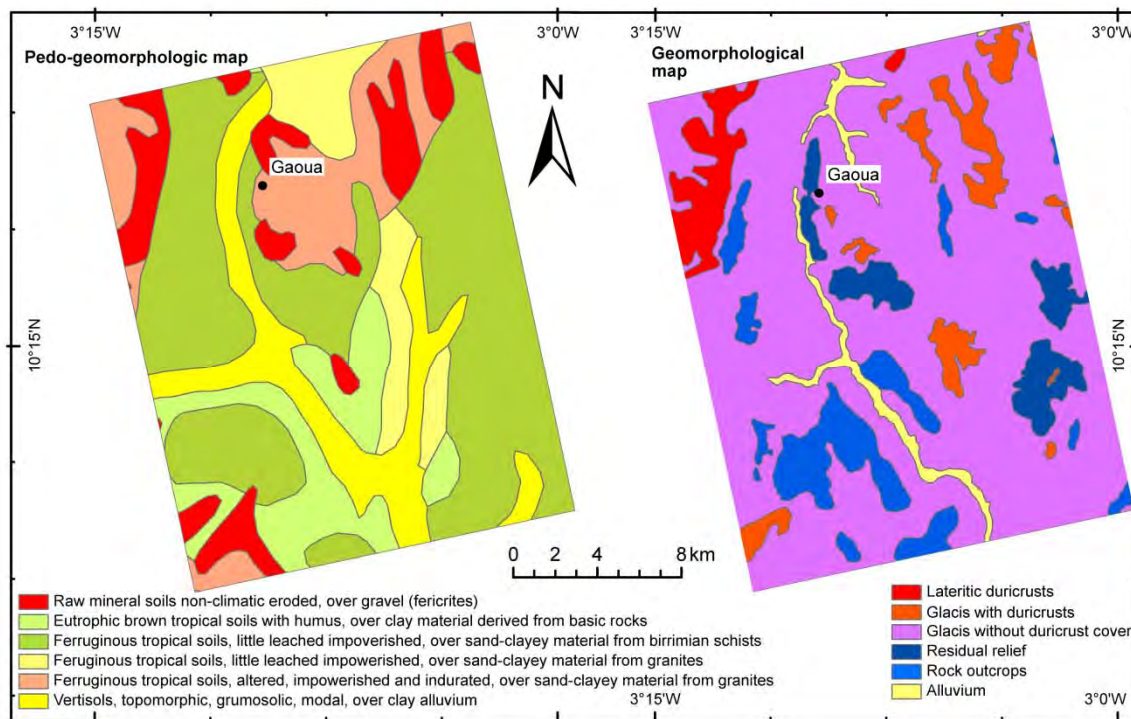


**Figure IV-2** Regolith landforms found in the area with chronological and petro-geochemical characteristics given, figure modified after Michel (1973), Grandin (1976) and Gunnell (2003).

processes where in situ formation (Leprun, 1979), down slope mechanical displacement, and subsequent recementation acted together (Beauvais, 1999).

The study area is located near the town of Gaoua (figure IV-1) in the southwest of Burkina Faso and encompasses 686 km<sup>2</sup>. The Gaoua region was intensively eroded to the extent that basement rocks are exposed to a considerable extent creating a variable surface with duricrust plateaus and buttes, inselbergs and rock ridges, flat lying or lightly inclined pediments of the Low glacia and alluvial sediments. The average height attains 300 m a. s. l. while varying between 200 m a. s. l and 560 m a. s. l. The area around Gaoua was previously thoroughly studied by Boeglin and Mazaltarim (1989) and Boeglin (1990) as a region that suites well the investigations of relationships between the lateritic profiles and the parent rocks. According to Boeglin (1990) and our field observations only three of the planation surfaces are present. Relics of the highest bauxitic African surface (Eocene, 59–45 Ma) are found at the top of the eroded sequences above 500 m. The Intermediate surface (Oligocene, 34–29 Ma) has not been observed and either has been completely eroded or did not exist in the region. The other ferruginous surfaces belong to the so-called High glacia (Late Oligocene-Early Miocene, 24–18 Ma) and Middle glacia (Late Miocene, 12–7 Ma). These surfaces are not easily distinguished and according to Boeglin (1990), there has been probably one continuous inclined or undulating surface rather than two distinct levels. The Low glacia, which are also called functional

glacis, referring to the fact that these surfaces are still developing, are not capped by duricrust cover nevertheless their formation started probably already in Late Miocene (6 Ma). The age estimations of formation of the different duricrust levels were derived from Beauvais et al. (2008), who dated the corresponding surfaces in the area of Tambao (North Burkina Faso). The area of Gaoua provides contrasting geological basement of alternating greenstone belt lithologies and granitic bodies. The belts constitute mainly volcanic and volcano-sedimentary sequences of Paleoproterozoic age (Marcelin, 1971; chapter I), which were later intruded by younger granitic rocks – TTGs (tonalite, trondhjemites, granodiorites), and granites. There seems to be some linkage between the chemical composition of the iron rich duricrusts and the underlying basement rocks (Boeglin, 1990). Tardy (1997) states the petrological and mineralogical differences are subtle and become progressively smaller with the evolution and ageing of the duricrusts. The composition of the parent rock correlates especially with the content of quartz and several elements such as P, Ba, Cr, Sc, Ni, Zn, Cu, Ce, and La. The existing maps at 1:500 000 scale, which describe the geomorphological (IGN, 2005) and pedo-geomorphological (Brossard, 2006) units that characterize the regolith units, are shown in figure IV-3.



**Figure IV-3** Existing 1:500 000 scale pedo-geomorphological and morphological maps of the region, a) pedo-geomorphological map (Brossard, 2006), b) geomorphological map (IGN, 2005).

Four main regolith landform units can be mapped in the study area. The iron rich duricrusts may be found on both of the maps. They form flat to slightly inclined plateaus with usually steep edges. The plateaus disintegrate by mechanical erosion into blocks and nodules. Most of the duricrust surfaces belong to the High and Middle glacis. Only one remnant of the bauxitic African surface has

been preserved in the southwest of the area. The largest duricrusts are found over granitic rocks, whereas the basaltic and andesitic volcanites and volcano-sedimentary rocks mostly represent other geomorphological units of Rock outcrops and Residual relief, which may be covered by thin pediment. The slopes and partially flattened surfaces between these two units belong to the class of Low glacis also called functional glacis – glacis in development. At the base of valleys, alluvial infill is deposited and represents the last unit.

### 3. Methodology and data use

#### 3.1 Data preprocessing

In order to classify all of the four basic regolith landform units that can be synthesized from the existing maps (Figures IV-3a, b) and field observations a multivariate dataset was formed constituting data layers from Landsat 7 ETM+(Enhanced Thematic Mapper), ASTER (Advanced Spaceborne Thermal Emission and Reflection Radiometer), ALOS PALSAR (Advanced Land

Dataset	Date acquired	Spatial resolution	Spectral coverage	Processing product
Landsat	1-02-2003	15-60 m*	0.45 – 12.5 $\mu\text{m}$	L1G
ASTER	3-01-2001	15-90 m*	0.5 – 11.6 $\mu\text{m}$	L1B, AST05
ALOS PALSAR	26-03-2009	30	L-band	P1.1 fine pol.
Radarsat-2	11-01-2010	12	C-band	Fine quad pol.
SRTM-3	2000	90 m	C-band	V4, CGIAR
Gamma-ray.	1998 - 1999	125 m	NA	abs. calibration

**Table IV-1** Utilized datasets with detailed description on original processing, spatial resolution, and spectral coverage. \*Landsat – only 30 m bands used, bands 1-5, 7; \*\*all 14 bands used and resampled to 30m, pol. – polarimetric, abs. – absolute.

Observing Satellite Phased Array type L-band Synthetic Aperture Radar), Radarsat-2, SRTM (Shuttle Radar Topography mission), and airborne gamma-ray spectrometry data.

#### *ASTER and Landsat data*

One ASTER scene and one Landsat scene were selected for subsequent processing with respect to the seasonal variation in vegetation cover during wet and dry periods. The acquisition dates and specific information is given in table IV-1. The Landsat dataset was used as base layer to which all data were georeferenced. The Landsat and ASTER visible and near infrared bands were calibrated to reflectance using the ATCOR algorithm (Richter, 1996). Field-acquired spectral signatures of vegetation and road construction lateritic material were employed to enhance the calibration results during in-flight calibration (Richter, 1997). Only the five thermal bands of ASTER, calibrated to emissivity by the algorithm of Gillespie et al. (1998), were used for subsequent classifications. The source layers were all resampled to 30 m spatial resolution utilizing the nearest neighbor method to



preserve the spectral information. Various techniques are applied in the classification of optical data. Four basic approaches may be followed visual (Zumsprekel and Prinz, 2000; Deller, 2006), pixel based, subpixel based (Dehaan and Taylor, 2004; Cudahy et al., 2006) and object-oriented classification.

### ***ALOS PALSAR and Radarsat-2 data***

The full-polarimetric Radarsat-2 and ALOS PALSAR data were newly acquired (table IV-1) in 2009 and 2010 (ESA project – SOAR 6788). The data were processed using the Polsarpro, Nest, and ASF MapReady software. The Radarsat 2 Fine Quad polarization data were multilooked with three azimuth to one range looks. The ALOS PALSAR data multilooking parameters were set at seven azimuth looks to one range look. The data scattering matrix was transformed into three band Pauli decomposition channels (Cloude and Pottier, 1996). The three channels correspond to elements of the scattering matrix such that RGB color bands correspond to the components  $S_{hh}-S_{vv}$ ,  $2*S_{hv}$ , and  $S_{hh}+S_{vv}$ , respectively of the scattering matrix  $S$ . The Pauli decomposition is often used for visual inspection of the data and visual classification; however, automated classifications based on Pauli decomposition source bands were reported as well (Huang et al., 2011). The Pauli decomposition images were then terrain corrected with the SAR simulation terrain correction algorithm (Schreier, 1993) utilizing the SRTM-3 as DEM source and 14.5 m and 30 m pixel spacing for Radarsat-2 and ALOS PALSAR respectively. The Radarsat-2 terrain corrected data were resampled to 30 m spatial resolution using a bilinear resampling method. Polarimetric classification is usually applied via classifying the four polarimetric channels, or classification based on polarimetric decompositions of the scattering matrix e.g. Cloude-Pottier decomposition (Cloude, 1997) or Freeman-Durden decompositions (McNairn et al., 2009).

### ***SRTM data***

The SRTM (Shuttle Radar Topography Mission) elevation model was accessed for the determination of geomorphological parameters of the earth's surface, which are controlled by the underlying geology, weathering, and regolith distribution. The SRTM global digital elevation processed data (Reuter et al., 2007) was acquired from the CGIAR (Consultative Group on International Agricultural Research) institute (Jarvis et al., 2008). This model supplied 90 m spatial resolution elevation data over the studied area. The data were reinterpolated using the method of Hutchinson (1989) at 30 m resolution. Derivatives of the elevation data were created to characterize the morphological parameters of the surfaces. These layers include slope, slope roughness (standard deviation of slope), curvature (Zeverbergen and Thorne, 1987), relative relief (elevation difference), and hypsometric integral (Pike and Wilson, 1971) in a 3x3 pixel window. Hydrologic network was derived as well using flow direction and flow accumulation raster where threshold of 6000 was selected to pick the main streams in the area. Euclidean distance to the streams was calculated and

relative height above the streams was derived in order to characterize the relative height of the surfaces above the current erosional base level. Landform mapping or geological mapping based on feature extraction from digital elevation models is a standard procedure and is becoming with the advent high precision and resolution DEMs acquired by LiDAR (Light Detection and Ranging) one of the recent research highlights (Grebby et al., 2010, Grebby et al., 2011; Mulder et al., 2011).

### ***Gamma ray spectrometry data***

The gamma ray signal sensed over the surface of the Earth reflects the content and distribution of the radioactive elements in both rocks and the derived regolith material including anomalies created by geochemical alterations (mineralization, hydrothermal alterations, weathering). Gamma ray spectrometry serves well as a tool for efficient regolith mapping (Jaques et al., 1997; Wilford et al., 1997; Martelet et al., 2006). It reveals the chemical properties of approximately the first 30 cm layer of the Earth's crust (Minty, 1997). The gamma ray spectrometry data were acquired during the 1998–1999 SYSMIN project. The data were supplied as corrected, NASVD (Noise-Adjusted Singular Value decomposition) smoothed (Hovgaard and Grasty, 1997) K, eU, eTh concentrations (U and Th are calculated based on gamma ray emissions from their daughter elements  $^{214}\text{Bi}$  and  $^{208}\text{Tl}$ , respectively and assumed equilibrium in the decay series) and were subsequently gridded at 125 m spatial resolution using the minimum curvature interpolation (Briggs, 1974). For the purposes of classification, the data were resampled to 30 m with the bilinear resampling method. Different techniques are proposed in the analysis of airborne gamma ray spectrometry data ranging from the ratios of the radiometric channels (Dickson and Scott, 1997; Wilford et al., 1997), color composites, and color space transformations (Jaques et al., 1997) to integrations with optical and near-infrared datasets (Anderson and Nash, 1997; Schetselaar et al., 2000). The eTh/K, eU/K, and eU/eTh images were derived from the original data in order to reduce the regional trends that might exist in the data.

## **3.2 Training-testing data selection**

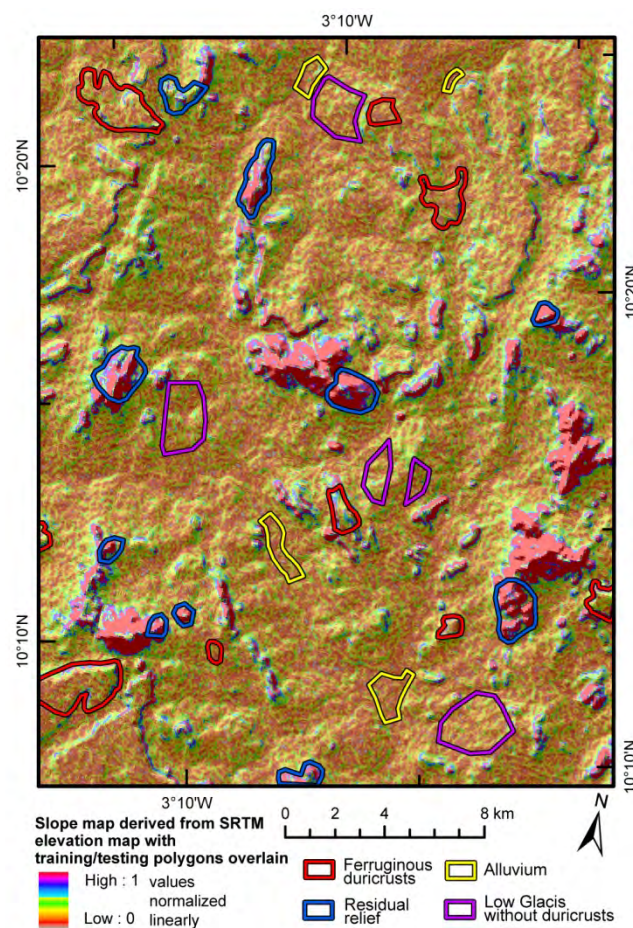
Optimal determination of training data is a crucial element during any classification (Campbell, 1996; Congalton and Green, 2009). For the application of neural networks, the normality and homogeneity of the training classes should not be as important for the classification is not necessarily linear. The training samples should generally cover the whole range of input values, so that optimal classification rules may be set. It is also beneficial to include boundary pixels, which was also one of the criteria for the sample selection.

The training data were selected based on visual analysis of the data, field observations, and existing geomorphological maps and data (IGN, 2005; Brossard, 2006). A total of 56449 pixels (table IV-2) have been selected from the full 762733 pixels covering the study area representing 13% of the

Class	N. of Training pixels	N. of Testing pixels
High/Middle glacis	8665	8665
Residual relief	8447	8446
Alluvium	2719	2718
Low glacis	8395	8394

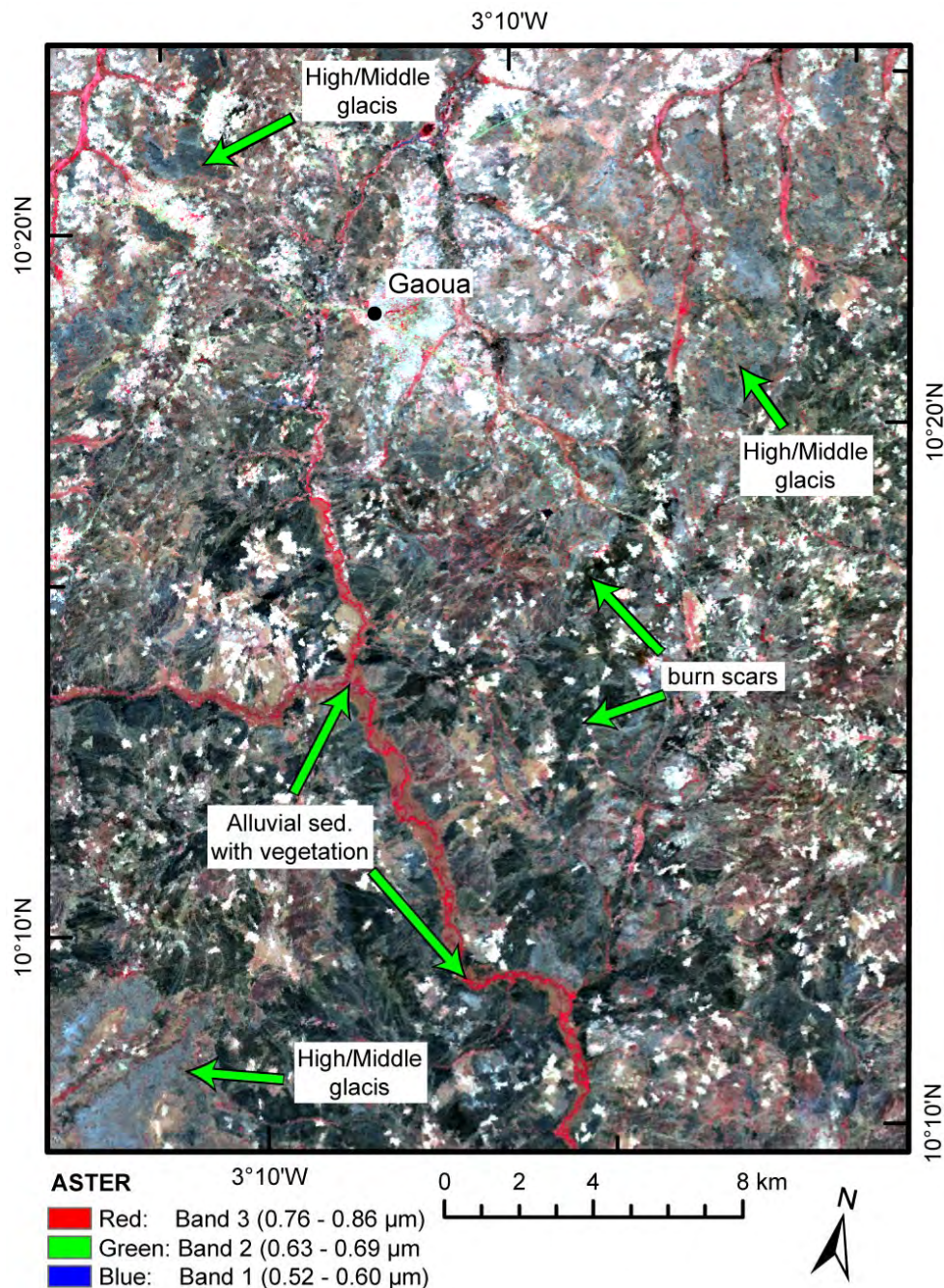
**Table IV-2** Training and testing pixels for the mapped classes, N. – number.

total area. An et al. (1995) demonstrated that increase in the number of training samples does not result in a significant change of the classification accuracy while using 0.23% and 0.76% of total



**Figure IV-4** An overview map with normalized slope values draped over shaded relief of the SRTM digital elevation model; the distribution of the training/testing polygons used in the classifications is given.

pixels for training. The areas selected for training and testing are depicted in figure IV-4. Random sampling was used to select half of the data applied to training and half for accuracy assessment. The training/testing areas are evenly distributed (figure IV-4) through the study area and appropriate coverage for each class should be satisfied. The number of training/testing pixels complies with the



**Figure IV-5** ASTER VNIR image showing the study area. Geomorphological units are marked along with examples of burn scars. Small white rectangular patches correspond to agricultural fields.

requirement for the quantity of training/testing samples for classification and subsequent accuracy assessment as discussed by (Congalton and Green, 2009).

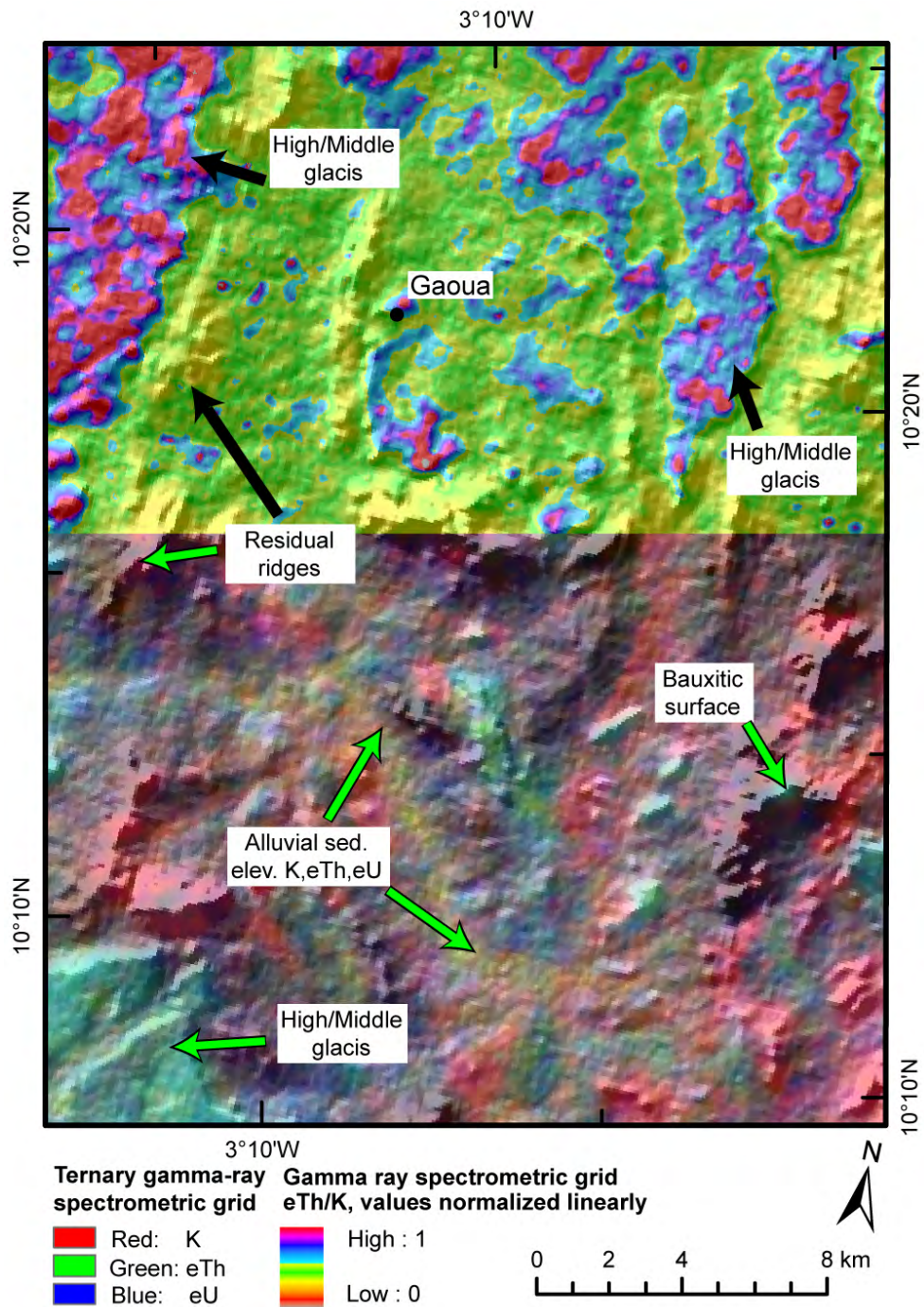
### 3.3 Variable definition

#### *Lateritic duricrusts of the High and Middle glacia*

The lateritic duricrusts form gently inclined or flat plateaus. In the SRTM data, these surfaces form elevated areas with sharp edges well visible in the slope image (figure IV-4). The relative relief and relative height above stream network show uniform distribution of values without large differences in the values. The visible and infrared spectral signatures of the plateaus show typical haematite, goethite absorption features causing an overall lower reflectance (figure IV-5) with a decreasing trend towards the shorter wavelengths bands 1-4 Landsat and 1-3 ASTER. Usually a second weaker absorption in band 7 Landsat and bands 6 and 7 ASTER connected with kaolinite content may be observable for some surfaces. There is usually no visible soil development. The thermal infrared data do not reveal a particular signature for the duricrust layers. Vegetation cover may mask the visible and infrared signature of the duricrust surfaces. In the gamma-ray spectrometry (figure IV-6) data, lateritic duricrusts accumulate both thorium and uranium, which makes them easily separable especially in the eTh/K ratio image. In the polarimetric data (figure IV-7), these surfaces are usually uniform with low backscatter the prevailing scattering mechanism is even bounce. All of the discussed variables show potential as descriptor variables for the classification.

#### *Residual relief and rock outcrops*

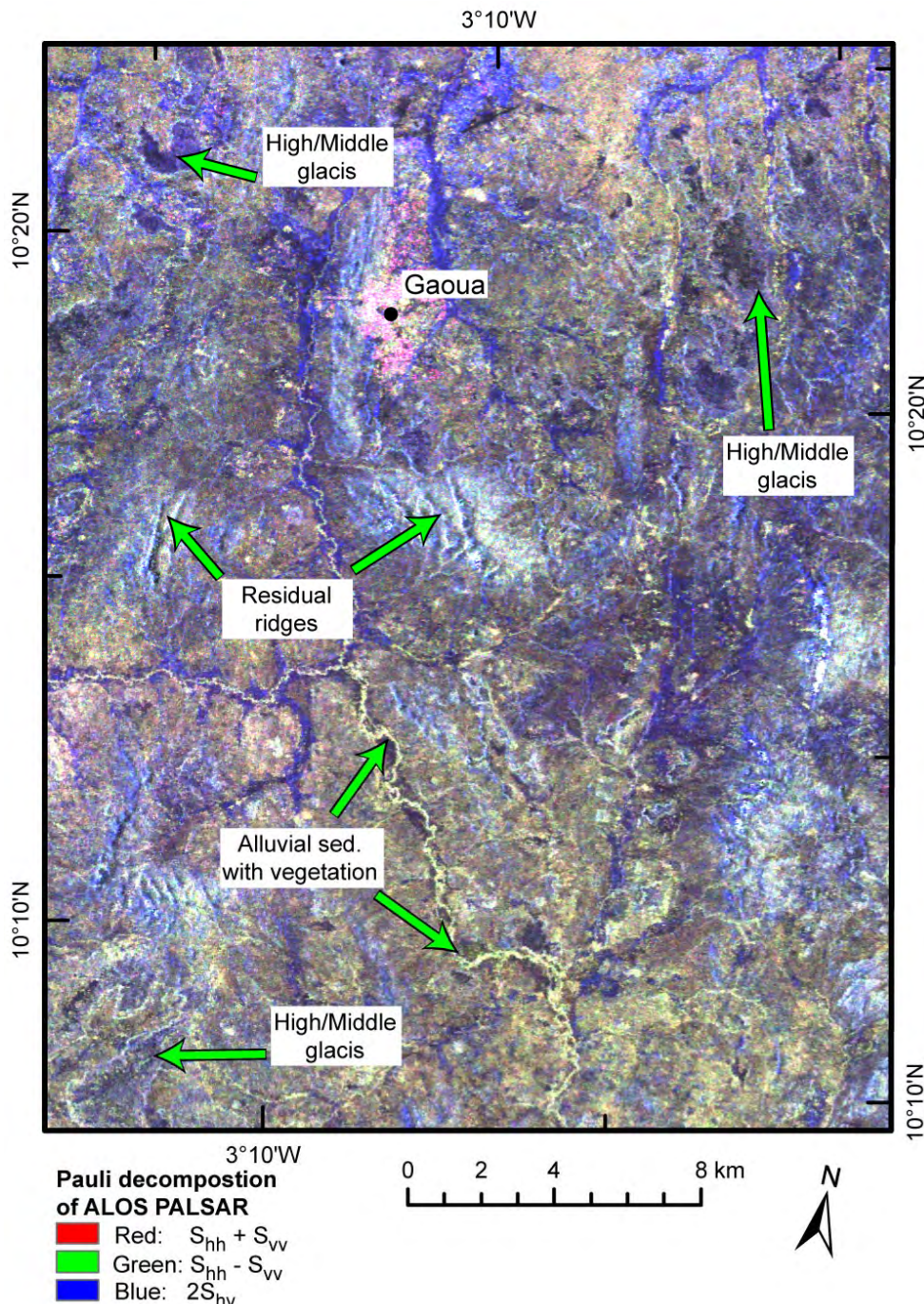
The Residual relief including also rock outcrops is best characterized by SRTM data and its derivatives. The unit consists of erosional ridges, where slope, relief, and curvature values reach high values compared to the other rather flat units. The spectral properties of the surfaces are again highly variable due to different proportions of vegetation cover, exposed soil, and outcropping basement rocks. All of the inselbergs in the Gaoua area belong to the greenstone belt lithologies including both volcano-sedimentary and volcanic rocks. The spectra of exposed rock surfaces might contain specific absorptions related especially to chlorite due to regional greenschist metamorphism. The unmetamorphosed granitic rocks usually form flat outcrops, which have a limited extent and do not crop out well in the study area. The radiometric data show relatively lower values for most of the radioelements over the basic rocks. Some of the andesitic layers show an increase in potassium levels visible in the RGB color composite of K, eTh, eU channels. The polarimetric data show high backscatter and no apparent affinity to particular scattering mechanism; however, volume scattering may play a significant role due to vegetation cover.



**Figure IV-6** Combined image with ratio  $eTh/K$  image (upper half of the image) and ternary radiometric image  $K, eTh, eU$  as RGB (lower half of the image) draped over shaded relief of the SRTM digital elevation model; the geomorphological units are marked with arrows, elev - elevated.

### Alluvial sediments of the valleys

The alluvial sediments that fill the bottom of the valleys form flat surfaces with distinct parameters in the SRTM elevation data and the derived datasets. Additionally the infill abundantly exposes clay rich surfaces and thus generates spectrally distinct properties. Rather dense tree lines also



**Figure IV-7** Pauli decomposition of ALOS PALSAR data with the geomorphological units marked where possible. Blue areas correspond to single bounce scattering, red around the Town of Gaoua – double bounce scattering (buildings), green channel-volume scattering related to vegetation, high intensity, white color – residual ridges.

follow the current stream network and their spectral signatures may be as well accounted for as

indirect indication of the alluvial sediment class. In the radiometric data, the sediments do exhibit elevated values for all radioelements even, as the source materials stem from all of the previously mentioned regolith landform classes. A relative height above the streams and distance to stream layer, derived from the SRTM dataset, has been calculated to constrain the occurrence of the alluvial sediment class to the current stream network.

### ***Soft pediments of the Low glacis***

The Low glacis possesses rather complicated signatures in most of the examined source data, as the characteristics of these surfaces are highly variable. This might be ascribed to the fact that the surface is similar to the alluvial sediments a surface which incorporates material from both the above lying duricrusts and erosional relief. Unlike the alluvial sediments, the Low glacis are variably inclined however, no sharp edges are found and the slope is rather uniform. In the gamma ray data these surfaces show again variable contents of the radioelements probably due to soil formation, where the soil horizon is thick a relative increase in potassium content may be observed. Due to patchy vegetation cover, the spectrometry signature varies accordingly. The soil types vary according to the basement rocks however the variation and the differences between the mainly granitic and greenstone belt lithologies is low. In the radar images, the backscatter is dominated by volume scattering owing to abundant vegetation.

## **3.4 Classification**

Different classification methods have been proposed in the past for regolith landform mapping using remote sensing data and geophysics (Papp, 2002; Wilford et al., 2007; Woolrych and Batty, 2007). The majority of regolith landform maps are still a product of visual analysis of the digitally enhanced data. During the process, we have evaluated spectral classifications based on the analysis of visible and infrared spectral information. The presence of vegetation; however, did not allow for accurate classification results. The main classification method of interest was a non-linear classification approach. Different types of artificial neural network (ANN) algorithms were applied in remote sensing data analysis including, multiperceptron networks (An et al. 1995), probabilistic networks (Zhang et al., 2009), or Kohonen's self-organizing maps (Grebby et al., 2010, 2011). A multiperceptron feedforward neural network classification implemented in ArcGIS environment ADVANGEO (Barth et al., 2009) has been tested. The RPROP backpropagation algorithm (Riedmiller and Braun, 1993) was used to train the network via a non-linear hyperbolic tangent error function. The networks were set up for each class separately and then resulting probability images were combined so that highest probability was assigned to each respective class. The neural networks were designed as three layer networks consisting of one input layer with the number of neurons corresponding to the number of input source layers ( $N$  input neurons), one hidden layer with  $2N + 1$  neurons and one output



neuron. The transfer functions were set to logistic sigmoid function with a steepness (bias) parameter of 0.5. The initialization of the network was tested for both random initializations and using the Nguyen-Widrow algorithm (Nguyen and Widrow, 1990) with no significant differences in classification results. The input layers were linearly normalized between zero and one using the min-max normalization prior to the classification. A limit of 1000 epochs or 0.001 MSE was selected for the termination of the particular training run. Four different scenarios were tested. The base dataset was formed by gamma-ray spectrometry data and SRTM data. Additionally three scenarios incorporating the polarimetric radar, Landsat, and ASTER data were tested. For comparisons a Bayesian maximum likelihood (ML) classification (Campbell, 1996) has been applied to the tested scenarios. The classification was based on the same training data as the neural network classification.

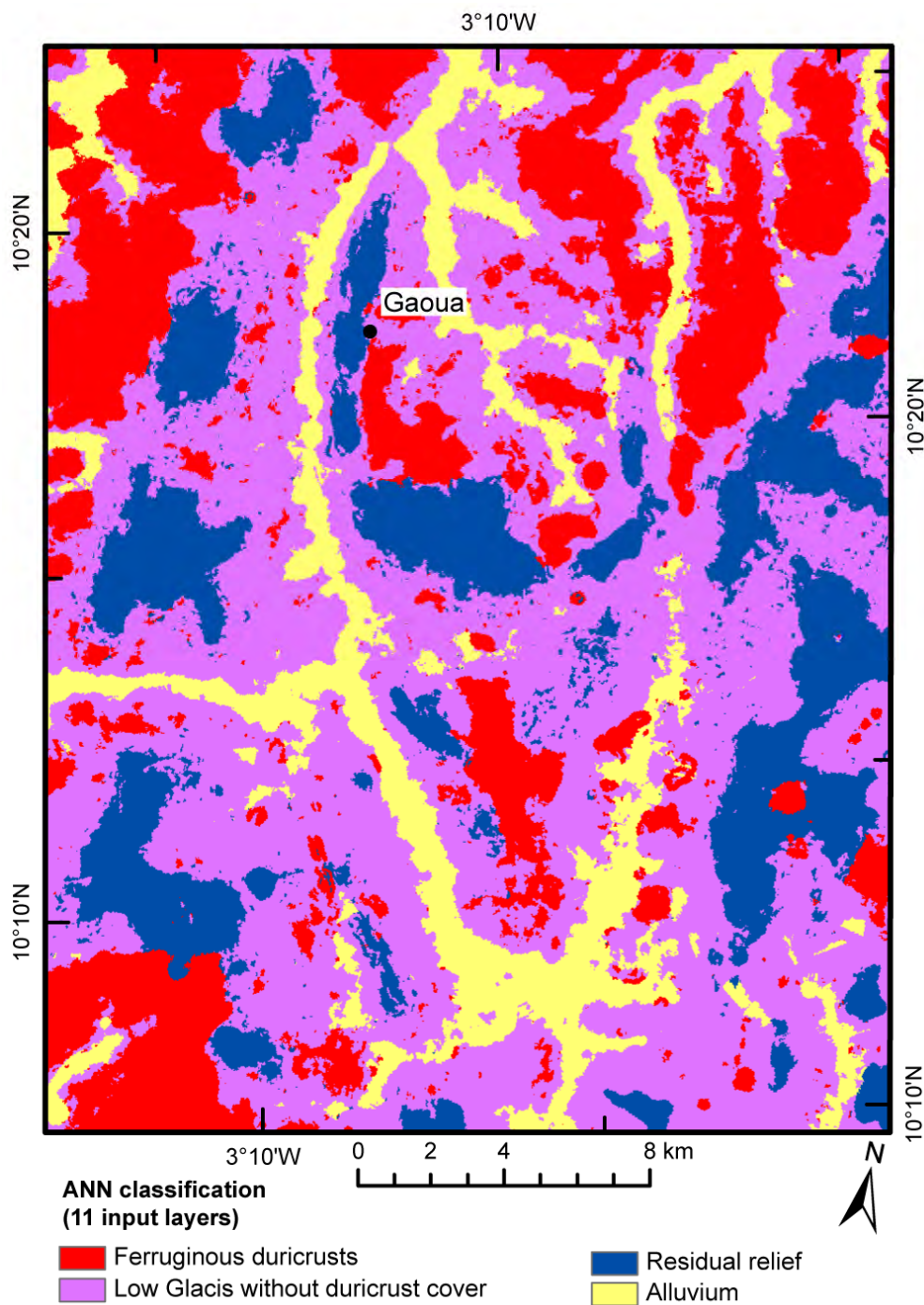
### **3.5 Accuracy assessment**

For accuracy assessment, the traditional approach of confusion matrices (Congalton, 1991; Congalton and Green, 2009) was used employing the testing portion of the training/testing dataset. The decision had been made not to use the existing maps as validation data as obvious errors were noted and the difference in the scale of the mapping may be noted. The concept of confusion matrices is frequently used during classifications of remote sensing data and provides several statistical measures, which can be used to quantify the accuracy of the classification. The overall accuracy gives the percentage of correctly classified pixels and the producers and users accuracies help in assessing individual class accuracies. An important measure is the kappa coefficient, which compares the classification with a result of a random assignment of pixels to the classes of interest.

## 4. Results

### 4.1 Neural network classification

The best result was obtained for the classification of 11 bands including the derivatives of the SRTM digital elevation model and the gamma-spectrometry data (figure IV-8). For this classification,



**Figure IV-8** Result of the neural network classification based on 11 input layers. red – Fe-rich duricrusts of the High/Middle glacis, blue – Residual relief, yellow – Alluvium, magenta – Low glacis.

all of the gamma-spectrometry images computed was used although correlation exists especially between K and eTh values. All of the classes seem to be correctly classified in this experiment

Validation Class	Predicted class					
	High/Mid. gl.	Res relief	Alluv.	Low glacis	Total	Prod. Acc. %
High/Mid. gl.	8377	17	17	254	8665	96.68
Res. relief	27	8138	0	281	8446	96.35
Alluvium	0	0	2650	68	2718	97.50
Low glacis	189	154	201	7850	8394	93.52
Total	8593	8309	2868	8453	28223	
User Acc. %	97.49	97.94	92.40	92.87		
Overall accuracy = 95.71 %, K = 0.94						

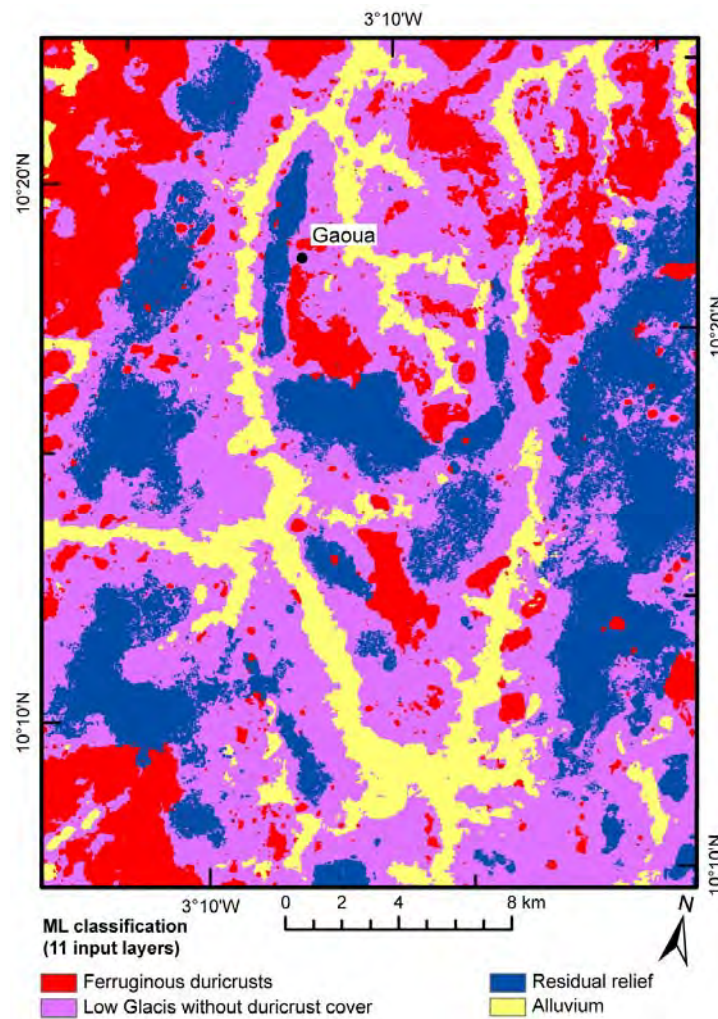
**Table IV-3** Confusion matrix for neural network classification compared with the validation data using 11 source data layers including only SRTM derivatives and gamma-ray spectrometry data.

(table IV-3). The lowest producer accuracy 93.52% was achieved for the class of Low glacis, which also shares the second lowest users' accuracy of 92.87%. The Low glacis represent a class of mixed surfaces with variable characteristics in both morphometry and gamma spectrometry. In the terrain, the surfaces may often be covered by material derived from the higher situated units (High/Middle glacis, Residual relief) and the surfaces show undulating surface. The highest producer accuracy overall holds the Alluvium class (97.5%). The class is rather well defined especially in the SRTM elevation data. The Alluvium also represents the smallest area compared to the other three classes. This also resulted in smaller amount of training/testing pixels used for this category. The user's accuracy is rather low (92.4%), which means that less pixels are actually classified as Alluvium than those included in the validation dataset. Most of the incorrectly classified pixels belong to the Low glacis, which is the most frequent neighboring class. The difference between the two categories is subtle and depends mostly on the distance to the current stream network and the relative elevation above the pixels defining the streams. The most consistent both in terms of producers and users accuracy are the High/Middle glacis and Residual relief. Both of these classes present accuracy values above 96%. The High and Middle glacis are rather well separable from the other classes thanks to its particular signature in the gamma-ray spectrometry data. Some confusion exists between this category and the Low glacis. When inspecting the resulting image we may encounter obvious misclassifications of the High/Middle glacis and the Residual relief especially for the boundary pixels of the glacis, which often form sharp escarpments. Even though we did not include the bauxitic African surface in the training/testing samples, because of its small spatial extent, the bauxitic surface in the southern part of the study area (figure IV-6) has been assigned in the High/Middle glacis class (figures IV-8, IV-9). This does not hold true for all of the classifications, which include additional input layers

(figure IV-10). The Residual relief was mapped correctly and all of the inselbergs and most of the smaller erosional ridges were recognized.

## 4.2 Comparison between all classification scenarios

The classification experiments were constructed consecutively with increasing number of input classes. The full confusion matrix with the number of pixels belonging to each class, the overall, users and producers accuracy along with the kappa coefficient is presented for the best classification in table. Two matrices describing the differences in the outcome of ANN classifier and ML classifier

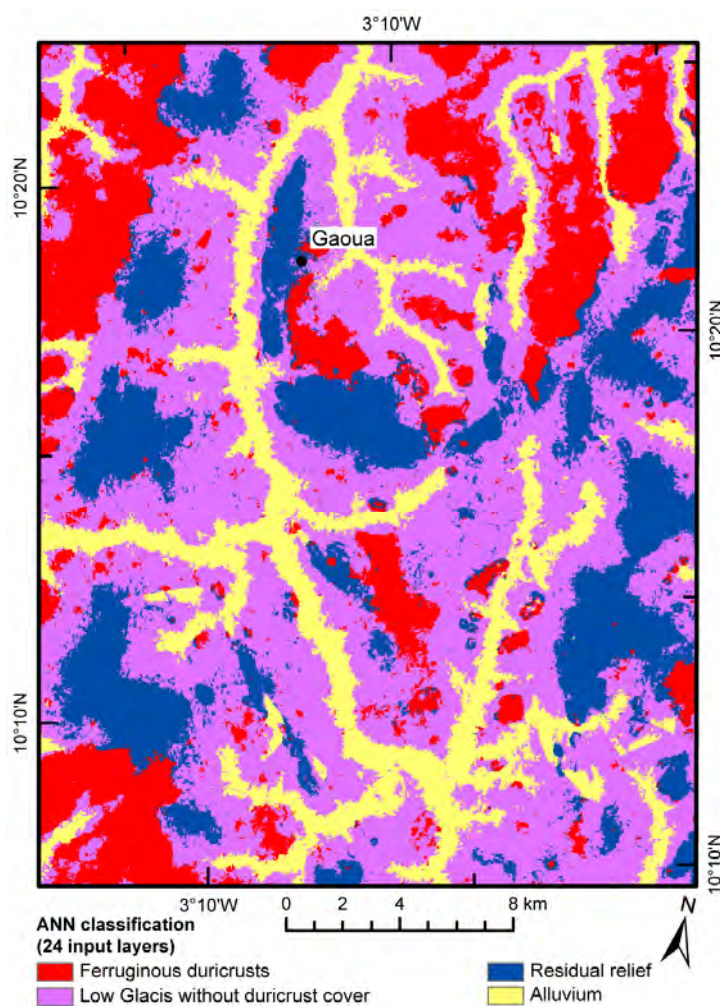


**Figure IV-9** Result of the maximum likelihood classification based on 11 input layers; red – Fe rich duricrusts of the High/Middle glacis, blue – Residual relief, yellow – Alluvium, magenta - Low glacis.

using 24 input layers are displayed in tables 4 and 5. An abbreviated outcome stating the overall accuracy and kappa coefficient for all of the classification experiments is then presented in table IV-6. The neural network classifier performed consistently better than the maximum-likelihood classifier in all of the four scenarios. Important is the fact that the overall classification accuracy generally

decreases with the inclusion of more input layers. The highest overall accuracy and kappa coefficient was obtained for the combination of gamma-ray spectrometry images and derivatives of the SRTM elevation data. Nonetheless, the differences between the classifications are small within 5 percent with the exception of maximum likelihood classifier applied to the combination of gamma-ray spectrometry data, SRTM data, and polarimetric radar data. Here the classification accuracy falls below 90%.

When we further compare the results of the 11-layer neural network classification and the 20 or 24 layer (figure IV-10) classification, which includes all of the available data, we have to conclude that the later produces apparently noisier data. The confusion between the High/Middle glacis and the Residual relief increases quite significantly which results in a drop of both producers and users



**Figure IV-10** Result of the neural network classification based on 24 input layers; red – Fe rich duricrusts of the High/Middle glacis, blue – Residual relief, yellow – Alluvium, magenta – Low glacis.

accuracy. The effect of this misclassification is obvious especially for the boundary pixels as has been already described for the edged of the duricrust plateaus. The duricrust-covered glacis seem to be however better defined from the Low glacis especially in the NW corner of the study area.

Although the maximum likelihood classification provides in terms of classification accuracies satisfactory results for the validation sites when the whole image is compared with the result, stemming from neural network classification of the same input layers considerable differences may be found. The extent of Residual relief class is greatly increased throughout the study area (figure IV-9)

Validation Class	Predicted class					Prod. Acc. %
	High/Mid. gl.	Res. relief	Alluv.	Low glacis	Total	
High/Mid. gl.	8131	173	13	348	8665	93.84
Res. relief	55	8110	0	281	8446	96.02
Alluvium	0	0	2613	105	2718	96.14
Low glacis	242	170	211	7771	8394	92.58
Total	8428	8453	2837	8505	28223	
User Acc. %	96.48	95.94	92.1	91.37		
Overall accuracy = 94.33 %, K = 0.92						

**Table IV-4** Confusion matrix for Neural network classification compared with the validation dataset using 24 source data layers - first 10 PCA bands ASTER, slope, slope roughness, hypsometric integral, residual relief, curvature, height above stream, 6 ALOS PALSAR and Radarsat – 2 Pauli decomposition bands, and two ratio grids  $eTh/K$ ,  $eU/K$ .

Validation Class	Predicted class					Prod. Acc. %
	High/Mid. gl.	Res. relief	Alluv.	Low glacis	Total	
High/Mid. gl.	7951	148	7	559	8665	91.76
Res. relief	550	7376	0	520	8446	87.33
Alluvium	11	8	2441	258	2718	89.81
Low glacis	247	151	105	7891	8394	94.01
Total	8759	7683	2553	9228	28223	
User Acc. %	90.78	96	95.61	85.51		
Overall accuracy = 90.91 %, K = 0.87						

**Table IV-5** Confusion matrix for maximum likelihood classification compared with the validation dataset using 24 source data layers. Layers are the same as in table IV-4.

and the effect is especially noticeable in the central eastern section east of Gaoua town. Confusion also increases between the Residual relief class and High/Middle glacis. Several high peaks become misclassified as High/Middle glacis. An increase in class of the Alluvium at the expense of reduction of the Low glacis is also obvious. The maximum likelihood classification result incorporating 24 input layers is again noisier than the 11 layer classifications (figure IV-11). A particular feature, which can be observed, is the confusion of lower slopes of the Residual relief class with the High/Middle glacis and vice versa mapping of some of the glacis escarpments in Residual relief class.

## 5. Discussion

### 5.1 Comparison with the existing maps

The neural network classification, which is based on an integrated dataset formed by gamma-ray spectrometry data and derivatives of the SRTM elevation model, provides the best classification result that might be compared with the existing maps. The differences between the pedo-geomorphological map (Brossard, 2006) and the results of the classifications are evidently tied with

	SRTM(6) Gamma-ray(5*)	Radarsat-2(3) ALOS PALSAR(3) Gamma-ray(2) SRTM(5)	Landsat 7 ETM+(6) Radarsat-2(3) ALOS PALSAR(3) Gamma-ray(2) SRTM(5)	ASTER(10**) Radarsat-2(3) ALOS PALSAR(3) Gamma-ray(2) SRTM(5)
N. of layers	11	14	20	24
ANN O.A.	95.71 %	93.20 %	94.4 %	94.33 %
Kappa	0.94	0.90	0.92	0.92
ML O.A.	91.55 %	88.78 %	91.04 %	90.91 %
Kappa	0.88	0.84	0.87	0.87

**Table IV-6** Summary of classification results according to the used layers. SRTM – derivative layers (slope, slope roughness, curvature, relative relief, hypsometric integral, height above closest stream), Gamma ray –  $eTh/K$ ,  $eU/K$ ,  $^{40}K$ ,  $eTh$ ,  $eU$ , Radarsat-2 – 3 Pauli decomposition channels, ALOS PALSAR – 3 Pauli decomposition channels, Landsat – 6 bands, ASTER – \*\*first 10 PCA bands. ANN – artificial neural network classification, O. A. – overall accuracy, ML – maximum likelihood classification.

the level of detail. A number of the smaller plateaus and buttes of the High/Middle glacis, which were correctly mapped by the neural network classifier and were verified by field mapping and work of Boeglin (1990), are not shown on either of the existing maps. In addition, the geomorphological map lacks completely even larger plateaus especially in the western part of the study area (see figures IV-3, IV-8, IV-9, and IV-10). The Residual relief class is in the existing maps divided into two or three classes based on the lithology forming the basement, yet the division is highly questionable especially in the geomorphological map. The pedo-geomorphological map draws on the knowledge of existing geological maps. From pedological point of view, the overlying soils are of the same type. Blot et al. (1973) showed that the chemical compositions of the duricrusts and soils depends on the source rock, nonetheless the differences in the radioelement concentrations are too subtle to be mapped by airborne or satellite data. It would be certainly possible to use the existing geological maps to divide the Residual relief class or the Low glacis class and assign an appropriate attribute from the geological map. Based on the result of the automatic classification little or no difference exists between Residual relief over different type of volcanic or volcano-sedimentary rocks. The Low glacis face the same

difficulties. It might be concluded that this class could probably be divided into two classes into Low glacia developing over granitic rocks and the rocks of the greenstone belts; however, differences are subtle and confusion between such two classes would probably be high. The alluvial sediments are defined by the active deposition of material by stream action. The stream network is intermittent in most of the study area while the channels are quite narrow. During the rainy season, frequent floods do occur and alluvial deposits may cover even areas situated further from the stream network and relatively higher from the active stream due to the overall flat morphology. The fact that the eleven source bands perform better than more input bands might be partially explained by the influence of vegetation cover on spectral characteristics of the regolith or rock surfaces (Siegal and Goetz, 1977; Murphy and Wedge, 1994; Serbin et al., 2009). Radar polarimetry is affected in a similar manner. Although longer wavelength L-band radars are partially able to penetrate vegetation cover the effect of volume scattering is quite apparent both in the Pauli decomposition or in Freeman-Durden decomposed data or when examining the H- $\alpha$  plane (Cloude and Pottier, 1996). A large problem noted already by Simpson (1990), Wilford (2002), or Hewson et al. (2006) are burn scars and the cultural activity. Burn scars might be seen in figure IV-4. In spectral data, these areas stand out as anomalous patches where one cannot determine the nature of the underlying material easily. Better results for classifications containing the radar and multispectral data might be expected further to the north in the Sahel zone where less vegetation may be found.

## **5.2 Perspectives for automated regolith landform mapping**

The results obtained favor the neural network classifier over the maximum likelihood. ANN classifications usually outperform standard classification procedures especially while using complex datasets when analyzing geomorphology or geological units (An et al., 1995; Ehsani and Quiel, 2008; Grebby et al., 2011). The prediction of class probability outside of the selected training/testing areas seems to be better for the neural network classifier. Important is also the ability of the network to act as a robust classifier capable of generalization and the ability to suppress layers that do not add information to the classification process. The neural network classification of gamma-ray spectrometry and digital elevation data provides rather uniform units, which are well suited for further post processing and conversion into polygon layers often utilized in regolith landform mapping (Pain et al., 2007). Even better results, in terms of later conversion to standard polygon based maps, would probably be obtained by object oriented classification as described for example by Dragut and Blaschke (2006). The results show that moderate resolution geophysical data and a freely available digital elevation model data provide feasible classification results. The importance of the information from elevation models stresses the requirements on the precision of these models and the level of detail that one can obtain. The application of finer resolution DEMs would probably further improve the accuracy of the classification. A similar effect would most probably have the utilization of high-



resolution gamma ray spectrometry (20–30 m pixel spacing). Visual interpretation of remote sensing and geophysical data certainly plays an important role in today's regolith mapping (Wilford et al., 1997; Craig, 2001; Deller, 2006; Woolrych and Batty, 2007). Automated approaches may provide a more objective interpretation of the spatial distribution of regolith landform units.

## **6. Conclusions**

An automatic approach to regolith landform mapping has been presented in a moderately vegetated region of southwestern Burkina Faso in the Gaoua area. Four main regolith landform units have been mapped with success and thirty-three input layers have been evaluated as candidate input layers for best classification results.

1) Best result was obtained for neural network classification with input layers constituting gamma-ray spectrometry data and derivatives of the SRTM digital elevation model.

2) Additional input layers including multispectral data and polarimetric data did not enhance the classification.

3) The neural network classifier provided overall better result than the standard maximum – likelihood classifier.

4) The results improve the current mapping as they supply higher spatial resolution and correctly identify especially the Fe-rich duricrust plateaus of the High and Middle glacis and areas exposing Residual relief, where erosion has partially uncovered the basement rocks.

5) The map may be employed in guiding geochemical exploration or accessing tectono-geomorphic evolution of the area.

## **Acknowledgements**

The project was funded by French government PhD fellowship to V.M., IRD (Institute de recherche pour le développement) post-doctoral research grant to L.B. and aided logistically by the project “West African Exploration Initiative-Phase I” (<http://waxi2.org>). The polarimetric radar data were kindly provided by ESA/CSA project SOAR-6788. We acknowledge also BEAK Consultants GmbH for giving us access to the ADVANGEO software and A. Knobloch and S. Noack for consultations. Numerous discussions and data provided by D. Chardon, J-L. Grimaud, A. Blot, B. Křibek, and others at various stages of the project significantly contributed to the understanding of West African regolith problematic. We are indebted to the mining companies SEMAFO, Volta Resources, Wega Mining, Sanu Resources, and Orezone for aiding us during fieldwork. We acknowledge in particular A. Naré, M. Crevier, D. Bondé, D. Boisvert, L. Ouedraogo, P. Marquis, A. Zongo, O. Derra, C. Diallo, and T. Amoah.

---

## GENERAL CONCLUSIONS

---

## **Conclusions générales**

L'objectif de cette thèse était double. Il s'agit d'une part de contribuer à la compréhension de l'évolution géodynamique du craton ouest africain à partir des données géologiques situées dans l'ouest du Burkina Faso. Il s'agit d'autre part d'appréhender la distribution du régolithe dans cette même région grâce à l'aide de la géophysique et de la télédétection. La zone d'étude géologique comprenait trois ceintures de roches vertes : Houndé, Boromo, Banfora et les domaines de granitoïdes associés. L'étude consistait en l'acquisition de nouvelles bases de données géologiques, pétrophysiques, et en particulier de données spectrales. Finalement le régolithe de la zone Boromo a été investi au moyen d'un système automatique de télédétection.

Une nouvelle carte litho-structurale a été réalisée en utilisant une méthode d'intégration des données de géophysiques aéroportées, des données satellitaires et des données géologiques de terrain dans un environnement SIG. Les unités lithologiques des ceintures des roches vertes ont été cartographiées, même sous une couverture latéritique. Quatre générations d'intrusions (ME1-ME4) ont été distinguées dans les domaines de granitoïdes, ce qui a des conséquences importantes pour le modèle géodynamique. De nombreuses zones de cisaillement à l'échelle régionale ont été nouvellement découvertes. L'application de la méthodologie de l'intégration des données multiples a un fort potentiel pour la cartographie des régions de l'Afrique de l'Ouest, mal accessibles et couvertes par la végétation et les latérites.

Notre étude de trois ceintures de roches vertes et des granitoïdes associés a mis en évidence trois phases principales de déformation compressive avec une phase potentiellement extensive qui ont contribué à la formation de la croûte continentale juvénile lors de l'orogénèse éburnéenne. Les arguments pétrologiques, structuraux, géochimiques et métamorphiques suggèrent l'existence d'un ou de plusieurs arcs volcaniques qui sont rentrés en collision. La tectonique des plaques opérait déjà à cette époque, même si les mécanismes de croissance crustale étaient modifiés par rapport au présent. Nous proposons un mécanisme par plissement des unités mafiques rigides à grande échelle, mais nous soulignons également le rôle important des granitoïdes dans cette croissance crustale.

Afin d'améliorer les interprétations des données multispectrales et hyperspectrales, une nouvelle bibliothèque spectrale comprenant plus de 700 spectres des roches et surfaces de régolithe, ainsi que des spectres végétaux complémentaires a été créée. L'échelle spectrale de la bibliothèque couvre une gamme entre 0,35  $\mu\text{m}$  et 2,5  $\mu\text{m}$ . Les observations in-situ et les données spectrales acquises montrent l'importance des phénomènes d'altérations météorologiques sur les propriétés spectrales des roches sous des conditions semi-arides. La formation du vernis de roche et des couches ferreuses sur la surface d'altération est contrôlée par la composition lithologique, par la texture et par les caractéristiques structurales des différents types de roches. La variété des signatures spectrales suggère une discrimination possible entre les matériaux échantillonnés, basée sur l'analyse

hyperspectrale. La nouvelle bibliothèque spectrale acquise fournit les informations primaires pour l'analyse des données de télédétection en Afrique de l'Ouest.

Une procédure automatique de classement des unités de régolithe a été présentée. Quatre unités de terrain régolithique - haut/moyen glacis, le relief résiduel, sédiments alluviaux et bas glacis ont été cartographiées. Le meilleur résultat a été obtenu en utilisant la classification des réseaux de neurones pour un scénario composé de 11 couches d'entrée comprenant la spectrométrie gamma aérienne et les dérivations de modèle numérique de terrain. Un ajout de couches d'entrée n'affecte pas de manière significative les résultats de la classification. La méthode de réseaux de neurones a donné de meilleurs résultats que la méthode de vraisemblance maximum. Les résultats représentent une amélioration des cartes existantes, en particulier en termes de précision spatiale et surtout pour les surfaces riches en Fe des haut/moyen glacis et le relief résiduel. Les résultats de cartographie peuvent être utilisés pour la prospection géochimique et l'analyse de l'évolution géomorphologique.

La recherche décrite dans cette thèse démontre l'importance de l'intégration de toutes les sources d'informations disponibles au cours des analyses géologiques et géomorphologiques de régolite menées dans des terrains anciens de l'Afrique. Les études géologiques effectuées dans ces régions peuvent bénéficier de la couverture à grande échelle qui caractérise ces méthodes, mais aussi de leur potentiel à pénétrer sous la couverture régolithique. Le modèle géotectonique proposé présente une nouvelle vue sur l'évolution précoce de la croûte continentale du craton ouest-africain. Le modèle étant basé sur l'intégration de plusieurs méthodologies, apporte une précision améliorée sur la géométrie 3D du système ainsi que la chronologie relative de certaines structures à grande échelle. Les mêmes méthodes fournissent également des données appropriées pour la cartographie et la caractérisation des unités régolithiques développées au dessus du socle.

Avec une disponibilité croissante de nouvelles sources de données qui sont actuellement libérées et qui seront publiées dans les prochaines décennies, des approches similaires à celles proposées dans cette thèse pourront être utilisées dans d'autres régions d'Afrique occidentale et au-delà.

## **GENERAL CONCLUSIONS**

This thesis focuses on enhancing our understanding of geological evolution and regolith distribution, using geophysical and remote sensing methodologies in western Burkina Faso. The area of geological investigations encompassed three greenstone belts, the Houndé, Boromo, Banfora and associated granitoid domains. The study involved the acquisition of new geological, petrophysical and in particular spectral property databases; finally, the regolith of part of the Boromo belt was investigated using an automatic regolith landform mapping system.

As a part of this work, a new synthetic geological map of western Burkina Faso at 1:500 000 scale was created. The map integrates existing and new field data, airborne geophysical and remote sensing data in order to provide a coherent litho-structural framework for the region. We have defined four groups of granitoid intrusions and related gabbros based on petrochemistry and magnetic data. The granitoid domains consist of many generations of individual intrusions. This has significant implications for the overall geotectonic model. Relic F1 fold hinges were recognized in the magnetic data within the Houndé and Banfora greenstone belts. The D1 structures are generally overprinted by S2 shear zones. Several new S2 shear zones were identified in magnetic data, including the Bossié shear zone transecting the Sidéradougou granitoid domain and abundant small-scale shear zones overprinting granites and other lithologies. Airborne gamma ray spectrometry data and SRTM digital elevation models allow for lithological discrimination in areas where regolith cover is minimal. At least three generations of doleritic dykes, oriented N40°, N100°, N120°, were identified in magnetic data. All three generations crosscut the Paleoproterozoic basement and two of them (N40°, N100°) intrude the sediments of the Taoudeni basin.

In total, three deformation events were identified in the polyphase orogenic cycle that has taken place in the study area. Two of the events play a key role in the crustal accretion during the Eburnean orogeny. The geochemical signature of the volcanic rocks is compatible with the evolution from tholeiitic oceanic crust or oceanic plateau to juvenile volcanic island arcs. Zinc and copper deposits are related to this volcanic arc stage. Lateral compression led to an E-W shortening of volcanic arcs during the D1 deformation events, accompanied by syntectonic emplacement of voluminous TTG and granitoid plutons. A megacrystic tholeiitic basalt unit allowed us to establish stratigraphic correlations between the Houndé and Boromo greenstone belts and propose a crustal scale anticline (D1). Shallow water Tarkwaian-type sediments were deposited during the late stages of the D1 phase. Their deposition was structurally controlled by faults, which were later reactivated as the Boni shear zone. When the orogen reached a critical thickness and the weak and hot mantle was not able to support further thickening, the deformation mechanism switched from E-W to WNW-oriented compression, to a transpression of the same orientation. An interconnected network of steeply dipping regional-scale transcurrent high strain zones, often bearing gold mineralization, characterizes the D2 deformation. Pluton emplacement contributed to the structural evolution of the greenstone belts

at local scales; however, coaxial shortening of the stiffer volcanic units supported by coeval magma input controlled the regional scale system geometry. The late-Eburnean or Pan-African N-S compression D3 is responsible for E-W trending crenulation cleavage, kink folds and shallow north or south dipping thrust faults.

In order to improve interpretations based on multispectral and hyperspectral remote sensing data, a new spectral library, containing over 700 spectra of rock and regolith surfaces with complementary spectra of vegetation, was created. The spectral range of the library (0.35  $\mu\text{m}$  to 2.5  $\mu\text{m}$ ) allows direct comparisons with remote sensing data acquired by satellites such as Landsat, ASTER, or Hyperion. The field observations and acquired spectral data show the importance of weathering related phenomena on the spectral properties of rock under semi-arid conditions. The lithological composition, texture, and structural features of the different rock types control the formation of rock varnish and iron coatings on the weathered surfaces. The Fe, Mg-OH absorption features related to the content of chlorite, amphibole, pyroxene, and epidote in mafic to intermediate volcanic rocks and the TTGs produce distinct spectral features centered at 2.33–2.34  $\mu\text{m}$  and 2.25  $\mu\text{m}$ . Al-OH absorptions around 2.2  $\mu\text{m}$  related to kaolinite, smectite, and muscovite/illite minerals are observable in the spectra of granitic rocks, sediments, and all of the weathered rock and soil surfaces. Ferrous iron and ferric iron absorptions situated around 1.0  $\mu\text{m}$ , 0.9–0.8  $\mu\text{m}$ , 0.65  $\mu\text{m}$ , and below 0.6  $\mu\text{m}$  are indicative of iron rich minerals. In the case of fresh rock surfaces of the gabbros, basalts, andesites and the TTGs these absorptions are tied to chlorite, amphibole, pyroxene, and biotite content. An abundance of hematite and goethite may be observed in most of the sampled weathered surfaces of rocks, soils, and Fe-rich duricrusts. The variation in spectral signatures implies that discrimination between the sampled materials based on hyperspectral data analysis should be possible. The newly acquired spectral library provides primary information for the analysis of remote sensing data in West Africa and other regions with similar combinations of climate and geology such as Australia.

An automatic approach to regolith landform mapping has been presented in a moderately vegetated region of southwestern Burkina Faso near the town of Gaoua. Four main regolith landform units constituting the High/Middle glaciais, Residual relief, Alluvial sediments, and soft pediments of the Low glaciais have been mapped in the area. Thirty-three input layers have been evaluated as candidate input layers during the classifications including data from airborne gamma-ray spectrometry, SRTM elevation model, Landsat, ASTER, Radarsat-2, and ALOS PALSAR sensor systems. The best results were obtained for neural network classification with input layers consisting of gamma-ray spectrometry data and derivatives of the SRTM digital elevation model. Classification based on additional input layers including multispectral data and polarimetric radar data did not enhance the classifications. This stresses the importance of high-resolution digital elevation data and gamma-ray spectrometry data for the analysis of regolith terrains similar to the Gaoua area. The neural network classifier provided an overall better result than the standard maximum -likelihood classifier in

all of the tested classifications scenarios. The results improve the current results of geomorphological or pedo-geomorphological regolith landform mapping as they furnish higher spatial resolution of the regolith landform units and correctly identified especially the Fe-rich duricrust plateaus of the high and Middle glaciais as well as areas exposing Residual relief, where erosion has partially uncovered the basement rocks. The resulting classification map may be employed in guiding geochemical exploration or accessing tectono-geomorphic evolution of the area.

The research described in this thesis demonstrates the importance of integrating all available information sources during geological and regolith analyses conducted in ancient terrains of Africa. Geological studies performed in these regions may profit from the large-scale view supplied by the methods and from the ability to penetrate regolith cover. The derived geotectonic model presents a new view on the early development of continental crust in the West African Craton. As the model is based on an integration of several methodologies, it supplies improved accuracy of the 3D geometry of the system as well as the relative chronology of some of the large-scale structures. In order to characterize and map the regolith landform units, which developed over the basement lithologies same methods provide sufficient data for successful automatic classifications.

In the future further investigations related especially to absolute dating of the major types of lithologies will answer some of the uncertainties regarding the timing of pluton emplacement and timing of the deformation events described. The automatic method of regolith landform mapping may be easily extended to the remaining area of Burkina Faso and other countries of the West African Craton, where coverage of at least moderate resolution gamma spectrometry and elevation data exists. In order to utilize fully the spectral measurements, further data of vegetation species may be collected. Automatic classifications of the rock and regolith surfaces may be attempted provided hyperspectral data of sufficient spatial resolution will become available. With an increasing availability of new sources of data, which are currently being released and will be released over the next decades, similar approaches that integrate multiple data sources or use state of the art geophysical methods and remote sensing sensors may be used in other regions of West Africa and beyond.

---

## REFERENCES

---



---

**REFERENCES**

- Abouchami, W., Boher, M., Michard, A., Albarède, F., 1990. A major 2.1 Ga event of mafic magmatism in West Africa; an early stage of crustal accretion. *J. Geophys. Res. B Solid Earth and Planets* 95, 17605–17629.
- Agyei Duodu, J., Loh, G.K., Hirdes, W., Boamah, K.O., Baba, M., Anokwa, Y.M., Asare, C., Brakohiapa, E., Mensah, R.B., Okla, R., Toloczyki, M., Davis, D.W., Glück, S., 2010. Geological map of Ghana 1:1 000 000. BGS, GGS, Accra (Ghana), Hannover (Germany).
- Aitken, A.R.A., Betts, P.G., 2009a. Constraints on the Proterozoic supercontinent cycle from the structural evolution of the south-central Musgrave Province, central Australia. *Precambrian Res.* 168, 284–300.
- Aitken, A.R.A., Betts, P.G., 2009b. Multi-scale integrated structural and aeromagnetic analysis to guide tectonic models: An example from the eastern Musgrave Province, Central Australia. *Tectonophysics* 476, 418–435.
- Albouy, Y., Boukeke, D., Legeley-Padovani, A., Villeneuve, J., Foy, R., Bonvalot, S., El Abbass, T., Poudjhom, Y., 1992. Données gravimétriques ORSTOM Afrique - Madagascar, Exploration Minière, Recherches d'Eau et Environnement, Ouagadougou, 1–14.
- Allibone, A., Teasdale, J., Cameron, G., Etheridge, M., Uttley, P., Soboh, A., Appiah-Kubi, J., Adanu, A., Arthur, R., Mamphye, J., Odoom, B., Zuta, J., Tsikata, A., Pataye, F., Famiyeh, S., Lamb, E., 2002. Timing and structural controls on gold mineralization at the Bogoso gold mine, Ghana, West Africa. *Econ. Geol.* 97, 949–969.
- Alric, G., 1990. Géochimie du volcanisme birimien (Protérozoïque inférieur) de l'Unité de Haute-Comoé. N-E de la Côte-d'Ivoire: Premiers résultats. *J. Afr. Earth Sci.* 10, 669–681.
- Ama Salah, I., Liégeois, J.P., Pouclet, A., 1996. Evolution d'un arc insulaire océanique birimien précoce au Liptako nigérien (Sirba): géologie, géochronologie et géochimie. *J. Afr. Earth Sci.* 22, 235–254.
- An, P., Chung, C.F., Rencz, A.N., 1995. Digital lithology mapping from airborne geophysical and remote sensing data in the Melville Peninsula, Northern Canada, using a neural network approach. *Remote Sens. Environ.* 53, 76–84.
- Annand, R.R., Paine, C., 2002. Regolith geology of the Yilgarn Craton, Western Australia: implications for exploration. *Aust. J. Earth Sci.* 49, 3–162.
- Anderson, H., Nash, C., 1997. Integrated lithostructural mapping of the Rossing area, Namibia using high resolution aeromagnetic, radiometric, Landsat data and aerial photographs. *Explor. Geophys.* 28, 185–191.
- Arndt, N.T., Albarède, E., Nisbet, E.G., 1997. Mafic and ultramafic magmatism, in: De Wit, M.J., Ashwaal, L.D. (Eds.), *Greenstone Belts*. Clarendon Press, Oxford, 233–254.

- Arnould, M., 1961. Etude géologique des migmatites et des granites précambriens du Nord-Est de la Côte d'Ivoire et de la Haute Volta méridionale. BRGM, Paris.
- Ashwal, L.D., Morrison, D.A., Phinney, W.C., Wood, J., 1983. Origin of Archean anorthosites; evidence from the Bad Vermilion Lake anorthosite complex, Ontario. *Contrib. Mineral. Petrol.* 82, 259–273.
- Attoh, K., 1982. Structure, gravity models and stratigraphy of an early Proterozoic volcanic-sedimentary belt in northeastern Ghana. *Precambrian Res.* 18, 275–290.
- Baghdadi, N., Grandjean, G., Lahondere, D., Paillou, P., Lasne, Y., 2005. Apport de l'imagerie satellitaire radar pour l'exploration géologique en zones arides C. R. *Geoscience*, 337, 719–728.
- Baldrige, A.M., Hook, S.J., Grove, C.I., Rivera, G., 2009. The ASTER spectral library version 2.0, *Remote Sens. of Environ.* 113, 711–715.
- Bamba, O., Parisot, J.C., Grandin, G., Beauvais A., 2002. Ferricrite genesis and supergene gold behaviour in Burkina Faso, West Africa. *Geochem. Explor. Environ. Anal.* 2, 3–14.
- Barth, A., Noack, S., Schmidt, F., Irkhin, A., 2009. Use of artificial intelligence for prediction of geo-spatial events: background, software and case studies. *Africa GIS 2009. International Conference on Geo-Spatial Information & sustainable Development in Africa; facing Challenges of Global Changes. 26th-30th October 2009, Kampala/Uganda, Book of Abstracts*, p. 232.
- Bassot, J.P., 1987. Le complexe volcano-plutonique calco-alkali de la riviere dalema (Est Senegal): discussion de sa signification géodynamique dans le cadre de l'orogénie eburnéenne (proterozoïque inférieur). *J. Afr. Earth Sci.* 6, 505-519.
- Beard, P., 2000. Detection and identification of north-south trending magnetic structures near the magnetic equator. *Geophys. Prospect.* 48, 745–761.
- Beauvais, A., 1999. Geochemical balance of lateritisation processes and climatic signatures in weathering profiles overlain by ferricretes in Central Africa. *Geochim. Cosmochim. Acta* 63, 3939–3957.
- Beauvais, A., Ruffet, G., Hénocque, O., Colin, F., 2008. Chemical and physical erosion rhythms of the West African Cenozoic morphogenesis: The <sup>39</sup>Ar-<sup>40</sup>Ar dating of supergene K-Mn oxides. *J. Geophys. Res.* 113, F04007.
- Becvar, M., Hirner, A., Heiden, U., 2008. DLR Spectral Archive, Available online at: [http://cocoon.caf.dlr.de/intro\\_en.html](http://cocoon.caf.dlr.de/intro_en.html) (accessed on: 5/2010).
- Begg, G.C., Griffin, W.L., Natapov, L.M., O'Reilly S.Y., Grand, S.P., O'Neill, C.J., Hronsky, J.M.A., Poudjom Djomani, Y., Swain, C.J., Deen, T., Bowden, P., 2009. The lithospheric architecture of Africa: Seismic tomography, mantle petrology, and tectonic evolution. *Geosphere* 5, 23–50.
- Ben-Dor, E., Chabrilat, S., Dematté, J.A.M., Taylor, G.R., Hill, J., Whiting, M.L., Sommer, S., 2009. Using imaging spectroscopy to study soil properties. *Remote Sens. Environ.* 113, S38–S55.

- Benn, K., Moyen, J.F., 2008. The late Archean Abitibi-Opatoca terrane, Superior Province; a modified oceanic plateau, in: Condie, K.C., Pease, V. (Eds.), *When did plate tectonics begin on planet Earth?* Geological Society of America (GSA):Boulder, CO, United States, United States, 173–197.
- Benn, K., Peschler, A., 2005. A detachment fold model for fault zones in the Late Archean Abitibi greenstone belt. *Tectonophysics* 400, 85–104.
- Bertrand-Sarfati, J., Moussine-Pouchkine, A., Affaton, P., Trompette, R., Bellion, Y., 1990. Cover sequences of the West African craton, in: Dallmeyer, R.D., Lecorche, J.P. (Eds.), *The West African Orogens and Circum-Atlantic Correlatives*. Springer-Verlag, 65–82.
- Bessoles, B., 1977. *Géologie de l’Afrique. Le craton Ouest-Africain*, Mémoires BRGM, Paris, p. 88.
- Betts, P., Williams, H., Stewart, J., Ailleres, L., 2007. Kinematic analysis of aeromagnetic data: Looking at geophysical data in a structural context. *Gondwana Res.* 11, 582–583.
- Betts, P.G., Valenta, R.K., Finlay, J., 2003. Evolution of the Mount Woods inlier, northern Gawler Craton, Southern Australia: an integrated structural and aeromagnetic analysis. *Tectonophysics* 366, 83–111.
- Béziat, D., Bourges, F., Debat, P., Lompo, M., Martin, F., Tollon, F., 2000. A Paleoproterozoic ultramafic-mafic assemblage and associated volcanic rocks of the Boromo greenstone belt: fractionates originating from island-arc volcanic activity in the West African Craton. *Precambrian Res.* 101, 25–47.
- Béziat, D., Dubois, M., Debat, P., Nikiema, S., Salvi, S., Tollon, F., 2008. Gold metallogeny in the Birimian craton of Burkina Faso (West Africa). *J. Afr. Earth Sci.* 50, 215–233.
- Blakely, R.J., Simpson, R.W., 1986. Approximating edges of source bodies from magnetic or gravity anomalies. *Geophysics* 51, 1494–1498.
- Blenkinsop, T.G., Schmidt Mumm, A., Kumi, R., Sangmor, S., 1994. Structural geology of the Ashanti gold mine, Obuasi, Ghana. *Geol. Jahrb.* D100, 131–154.
- Blot, A., 1980. *L’altération des massifs de granite du Sénégal*, Travaux et documents de l’ORSTOM. ORSTOM, Bondy.
- Blot, A., Pion, J.C., Wackermann, J.-M., 1973. Un exemple de corrélation de rang en géochimie: les altérations du socle birimien en zone tropicale sèche (Sénégal oriental et Haute-Volta), *Cahier ORSTOM séries Géologiques*, 25–34.
- Boeglin, J.L., 1990. *Evolution minéralogique et géochimique des cuirassés ferrugineuses de la région de Gaoua (Burkina Faso)*. Doctoral thesis, Univ. Louis Pasteur, Strasbourg.
- Boeglin, J.L., Mazaltarim, D., 1989. Géochimie, degrés d’évolution et lithodépendance des cuirasses ferrugineuses de la région de Gaoua au Burkina Faso. *Bull. Sci. Géol.*, Strasbourg, 42, 27–44.
- Boher, M., Abouchami, W., Michard, A., Albarède, F., Arndt, N.T., 1992. Crustal growth in West Africa at 2.1 Ga. *J. Geophys. Res. B Solid Earth and Planets* 97, 345–369.

- Bonham-Carter, G.F., 1994. Geographic information systems for geoscientists: modelling with GIS  
1ed. Pergamon, Kidlington.
- Bonhomme, M., 1962. Contribution à l'étude géochronologique de la plate-forme de l'Ouest Africain,  
Ann. Fac. Sci. Univ. Clermont-Ferrand, Géol. Minéral., 5.
- Bonkougou, I., 1994. Le Tarkwaïen du sillon de Houndé (Burkina-Faso): Un ensemble volcano-  
détritique acide calcoalcalin à 2.15 Ga. Etude pétrologique, métamorphique et structurale. Univ.  
Nantes.
- Bossière, G., Bonkougou, I., Peucat, J.J., Pupin, J.P., 1996. Origin and age of Paleoproterozoic  
conglomerates and sandstones of the Tarkwaïan Group in Burkina Faso, West Africa.  
Precambrian Res. 80, 153–172.
- Bourges, F., Debat, P., Tollon, F., Munoz, M., Ingles, J., 1998. The geology of the Taparko gold  
deposit, Birimian greenstone belt, Burkina Faso, West Africa. Mineral. Deposita 33, 591–605.
- Boyce, J.I., Morris, W.A., 2002. Basement-controlled faulting of Paleozoic strata in southern Ontario,  
Canada: new evidence from geophysical lineament mapping. Tectonophysics 353, 151–171.
- Briggs, I.C., 1974. Machine contouring using minimum curvature. Geophysics 39, 39–48.
- Bronner, G., Roussel, J., Trompette, R., 1980. Genesis and geodynamic evolution of the Taoudeni  
cratonic basin (Upper Precambrian and Paleozoic), Western Africa. Dyn. Plate Int. Geodyn.  
Series 1, 81–90.
- Brossard, M., 2006. Analyse thématique de données pédologiques sur le Burkina Faso: Application à  
la cartographie des cuirasses ferrugineuses. VALPÉDO, IRD, Montpellier.
- Brown, E.T., Bourles, D.L., Colin, F., Zarakira, S., Raisbeck, G.M., Yiou, F., 1994. The development  
of iron crust lateritic systems in Burkina Faso West Africa examined with in-situ-produced  
cosmogenic nuclides. Earth and Planet. Sci. Lett. 124, 19–33.
- Burke, K., Gunnell, Y., 2008. The African Erosion Surface: A Continental-Scale Synthesis of  
Geomorphology, Tectonics, and Environmental Change over the Past 180 Million Years.  
Geological Society of America Memoirs 201, 1–66.
- Caby, R., Delor, C., Agoh, O., 2000. Lithology, structure and metamorphism of the Birimian  
formations in the Odienné area (Ivory Coast): the major role played by plutonic diapirism and  
strike-slip faulting at the border of the Man Craton. J. Afr. Earth Sci. 30, 351–374.
- Cagnard, F., Brun, J.P., Gapais, D., 2006a. Modes of thickening of analogue weak lithospheres.  
Tectonophysics 421, 145–160.
- Cagnard, F., Durrieu, N., Gapais, D., Brun, J.-P., Ehlers, C., 2006b. Crustal thickening and lateral flow  
during compression of hot lithospheres, with particular reference to Precambrian times. Terra  
Nova 18, 72–78.
- Campbell, J. B., 1996, Introduction to Remote Sensing, 2nd ed., The Guilford Press, New York.
- Castaing, C., Billa, M., Milési, J.P., Thiéblemont, D., Le Métour, J., Egal, E., Donzeau, M., Guerrot,  
C., Cocherie, A., Chèvremont, P., Tegye, M., Itard, Y., Zida, B., Ouedraogo, I., Koté, S.,

- Kabore, B.E., Ouedraogo, C., Ki, J.C., Zunino, C., 2003. Notice explicative de la carte géologique et minière du Burkina Faso à 1/1 000 000.
- Cawood, P.A., Kroener, A., Pisarevsky, S., 2006. Precambrian plate tectonics: Criteria and evidence. *GSA Today* 16, 4–11.
- Chabrillat, S., Goetz, A.F.H., Krosley, L., Olsen, H.W., 2002. Use of hyperspectral images in the identification and mapping of expansive clay soils and the role of spatial resolution. *Remote Sens. Environ.* 82, 431–445.
- Champion, D.C., Cassidy, K.F., Budd, A., 2001. Chapter 8. Overview of the Yilgarn magmatism: implications for crustal development, in: C.E.A. (Ed.), *Characterization and metallogenic significance of Archaean granitoids of the Yilgarn Craton. Western Australia. MERIWA Report*, East Perth.
- Chardon, D., Chevillotte, V., Beauvais, A., Grandin, G., Boulangé, B., 2006. Planation, bauxites and epeirogeny: One or two paleosurfaces on the West African margin? *Geomorphology* 82, 273–282.
- Chardon, D., Choukroune, P., Jayananda, M., 1998. Sinking of the Dharwar Basin (South India); implications for Archaean tectonics. *Precambrian Res.* 91, 15–39.
- Chardon, D., Gapais, D., Cagnard, F., 2009. Flow of ultra-hot orogens: A view from the Precambrian, clues for the Phanerozoic. *Tectonophysics* 477, 105–118.
- Chardon, D., Peucat, J.J., Jayananda, M., Choukroune, P., Fanning, C.M., 2002. Archean granite-greenstone tectonics at Kolar (South India): interplay of diapirism and bulk inhomogeneous contraction during magmatic juvenile accretion. *Tectonics* 21, 1016.
- Chèvremont, P., Donzeau, M., Le Métour, J., Egal, E., Castaing, C., Thiéblemont, D., Tegye, M., Guerrot, C., Billa, M., Itard, Y., Delpont, G., Ki, J.C., 2003. Notice explicative de la Carte géologique du Burkina Faso à 1/200 000, Feuille Koudougou, BRGM, BUMIGEB, Ouagadougou.
- Choukroune, P., Bouhallier, H., Arndt, N.T., 1995. Soft lithosphere during periods of Archaean crustal growth or crustal reworking. *Geological Society Special Publications* 95, 67–86.
- Choukroune, P., Ludden, J.N., Chardon, D., Calvert, A.J., Bouhallier, H., 1997. Archaean crustal growth and tectonic processes; a comparison of the Superior Province, Canada and the Dharwar Craton, India. *Geological Society Special Publications* 121, 63–98.
- Christensen, P.R., Bandfield, J.L., Hamilton, V.E., Howard, D.A., Lane, M.D., Piatek, J.L., Ruff, S.W., Stefanov, W.L., 2000. A thermal emission spectral library of rock-forming minerals, *J. Geophys. Res. (Planets)* 105, 9735–9739.
- Clark, R.N., Roush, T.L., 1984. Reflectance Spectroscopy: Quantitative Analysis Techniques for Remote Sensing Applications. *J. of Geophys. Res.* 89, 6329–6340.
- Clark, R.N., Swayze, G.A., Wise, R., Livo, E., Hoefen, T., Kokaly, R., Sutley, S.J., 2007. USGS Digital Spectral Library splib06a: U.S. Geological Survey, Digital Data Series 231, U.S.

- Geological Survey, Denver, Available online at <http://speclab.cr.usgs.gov/spectral.lib06> (accessed on: 5/2010).
- Clarke, J.D.A., 1994. Geomorphology of the Kambalda region, Western Australia. *Aust. J. Earth Sci.* 41, 229–239.
- Cloude, S.R., 1997. An entropy based classification scheme for land applications of polarimetric SAR. *IEEE Trans. Geosci. Remote Sens.* 35, 68–78.
- Cloude, S.R., Pottier, E., 1996. A review of target decomposition theorems in radar polarimetry. *IEEE Trans. Geosci. Remote Sens.* 34, 498–518.
- Cloutis, E. A., 1992. Weathered and unweathered surface spectra of rocks from cold deserts: identification of weathering processes and remote sensing implications. *Geol. Fören. Stockholm Förhandl.* 114, 181–191.
- Collins, W.J., van Kranendonk, M.J., Teyssier, C., 1998. Partial convective overturn of Archaean crust in the East Pilbara Craton, Western Australia; driving mechanisms and tectonic implications. *J. Struct. Geol.* 20, 1405–1424.
- Commission de Pedologie et de Cartographie des Sols (C.P.C.S.) (1967), *Classification des sol*, Grignon, France.
- Condie, K.C., 1998. Episodic continental growth and supercontinents; a mantle avalanche connection? *Earth Planet. Sci. Lett.* 163, 97–108.
- Condie, K.C., 2005. *Earth as an evolving planetary system*. Elsevier Academic Press, Burlington.
- Condie, K.C., 2008. Did the character of subduction change at the end of the Archean? Constraints from convergent-margin granitoids. *Geology* 36, 611–614.
- Condie, K.C., Pease, V., 2008. When did plate tectonics begin on planet Earth? Geological Society of America (GSA), Boulder.
- Congalton, R.G., 1991. A review of assessing the accuracy of classifications of remotely sensed data. *Remote Sens. Environ.* 37, 35–46.
- Congalton, R.G., Green, K., 2009. *Assessing the accuracy of remotely sensed data: principles and practices*. 2nd ed. Taylor and Francis, Boca Raton.
- Cox, S., 2005. Coupling between deformation, fluid pressures, and fluid flow in ore-producing hydrothermal systems at depth in the crust. *Econ. Geol.* 100, 39–75.
- Craig, M.A., 2001. Regolith mapping for geochemical exploration in the Yilgarn Craton, Western Australia. *Geochem. Explor. Environ. Anal.* 1, 383–390.
- Craig, M.A., Wilford, J.R., Tapley, I.J., 1999. Regolith-landform mapping in the Gawler Craton – an alternative approach. *MESA Journal* 12, 17–21.
- Cudahy, T., Caccetta, M., Wells, M., Skwarnecki, M., 2006, Mapping alteration through the regolith at Kalgoorlie using airborne hyperspectral data, ASEG Extended Abstracts, ASEG 2006 – 18th Geophysical Conference, 2-6 July, Melbourne, 1–8.

- Davis, D.W., Hirdes, W., Schaltegger, U., Nunoo, E.A., 1994. U-Pb age constraints on deposition and provenance of Birimian and gold-bearing Tarkwaian sediments in Ghana, West Africa. *Precambrian Res.* 67, 89–107.
- de Kock G.S., Armstrong, R.A., Siegfried H.P., Thomas E., 2011. Geochronology of the Birim Supergroup of the West African craton in the Wa-Bolé region of west-central Ghana: Implications for the stratigraphic framework. *J. Afr. Earth Sci.* 59, 291–294.
- de Souza Filho, C., Nunes, A., Leite, E., Monteiro, L., Xavier, R., 2007. Spatial analysis of airborne geophysical data applied to geological mapping and mineral prospecting in the Serra Leste Region, Carajás Mineral Province, Brazil. *Surv. Geophys.* 28, 377–405.
- de Wit, M.J., Ashwal, L.D., 1997. *Greenstone Belts*. Oxford University Press, Oxford.
- Debat, P., Nikiema, S., Mercier, A., Lompo, M., Béziat, D., Bourges, F., Roddaz, M., Salvi, S., Tollon, F., Wenmenga, U., 2003. A new metamorphic constraint for the Eburnean orogeny from Paleoproterozoic formations of the Man Shield (Aribinda and Tampilga countries, Burkina Faso). *Precambrian Res.* 123, 47–65.
- Dehaan, R.L., Taylor, G.R., 2004. Field-derived spectra of salinized soils and vegetation as indicators of irrigation-induced salinization. *Remote Sens. Environ.* 80, 406–417.
- Deller, M.E.A., 2006. Facies discrimination in laterites using Landsat Thematic Mapper, ASTER and ALI data—examples from Eritrea and Arabia. *Int. J. Remote Sens.* 27, 2389–2409.
- Delor, C., Siméon, Y., Vidal, M., 1995. Peri-plutonic gravity driven deformations and transcurrent tectonics between 2.2 and 2.1 By: a case study from the Birimian Cycle in Ivory Coast, EUG 8, Strasbourg, 9–13 april 1995, p. 102.
- Denith, M., Clark, D., Featherstone, W., 2009. Aeromagnetic mapping of Precambrian geological structures that controlled the 1968 Meckering earthquake (Ms 6.8): Implications for intraplate seismicity in Western Australia. *Tectonophysics* 475, 544–553.
- Deynoux, M., 1983. Les formations de plate-forme d'âge Précambrien supérieur et Paléozoïque dans l'Ouest africain, corrélation avec les zones mobiles. Pergamon Press, Oxford.
- Dia, A., 1988. Caractères et significations des complexes magmatiques et métamorphiques du secteur de Sandikounda-Laminia (Nord de la boutonnière de Kédougou, Est Sénégal). Un modèle géodynamique du Birimien de l'Afrique de l'Ouest. UCAD, Dakar.
- Dia, A., Van Schmus, W.R., Kroner, A., 1997. Isotopic constraints on the age and formation of a Palaeoproterozoic volcanic arc complex in the Kedougou Inlier, eastern Senegal, West Africa. *J. Afr. Earth Sci.* 24, 197–213.
- Dickson, B.L., Scott, K.M., 1997. Interpretation of aerial gamma-ray surveys—adding the geochemical factors. *AGSO J. Aust. Geol. Geophys.* 17, 187–200.
- Dioh, E., Béziat, D., Grégoire, M., Debat, P., 2009. Origin of rare earth element variations in clinopyroxene from plutonic and associated volcanic rocks from the Fouldé basin, Northern Kédougou inlier, Sénégal, West Africa. *Eur. J. Mineral.* 21, 1029–1043.

- Direen, N.G., Cadd, A.G., Lyons, P., Teasdale, J.P., 2005. Architecture of Proterozoic shear zones in the Christie Domain, western Gawler Craton, Australia: Geophysical appraisal of a poorly exposed orogenic terrane. *Precambrian Res.* 142, 28–44.
- Dorigo, W., Bachmann, M., Heldens, W., 2006. AS Toolbox & Processing of field spectra – User's manual v.1.12, DLR, Munich.
- Dorn, R. I., 2009. Desert rock coatings, in *Geomorphology of desert environments*, 2nd ed., edited by A. J. Parsons, A. D. Abrams, 153–186, Springer, Netherlands.
- Doumbia, S., Pouclet, A., Kouamelan, A., Peucat, J.J., Vidal, M., Delor, C., 1998. Petrogenesis of juvenile-type Birimian (Paleoproterozoic) granitoids in Central Cote-d'Ivoire, West Africa: geochemistry and geochronology. *Precambrian Res.* 87, 33–63.
- Dragut, L., Blaschke, T., 2006. Automated classification of landform elements using object-based image analysis. *Geomorphology* 81, 330–344.
- Drummond, M.S., Defant, M.J., 1990. A model for trondhjemite-tonalite-dacite genesis and crustal growth via slab melting; Archean to modern comparisons. *J Geophys. Res. [Solid Earth]* 95, 21503–21521.
- Drury, S.A., 1993. *Image Interpretation in Geology*, 2nd ed., Chapman and Hall, London.
- Drury, S.A., Hunt, G.A., 1989. Geological uses of remotely-sensed reflected and emitted data of lateritized Archaean terrain in Western Australia. *Int. J. Remote Sens.* 10, 475–497.
- Egal, E., Thiéblemont, D., Lahondère, D., Guerrot, C., Costea, C.A., Iliescu, D., Delor, C., Goujou, J.-C., Lafon, J.M., Tegye, M., 2002. Late Eburnean granitization and tectonics along the western and northwestern margin of the Archean Kenema-Man domain (Guinea, West African Craton). *Precambrian Res.* 117, 57–84.
- Eggleton, R.A. (Ed.), 2001. *The regolith glossary*, CRC LEME, Perth.
- Ehsani, A.H., Quiel, F., 2008. Geomorphometric feature analysis using morphometric parameterization and artificial neural networks. *Geomorphology* 99, 1–12.
- Elvidge, C. D. 1990, Visible and near-infrared reflectance characteristics of dry plant materials, *Int. J. Remote Sens.*, 11, 1775–1795.
- Epema, G. F., B. C. J. Bom 1994, Spatial and temporal variability of field reflectance as a basis for deriving soil surface characteristics from multiscale remote sensing data in Niger, *ITC Journal*, 1, 23–28.
- Eriksson, K.A., Krapez, B., Fralick, P.W., 1994. Sedimentology of Archean greenstone belts; signatures of tectonic evolution. *Earth-Science Reviews* 37, 1–88.
- Feybesse, J.L., 1990. The Bororno-Goren lower Proterozoic "belt" (Burkina-Faso): an example of interference between two Eburnean transcurrent phases. *C. Rend. Acad. Sci. Géosci.* 310, série II, 1353–1360.



- Feybesse, J.L., Billa, M., Guerrot, C., Duguey, E., Lescuyer, J.L., Milési, J.P., Bouchot, V., 2006. The paleoproterozoic Ghanaian province: Geodynamic model and ore controls, including regional stress modeling. *Precambrian Res.* 149, 149–196.
- Feybesse, J.L., Milési, J.P., 1994. The Archaean/Proterozoic contact zone in West Africa: a mountain belt of decollement thrusting and folding on a continental margin related to 2.1 Ga convergence of Archaean cratons? *Precambrian Res.* 69, 199–227.
- Feybesse, J.L., Milési, J.-P., Johan, V., Dommange, A., Calvez, J.-Y., Boher, M., Abouchami, W., 1989. The Archean/Lower Proterozoic boundary of West Africa: a major thrust area predating the Sassandra fault; example of the Odienné and Touba regions (Ivory Coast). *C. Rend. Acad. Sci. Geosci.* 309, série II, 1847–1853.
- Foley, S., 2008. A trace element perspective on Archean crust formation and on the presence or absence of Archean subduction, in: Condie, K.C., Pease, V. (Eds.), *When did plate tectonics begin on planet Earth?* Geological Society of America (GSA), Boulder. 31–50.
- Fraser, S.J., Green, A.A., 1987. A software defoliant for geological analysis of band ratios. *Int. J. Remote Sens.* 8, 525–532.
- Galipp, K., Klemd, R., Hirdes, W., 2003. Metamorphism and geochemistry of the Paleoproterozoic Birimian Sefwi volcanic belt (Ghana, West Africa). *Geol. Jahrb.* D111, 151–191.
- Gapais, D., Cagnard, F., Gueydan, F., Barbey, P., Ballèvre, M., 2009. Mountain building and exhumation processes through time; influences from nature and models. *Terra Nova* 21, 188–194.
- Gasquet, D., Barbey, P., Adou, M., Paquette, J.L., 2003. Structure, Sr-Nd isotope geochemistry and zircon U-Pb geochronology of the granitoids of the Dabakala area (Cote d'Ivoire): evidence for a 2.3 Ga crustal growth event in the Palaeoproterozoic of West Africa? *Precambrian Res.* 127, 329–354.
- Giles, P.T., 1998. Geomorphological signatures: classification of aggregated slope unit objects from digital elevation and remote sensing data. *Earth Surf. Processes Landforms* 23, 581–594.
- Gillespie, A., Rokugawa, S., Matsunaga, T., Cothorn, J.S., Hook, S. & Kahle, A.B., 1998. A temperature and emissivity separation algorithm for Advanced Spaceborne Thermal Emission and Reflection Radiometer (ASTER) images. *IEEE Trans. Geosc. Rem. Sens.* 36, 1113–1126.
- Gomez, C., Delacourt, C., Allemand, P., Ledru, P., Wackerle, R., 2005. Using ASTER remote sensing data set for geological mapping, in Namibia. *Phys. Chem. Earth, Parts A/B/C* 30, 97–108.
- Goscombe, B., Blewett, R.S., Czarnota, K., Groenewald, P.B., Maas, R., 2009. Metamorphic evolution and integrated terrane analysis of the eastern Yilgarn Craton: rationale, methods, outcomes and interpretation, *Geoscience Australia, Record 2009/23*, Canberra.
- Grandin, G., 1976. Aplanissements cuirassés et enrichissement des gisements de manganèse dans quelques régions d'Afrique de l'Ouest, *Mémoire ORSTOM*, Paris.

- Grebby, S., Cunningham, D., Naden, J., Tansey, K. 2010. Lithological mapping of the Troodos ophiolite, Cyprus, using airborne LiDAR topographic data. *Remote Sens. Environ.* 114, 713–724.
- Grebby, S., Naden, J., Cunningham, D., Tansey, K. 2011. Integrating airborne multispectral imagery and airborne LiDAR data for enhanced lithological mapping in vegetated terrain. *Remote Sens. Environ.* 115, 214–226.
- Groves, D.I., Goldfarb, R.J., Robert, F., Hart, C.J.R., 2003. Gold deposits in metamorphic belts: Overview of current understanding, outstanding problems, future research, and exploration significance. *Econ. Geol.* 98, 1–29.
- Gürbüz, A., 2010. Geometric characteristics of pull-apart basins. *Lithosphere* 2, 199–206.
- Gunnell, Y., 2003. Radiometric ages of laterites and constraints on long-term denudation rates in West Africa. *Geology* 31, 131–134.
- Hackney, R., 2004. Gravity anomalies, crustal structure and isostasy associated with the Proterozoic Capricorn Orogen, Western Australia. *Precambrian Res.* 128, 219–236.
- Hastie, A.R., Kerr, A.C., McDonald, I., Mitchell, S.F., Pearce, J.A., Wolstencroft, M., Millar, I.L., 2010. Do Cenozoic analogues support a plate tectonic origin for Earth's earliest continental crust? *Geology* 38, 495–498.
- Hein, K.A.A., 2010. Succession of structural events in the Goren greenstone belt (Burkina Faso): Implications for West African tectonics. *J. Afr. Earth Sci.* 56, 83–94.
- Hein, K.A.A., Morel, V., Kagone, O., Kiemde, F., Mayes, K., 2004. Birimian lithological succession and structural evolution in the Goren segment of the Boromo-Goren Greenstone Belt, Burkina Faso. *J. Afr. Earth Sci.* 39, 1–23.
- Henderson, F., Lewis, A., 1998. Principles and applications of imaging radar. *Manual of Remote Sensing*. 3rd Edition, Volume 2. American Society for Photogrammetry and Remote Sensing. John Wiley & Sons Inc., Canada.
- Henquin, B., Totté, M., 1993. Le traitement d'un modèle numérique de terrain pour la caractérisation du milieu physique: Cas d'étude dans le sud-ouest du Burkina Faso. *Cah. Orstom, sér. Pédol.* 28, 55–65.
- Hewson, R. D., Cudahy, T.J., Mizuhiko, S., Ueda, K., Mauger, A.J., 2005. Seamless geological map generation using ASTER in the Broken Hill-Curnamona province of Australia, *Remote Sens. Environ.*, 99, 159–172.
- Hewson, R.D., Cudahy, T.J., Drake-Brockman, Meyers, J., Hashemi, A., 2006. Mapping geology associated with manganese mineralization using spectral remote sensing techniques at Woodie Woodie, East Pilbara. *Exploration Geophysics* 37, 389–400.
- Hirdes, W., Davis, D.W., 1998. First U-Pb zircon age of extrusive volcanism in the Birimian Supergroup of Ghana/West Africa. *J. Afr. Earth Sci.* 27, 291–294.

- Hirdes, W., Davis, D.W., 2002. U-Pb geochronology of Paleoproterozoic rocks in the southern part of the Kedougou-Kenieba inlier, Senegal, West Africa: evidence for diachronous accretionary development of the Eburnean province. *Precambrian Res.* 118, 83–99.
- Hirdes, W., Davis, D.W., Eisenlohr, B.N., 1992. Reassessment of Proterozoic granitoid ages in Ghana on the basis of U/Pb zircon and monazite dating. *Precambrian Res.* 56, 89–96.
- Hirdes, W., Davis, D.W., Ludtke, G., Konan, G., 1996. Two generations of Birimian (Paleoproterozoic) volcanic belts in northeastern Cote d'Ivoire (West Africa): consequences for the 'Birimian controversy'. *Precambrian Res.* 80, 173–191.
- Holland, T.J.B., Blundy, J., 1994. Non-ideal interactions in calcic amphiboles and their bearing on amphibole-plagioclase thermometry. *Contrib. Mineral. Petrol.* 116, 433–447.
- Hovgaard, J., Grasty, R.L., 1997. Reducing statistical noise in airborne gamma ray data through spectral component analysis, in: Gubins, A.G. (Ed.), *Proceedings Of Exploration 97: Fourth Decennial Conference On Mineral Exploration*. Prospectors and Developers Association of Canada, Toronto, 753–764.
- Huang, L., Li, Z., Tian, B.S., Chen, Q., Liu, J.L., Zhang, R., 2011. Classification and snow line detection for glacial areas using the polarimetric SAR image. *Remote Sens. Environ.* 115, 1721–1732.
- Hueni, A., Nieke, J., Schopfer, J., Kneubuhler, M., Itten, K.I., 2009. The spectral database SPECCHIO for improved long-term usability and data sharing. *Comput. Geosci.* 35, 557–565.
- Hunt, G.R., 1977. Spectral signatures of particulate minerals in the visible and near-infrared. *Geophysics* 42, 501–513.
- Hunt, G.R., Salisbury, J.W., 1970. Visible and near-infrared spectra of minerals and rocks: I. Silicate minerals. *Mod. Geol.* 1, 283–300.
- Hunt, G.R., Salisbury, J.W., Lenhoff, C.J., 1971. Visible and near infrared reflectance spectra of minerals and rocks: III. Oxides and Hydroxides. *Mod. Geol.* 2, 195–205.
- Hunt, G.R., Salisbury, J.W., Lenhoff, C.J., 1973a. Visible and near infrared reflectance spectra of minerals and rocks: VI. Additional silicates. *Mod. Geol.* 4, 85–106.
- Hunt, G.R., Salisbury, J.W., Lenhoff, C.J., 1973b. Visible and near infrared reflectance spectra of minerals and rocks: VIII. Intermediate igneous rocks. *Mod. Geol.* 4, 237–244.
- Hunt, G.R., Salisbury, J.W., Lenhoff, C.J., 1974. Visible and near infrared reflectance spectra of minerals and rocks: IX. Basic and ultrabasic igneous rocks. *Mod. Geol.* 5, 15–22.
- Hutchinson, M.F., 1989. A new procedure for gridding elevation and stream line data with automatic removal of spurious pits. *J. Hydrol.*, 106, 211–232.
- ICRAF-ISRIC, 2010. A Globally Distributed Soil Spectral Library: Visible Near Infrared Diffuse Reflectance Spectra, World Agroforestry Centre (ICRAF) and ISRIC - World Soil Information, Available online at: <http://africasoils.net/data/ICRAF-ISRICspectra> (accessed 01/2011).

- IGN, 2005. Projet BDOT\_2002, BDOT\_1992 - Base de données d'occupation des terres, Burkina Faso, Rapport final, IGN France International, France.
- Irvin, B.J., Ventura, S.J., Slater, B.K., 1997. Fuzzy and isodata classification of landform elements from digital terrain data in Pleasant Valley, Wisconsin. *Geoderma* 77, 137–154.
- Irvine, T.N., Baragar, W.R.A., 1971. A guide to the chemical classification of the common volcanic rocks. *Can. J. Earth Sci.* 8, 523–548.
- James, M., 1988. *Pattern Recognition*, John Wiley and Sons, New York, 36–40.
- Janoušek, V., Farrow, C.M., Erban, V., 2006. Interpretation of whole-rock geochemical data in igneous geochemistry: introducing Geochemical Data Toolkit (GCDkit). *J. Petrol.* 47, 1255–1259
- Jaques, A.L., Wellman, P., Whitaker, A., Wyborn, D., 1997. High-resolution geophysics in modern geological mapping. *AGSO J. Aust. Geol. Geophys.* 17, 159–173.
- Jarvis, A., Reuter, H.I., Nelson, A., Guevara, E., 2008. Hole-filled seamless SRTM data V4. International Centre for Tropical Agriculture (CIAT), <http://srtm.csi.cgiar.org/>, last accessed 10/05/2010.
- Jessell, W.M., Santoul, J., Baratoux, L., Rouse, S., Naba, S., 2010. A more complete database of West African mafic dykes, EGU General Assembly 2010, Vienna, <http://meetingorganizer.copernicus.org/EGU2010/EGU2010-2226-2011.pdf> (last accessed 14/12/2010).
- John, T., Klemm, R., Hirdes, W., Loh, G., 1999. The metamorphic evolution of the Paleoproterozoic (Birimian) volcanic Ashanti belt (Ghana, West Africa). *Precambrian Res.* 98, 11–30.
- Junner, N.R., 1935. Gold in the Gold Coast. *Gold Coast Geol. Surv. Mem.* 4, 1–67.
- Junner, N.R., 1940. Geology of the Gold Coast and western Togoland. *Gold Coast Geol. Surv. Bull.* 11, 1–40.
- Kettles, I.M., Rencz, A.N., Bauke, S.D., 2000. Integrating Landsat, geologic, and airborne gamma ray data as an aid to surficial geology mapping and mineral exploration in the Manitowadge area, Ontario. *Photogramm. Eng. Remote Sens.* 66, 437–445.
- King, L.C., 1962. *The Morphology of the Earth*. Oliver and Boyd, London.
- Kitson, A.E., 1918. Ann. Report, Gold Coast Geol. Surv. for 1916/17, Accra. (non publ.), Accra.
- Klemm, R., Hirdes, W., 1997. Origin of an unusual fluid composition in early Proterozoic palaeoplacer and lode-gold deposits in Birimian greenstone terranes of West Africa. *S. Afr. J. Geol.* 100, 405–414.
- Klemm, R., Hunken, U., Olesch, M., 2002. Metamorphism of the country rocks hosting gold-sulfide-bearing quartz veins in the Paleoproterozoic southern Kibi-Winneba belt (SE-Ghana). *J. Afr. Earth Sci.* 35, 199–211.
- Koté, S., Ouedraogo, I., Donzeau, M., Le Métour, J., Castaing, C., Egal, E., Thiéblemont, D., Tegye, M., Guerrot, C., Chèvremont, P., Milési, J.P., Billa, M., Itard, Y., Ki, J.C., 2003. Notice

- explicative de la Carte géologique du Burkina Faso à 1/200 000, Feuille Léo, BRGM/BUMIGEB, Ouagadougou.
- Kouamelan, A.N., Delor, C., Peucat, J.-J., 1997. Geochronological evidence for reworking of Archean terrains during the Early Proterozoic (2.1 Ga) in the western Côte d'Ivoire (Man Rise-West African Craton). *Precambrian Res.* 86, 177–199.
- Krapez, B., 1989. Depositional Styles and Geotectonic Settings of Archaean Metasedimentary Sequences: Evidence from the Lalla Rookh Basin, Pilbara Block, Western Australia. Univ. Western Australia, Nedlands.
- Kříbek, B., Sýkorová, I., Machovič, V., Laufek, F., 2008. Graphitization of organic matter and fluid-deposited graphite in Palaeoproterozoic (Birimian) black shales of the Kaya-Goren greenstone belt (Burkina Faso, West Africa). *J. Metamorph. Geol.* 26, 937–958.
- Kusky, T.M., Vearncombe, J.R., 1997. Structural aspects, in: de Wit, M.J., Ashwal, L.D. (Eds.), *Greenstone Belts*. Oxford Science Publications, Oxford, 91–123.
- Ladmirant, H., Legrand, J.M., 1977. Notice explicative de la carte géologique au 1/200000 de la feuille de Houndé. Dir. de la Géologie et des Mines, Haute Volta, Ouagadougou.
- Lau, I.C., Cudahy, T.J., Heinson, G., Mauger, A.J., James, P.R., 2003. Practical applications of hyperspectral remote sensing in regolith research, in: Roach, I.C. (Ed.), *Advances in Regolith*. CRC LEME, pp. 249–253.
- Lavaud, T., Beziat, D., Blot, A., Debat, P., Lompo, Martin, F., Ouangrawa, M., Tollon, F., 2004. Paleo-gossans within the lateritic iron crust: example of the nickeliferous prospect of Bonga, Burkina Faso. *J. Afr. Earth Sci.* 39, 465–471.
- Le Métour, J., Chèvremont, P., Donzeau, M., Egal, E., Thiéblemont, D., Tegey, M., Guerrot, C., Billa, M., Itard, Y., Castaing, C., Delpont, G., Ki, J.C., Zunino, C., 2003. Notice explicative de la carte géologique du Burkina Faso à 1/200 000, Feuille Houndé, BRGM/BUMIGEB, Ouagadougou.
- Ledru, P., Johan, V., Milési, J.P., Tegey, M., 1994. Markers of the last stages of the Palaeoproterozoic collision: evidence for a 2 Ga continent involving circum-South Atlantic provinces. *Precambrian Res.* 69, 169–191.
- Ledru, P., Pons, J., Milési, J.P., Feybesse, J.L., Johan, V., 1991. Transcurrent tectonics and polycyclic evolution in the lower Proterozoic of Senegal-Mali. *Precambrian Res.* 50, 337–354.
- Lemoine, S., 1988. Evolution géologique de la région de Dabakala (NE Côte d'Ivoire) au Protérozoïque inférieur. Université Clermont-Ferrand, p. 338.
- Lemoine, S., 1990. Le faisceau d'accidents Greenville-Ferkessedougou-Bobo-Dioulasso (Libéria, Côte d'Ivoire, Burkina Faso); témoin d'une collision oblique éburnéenne, 15e colloque de géologie africaine. CIFEG, Paris, Nancy, France, 67–70.
- Lemoine, S., Tempier, P., Bassot, J.P., Caen-Vachette, M., Vialette, Y., Taure, S., Wenmenga, U., 1990. The Burkinian orogenic cycle, precursor of the Eburnian Orogeny in West Africa. *Geol. J.* 25, 171–188.

- Lemoine, S., Tempier, P., Bassot, J.P., Caen-Vachette, M., Vialette, Y., Wenmenga, U., Toure, S., 1985. The Burkinian, an orogenic cycle, precursor of the Eburnean of West Africa, 13th colloquium of African geology--13e colloque de géologie Africaine. . CIFEG, Paris, St. Andrews, United Kingdom, 26–27.
- Leprun, J.C., 1979. Les cuirasses ferrugineuses des pays cristallins de l’Afrique occidentale sèche. Genèse. Transformation-dégradation, Mémoire Sciences Géologiques, Strasbourg.
- Leube, A., Hirdes, W., Mauer, R., Kesse, G.O., 1990. The early Proterozoic Birimian Supergroup of Ghana and some aspects of its associated gold mineralization. *Precambrian Res.* 46, 139–165.
- Leverington, D.W., 2010. Discrimination of sedimentary lithologies using Hyperion and Landsat Thematic Mapper data: a case study at Melville Island, Canadian High Arctic. *Int. J. Remote Sens.* 31, 233–260.
- Li, X., 2006. Understanding 3D analytic signal amplitude. *Geophysics* 71, L13–L16.
- Li, X., 2008. Magnetic reduction-to-the-pole at low latitudes: Observations and considerations. *The Leading Edge* 27, 990–1002.
- Liberti, M., Simoniello, T., Carone, M.T., Coppola, R., D’Emilio, M., Macchiato, M., 2009. Mapping badland areas using LANDSAT TM/ETM satellite imagery and morphological data. *Geomorphology* 106, 333–343.
- Liégeois, J.P., Claessens, W., Camara, D., Klerkx, J., 1991. Short-lived Eburnian orogeny in southern Mali. *Geology, tectonics, U-Pb and Rb-Sr geochronology. Precambrian Res.* 50, 111–136.
- Liu-Zeng, J., Tapponnier, P., Gaudemer, Y., Ding, L., 2008. Quantifying landscape differences across the Tibetan plateau: Implications for topographic relief evolution. *J. Geophys. Res.* 113, F04018.
- Loh, G., Hirdes, W., 1996. Explanatory notes for the geological map of southwest Ghana 1:100 000-Sheets Sekondi (0402A) and Axim (0403B), *Ghana Geol. Surv. Bull.* 49, Acra.
- Lompo, M., 1991. Etude structurale et géologique des séries birimiennes de la région de Kwademen, Burkina Faso, Afrique de l’Ouest. Evolution et contrôle structural des minéralisations sulfurées et aurifères pendant l’Eburnéen. Université de Clermont Ferrand, Clermont Ferrand.
- Lompo, M., 2009. A model of subsidence of an oceanic plateau magmatic rocks in the Man-Leo Shield of the West African Craton. Geodynamic evolution of the 2.25–2.0 Ga Palaeoproterozoic, in: Reddy, S.M., Mazumder, R., Evans, D.A.D., Collins, A.S. (Eds.), *Special Publications. Geological Society, London*, 231–254.
- Lompo, M., 2010. Paleoproterozoic structural evolution of the Man-Leo Shield (West Africa). Key structures for vertical to transcurrent tectonics. *J. Afr. Earth Sci.* 58, 19–36.
- Lompo, M., Caby, R., Robineau, B., 1991. Evolution structurale du Birimien au Burkina Faso – exemple de la ceinture de Boromo-Goren dans le secteur de Kwademen (Afrique de l’Ouest). *Comptes Rendus Académie des Sciences, Paris* 313, 945–950.

- Lüdtke, G., Hirdes, W., Konan, G., Koné, Y., N'da, D., Traore, Y., Zamblé, Z., 1999. Géologie de la région Haute Comoé Sud—feuilles Dabakala (2b, d et 4b, d), Direction de la Géologie Abidjan Bulletin, Abidjan.
- Lüdtke, G., Hirdes, W., Konan, G., Koné, Y., Yao, C., Diarra, S., Zamblé, Z., 1998. Géologie de la région Haute Comoé Nord—feuilles Kong (4b et 4d) et Téhini-Bouna (3a à 3d), Direction de la Géologie Abidjan Bulletin, Abidjan.
- MacLeod, I.N., Jones, K., Dai, T.F., 1993. 3-D Analytic signal in the interpretation of total magnetic field data at low magnetic latitudes. *Explor. Geophys.* 24, 679–687.
- Madeira, J., Bedidi, A., Cervelle, B., Pouget, M., Flay, N., 1997. Visible spectrometric indices of hematite (Hm) and goethite (Gt) content in lateritic soils: the application of a Thematic Mapper (TM) image for soil-mapping in Brasília, Brazil. *Int. J. Remote Sens.* 18, 2835–2852.
- Marcelin, J., 1971. Notice explicative de la carte géologique au 1/200000 Gaoua-Batié, Edition, BRGM, Orleans.
- Marcelin, J., Serre, J.C., 1971. Notice explicative de la carte géologique au 1/200000 de Banfora-Sindou-Mangodara, Édition BRGM, Orléans.
- Martelet, G., Truffert, C., Tourliere, B., Ledru, P., Perrin, J., 2006. Classifying airborne radiometry data with Agglomerative Hierarchical Clustering: A tool for geological mapping in context of rainforest (French Guiana). *Int. J. Appl. Earth Obs. Geoinf.* 8, 208–223.
- Martin, H., 1986. Effect of steeper Archean geothermal gradient on geochemistry of subduction-zone magmas. *Geology* 14, 753–756.
- Martin, H., 1994. The Archean grey gneisses and the genesis of continental crust. *Dev. Precambrian Geol.* 11, 205–259.
- Martin, H., Smithies, R.H., Rapp, R., Moyen, J.F., Champion, D.C., 2005. An overview of adakite, tonalite–trondhjemite–granodiorite (TTG), and sanukitoid: relationships and some implications for crustal evolution. *Lithos* 79, 1–24.
- McCuaig, C.T., 2007. Seeing through deformation to early basin architecture in the Birimian: the Northern Burkina Faso example, West African Exploration Initiative project final conference, Ouagadougou, <http://waxi2.org> (last accessed 14/12/2010).
- McDonough, W.F., Sun, S.S., 1995. The composition of the Earth. *Chem. Geol.* 120, 223–253.
- McNairn, H., Jiali Shang, Xianfeng Jiao, Champagne, C., 2009. The contribution of ALOS PALSAR multipolarization and polarimetric data to crop classification, *IEEE Trans. Geosci. Remote Sens.* 47, 3981–3992.
- Michel, P., 1973. Les bassins des fleuves Sénégal et Gambie, étude géomorphologique. *Mém. ORSTOM* 63, Paris.
- Middlemost, E.A.K., 1994. Naming materials in the magma/igneous rock system. *Earth-Science Reviews* 37, 215–224.

- Milési, J.P., Feybesse, J.L., Ledru, P., Dommanget, A., Ouedraogo, M.F., Marcoux, E., Prost, A., Vinchon, C., Sylvain, J.P., Johan, V., Tegye, M., Calvez, J.Y., Lagny, P., 1989. Minéralisations aurifères de l'Afrique de l'Ouest, leurs relations avec l'évolution litho-structurale au Protérozoïque inférieur. Carte géologique au 1/2.000.000. Chronique de la recherche minière 497, 3–98.
- Milési, J.P., Feybesse, J.L., Pinna, P., Deschamps, Y., Kampunzu, H., Muhongo, S., Lescuyer, J.L., Le Goff, E., Delor, C., Billa, M., Ralay, F., Henry, C., 2004. Geological map of Africa 1:10 000 000, SIGAfrique Project, 20th Conference of African Geology, BRGM, Orléans, France, 2–7 June, <http://www.sigafrique.net>, last accessed 13/12/2010.
- Milési, J.P., Ledru, P., Ankrah, P., Johan, V., Marcoux, E., Vinchon, C., 1991. The metallogenic relationship between Birimian and Tarkwaian gold deposits in Ghana. *Mineral. Deposita* 26, 228–238.
- Milési, J.P., Ledru, P., Feybesse, J.-L., Dommanget, A., Marcoux, E., 1992. Early Proterozoic ore deposits and tectonics of the Birimian orogenic belt, West Africa. *Precambrian Res.* 58, 305–344.
- Miller, H.G., Singh, V., 1994. Potential field tilt—a new concept for location of potential field sources. *J. Appl. Geophys.* 32, 213–217.
- Milligan, P.R., Gunn, P.J., 1997. Enhancement and presentation of airborne geophysical data. *AGSO J. Aust. Geol. Geophys.* 17, 63–75.
- Milton, E.J., M. E. Schaepman, K. Anderson, M. Kneubuhler, N. Fox (2009), Progress in field spectroscopy, *Remote Sens. Environ.*, 113, 92–109.
- Minty, B.R.S., 1997. Fundamentals of airborne gamma-ray spectrometry. *AGSO J. Aust. Geol. Geophys.* 17, 39–50.
- Moyen, J.F., Martin, H., Jayananda, M., Auvray, B., 2003. Late Archaean granites; a typology based on the Dharwar Craton, India. *Precambrian Res.* 127, 103–123.
- Mueller, W., Donaldson, J.A., Dufresne, D., Rocheleau, M., 1991. The Duparquet Formation: Sedimentation in a late Archean successor basin, Abitibi greenstone belt, Quebec, Canada. *Can. J. Earth Sci.* 28, 1394–1406.
- Mulder, V.L., de Bruin, S., Schaepman, M.E., Mayr, T.R., 2011. The use of remote sensing in soil and terrain mapping – A review. *Geoderma* 162, 1–19.
- Murphy, R.J., Wadge, G., 1994. The effects of vegetation on the ability to map soils using imaging spectrometer data. *Int. J. Remote Sens.* 15, 63–86.
- Naba, S., Lompo, M., Debat, P., Bouchez, J.L., Béziat, D., 2004. Structure and emplacement model for late-orogenic Paleoproterozoic granitoids: the Tenkodogo-Yamba elongate pluton (Eastern Burkina Faso). *J. Afr. Earth Sci.* 38, 41–57.



- Nguyen, D., Widrow, B., 1990. Improving the learning speed of 2-layer neural networks by choosing initial values of the adaptive weights. *Proceedings of the International Joint Conference on Neural Networks*, 3:21–26.
- Nikiéma, S., Benkhelil, J., Corsini, M., Bourges, F., Abdoulaye, D., Maurin, J.-C., 1993. Tectonique transcurrente éburnéenne au sein du craton ouest-africain: exemple du sillon de Djibo (Burkina Faso). *C. Rend. Acad. Sci.* 316, 661–668.
- Oberthuer, T., Vetter, U., Davis, D.W., Amanor, J.A., 1998. Age constraints on gold mineralization and Paleoproterozoic crustal evolution in the Ashanti belt of southern Ghana. *Precambrian Res.* 89, 129–143.
- Ouedraogo, C., 2004. Carte géologique de Dédougou au 1:200 000. BUMIGEB, Ouagadougou.
- Ouedraogo, M.F., Prost, A.E., 1986. Relationships between schistosity and folding within the Birimian greenstone-belt from Yako to Batie (Burkina-Faso). *C. Rend. Acad. Sci.* 303, 1713–1718.
- Pain, C., Chan, R., Craig, M., Gibson, D., Ursem, P., Wilford, J., 2007. RTMAP regolith database field book and users guide (second edition): CRC LEME Report 138, Perth.
- Papp, É. ed., 2002. *Geophysical and Remote Sensing Methods for Regolith Exploration*. CRC LEME Open File Report 144, CRC LEME, Perth.
- Peschler, A.P., Benn, K., Roest, W.R., 2004. Insights on Archean continental geodynamics from gravity modelling of granite-greenstone terranes. *J. Geodyn.* 38, 185–207.
- Peschler, A.P., Benn, K., Roest, W.R., 2006. Gold-bearing fault zones related to Late Archean orogenic folding of upper and middle crust in the Abitibi granite-greenstone belt, Ontario. *Precambrian Res.* 151, 143–159.
- Piazolo, S., Passchier, C.W., 2002. Controls on lineation development in low to medium grade shear zones: a study from the Cap de Creus peninsula, Spain. *J. Struct. Geol.* 24, 25–44.
- Pike, R. J., Wilson, S.E., 1971. Elevation–relief ratio, hypsometric integral, and geomorphic area–altitude analysis. *Geological Society of America Bulletin*, 82, 1079–1084.
- Pilkington, M., Keating, P.B., 2009. The utility of potential field enhancements for remote predictive mapping. *Can. J. Remote Sensing* 35, Suppl. 1, S1–S11.
- Pons, J., Barbey, P., Dupuis, D., Leger, J.M., 1995. Mechanisms of pluton emplacement and structural evolution of a 2.1 Ga juvenile continental crust: the Birimian of southwestern Niger. *Precambrian Res.* 70, 281–301.
- Pons, J., Debat, P., Oudin, C., Valero, J., 1991. Emplacement and evolution of a synkinematic pluton (Saraya granite, Senegal, W. Africa). *Bull. Soc. Geol. Fr.* 162, 1075–1082.
- Pons, J., Oudin, C., Valero, J., 1992. Kinematics of large syn-orogenic intrusions: example of the Lower Proterozoic Saraya Batholith (Eastern Sénégal). *Geol. Rundsch.* 81, 473–486.
- Popowski, T., Connard, G., French, R., 2009. *GMSYS Profile Modeling: Gravity & Magnetic Modeling Software for Oasis montaj - USER GUIDE v 4.1*. Geosoft Inc., Toronto.

- Poucllet, A., Doumbia, S., Vidal, M., 2006. Geodynamic setting of the Birimian volcanism in central Ivory Coast (western Africa) and its place in the Palaeoproterozoic evolution of the Man Shield. *Bull. Soc. Geol. Fr.* 177, 105–121.
- Poucllet, A., Vidal, M., Delor, C., Simeon, Y., Alric, G., 1996. Le volcanisme birimien du nord-est de la Côte-d'Ivoire, mise en évidence de deux phases volcano-tectoniques distinctes dans l'évolution géodynamique du Paléoprotérozoïque. *Bull. Soc. Geol. Fr.* 167, 529–541.
- Pupier, E., Barbey, P., Toplis, M.J., Bussy, F., 2008. Igneous layering, fractional crystallization and growth of granitic plutons; the Dolbel Batholith in SW Niger. *J. Petrol.* 49, 1043–1068.
- Ratomaharo, S., Demange, M., Fonteilles, M., Joron, J.L., Treuil, M., 1988. La série birrimienne de Perkoa (Burkina Faso); géochimie et minéralogie, interprétation lithostratigraphique, conséquences sur l'interprétation géodynamique du Birrimien. *C. Rend. Acad. Sci.* 307, 2033–2040.
- Reeves, C., 2005. Aeromagnetic Surveys. Geosoft, e-book, <http://www.geosoft.com/knowledge>, last accessed 13/12/2010.
- Reuter, H.I., Nelson, A., Jarvis, A., 2007. An evaluation of void filling interpolation methods for SRTM data. *Int. J. Geog. Inf. Sci.* 21, 983–1008.
- Rey, P.F., Philippot, P., Thébaud, N., 2003. Contribution of mantle plumes, crustal thickening and greenstone blanketing to the 2.75–2.65 Ga global crisis. *Precambrian Res.* 127, 43–60.
- Richter, R., 1996. Atmospheric correction of satellite data with haze removal including a haze/clear transition region. *Comput. Geosci.* 22, 675–681.
- Richter, R., 1997. On the in-flight absolute calibration of high spatial resolution spaceborne sensors using small ground targets. *Int. J. Remote Sens.* 18, 2827–2883.
- Riedmiller, M., Braun, H., 1993. A direct adaptive method for faster backpropagation learning: The RPROP algorithm. *IEEE International Conference on Neural Networks*, San Francisco, 586–591.
- Rivard, B., Arvidson, R.E., Duncan, I.J., Sultan, M., El Kaliouby, B., 1992. Varnish, sediment, and rock controls on spectral reflectance outcrops in arid regions. *Geology*, 20, 295–298.
- Rivard, B., Zhang, J., Feng, J., Sanchez-Azofeifa, G.A., 2009. Remote predictive lithologic mapping in the Abitibi Greenstone Belt, Canada, using airborne hyperspectral imagery. *Can. J. Remote Sens.* 35, S95–S105.
- Rocci, G., Bronner, G., Deschamps, M., 1991. Crystalline basement of the West African Craton, in: Dallmeyer, R.D., Lécroché, J.P.; (Eds.), *The west African orogens and circum-Atlantic correlatives*. Springer-Verlag, Berlin, pp. 31–61.
- Roddaz, M., Debat, P., Nikiéma, S., 2007. Geochemistry of Upper Birimian sediments (major and trace elements and Nd–Sr isotopes) and implications for weathering and tectonic setting of the Late Paleoproterozoic crust. *Precambrian Res.* 159, 197–211.
- Rodger, A., Cudahy, T., 2009. Vegetation corrected continuum depths at 2.20  $\mu\text{m}$ : An approach for hyperspectral sensors. *Remote Sens. Environ.* 113, 2243–2257.

- Rowan, L.C., Mars, J.C., 2003. Lithologic mapping in the Mountain Pass, California area using Advanced Spaceborne Thermal Emission and Reflection Radiometer (ASTER) data. *Remote Sens. Environ.* 84, 350–366.
- Rowan, L.C., Mars, J.C., Simpson, C.J., 2005. Lithologic mapping of the Mordor, NT, Australia ultramafic complex by using the Advanced Spaceborne Thermal Emission and Reflection Radiometer (ASTER). *Remote Sens. Environ.* 99, 105–126.
- Rowan, L.C., Simpson, C.J., Mars, J.C., 2004. Hyperspectral analysis of the ultramafic complex and adjacent lithologies at Mordor, NT, Australia. *Remote Sens. Environ.* 91, 419–431.
- Saadat, H., Bonnell, R., Sharifi, F., Mehuys, G., Namdar, M., Ale-Ebrahim, S., 2008. Landform classification from a digital elevation model and satellite imagery. *Geomorphology* 100, 453–463.
- Savitzky, A., Golay, M.J.E., 1964. Smoothing and differentiation of data by simplified least squares procedures. *Anal. Chem.* 36, 1627–1639.
- Schaepman-Strub, G., Shaepman, M.E., Painter, T.H., Dangel, S., Martonchik, J.V., 2006. Reflectance quantities in optical remote sensing—definitions and case studies. *Remote Sens. Environ.* 103, 27–42.
- Schetselaar, E.M., Chung, C.J.F., Kim, K.E., 2000. Integration of Landsat TM, gamma-ray, magnetic, and field data to discriminate lithological units in vegetated granite-gneiss terrain. *Remote Sens. Environ.* 71, 89–105.
- Schetselaar, E.M., Harris, J.R., Lynds, T., de Kemp, E.A., 2007. Remote predictive mapping (RPM): A strategy for geological mapping of Canada's north. *Geosci. Can.* 34, 93–111.
- Schetselaar, E.M., Tiainen, M., Woldai, T., 2008. Integrated geological interpretation of remotely sensed data to support geological mapping in Mozambique. *Geol. Surv. Finland, Special Paper* 48, 35–63.
- Schreier G., 1993. SAR geocoding: data and systems, Wichmann-Verlag, Karlsruhe.
- Schwartz, M.O., Melcher, F., 2003. The Perkoa zinc deposit, Burkina Faso. *Econ. Geol.* 98, 1463–1485.
- Sengör, A.M.C., Natal'in, B.A., Burtman, V.S., 1993. Evolution of the Altaid tectonic collage and Palaeozoic crustal growth in Eurasia. *Nature* 364, 299–307.
- Serbin, G., Daughtry, C.S.T., Hunt Jr., E.R., Reeves III, J.B., Brown, D.J., 2009. Effects of soil composition and mineralogy on remote sensing of crop residue cover. *Remote Sens. Environ.* 113, 224–238.
- Sestini, G., 1973. Sedimentology of a paleoplacer: The gold-bearing Tarkwaian of Ghana. *International Union of Geological Sciences Series A* 3, 275–305.
- Shirey, S.B., Kamber, B.S., Whitehouse, M.J., Mueller, P.A., Basu, A.R., 2008. A review of the isotopic and trace element evidence for mantle and crustal processes in the Hadean and Archean; implications for the onset of plate tectonic subduction, in: *Condie, K.C., Pease, V.*

- (Eds.), When did plate tectonics begin on planet Earth? Geological Society of America (GSA):Boulder. pp. 1–29.
- Siart, C., Bubenzer, O., Eitel, B., 2009. Combining digital elevation data (SRTM/ASTER), high resolution satellite imagery (Quickbird) and GIS for geomorphological mapping: A multi-component case study on Mediterranean karst in Central Crete. *Geomorphology* 112, 106–121.
- Siegal, B.S., Goetz, F. H., 1977. Effect of vegetation on rock and soil type discrimination, *Photogramm. Eng. Remote Sens.* 43, 191–196.
- Siegfried, P., De Kock, G.S., Clarke, B., Agenbacht, A., Delor, C., Van Rooyen, R.C., 2009. Geological map explanation - map sheet 0903D (1:100 000), Mining Sector Support Programme. CGS, BRGM, Geoman, GSD, Accra.
- Simpson, C.J., 1990. Deep weathering, vegetation and fireburn Significant obstacles for geosciences remote sensing in Australia. *Int. J. Remote Sens.* 29, 2019–2034.
- Soumaila, A., Garba, Z., 2006. Le métamorphisme des formations de la ceinture de roches vertes birimiennes (Paléoproterozoïque) de Diagorou-Darbani (Liptako, Niger, Afrique de l'Ouest). *Africa Geoscience Review* 13, 107–128.
- Soumaila, A., Henry, P., Rossy, M., 2004. Contexte de mise en place des roches basiques de la ceinture de roches vertes birimiennes de Diagorou-Darbani (Liptako, Niger, Afrique de l'Ouest); plateau océanique ou environnement d'arc/bassin arrière-arc océanique. *C. Rend. Acad. Sci.* 336, 1137–1147.
- Stewart, J.R., Betts, P.G., 2010. Late Paleo-Mesoproterozoic plate margin deformation in the southern Gawler Craton: Insights from structural and aeromagnetic analysis. *Precambrian Res.* 177, 55–72.
- Stewart, J.R., Betts, P.G., Collins, A.S., Schaefer, B.F., 2009. Multi-scale analysis of Proterozoic shear zones: An integrated structural and geophysical study. *J. Struct. Geol.* 31, 1238–1254.
- Sylvester, P.J., Attoh, K., 1992. Lithostratigraphy and composition of 2.1 Ga greenstone belts of the West African Craton and their bearing on crustal evolution and the Archean-Proterozoic boundary. *J. Geol.* 100, 377–393.
- Sylvester, P.I., Harper, G.D., Byerly, G.R., Thurston, P.C., 1997. Volcanic aspects, in: de Wit, M.J., Ashwal, L.D. (Eds.), *Greenstone belts*. Clarendon Press, Oxford, pp. 55–90.
- Tagini, B., 1971. Esquisse structurale de la Côte d'Ivoire. Essai de géotectonique régionale. Université Lausanne, p. 302.
- Tagini, B., 1972. Carte Géologique de la Côte d'Ivoire 1:2 000 000. SODEMI, Abidjan.
- Tapley, I.J., 2002. Radar Imaging, in: Papp, É. (Ed.), *Geophysical and Remote Sensing Methods for Regolith Exploration*. CRCLEME Open File Report 144, pp. 22–32.
- Tardy, Y., 1997. *Petrology of laterites and tropical soils*. A.A. Balkema Publishers, Brookfield.
- Taylor, G., Eggleton, R.A., 2001. *Regolith geology and geomorphology*. Wiley, Chichester.

- Taylor, P.N., Moorbath, S., Leube, A., Hirdes, W., 1992. Early Proterozoic crustal evolution in the birimian of Ghana: constraints from geochronology and isotope geochemistry. *Precambrian Res.* 56, 97–111.
- Tempier, P., 1986. Le Burkinien; cycle orogénique majeur du Proterozoïque inférieur en Afrique de l'Ouest, Journée scientifique du C.I.F.E.G. CIFEG, Paris, France, 17–23.
- Teruiya, R.K., Paradella, W.R., Dos Santos, A.R., Dall'Agnol, R., Veneziani, P., 2008. Integrating airborne SAR, Landsat TM and airborne geophysics data for improving geological mapping in the Amazon region: the Cigano Granite, Carajas Province, Brazil. *Int. J. Remote Sens.* 29, 3957–3974.
- Thiéblemont, D., Goujou, J.C., Egal, E., Cocherie, A., Delor, C., Lafon, J.M., Fanning, C.M., 2004. Archean evolution of the Leo Rise and its Eburnean reworking. *J. Afr. Earth Sci.* 39, 97–104.
- Thomas, E., De Kock, G.S., Baglow, N., Viljoen, J.H.A., Z., S., 2009. Geological map explanation - map sheet 0903B (1:100 000), Mining Sector Support Programme. CGS, BRGM, Geoman, GSD, Accra.
- Tromp, M., Epema, G.F., 1999. Spectral mixture analysis for mapping land degradation in semi-arid areas. *Geol. Mijnbouw* 77, 153–160.
- Tromp, M., Steenis, M.Z., 1996. Deriving sub-pixel soil characteristics in northern Burkina Faso with spectral unmixing, in: Proc. ISSS Internat. Sympos. 'Monitoring Soils in the Environment with Remote Sensing and GIS', Ouagadougou, Burkina Faso 6–10 Feb. 1995.
- Tshibubudze, A., Hein, K.A.A., Marquis, P., 2009. The Markoye Shear Zone in NE Burkina Faso. *J. Afr. Earth Sci.* 55, 245–256.
- Vandervoort, D.S., Jordan, T.E., Zeitler, P.K., Alonso, R.N., 1995. Chronology of internal drainage development and uplift, southern Puna plateau, Argentine central Andes. *Geology* 23, 145–148.
- Vegas, N., Naba, S., Bouchez, J.L., Jessell, M., 2008. Structure and emplacement of granite plutons in the Paleoproterozoic crust of Eastern Burkina Faso: rheological implications. *Int. J. Earth Sci. (Geol. Rundsch.)* 97, 1165–1180.
- Verduzco, B., Fairhead, J.D., Green, C.M., MacKenzie, C., 2004. New insights into magnetic derivatives for structural mapping. *The Leading Edge* 23, 116–119.
- Vidal, M., Alric, G., 1994. The Palaeoproterozoic (Birimian) of Haute-Comoe in the West African craton, Ivory Coast: a transtensional back-arc basin. *Precambrian Res.* 65, 207–229.
- Vidal, M., Delor, C., Pouclet, A., Siméon, Y., Alric, G., 1996. Evolution géodynamique de l'Afrique de l'Ouest entre 2.2 Ga et 2 Ga; le style "archéen" des ceintures vertes et des ensembles sédimentaires birimiens du nord-est de la Côte-d'Ivoire. *Bull. Soc. Geol. Fr.* 167, 307–319.
- Vidal, M., Gumiaux, C., Cagnard, F., Pouclet, A., Ouattara, G., Pichon, M., 2009. Evolution of a Paleoproterozoic "weak type" orogeny in the West African Craton (Ivory Coast). *Tectonophysics* 477, 145–159.

- Whitelaw, O.A.L., 1929. The geological and mining features of the Tarkwa-Abosso Goldfield, Gold Coast Geol. Surv. Mem., 1–45.
- Wilford, J.R., 2002. Airborne gamma-ray spectrometry, in: Papp, É. (Ed.), Geophysical and remote sensing methods for regolith exploration. CRCLEME Open File Report 144, pp. 46–52.
- Wilford, J.R., Bierwirth, P.N., Craig, M.A., 1997. Application of airborne gamma-ray spectrometry in soil/regolith mapping and applied geomorphology. AGSO J. Aust. Geol. Geophys. 17, 201–216.
- Wilford, J.R., Murphy, B., Summerell, G., 2007. Delineating regolith materials using multi-scaled terrain attributes and gamma-ray imagery – applications for updating soil-landscape maps and managing dryland salinity, in: Oxley, L. and Kulasiri, D. (Eds.) MODSIM 2007 International Congress on Modelling and Simulation. Modelling and Simulation Society of Australia and New Zealand, December 2007, pp. 74–80.
- Windley, B., 1992. Proterozoic collisional and accretionary orogens, in: Condie, K.C. (Ed.), Proterozoic Crustal Evolution. Elsevier, Amsterdam, pp. 419–446.
- Windley, B.F., 1995. The evolving continents. John Wiley & Sons, Chichester.
- Woolrych, A., Batty, S., 2007. A Semi automated technique to Regolith-landform mapping in West Africa. ASEG Extended Abstracts 2007, Perth, 1–4.
- Wright, J.B., Hastings, D., Jones, W.B., Williams, H.R., 1985. Geology and Mineral Resources of West Africa. Allen and Unwin, London.
- Younis, M.T., Gilabert, M.A., Melia, J., Bastida J., 1997. Weathering process effects on spectral reflectance of rocks in a semi-arid environment. Int. J. Remote Sens., 18, 3361–3377.
- Zeuberger, L. W., Thorne, C.R., 1987. Quantitative Analysis of Land Surface Topography. Earth Surface Processes and Landforms 12, 47–56.
- Zhang Y., Wu L., Neggaz N., Wang S., Wei G., 2009. Remote-Sensing Image Classification Based on an Improved Probabilistic Neural Network. Sensors 9, 7516–7539.
- Zonou, S., 1987. Les formations leptyno-amphibolitiques et le complexe volcanique et volcano-sédimentaire du Protérozoïque inférieur de Bouroum-nord (Burkina Faso - Afrique de l'Ouest): Etude pétrographique, géochimique, approche pétrogénétique et évolution géodynamique. Université de Nancy I, Nancy.
- Zumsprekel, H., Prinz, T., 2000. Computer-enhanced multispectral remote sensing data: a useful tool for the geological mapping of Archean terrains in (semi)arid environments. Comput. Geosci. 26, 87–100.

## LIST OF APPENDICES

---

## **LIST OF APPENDICES**

All of the appendices may be found on the enclosed CD in electronic version.

APPENDIX 1 – Data description

APPENDIX 2 – Methods description

APPENDIX 3 – ArcReader project with interpretation layers



---

## **ANNEX 1**

---

# ANNEX 1

## DATA DESCRIPTION

### Magnetometry and Gamma ray spectrometry data

The used data were acquired as part of the SYSMIN project, which was financed by the European Union. The data were delivered to the Ministry of Energy and Mineral Resources of Burkina Faso and are distributed by the Bureau of Mineral Resources and Geology of Burkina Faso. The acquisition of the data was performed during a joint magnetometry and gamma-ray spectrometry survey by CGG France. Two aircraft (Cessna 404 and Cessna 208) equipped with a dynamically compensated magnetometer (Scintrex CS2 cesium vapor) installed on a beam extended from the tail of the aircraft on a stinger and an auto-stabilized gamma-ray spectrometer (Exploranium GR-820) with two NaI(Tl) detectors (33.6 liters downward-looking and 8.4 upward looking) located inside of the aircraft. The first part of the survey took place between September 1998 and January 1999 while second part was flown during June and July 1999. The sampling rate was 10 Hz for the magnetometry measurements and 1 Hz for the gamma-ray spectrometry readings. The position of the readings was determined with the help of Differential GPS system. The GPS base stations were installed at Ouagadougou and Bobo-Dioulasso. The aircraft was also equipped with auxiliary instruments such as radar altimeter, barometric altimeter, and temperature and pressure sensors.

<b>Spacing between lines</b>	500 m and 1000 m
<b>Flight line direction</b>	NW-SE
<b>Spacing between tie-lines</b>	10000 m
<b>Tie-line direction</b>	NE-SW
<b>Flight altitude</b>	100 m ground clearance
<b>Average speed</b>	70-80 m/s

**Table 1** Design and characteristics of the SYSMIN 1998-1999 airborne geophysical survey performed in Burkina Faso

### Preprocessing of the magnetometry data

The magnetometry data were subject to standard pre-processing procedures (Telford, 1990; Reeves, 2005). The raw readings were corrected for instrument noise and lag (time-space discrepancy between measurements and geographic position reading). The lag corrected data were compensated for the effects of aircraft magnetization and the diurnal variation of the magnetic field was subtracted from

the readings using a ground based measuring station. The data were then leveled with the help of the tie lines. Finally, the regional magnetic field was subtracted from the data employing the IGRF 1995 model adjusted for the date and the altitude of the survey. The data were gridded with 125 and 250 m spatial resolution using the bi-directional gridding method (Reeves, 2005). The two grids were then merged together to a single grid while the coarser was resampled to 125 m.

### **Preprocessing of the gamma-ray spectrometry data**

The gamma-spectrometric readings were derived from the 256 channels using the characteristic spectrometric bands corresponding to potassium (1.37–1.57 MeV), uranium (1.66–1.86 MeV), and thorium (2.41–2.81 MeV). The Uranium and Thorium measurements are actually referred to as the equivalent of U, Th or eU, eTh, respectively. This convention results from the fact that the amount of the emitted gamma rays from U and Th are calculated based on emissions from, further down the decay series, daughter elements  $^{214}\text{Bi}$  and  $^{208}\text{Tl}$ , respectively and assumed in equilibrium. The total count readings correspond to an energy spectrum spanning 0.41–2.81 MeV. The data were subject to standard pre-processing procedures (Telford et al., 1990; Minty, 1997). The readings were first corrected for background noise caused by the aircraft and the cosmic radiation. The Compton scattering correction was applied along with the altitude compensation utilizing the coefficients gathered during calibration flights. The data were also corrected for the presence of atmospheric radon using the upward looking detector. Finally, the data were normalized according to the measured sensitivity of the system established during a calibration survey. The corrected data were then smoothed using the NASVD algorithm (Noise-Adjusted singular Value decomposition) developed by Hovgaard and Grasty (1997). The minimum curvature gridding procedure (Reeves, 2005) was utilized to produce two grids at 125 m and 250 m spatial resolution. The grids were ultimately merged to one single grid retaining a 125 m spatial resolution.

### **Gravimetric data**

The gravity data available for western Burkina Faso stem from the ORSTOM west and central African gravimetric data acquisition campaign and were acquired in 1958 (Albouy et al., 1992). The data have a maximum spacing of 4000 m between sampling points and were mainly acquired along major roads. The data density is about 220 stations per square degree. Station locations were determined from topographic maps and elevations by barometric leveling, using Wallace and Tiernan altimeters. The Gravimeters were North American, Worden, or Lacoste and Romberg, with a resolution of 0.01 mGal. The reported accuracy of the gravity measurements after earth-tide and instrument drift correction is about 0.5 mGal. The positioning error is estimated to be less than 5 m in the vertical and about 200 m in the horizontal direction. Free air and Bouguer corrections were applied

to the data using  $2.67 \text{ g/cm}^3$  as the reduction density. The Bouguer anomaly was computed at each location according to equation 1.

$$\text{(equation 1) } g_B = g_{obs} - (g_t - \Delta g_{FA} + \Delta g_B + \Delta g_T),$$

where: $g_{obs}$	measured gravity
$G_t$	Theoretical gravity (2 different reference systems: Potsdam and IGSN71)
$\Delta g_{FA}$	Free air correction
$\Delta g_B$	Bouguer correction
$\Delta g_T$	Topographic correction

For Burkina Faso, the topographic correction was not accounted for, as errors were less than 0.5 mGal. The largest source of errors is tied to the correct determination of  $\Delta g_B$ , which is linearly dependant on the altitude errors and thus 1 mGal corresponds to 5 m error in altitude.

The data were gridded at 3000 m spatial resolution to produce a Bouguer anomaly map using the minimum curvature gridding method.

### **SRTM-3 Digital elevation data**

SRTM datasets were produced by a collaborative effort of NASA and NIMA (National Imagery and Mapping Agency), and German and Italian space agencies. The goal was to generate a near-global digital elevation model (DEM) of the Earth using radar interferometry. The data collection took place during the STS-99 mission of the space shuttle Endeavour while using modified SIR-C sensor. The SRTM-30 data with 90 m spatial resolution at the equator are available from a number of sources with different processing steps applied to the original data published by NASA. The vertical error was reported to be less than 16 m (Rodriguez et al., 2006). The original data contain no-data holes where water or radar shadow effect did not allow for correct height estimation. The CGIAR SRTM database version 4 (Jarvis et al., 2008) offers the SRTM-3 global dataset as void-filled data using the method described by Reuter et al. (2007). The interpolation of the data voids utilizes several interpolation methods based on the size of the void and the availability of auxiliary height information from other sources. The data are provided in ARC GRID, ARC ASCII, and GeoTiff format as unprojected 5 by 5 degrees data tiles with WGS84 datum.

## Landsat 7 ETM+ data

Landsat 7 was launched on April 15, 1999 under the cooperation of NASA and USGS as a prolongation of the 33 years long and successful Landsat Program. The exact specifications of the satellite's orbit and characteristics are provided in Table 1.

<b>Swath width:</b>	185 kilometers
<b>Repeat coverage interval:</b>	16 days (233 orbits)
<b>Altitude:</b>	705 kilometers
<b>Quantization:</b>	Best 8 of 9 bits
<b>Orbit and Inclination:</b>	Sun-synchronous, 98.2 degrees
<b>Equatorial crossing:</b>	Descending node; 10:00 A.M.

**Table 2** Landsat 7 ETM+ satellite and data specifications

The earth observing instrument on Landsat 7, the Enhanced Thematic Mapper Plus has the capabilities of the previous Thematic Mapper sensors aboard Landsat 4 – 5 systems, but it also includes new features, which further enhance the potential of the sensor in global change studies, land cover monitoring and assessment, and large area mapping. The new features are primarily the incorporation of a 15 meters ground resolution panchromatic band, 5% radiometric calibration with full aperture and a thermal IR channel with 60 meters spatial resolution (NASA, 2008). The specifications of the satellite and sensor onboard are provided in Table 3.

<b>Spectral Band</b>	<b>Half Amplitude Bandwidth (<math>\mu\text{m}</math>)</b>	<b>Nominal Ground Sample Distance (m)</b>
Panchromatic	0.522-0.90	15
1	0.45-0.52	30
2	0.52-0.60	30
3	0.63-0.69	30
4	0.76-0.90	30
5	1.55-1.75	30
6	10.4-12.5	60
7	2.08-2.35	30

**Table 3** Spectral and spatial resolution of the bands captured by the Enhanced Thematic Mapper Plus sensor aboard the Landsat 7 satellite

The main site for receiving data streams is the EROS data center maintained by USGS in Sioux Falls, South Dakota. There are also other receiving sites including international ground stations (e.g. ESA in Europe). The data can be obtained in different formats depending on the processing facility. The USGS L1T product consists of geometrically and radiometrically corrected Landsat data, where the geometric correction employs ground control points and digital elevation models. The scenes that were utilized in our study included seven Landsat-7 L1T images provided as courtesy of the USGS.

## ASTER data

The ASTER instrument is a cooperative effort between NASA; Japan's Ministry of Economy, Trade and Industry (METI); and Japan's Earth Remote Sensing Data Analysis Center (ERSDAC). The instrument provides spectral coverage in fourteen bands (see Table 4) with three subsystems (VNIR, SWIR, and TIR). ASTER VNIR optical system further includes a backward pointing telescope for registration of stereoscopic images, which are used, for generating Digital Elevation Models (Abrams et al, 2002).

Subsystem	Band Number	Spectral range ( $\mu\text{m}$ )	Nominal ground sample distance (m)
VNIR	1	0,520-0,600	15
	2	0,630-0,690	
	3N	0,780-0,860	
	3B	0,780-0,860	
SWIR	4	1,600-1,700	30
	5	2,145-2,185	
	6	2,185-2,225	
	7	2,235-2,285	
	8	2,295-2,365	
	9	2,360-2,430	
TIR	10	8,125-8,475	90
	11	8,475-8,825	
	12	8,925-9,275	
	13	10,250-10,950	
	14	10,950-11,650	

**Table 4** Spectral and spatial resolution of the bands captured by the ASTER sensor aboard the EO-1 TERRA satellite

The Advanced Spaceborne Thermal Emission and Reflection Radiometer (ASTER) is one of the instruments present on the platform TERRA that was launched on December 18, 1999. TERRA also called EOS-AM1 is the flagship of the large multinational, multi-disciplinary project EOS (Earth Observation System) involving partnerships with the aerospace agencies of Canada and Japan

(Abrams et al, 2002). Data coverage of ASTER is not continuous, instead only a number of selected scenes are acquired during one orbit of the platform. The orbit was designed to follow that of Landsat (see table 5). The main receiving station is located in White Sands, New Mexico. The data are distributed in HDF (Hierarchical Data File) format, a standard data format for all NASA Earth Observing System (EOS) data products. There are several processing options available on demand. The L1B data product contains radiometrically and geometrically corrected data (Abrams et al., 2002). Before further processing the data were corrected for the cross-talk phenomenon (Iwasaki et al., 2001). For the study area, 30 scenes were made available as courtesy of JAXA and NASA.

<b>Swath width:</b>	60 kilometers
<b>Repeat coverage interval:</b>	16 days (233 orbits)
<b>Altitude:</b>	705 kilometers
<b>Quantization:</b>	VNIR, SWIR 8 bits; TIR 12 bits
<b>Orbit and Inclination:</b>	Sun-synchronous, 98.3 degrees
<b>Equatorial crossing:</b>	Descending node; 10:30 A.M.

**Table 5** *EO-1 TERRA satellite orbit specifications and ASTER sensor data specifications*

## ALOS PALSAR data

The Advanced Land Observing Satellite (ALOS) was launched on January 24, 2006 by the Japanese Aerospace Exploration Agency (JAXA). The PALSAR L-band sensor was developed in cooperation with the Japan Resources Observation System Organization (JAROS). The PALSAR sensor represented the only space-borne operational L-band SAR system until its power failure in 2011.

<b>Repeat coverage interval</b>	46 days (296 orbits)
<b>Swath width</b>	20–350 km
<b>Look direction</b>	right-looking
<b>Incidence angle</b>	8–60 deg
<b>Altitude</b>	691 km
<b>Quantization</b>	5 bits
<b>Spatial resolution</b>	7 to 100 m
<b>Orbit and inclination</b>	Sun-synchronous 98.1 deg
<b>Frequency/Wavelength</b>	1.270 GHz (L-band)/23.6 cm
<b>Equatorial crossing</b>	Descending node; 6:00 A.M.
<b>Polarization</b>	HH, VV, HV, VH

**Table 6** ALOS PALSAR satellite sensor system and its specifications

The experimental polarimetric mode of the PALSAR sensor allows for acquisition of full-polarimetric data. Specifications of the product (JAXA, 2009) are given in table 7. The data are provided in several processing levels. The level 1.1 processing includes calibration and compression of the data, which are then provided in standard CEOS format where each polarimetric band is stored separately with pixel type being complex integer. A leader file containing all of the data necessary for further processing is provided with the data set. The two scenes processed for the Gaoua area were provided as a courtesy of ESA and JAXA for the SOAR project 6788.



<b>Nominal pixel spacing</b>	4.7 x 5.1 m (Range x Azimuth)
<b>Resolution</b>	5.2 x 7.6 m (Range x Azimuth)
<b>Nominal scene size</b>	25 x 25 km (Range x Azimuth)
<b>Range of incidence angles</b>	18 to 49 degrees
<b>Number of looks</b>	1 x 1 (Range x Azimuth)

**Table 7** PALSAR polarimetry mode L1.1 SLC (single look complex) product specifications

## Radarsat-2 data

The Radarsat-2 satellite is the second radar system satellite launched by the Canadian Space Agency in cooperation with MDA (MacDonald, Dettwiller and Associates Ltd.) a privately owned geospatial information company on December 14, 2007. This next generation radar system has full polarimetric capability and adjustable imaging geometry for increased re-visit time (satellite and sensor specifications are given in table 8).

<b>Repeat coverage interval</b>	24 days (296 orbits)
<b>Swath width</b>	5–500 km
<b>Look direction</b>	left- and right-looking
<b>Incidence angle</b>	10–60 deg
<b>Altitude</b>	798 km
<b>Quantization</b>	8 bits (block-adaptive quantizer)
<b>Spatial resolution</b>	3 to 100 m
<b>Orbit and inclination</b>	Sun-synchronous 98.6 deg
<b>Frequency/Wavelength</b>	5.405 GHz (C-band)/5.55 cm
<b>Equatorial crossing</b>	Descending node; 6:00 A.M.
<b>Polarization</b>	HH, VV, HV, VH

**Table 8** Radarsat-2 satellite sensor system and its specifications

The Fine Quad Polarization data product (Slade, 2011) provides fully polarimetric images. The specifications of the data and imaging geometry are given in table 9. The complex-valued Quad polarization products contain the inter-channel phase information, which enables complex-valued polarimetry to be performed. The data is provided in standard GeoTiff format, where each pixel is

represented by a complex I/Q (In phase/Quadrature) signed integer value. Along with the image files is stored and xml product information file containing all of the data necessary for further processing and LUT tables which are used for radiometric calibration of the digital numbers. The scene processed from the Gaoua area was provided as courtesy of CSA, MDA, and ESA for the SOAR project 6788.

<b>Nominal pixel spacing</b>	4.7 x 5.1 m (Range x Azimuth)
<b>Resolution</b>	5.2 x 7.6 m (Range x Azimuth)
<b>Nominal scene size</b>	25 x 25 km (Range x Azimuth)
<b>Range of incidence angles</b>	18 to 49 degrees
<b>Number of Looks</b>	1 x 1 (Range x Azimuth)

**Table 9** Radarsat-2 fine quad-pol SLC (single look complex) product specifications

## ASD PRO FR infra-red spectrometric data

The ASD Pro FR field-portable visible and infrared spectroradiometer collects data in the 35  $\mu\text{m}$  to 2.5  $\mu\text{m}$  spectral range with 10 nm nominal spectral resolution (3 nm @ 0.7  $\mu\text{m}$ , 1.0  $\mu\text{m}$  at 1.4/ 2.1 nm. The field of view of the instrument is 25 degrees but can be adjusted using fore optic elements. The instrument allows for acquisition of raw digital numbers, reflectance, radiance, or irradiance measurements. The spectroradiometer combines three sensors. A Si photodiode array VNIR spectrometer is used to cover the 0.35 to 1  $\mu\text{m}$  range. Two separate, thermoelectrically cooled, graded index InGaAs photodiode spectrometers provide the coverage from 1  $\mu\text{m}$  to 1.75  $\mu\text{m}$  and 1.75  $\mu\text{m}$  to 2.5  $\mu\text{m}$ . The spectrometer allows for direct relative reflectance estimation when known white reference (total reflection) material is used. A spectralon Labsphere calibration panel was used for such purposes. The preprocessing of the spectra consisted of correcting detector offsets using the additive method (Dorigo et al., 2006) and data smoothing, including averaging of the measurements. The data collected for the spectral library is separated into three folders:

Spectra\_original\_field - averaged spectra corrected only for detector offset.

Spectra original lab - averaged spectra corrected for detector offset.

Spectra\_smooth\_field - averaged and smoothed spectra corrected for detector offset.

The spectra are saved as text files containing an 18-line header and measured wavelength and reflectance as two columns of data. The name is set up from the spectral measurement site number, an abbreviation of the measured material followed by an abbreviation for measured surface (C-cut surface rock, W-weathered surface rock, M-mixed surfaces, S-soil surface, G-green vegetation, D-dry vegetation). It also contains the date of measurement and a sequential number of measurements made during the day.

---

## References

- Abrams M, Hook S., Ramachandran, B. 2002. ASTER user handbook, Version 2, [http://asterweb.jpl.nasa.gov/content/03\\_data/04\\_documents/aster\\_user\\_guide\\_v2.pdf](http://asterweb.jpl.nasa.gov/content/03_data/04_documents/aster_user_guide_v2.pdf), last accesse 15/12/2011.
- Albouy, Y., Boukeke, D., Legeley-Padovani, A., Villeneuve, J., Foy, R., Bonvalot, S., El Abbass, T., Poudjhom, Y., 1992. Données gravimétriques ORSTOM Afrique - Madagascar, Exploration Minière, Recherches d'Eau et Environnement, Ouagadougou, 1–14.
- Dorigo, W., Bachmann, M., Heldens, W., 2006. AS Toolbox & Processing of field spectra – User’s manual v.1.12, DLR, Munich.
- Hovgaard, J., Grasty, R.L., 1997. Reducing statistical noise in airborne gamma ray data through spectral component analysis, in: Gubins, A.G. (Ed.), Proceedings Of Exploration 97: Fourth Decennial Conference On Mineral Exploration. Prospectors and Developers Association of Canada, Toronto, 753–764.
- Iwasaki, A., Tonooka, H., 2005. Validation of Crosstalk Correction Algorithm for ASTER/SWIR, IEEE Trans. Geosci. Remote Sens., 2747–2751.
- Jarvis, A., Reuter, H.I., Nelson, A., Guevara, E., 2008. Hole-filled seamless SRTM data V4. International Centre for Tropical Agriculture (CIAT), <http://srtm.csi.cgiar.org/>, last accessed 10/05/2010.
- JAXA, 2009. ALOS/PALSAR level 1.1/1.5 product format description, , last accessed 15/12/2011.
- Minty, B.R.S., 1997. Fundamentals of airborne gamma-ray spectrometry. AGSO J. Aust. Geol. Geophys. 17, 39–50.
- NASA, 2008, The Landsat Science User handbook, NASA, [http://landsathandbook.gsfc.nasa.gov/pdfs/Landsat7\\_Handbook.pdf](http://landsathandbook.gsfc.nasa.gov/pdfs/Landsat7_Handbook.pdf), last accesse 15/12/2011.
- Reeves, C., 2005. Aeromagnetic Surveys. Geosoft, e-book, <http://www.geosoft.com/knowledge>, last accessed 13/12/2010.
- Reuter, H.I., Nelson, A., Jarvis, A., 2007. An evaluation of void filling interpolation methods for SRTM data. Int. J. Geog. Inf. Sci. 21, 983–1008.
- Rodriguez, E., Morris, C.S., Belz, J.E. 2006. A global assessment of the SRTM performance, Photogramm. Eng. Rem. Sens., 72, 249–260.
- Slade, B., 2011. Radarsat-2 product description, MDA, Richmond, [http://gs.mdacorporation.com/includes/documents/51-2713\\_-\\_RSAT-2\\_Product\\_Format\\_Definition\\_-\\_Iss1\\_9.pdf](http://gs.mdacorporation.com/includes/documents/51-2713_-_RSAT-2_Product_Format_Definition_-_Iss1_9.pdf), last accessed 15/12/2011.
- Telford, W.M., Geldart, L.P., Sheriff, R.E., 1990. Applied geophysics, 2nd ed., Cambridge University Press, Cambridge.

---

## **ANNEX 2**

---

# ANNEX 2

## METHODS DESCRIPTION

### Magnetometry and Gamma ray spectrometry data processing

The processing of the magnetometry and gamma ray spectrometry grids contains several steps that are used to enhance different aspects of the acquired data or are necessary steps to obtain better interpretable data.

#### Fourier transform filtering

Fourier Transform filtering is routinely used in image processing (Pratt, 2007) and is well suited for potential field data filtering (Telford et al., 1990; Li and Oldenburg, 1998), especially because the wavenumber (frequency) content of the potential field grids can be easily analyzed. The filtering process makes use of the Fourier transform of 2D spatial data to the wavenumber domain (equation 1 and 2; 2D example)

$$\text{(equation 1) } f(x, y) = \iint_{-\infty}^{\infty} F(u, v) e^{i2\pi(ux+vy)} du dv$$

$$\text{(equation 2) } F(u, v) = \iint_{-\infty}^{\infty} f(x, y) e^{-i2\pi(ux+vy)} dx dy$$

and its properties when conducting operations such as convolutions of the original data with filter functions e.g. equation 3 becomes simple multiplication (equation 4) in frequency domain.

$$\text{(equation 3) } g(x, y) = \iint_{-\infty}^{\infty} f(x - \alpha, y - \beta) w(\alpha, \beta) d\alpha d\beta$$

$$\text{(equation 4) } G(u, v) = \iint_{-\infty}^{\infty} F(u, v) W(u, v)$$

The transform into wavenumber domain is usually implemented in most computer systems as Fast Fourier Transform (FFT) of discrete 2D grids. The operation requires pretreatment of the data including trend removal, grid expansion to produce a smoothly periodic square grid, and grid filling of data voids within the grid. The filter functions are simply multiplied by the transformed grid to produce a filtered transformed grid, which is then transformed back to space domain.

Reduction to the pole of the magnetic data is used to simplify the interpretation of the magnetic anomalies as it centers the peaks of the anomalies over their sources and eliminates the dipolar effect that magnetic anomalies exhibit because of the orientation of the Earth's magnetic field. The filter function for the reduction to the pole is given in equation 5.

(equation 5)

$$W(\theta) = \frac{[\sin(I) - i \cdot \cos(I) \cdot \cos(D - \theta)]^2}{[\sin^2(Ia) + \cos^2(Ia) \cdot \cos^2(D - \theta)] \cdot [\sin^2(I) + \cos^2(I) \cdot \cos^2(D - \theta)]}, \text{ if } (|Ia| < |I|), Ia = I$$

where: $\theta$	$\theta = \tan^{-1}(u/v)$ wavenumber direction in degrees of azimuth
$I$	geomagnetic inclination
$Ia$	inclination for magnitude correction (never less than $I$ )
$D$	geomagnetic declination
$i$	$i = \sqrt{-1}$

The reduction to the pole was applied to the magnetometry data before further filtering processes. As the study area lies close to the equator the magnitude correction for N-S oriented features would be exaggerated and thus a magnitude inclination of 90 degrees was used, which meant that only the phase component was applied to the original data. The correction still resulted in enhancing the inherent noise in the data and caused declination oriented striping, thus a directional cosine filter was applied (equation 6) in order to remove the high frequency artifacts oriented along the declination (~-5.4 degrees).

(equation 6)  $W(\theta) = \left| \cos^n \left( \alpha - \theta + \frac{\pi}{2} \right) \right|$ , where  $\alpha$  is the direction to reject and  $n$  is a parameter controlling the falloff rate of the filter

Subsequently derivatives in the X, Y, and Z directions were computed using the following filter functions  $W(u) = (ui)$ ,  $W(v) = (vi)$ , and  $W(r) = r$ , where  $u$  is the X component of the wavenumber,  $v$  is the Y component of the wavenumber, and  $r$  corresponds to the wavenumber (radians/unit). These filtered grids were used to enhance shallow geologic sources in the data such as lithological boundaries and structural features (Blakely and Simpson, 1986; Miller and Singh, 1994) sought for in the litho-structural map.

The analytical signal (AS) corresponds to complex field intensity due to a complex potential (Nabighian, 1972). Its absolute amplitude

$$\text{(equation 7)} |A(x, y)| = \sqrt{\left(\frac{\partial f}{\partial x}\right)^2 + \left(\frac{\partial f}{\partial y}\right)^2 + \left(\frac{\partial f}{\partial z}\right)^2}$$

was shown to be independent of field inclination and declination, the dip of the contacts, and any remanent magnetization. In low latitudes the AS provides means for centering the anomaly over its source and eliminating the dipolar effect, which may prove beneficial during the interpretation. The drawbacks are that the centers are in fact broader and less well defined and thus may result in positional errors.

The potential field tilt derivative and its total horizontal derivative (Miller and Singh, 1994; Verduzco et al., 2004; and Pilkington, 2008) were also computed as these enhance equally well low and high amplitude anomalies. The tilt and its derivative were computed according to (equations 8 and 9).

$$\text{(equation 8) } TDR = \tan^{-1} \left[ \frac{\frac{\partial f}{\partial z}}{\sqrt{\left(\frac{\partial f}{\partial x}\right)^2 + \left(\frac{\partial f}{\partial y}\right)^2}} \right]$$

$$\text{(equation 9) } THDR_{TDR} = \sqrt{\left(\frac{\partial TDR}{\partial x}\right)^2 + \left(\frac{\partial TDR}{\partial y}\right)^2}$$

To most of the grids, shading was applied to produce shaded relief grids (Burrough and McDonnel, 1988) in order to enhance features oriented in different directions. The amplitude or intensity of the derived values was usually displayed with the help of color scales.

## Principal component analysis

Principal component analysis (PCA) is frequently used in dimension reduction and interpretation of multivariate data in statistics and geostatistics (Davis, 2002; Wackernagel, 2003) and is well known and utilized in remote sensing (Campbell, 1996; Pratt, 2007) or geophysical data interpretation (Harris et al., 1987). The primary goal of the PCA is a linear transformation of a set of correlated variables  $Z$  into a set of uncorrelated components  $Y$ , which are formed in the order of decreasing explained variance of the original set of variables. The method is based on the analysis of the variance-covariance matrix  $V$  and the determination of a matrix of eigenvectors  $Q$  and eigenvalues  $\Lambda$  such that

$$\text{(equation 10) } VQ = Q\Lambda, \text{ where } Q^T Q = I \text{ and } I \text{ corresponds to the identity matrix.}$$

The corresponding uncorrelated components are then defined as in

$$\text{(equation 11) } Y = ZQ.$$

When data are of different scales, the correlation matrix is used instead of the variance-covariance matrix. The Principal components were computed for the gamma-ray spectrometric data after the analysis of correlation matrix, which revealed the mutual dependence of the gamma-ray spectrometric channels. A color combination of the resulting first three principal components was used for the interpretation.

## Landsat 7 ETM+ and ASTER data processing

The optical remote sensing data from the Landsat 7 ETM+ and ASTER sensors required both similar processing steps. The Landsat 7 ETM+ L1T product has been received already orthorectified using an elevation model (SRTM) (NASA, 2008). The accuracy of the orthorectified image proved to be acceptable after inspection of the image in the field and comparisons with GPS measurements of known features and thus it was decided to use the Landsat images as base data to which all of the other data were georeferenced.

The orthorectification of the ASTER data was conducted using the rational polynomial coefficient (RPC) orthorectification model (Grodecki and Dial, 2003), which was enhanced by selecting 5 ground control points per an ASTER scene from the Landsat 7 images and introduction of the SRTM-3 digital elevation model data. The root mean square error (RMSE), which describes the fit of the transformation at the selected ground control points, was maintained below 15 m for all of the orthorectified ASTER scenes.

## Atmospheric correction

The atmospheric correction of the data was completed using the ATCOR-2 software (Richter, 1996), which builds on the MODTRAN-4 radiative transfer model code (Berk et al., 1998) and uses LUTs (lookup tables) of selected model atmospheres to conduct the correction. The radiance signal gathered by a remote sensing system consists of three components

$$\text{(equation 10) } L = L_{path} + L_{reflected} + L_{adjacency}.$$

The radiance at sensor  $L$  usually has to be computed from the recorded digital number (DN), as calibrations, digitizing and data compression occurs during the acquisition of the data. The radiance is then derived with the help of

(equation 11)  $L = c_0 + c_1 \cdot DN$ , where  $c_0$  and  $c_1$  correspond to radiometric calibration coefficients. To obtain the surface reflectance  $\rho$  from the acquired data, the following equation has to be solved

$$\text{(equation 12) } \rho = \frac{\pi\{d^2(c_0+c_1 \cdot DN)-L_{path}\}}{\tau E_g},$$

where  $d$  corresponds to the sun to earth distance,  $\tau$  to the ground-to-sensor atmospheric transmittance, and  $E_g$  to global flux on the ground. The atmospheric correction was enhanced using acquired ground spectra during in-flight calibration (Richter, 1997).



## ALOS PALSAR and Radarsat 2 data processing

Both ALOS PALSAR and Radarsat 2 data represent fully polarimetric radar data and require slightly different processing steps than regular radar data. Radar polarimetry examines the polarization state of an electromagnetic field. Before actual image analysis, the data need to be extracted into the elements of the scattering (Sinclair) matrix

$$\text{(equation 13)} [S] = \begin{bmatrix} S_{HH} & S_{HV} \\ S_{VH} & S_{VV} \end{bmatrix} \text{ expressed in the linear (H,V) basis or coherency matrix}$$

$$\text{(equation 14)} [T] = \underline{k} \cdot \underline{k}^{*T}, \text{ where the Pauli spin elements } \underline{k} \text{ are expressed in vector form as}$$

$$\text{(equation 15)} \underline{k} = \frac{1}{\sqrt{2}} [S_{HH} + S_{VV} \quad S_{HH} - S_{VV} \quad 2S_{HV}]^T \text{ (when reciprocity is assumed, i.e. } S_{HV} = S_{VH}).$$

These matrices thoroughly describe the scattering process. Advanced concepts in polarimetry may be found by consulting the works of Lee and Pottier (2009) or van Zyl (2011). During the extraction of the components multilooking may be performed. Multilooking uses the fact that the radar system obtains more observations in the azimuth direction (along track direction of the satellite) than in the range direction (across track direction of the satellite). The multilooking procedure averages the observations in the azimuth direction.

## Polarimetric decompositions

Polarimetric decompositions are used in order to express the measured scattering matrix, i.e. [S] or [T], as a combination scattering responses of simpler objects, according to

$$\text{(equation 13)} [S] = \sum_{i=1}^k c_i [S]_i$$

, where  $[S]_i$  represents the scattering response of the objects and  $c_i$  stands for a weighting parameter. A number of decompositions has been proposed by different authors for a review see Cloude and Pottier (1996) or van Zyl (2011).

One of the frequently used decompositions, the Pauli decomposition, was produced during the processing of the polarimetric radar and used for further classifications. The Pauli decomposition expresses the scattering matrix in the so-called Pauli basis (Cloude and Pottier, 1996), which is given by four 2x2 matrices

$$[S]_a = \frac{1}{\sqrt{2}} \begin{bmatrix} 1 & 0 \\ 0 & 1 \end{bmatrix}, [S]_b = \frac{1}{\sqrt{2}} \begin{bmatrix} 1 & 0 \\ 0 & -1 \end{bmatrix}, [S]_c = \frac{1}{\sqrt{2}} \begin{bmatrix} 0 & 1 \\ 1 & 0 \end{bmatrix}, [S]_d = \frac{1}{\sqrt{2}} \begin{bmatrix} 0 & -1 \\ 1 & 0 \end{bmatrix}, \text{ under the}$$

concept of reciprocity, only first three matrices are needed. Consequently, the scattering matrix [S] may be expressed as span (absolute power) of [S],

$$\text{(equation 14)} SPAN = |S_{HH}|^2 + |S_{VV}|^2 + 2|S_{HV}|^2 = |\alpha|^2 + |\beta|^2 + |\gamma|^2.$$

The interpretation of the Pauli decomposition is straightforward. In a RGB color image, the three intensities from (equation 14) are used. The physical meaning of the three intensities is as follows the  $|\alpha|^2$  corresponds to targets characterized by single- bounce (e.g. flat surfaces), the  $|\beta|^2$

stands for double-bounce scattering (e.g. corner reflectors), and  $|\gamma|^2$  represents volume scattering (e.g. forest canopy).

## Classification methodology

Two classification approaches were tested during the evaluation of an automatic approach to the classification of the regolith. The classifications present two different approaches to the decision boundary definition in feature space. The maximum likelihood classification represents the linear approach while the neural network algorithm the non-linear approach.

### Maximum likelihood classification

The maximum likelihood/Bayesian classifier is based on the probability that a pixel belongs to a specific class. The equations used in this method assume that all of the input variables have normal distributions. The Bayesian decision rules represent essentially linear hyperplanes that separate the feature space into classes. The maximum likelihood/Bayesian classifier used in the classification process utilized the following discriminant function

$$\text{(equation 13) } D = \ln(a_i) - \left[ \frac{1}{2} \ln(|V_i|) \right] - \left[ \frac{1}{2} (x - m_i)^T (V_i^{-1}) (x - m_i) \right]$$

Where:

$D$	weighted distance
$x$	the measurement vector of the candidate pixel
$m_i$	the mean vector of the sample of class $i$
$a_i$	percent probability that any candidate pixel is a member of class $i$
$V_i$	the variance-covariance matrix of the pixels in the sample of class $i$
$ V_i $	determinant of $V_i$
$V_i^{-1}$	inverse of $V_i$

to assign a pixel to the class  $i$ , for which  $D$  is the lowest. The maximum likelihood classification is one of the most powerful classification techniques, but it is strongly affected by the quality of the training patterns and the assumption that the input variables have normal distributions (Campbell, 1996). It takes into account the variability of classes by using the variance-covariance matrix in the computation.

### Neural networks

An artificial neural network can be described as classification tool, which is mapping an input space into an output space (Priddy and Keller, 2005), using interconnected sets of mathematical

functions. The networks are composed of neurons, which are modeled by neurons whose input variables are assigned weights and outputs are transformed by transfer functions so that the net output of a neuron corresponds to

$$\text{(equation 14) } o_j^l = f_j^l(\text{net}_j^l) = f_j^l\left(\sum_{i=1}^{N^{l-1}} w_{ji}^l o_i^{l-1} + w_{j0}^l\right),$$

where:

$o_j^l$	output of $i^{\text{th}}$ neuron in $l^{\text{th}}$ layer
$f_j^l$	activation function for the $j^{\text{th}}$ neuron in $l^{\text{th}}$ layer
$\text{net}_j^l$	net stimulus to the $i^{\text{th}}$ neuron in $l^{\text{th}}$ layer
$N^l$	number of neurons in the $l^{\text{th}}$ layer
$w_{j0}^l$	neuron bias term written as a weight to a unitary input
$w_{ji}^l$	weights linking the $i^{\text{th}}$ neuron in the $l-1^{\text{st}}$ layer to the $j^{\text{th}}$ neuron in the $l^{\text{th}}$ layer

The commonly used transfer functions are for example the sigmoid function, which was used during the classification process,

$$\text{(equation 15) } z = \frac{1}{1+e^{-(\sum_i w_i x_i + w_0)}}$$

or the logistic function. Both of these functions are monotonous, continuous, and differentiable. These properties are important in the course of training of the network with error backpropagation (Verbos, 1994). The used classification used a multiperceptron 3-layer feedforward network with one input layer, one hidden layer and one output layer. Feedforward networks are formed by layers of neurons, which directly feed inputs to the next layer in the network. The data were first normalized between zero and one using the min-max normalization given by

$$\text{(equation 16) } 'x_i = \frac{(x_i - \min_x)}{(\max_x - \min_x)}$$

to form the input layers to the network. The network was trained during supervised training using the error backpropagation. The training consisted of several steps: (1) input training vector  $x$  was passed into the network while the weights were initialized using the Nguyen-Widrow algorithm (1990). (2) The network computed the first mapping using the initialized weights and calculated the error between the target and actual output according to

$$\text{(equation 17) } E_p = \frac{1}{2} \sum_{j=1}^{N^L} (t_{pj} - y_{pj})^2.$$

The error was then backpropagated through the network and the weights were updated in an iterative manner according to

$$\text{(equation 19) } \Delta w_{pji}^l(n) = \mu o_{pj}^l o_{pi}^{l-1} + \varphi \Delta w_{pji}^l(n-1)$$

where:

$E_p$	total output error when pattern $p$ is presented
$N^l$	number of neurons in the $l^{\text{th}}$ layer
$t_{pj}$	target output for the $j^{\text{th}}$ neuron in the final layer when pattern $p$ is presented
$y_{pj}$	output of the $j^{\text{th}}$ neuron in the final layer when pattern $p$ is presented
$\Delta w_{pji}^l$	weight update for the connection linking the $i^{\text{th}}$ neuron in the $(l-1)^{\text{st}}$ layer to the $j^{\text{th}}$ neuron in the $l^{\text{th}}$ layer, when training pattern $p$ is presented
$\mu$	learning rate
$o_{pj}^l$	output of the $j^{\text{th}}$ neuron in the $l^{\text{th}}$ layer
$n$	the iteration number
$\varphi$	the momentum

The learning rate  $\mu$  of the network was supplied to the network during training, to control the speed of the convergence rate of the algorithm, while the momentum parameter assured that the network did not terminate in a local minimum due to the nature of the iterative process. (3) The training process terminated by meeting a criterion imposed on the error parameter  $E$ , which is the sum of the errors for all presented patterns

$$\text{(equation 19) } E = \sum_{p=1}^P E_p.$$

The actual classification was performed for each pixel value by passing through the trained network.

## Accuracy assessment

During classification of remote sensing data, it is often necessary to quantify the accuracy of the process. Accuracy assessment requires comparisons to be made between the results of a classification and available reference data. The reference data should not be used during the training of the classifier. For multiclass classifications, performed during the regolith landform mapping, the accuracy assessment utilized the concept of confusion or error matrices (figure 1), which was proposed by Congalton (1991). A confusion matrix thoroughly summarizes the agreement between the produced classification and the reference data. The overall accuracy (OA), the sum of the diagonal divided by number of samples, is one of the most commonly used values when describing the accuracy assessment results. However, both the producer's accuracy (PA) and user's accuracy (UA) are useful measures, which explain how well the classification performed for the individual classes.

		$j = \text{Columns}$			$\text{Row}$
		$(\text{Reference})$			$\text{Total}$
		$1$	$2$	$k$	$n_{i+}$
$i = \text{Rows}$ (Classification result)	$1$	$n_{11}$	$n_{12}$	$n_{1k}$	$n_{1+}$
	$2$	$n_{21}$	$n_{22}$	$n_{2k}$	$n_{2+}$
	$k$	$n_{k1}$	$n_{k2}$	$n_{kk}$	$n_{k+}$
Column Total	$n_{+j}$	$n_{+1}$	$n_{+2}$	$n_{+k}$	$n$

**Figure 1** Mathematical concept of a confusion/error matrix modified from Congalton and Green (2008).

where:

$n_{i+} = \sum_{j=1}^k n_{ij}$  number of samples classified into category  $i$  in the performed classification

$n_{+j} = \sum_{i=1}^k n_{ij}$  number of samples classified into category  $j$  in the reference data set

$OA = \frac{\sum_{i=1}^k n_{ii}}{n}$  overall accuracy

$PA = \frac{n_{jj}}{n_{+j}}$  producer's accuracy of category  $j$

$UA = \frac{n_{ii}}{n_{i+}}$  user's accuracy of category  $i$

The Kappa analysis, actually an estimate of kappa, a KHAT statistic ( $\hat{K}$ ), which was also used in the accuracy assessment draws on the properties of the error matrix and can be computed according to

$$(\text{equation 20}) \hat{K} = \frac{n \sum_{i=1}^k n_{ii} - \sum_{i=1}^k n_{i+} n_{+i}}{n^2 - \sum_{i=1}^k n_{i+} n_{+i}}$$

The KHAT statistic is a measure for determining if one error matrix is significantly different from another (Cohen, 1960). The quantification of agreement is based on the difference between the actual agreement in the error matrix (the major diagonal) and the chance agreement, the row and column totals (marginals) (Congalton and Green, 2009). The ‘‘Kappa coefficient’’ (as it is often called) is usually presented as the percent of reduction in error generated by a classification when compared with the error of a completely random classification.

---

## References

- Berk, A., Bernstein, L.S., Anderson, G.P., Acharya, P.K., Robertson, D.C., Chetwynd, J.H., Adler-Golden, S.M., 1998. MODTRAN cloud and multiple scattering upgrades with application to AVIRIS, *Remote Sens. Environ.*, 65, 367–375.
- Blakely, R.J., Simpson, R.W., 1986. Approximating edges of source bodies from magnetic or gravity anomalies. *Geophysics* 51, 1494–1498.
- Burrough, P.A., McDonell, R.A., 1998. *Principles of Geographical Information Systems*, Oxford University Press, New York.
- Campbell, J. B., 1996, *Introduction to Remote Sensing*, 2nd ed., The Guilford Press, New York.
- Cloude, S.R., Pottier, E., 1996. A review of target decomposition theorems in radar polarimetry. *IEEE Trans. Geosci. Remote Sens.* 34, 498–518.
- Cohen, J., 1960. A coefficient of agreement for nominal scales, *Educ. Psychol. Measurement*, 37–46.
- Congalton, R.G., 1991. A review of assessing the accuracy of classifications of remotely sensed data. *Remote Sens. Environ.* 37, 35–46.
- Congalton, R.G., Green, K., 2009. *Assessing the accuracy of remotely sensed data: principles and practices*. 2nd ed. Taylor and Francis, Boca Raton.
- Davis, J. C. 2002. *Statistics and Data Analysis in Geology*. John Wiley and Sons, New York.
- Grodecki, J., Dial, G., 2003. Block adjustment of high-resolution satellite images described by rational polynomials, *Photogram. Eng. Remote Sens.*, 69, 59–68.
- Harris, J.R., Neily, Pultz, T., Slaney, V.R., 1987. Principal component analysis of airborne geophysical data for lithologic discrimination using an image analysis system, *International Symposium on Remote Sensing of Environment*, 20th, Nairobi, Kenya; 4-10 Dec. 1986, 641–657.
- Lee, J.S., Pottier, E., 2009. *Polarimetric radar imaging: from basics to applications*, *Optical science and engineering*, Vol. 142, CRC Press, Taylor and Francis, Boca Raton.
- Li, Y. and Oldenburg, D.W., 1998. Separation of regional and residual magnetic field data. *Geophysics*, 63, 431–439.
- Miller, H.G., Singh, V., 1994. Potential field tilt-a new concept for location of potential field sources. *J. Appl. Geophys.* 32, 213–217.
- Nabighian, M.N., 1972. The analytic signal of two-dimensional magnetic bodies with polygonal cross-section: Its properties and use for automated anomaly interpretation. *Geophysics*, 37, 507–517.
- Nguyen, D., Widrow, B., 1990. Improving the learning speed of 2-layer neural networks by choosing initial values of the adaptive weights. *Proceedings of the International Joint Conference on Neural Networks*, 21–26.

- Pilkington, M., Keating, P.B., 2009. The utility of potential field enhancements for remote predictive mapping. *Can. J. Remote Sensing* 35, Suppl. 1, S1–S11.
- Pratt, W.K., 2007. *Digital image processing*, 4th ed., John Wiley and Sons, Hoboken.
- Priddy, K.L., Keller, P.E., 2005. *Artificial neural networks: an introduction*, SPIE, Washington.
- Richter, R., 1996. Atmospheric correction of satellite data with haze removal including a haze/clear transition region. *Comput. Geosci.* 22, 675–681.
- Richter, R., 1997. On the in-flight absolute calibration of high spatial resolution spaceborne sensors using small ground targets. *Int. J. Remote Sens.* 18, 2827–2883.
- Telford, W.M., Geldart, L.P., Sheriff, R.E., 1990. *Applied geophysics*, 2nd ed., Cambridge University Press, Cambridge.
- Verbos, P.J., 1994. *The roots of backpropagation*, John Wiley and Sons, New York.
- Verduzco, B., Fairhead, J.D., Green, C.M., MacKenzie, C., 2004. New insights into magnetic derivatives for structural mapping. *The Leading Edge* 23, 116–119.
- Wackernagel, H., 2003. *Multivariate geostatistics: an introduction with applications*, 3rd ed., Springer, Heidelberg.
- Zyl, J.J., 2011. *Synthetic Aperture Radar Polarimetry*. John Wiley and Sons, Hoboken.